UNIVERSITY OF CALIFORNIA

Los Angeles

Optic Nerve Deformation by Eye Movements

A dissertation submitted in partial fulfillment of the requirements for the degree of Doctor of Philosophy (PhD) in Bioengineering in the Graduate School of Engineering of the University of California, Los Angeles.

by

Alan Le

2020

ABSTRACT OF THE DISSERTATION

Optic Nerve Deformation by Eye Movements

by

Alan Le

Doctor of Philosophy in Bioengineering

University of California, Los Angeles, 2020

Professor Joseph L. Demer, Co-Chair

Professor Wentai Liu, Co-Chair

Ocular rotation can cause mechanical deformation of the optic nerve head and surrounding tissues. During extreme angles of gaze, the optic nerve can become stretched and impose strain on other ocular tissues. Over a lifetime, the ill effects of repetitive mechanical injury from large adduction can compound, resulting in progressive optic neuropathy in some glaucoma patients.

We investigated the etiology of this form of glaucoma through a series of papers focusing on anatomical analysis of the human optic nerve from donated tissue and clinical studies utilizing optical coherence tomography (OCT) and confocal scanning laser ophthalmoscopy (cSLO). The

optic nerve is surrounded and protected by a bi-layered dural sheath that bears the bulk of exerted mechanical force. Elastin fibers embedded within the sheath and peripapillary tissues around the nerve head form a three-dimensional meshwork that reinforces the tissue against mechanical strain. While the tissue at the globe optic nerve junction is heavily fortified with organized layers of collagen and elastin fibers, irregularities in the elastin fiber arrangement resulting in large dense elastin deposits were observed to correlate with older age. These elastin deposits could be a pathologic byproduct of optic nerve injury from mechanical strain, or serve as a protective mechanism to further reinforce the ocular tissues.

In OCT studies, adduction of angles beyond 26° caused marked deformation of the peripapillary tissues around the optic nerve head, and choroidal volume change. cSLO imaging showed similar deformations of the retina surface during large angle adduction. Ocular tissue of younger subjects appears more compliant, while those of glaucoma patients were stiffer and thus experienced less deformation.

We explored possible therapies for optic nerve traction during eye movement. Using collagen crosslinking to fortify ocular tissue, we observed that exposure to riboflavin and UV light can stiffen scleral tissue. In addition, we investigated whether prostaglandin agonists could be used to reduce ocular fat and found that topical administration of these agonists had insignificant effects on the retrobulbar fat.

The dissertation of Alan Le is approved.

Jean-Pierre Hubschman

Ben J. Glasgow

Wentai Liu, Committee Co-Chair

Joseph L. Demer, Committee Co-Chair

University of California, Los Angeles

2020

Table of Contents

List of Acronyms

AB	abduction
AD	adduction
ARVO	Association for Research in Vision and Ophthalmology
BMO	Bruch's membrane opening
BVs	blood vessels
CF	circumferential fibers
CH	corneal hysteresis
CPS	circumferential peripapillary sclera
cSLO	scanning laser ophthalmoscope
DF	diagonal fibers
EDI	enhanced depth imaging
EVG	van Gieson’s elastin
FEA	finite element analysis
GEE	generalized estimating equations
IL	inner layer
IOP	intraocular pressure
LC	lamina cribrosa
LF	longitudinal fibers
MRI	magnetic resonance imaging
MT	Masson's trichrome
nBMO	nasal Bruch's membrane opening
NTG	normal tension glaucoma
OC	optic cup
OL	outer layer
ONH	optic nerve head
ONS	optic nerve dural sheath
POAG	primary open angle glaucoma
PPA	peripapillary atrophy
ppBM	peripapillary Bruch's membrane
ppC	peripapillary choroid
PPR	peripapillary retina
RNFL	retinal nerve fiber layer
SD	standard deviation
SEM	standard error of the mean
tBMO	temporal Bruch's membrane opening
TIFF	tagged image file format
UV	ultra violet
YM	Young's modulus

Acknowledgements

My thanks go out firstly to Dr. Demer who has through the years shown me many creative approaches to tackle the challenges of science and for providing virtually unlimited resources to build the most fantastical computer systems. To Dr. Hubschman, whose clinic was where my journey in ophthalmology first began and where I met my wife. Thank you Dr. Glasgow for the many conversations about topics beyond my comprehension and always guiding me to the more pragmatic path, and Dr. Liu whose Neuroengineering course gave me the proper segue from my neuroscience background to an engineering career.

My work through the years would not have been possible if not for the many undergraduate students who've come and gone. Most notable are Ayesha Baig and Jessica Chen. Thanks to Ayesha for sticking out in lab with me for last minute ARVO deadlines and poster making. And tremendous appreciation and respect goes to Jessica, who raised the bar for all undergrads as a freshman and whose collaboration with has resulted in my most productive period as a graduate student. I also would like to thank the many other past and present lab members: Nicolasa DeSalles, Andrew Shin, Lawrence Yoo, Zia Chaudhuri, Soh Youn Suh, Rui Hao, Joseph Park, Dave Burgess and Yolanda McNair.

Lastly, I like to thank my wife for sticking by me through the years and whose presence is always a joy in my life, and my parents for their encouragement of a progression forward.

The following thesis is comprised of multiple published and under manuscripts. Dr. Demer served as the PI for all works included. Chapter 1 includes versions of Le A, Shin A, Park J, Poukens V, Demer JL. Bilaminar structure of the human optic nerve

sheath. Curr Eye Res. 2020 Mar 16:1-9. doi: 10.1080/02713683.2020.1739314. Epub ahead of print. PMID: 32155090 and Shin A, Park J, Le A, Poukens V, Demer JL Bilaminar mechanics of the human optic nerve sheath. Curr Eye Res. 2019, doi: 10.1080/02713683.2019.1701689. Dr. Poukens processed the histology, Dr. Shin and myself performed the experiments and each primarily wrote our first author manuscript. Park aided in mechanical tests and manuscript preparation.

Chapter 2 includes versions of the following works:
Suh SY, Le A, Shin A, Park J, Demer JL. Progressive deformation of the optic nerve head and peripapillary structures by graded horizontal duction. Invest Ophthalmol Vis Sci. 2017;58:5015-21. Dr. Suh and myself performed OCT scans and analyzed the data. Shin and Park provided guidance on mechanical properties of tissues.

Chen JY, Le A, De Andrade LM, Goseki T, Demer JL. Compression of the Choroid by Horizontal Duction. Invest Ophthalmol Vis Sci. 2019 Oct 1;60(13):4285-4291. doi:10.1167/iovs.19-27522. All authors helped perform OCT scans. Chen and I completed the image analysis.

Le A, Chen J, Lesgart M, Gawargious BA, Suh SY, Demer JL. Age-dependent Deformation of the Optic Nerve Head and Peripapillary Retina by Horizontal Duction. Am J Ophthalmol. 2020 Jan;209:107-116. doi:10.1016/j.ajo.2019.08.017. Epub 2019 Aug 29. I and Chen acquired the data via OCT scans with assistance from Lesgart, Gawargious and Dr. Suh.

Le A, Chen JY, Caprioli J, Giaconi JA, Nouri-Mahdavi K, Law SK, Bonelli L, Coleman AL, Demer JL. Adduction Deformation of Optic Disc and Peripapillary Region in Primary Open Angle Glaucoma with Normal Intraocular Pressure. Summited to Current Eye Research, 2020. I and Chen acquired and analyzed the data. Caprioli, Giaconi, Nouri-

Mahdavi, Law, Bonelli, and Coleman help recruit subjects and provided medical guidance.

Le A, Chen JY, Caprioli J, Giaconi JA, Nouri-Mahdavi K, Law SK, Bonelli L, Coleman AL, Demer JL. Peripapillary Atrophy and Optic Disc Stiffening in Primary Open Angle Glaucoma at Normal Intraocular Pressure. Summited to Current Eye Research, 2020.I and Chen acquired OCT scans and analyzed the data. Caprioli, Giaconi, Nouri-Mahdavi, Law, Bonelli, and Coleman help recruit subjects and provided medical guidance.

Chapter 3 includes versions of the following:
Gawargious B, Le A, Lesgart M, Ugardar S, Demer JL. Differential Regional Stiffening of Sclera by Collagen Cross-linking. Curr Eye Res.10.1080/02713683.2019.1694157. I, Gawargious, and Lesgart performed the experiment and authored the paper. Ugardar provided specimen and medical guidance.

Chen JY, Le A, Caprioli J, Giaconi JA, Nouri-Mahdavi K, Law SK, Bonelli L, Coleman AL, Demer JL. Orbital Fat Volume After Treatment with Topical Prostaglandin Agonists. Summited to *Current Eye Research*. I and Chen analyzed the data and cowrite the manuscript. Caprioli, Giaconi, Nouri-Mahdavi, Law, Bonelli, and Coleman help recruit subjects and provided medical guidance.

Research for this thesis was supported by U.S. Public Health Service, National Eye Institute Grants EY008313 and EY000331, and an unrestricted grant from Research to Prevent Blindness.

Vita

Education

B.S. Neuroscience University of California, Los Angeles 2009

Publications

Le A, Shin A, Park J, Poukens V, Demer JL. Bilaminar structure of the human optic nerve sheath. Curr Eye Res. 2020 Mar 16:1-9. doi: 10.1080/02713683.2020.1739314. Epub ahead of print. PMID: 32155090

Le A, Chen J, Lesgart M, Gawargious B, Suh SY, Demer JL. Age-dependent deformation of the optic nerve head and peripapillary retina by horizontal duction. Am J Ophthalmol. 2020 Jan;209:107-116. doi: 10.1016/j.ajo.2019.08.017. Epub 2019 Aug 29. PMID: 31472159

Le A, Poukens V, Ying H, Rootman D, Goldberg RA, Demer JL. Compartmental innervation of the superior oblique muscle in mammals. Invest Ophthalmol Vis Sci. 2015 Oct;56(11):6237-46. doi: 10.1167/iovs.15-17602. PMID: 26426404

Li Y, Wei Q, Le A, Gawargious BA, Demer JL. Rectus Extraocular Muscle Paths and Staphylomata in High Myopia. Am J Ophthalmol. 2019 May;201:37-45. doi: 10.1016/j.ajo.2019.01.029. Epub 2019 Feb 4. PMID: 30731081; PMCID: PMC6511469.

Ugradar S, Le A, Lesgart M, Goldberg RA, Rootman D, Demer JL. Biomechanical and Morphologic Effects of Collagen Cross-Linking in Human Tarsus. Transl Vis Sci Technol. 2019 Dec 5;8(6):25. doi: 10.1167/tvst.8.6.25. PMID: 31832279; PMCID: PMC6900964.

Suh SY, Clark RA, Le A, Demer JL. Extraocular Muscle Compartments in Superior Oblique Palsy. Invest Ophthalmol Vis Sci. 2016 Oct 1;57(13):5535-5540. doi: 10.1167/iovs.16-20172. PMID: 27768791; PMCID: PMC5080936.

Chen JY, Le A, De Andrade LM, Goseki T, Demer JL. Compression of the Choroid by Horizontal Duction. Invest Ophthalmol Vis Sci. 2019 Oct 1;60(13):4285-4291. doi: 10.1167/iovs.19-27522. PMID: 31618765.

Gawargious BA, Le A, Lesgart M, Ugradar S, Demer JL. Differential Regional Stiffening of Sclera by Collagen Cross-linking. Curr Eye Res. 2019 Nov 21:1-8. doi: 10.1080/02713683.2019.1694157. Epub ahead of print. PMID: 31735063.

Shin A, Park J, Le A, Poukens V, Demer JL. Bilaminar Mechanics of the Human Optic Nerve Sheath. Curr Eye Res. 2019 Dec 17:1-10. doi: 10.1080/02713683.2019.1701689. Epub ahead of print. PMID: 31821056.

Hao R, Suh SY, Le A, Demer JL. Rectus Extraocular Muscle Size and Pulley Location in Concomitant and Pattern Exotropia. Ophthalmology. 2016 Sep;123(9):2004-12. doi: 10.1016/j.ophtha.2016.05.053. Epub 2016 Jul 19. PMID: 27448831; PMCID: PMC4995140.

Suh SY, Le A, Clark RA, Demer JL. Rectus Pulley Displacements without Abnormal Oblique Contractility Explain Strabismus in Superior Oblique Palsy. Ophthalmology. 2016 Jun;123(6):1222-31. doi: 10.1016/j.ophtha.2016.02.016. Epub 2016 Mar 13. PMID: 26983977; PMCID: PMC4877286.

Biosketch

Alan Le has a bachelor degree in Neuroscience from the University of California, Los Angeles. He has published work on the intramuscular innervation of the extraocular muscles with 3-D rendered models of ocular tissues from magnetic resonance imaging (MRI) and histologic sections, and optical coherence tomography (OCT) studies of optic nerve deformation caused by horizontal duction. He has developed novel techniques to automate image analysis with custom Python and ImageJ code. Alan is currently a senior software engineer at Alcon involved in development of OCT diagnostic medical devices.

Introduction

Progressive optic neuropathy from glaucoma is a leading cause of blindness. An acute rise in intraocular pressure (IOP) pushes against and damages the optic nerve head. While this mechanism causes glaucoma in some patients, there are many around the world who do not exhibit high intraocular pressure, yet still suffer from progressive damage to the optic nerve head and peripapillary regions. Therapeutic attempts to lower IOP in these patients have yielded limited success. In some Asian countries, the majority of glaucoma patients do not have high IOP. These patients with seemingly normal IOP still exhibit nerve fiber layer loss and visual field defects that is characteristic of glaucoma.

This thesis explores another etiology of glaucoma: large angle eye rotation. In MRI studies, during large angle adduction, the optic nerve appears to straighten and become stretched. It is possible that traction from a taut optic nerve can induce mechanical deformation to the optic nerve head and surrounding tissues that will cause injury over a lifetime of cyclic eye rotations.

The following is a series of studies including published papers, international conference presentations, and under-review manuscripts that collectively explores the evidence for eye rotation-induced glaucoma. Chapter 1 focuses on anatomic studies of the ocular tissue. It comprises of two complementary papers on the dual-layered optic nerve sheath; the first focusing on the anatomic makeup of the optic nerve sheath that give rise to the biomechanical properties discussed in the second paper. In addition, excerpts from two Association for Research in Vision and Ophthalmology (ARVO) conference presentations are presented that highlight elastin structures in the laminar cribrosa, and elastin deposits in the peripapillary sclera.

Chapter 2 presents five papers that explores clinical evidence of optic nerve tethering utilizing optical coherence tomography (OCT) scans along with confocal scanning laser ophthalmoscopy (cSLO). Two OCT studies are presented: one measuring the deformation of Bruch's membrane and peripapillary structures, while the second quantifies deformation of the choroid during horizontal duction. Three manuscripts utilizing cSLO quantify the extent of retinal surface deformations in various age groups, diseased versus healthy subjects, and the relationship of deformation to peripapillary atrophy.

Chapter 3 explores remedies to the problem of optic nerve traction. Two papers are presented here. The first investigates collagen crosslinking as a means to reinforce ocular tissue to resist the damage from repetitive mechanical stress. The second is a study of the effectiveness of prostaglandin agonists that have shown to reduce orbital fat as a side effect in glaucoma patients. We investigated whether these drops have any effect on the retrobulbar orbital fat which could allow for retraction of the globe and alleviate strain from a taut optic nerve.

Chapter 1: Anatomical Studies of the Optic Nerve

The following studies explore the anatomical features of the optic nerve and their relationship with mechanical deformation. The first pair of papers, published in *Current Eye Research*, are complimentary as they focus on the bilaminar structure of the optic nerve sheath and the resulting biomechanics. Next is an evaluation on the elastin beams of the lamina cribrosa which was presented at ARVO in 2017, followed by a study on elastin deposits in the peripapillary sclera, presented at ARVO in 2018.

Publications included in this chapter by Candidate:

Published Journal Papers

1. **Le A**, Shin A, Park J, Poukens V, Demer JL. Bilaminar structure of the human optic nerve sheath. Curr Eye Res. 2020 Mar 16:1-9. doi: 10.1080/02713683.2020.1739314. Epub ahead of print. PMID: 32155090
2. Shin A, Park J, **Le A**, Poukens V, Demer JL Bilaminar mechanics of the human optic nerve sheath. Curr Eye Res. 2019, doi: 10.1080/02713683.2019.1701689.

1.1 Bilaminar Structure of the Human Optic Nerve Sheath

Alan Le[1,2], Andrew Shin[2,7], Joseph Park[1,2], Vadims Poukens[2],

and Joseph L. Demer[2-6]

[1]Department of Bioengineering, [2]Department of Ophthalmology and Stein Eye Institute, [3]Department of Neurology, [4]Neuroscience and [5]Bioengineering Interdepartmental Programs, [6]David Geffen Medical School at University of California, Los Angeles.

[7]Wellman Center for Photomedicine, Harvard Medical School and Massachusetts General Hospital, Boston.

1.1.1 Abstract

Purpose: We aimed to characterize the connective tissue microanatomy, elastin abundance, and fiber orientation in the human optic nerve sheath, also known as the optic nerve dura mater, for correlation with its biomechanical properties.

Methods: Seven whole human orbits aged 4-93 years, and five isolated human optic nerve sheaths aged 26-75 years were formalin fixed, paraffin embedded, coronally sectioned, stained by Masson trichrome and van Gieson's elastin methods, and analyzed quantitatively for elastin fiber abundance and orientation. Elastin area fraction was defined as area stained for elastin divided by total area.

Results: While unilaminar in children, the adult ON sheath exhibited distinct inner and outer layers. Collagen was denser and more compact in the inner layer. Elastin area fraction was significantly greater at 6.0±0.4% (standard error of mean, SEM) in the inner than outer layer at 3.6±0.4% ($P<10^{-5}$). Elastin fibers had three predominant orientations: longitudinal, diagonal, and circumferential. Of circumferential fibers, 63±4.7% were in the inner and 37±4.7% in the outer layer ($P<10^{-4}$). Longitudinal and diagonal fibers were uniformly distributed in both layers. Elastin density and sheath thickness increased significantly with age ($P<0.01$).

Conclusions: The adult human optic nerve sheath is bilaminar, with each layer containing elastin fibers oriented in multiple directions consistent with isotropic properties. Differences in laminar elastin density and orientation may reflect greater tensile loading in the inner than outer layer.

1.1.2 Introduction

It has recently been recognized that length of the optic nerve (ON) is not quite sufficient to permit adduction of the eye without tethering it[1]. Magnetic resonance imaging (MRI) in multiple gaze positions demonstrates that the ON of the adducting eye becomes straightened when its length redundancy is exhausted[1], and that further adduction shifts the globe center medially in healthy subjects, or retracts the globe in chronic open angle glaucoma[2]. Although the range of human horizontal eye movements is approximately ±55° [3], and 25-45°saccades are not infrequent in daily life[4], optical coherence tomography (OCT) demonstrates that gaze-related optic disc and peripapillary deformations[5] increase markedly for adduction exceeding about 26° [6], consistent with MRI showing this angle to be the average onset of tethering. Subjects touching targets in a laboratory setting made saccades up to 40-45°.[7] Saccadic eye movements are ubiquitous: three saccades typically occur every second[8], amounting ~183,000 saccades daily[9], not even ceasing during sleep[10]. When sufficient adduction tethers the ON, reaction force to medial rectus contraction is exerted on the eye by the ON and its sheath, implying that these tissues must have mechanical properties sufficient to withstand hundreds of millions of rapid and vigorous mechanical perturbations over a lifetime.

While myelination and glial composition of the ON itself are characteristic of the central nervous system rather than peripheral nerve, ON microanatomy differs markedly from brain and spinal cord. Unlike the central nervous system proper, the ON contains a dense, intrinsic network of connective tissue that comprises as much as 30% of its total cross section[11] and makes the nerve much stiffer than brain[12]. For example, the tensile elastic modulus of human brain white matter is roughly 4 kPa and the indentation modulus of bovine white matter is around 2 kPa[13], but the tensile elastic modulus of the

bovine ON is 2,500 fold greater at around 5 MPa[14], similar to the corresponding value of about 6 MPa for human ON[15]. The ON is thus very much stiffer than brain. Given its severe mechanical loading during eye movement, it is understandable why stiffening connective tissue would be present within the ON to protect its visually-critical axons. However, it would also seem functionally essential that the ON's meninges be adapted to bear most of the loading to protect visual sensory function. Unlike the pia mater loosely covering the human spinal cord that has an elastic modulus of 2.3 MPa[16], the ON's pia mater is densely applied to its surface and so intrinsically joined to the connective tissue within the ON that its pia cannot be separated for mechanical testing in isolation. While there is very little data on the mechanical properties of the arachnoid mater, its elastic modulus has been estimated to be very compliant at about 1.2 kPa over the brain[17], and if the ON arachnoid is similar, it would be far too compliant to protect axons in the ON.

As the world's leading cause of irreversible blindness[18, 19], glaucoma was historically understood to constitute ON damage caused by elevated intraocular pressure (IOP)[20]. Statistically normal IOP averages 14.5 mmHg in the fifth decade of life in all ethnicities, but increases to around 16.5 mmHg by the 7th decade, with 4 mmHg standard deviation, and only minimally altered by corneal thickness[21]. The pathogenic role of IOP elevated well above the statistically normal range of less than 21mmHg is unequivocal in congenital and juvenile glaucoma[22], as well as in secondary glaucomas such as angle closure[23], uveitic[24], and traumatic[25], because IOP is typically highly elevated, and optic neuropathy is decisively slowed or halted after IOP is normalized. Elevation of IOP in animal models reliably damages the ON with a pattern consistent with human glaucoma [26-29]. Nevertheless, while IOP remains the only modifiable risk factor, the causal role of IOP was long ago stricken from the definition of primary open

angle glaucoma (POAG) because, among other things, observations that many patients, particularly those in Asia[30-34], lack excessively high IOP[35] and sustain glaucomatous ON damage at normal IOP[20]. In patients with POAG, IOP is normal in 30-39% of whites[36-38], 57% of blacks[39], 70% of Chinese[34], and 92% of Japanese[31]. Meta-analysis of more than 30,000 people found absence of statistical relationship of IOP to POAG [34]. Many patients with POAG suffer progressive ON damage at normal or below normal IOP, and consequently are diagnosed with normal tension glaucoma (NTG). However, even when therapeutically reduced, untreated IOP does not predict progressive optic neuropathy[40], and about 20% of patients suffer it five years after 30% IOP reduction from levels that were statistically normal even before treatment[20].

Eye-movement related deformation has been proposed as another mechanical etiology for optic neuropathy in NTG operating alternatively or in addition to IOP[1, 2, 14, 41]. Adduction is particularly important, because ON length is insufficient to permit unhindered rotation, tethering the globe in adduction[1] exceeding about 26° [6]. Deformations of the optic disc and Bruch's membrane produced by eye movements exceed many-fold those resulting from extreme IOP elevation[42], or IOP-related deformations recently proposed as pathological to retina[43].

While medial rectus muscle force acts across a broad tendon insertion[44], reaction force to it when the globe is tethered in adduction is concentrated on the smaller ON canal and peripapillary sclera. Presumably reaction force is concentrated on the ON sheath to protect the more delicate ON within it. In this study, we examined the structural characteristics of the human ON sheath, emphasizing its dimensions, structure, and elastin fiber characteristics due to the mechanical properties of this tissue constituent under low strain mechanical loading[45]. Elastin endows tissue with reversible extensibility

and hence is abundant in tissues that endure repetitive mechanical stress, such as skin, lung, arteries, and cartilage[45-49]. In the orbital connective tissue system, elastin fibers are preferentially located in tissues that experience repetitive mechanical loading by the extraocular muscles[50]. Elastin in canine carotid artery was shown to resist both circumferential and longitudinal loads, whereas collagen only bears circumferential loads[51]. In mouse aorta, exposure to elastase resulted in decrease of axial stretch of vessel walls[48].

Elastin synthesis, maturation, and maintenance in the ON head have been reported[52-54]. In the glaucomatous human lamina cribrosa (LC), elastin fibers deteriorate and became disorganized[56] with marked elastosis that is associated with changes in tissue compliance[57]. Park et al. found that the LC and peripapillary sclera of Koreans contains more elastic fiber components (elastin and fibrillin-1) than observed in Caucasians[58].

The foregoing studies have emphasized elastin distributions in the LC and peripapillary sclera. In light of MRI evidence of ON sheath tethering during adduction, we investigated elastin composition and organization in the ON sheath to inform studies of its mechanical behavior in relation to its the possible role in glaucoma.

1.1.3 Methods

This work was conducted in accordance with the Code of Ethics of the World Medical Association (Declaration of Helsinki) using legally obtained post-mortem human tissues. Seven whole human orbits were obtained from cadavers aged 4, 44, 57, 59, 64, 65, and 93 years, and immersion fixed in 10% neutral buffered formalin. Orbits were then lightly decalcified with 0.003 M ethylenediaminetetraacetic acid and 1.35 N HCl, dehydrated, embedded in paraffin, coronally sectioned at 10μm thickness, and mounted on 50x75 mm glass slides. Some sections were stained with Masson's trichrome (MT) while others were stained with van Gieson's elastin (EVG) method[59] (Fig. 1).

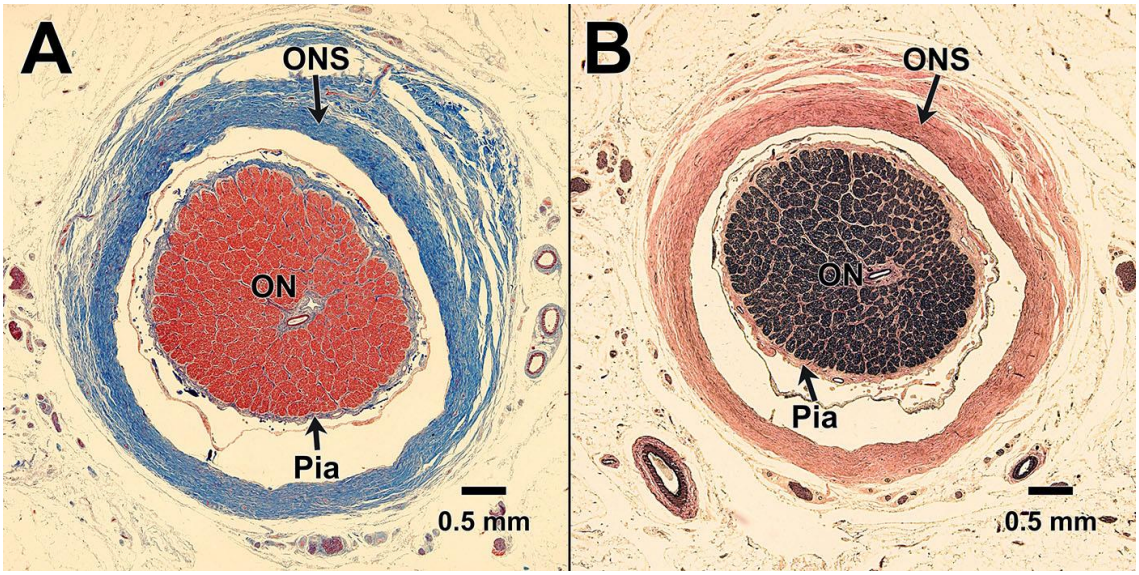

Figure 1. A. Masson's trichrome stain of coronal section of 44 year old ON and ON sheath (ONS). Collagen stains blue and nerve axon bundles red. B. van Gieson elastin stain of same specimen. Collagen appears salmon pink, nerve bundles and elastin fibers black.

Five fresh human globes with long attached ONs aged 26–75 years were obtained from eye banks within three days of death. Samples containing the peripapillary sclera and 2-3 mm of the anterior retrobulbar ON were fixed and processed using the same methods as whole orbits. One specimen was embedded and sectioned

longitudinally near its greatest transverse dimension. Specimens were imaged using a Nikon D1X digital camera coupled to an Eclipse E800 microscope (Nikon, Tokyo, Japan). To maximize resolution over a wide field of view, multiple overlapping fields of view from each section were merged using Adobe Photoshop (Adobe Systems, San Jose, CA), and analyzed using *ImageJ* (http://imagej.nih.gov/ij/; provided in the public domain by the National Institutes of Health, Bethesda, MD). Because we did not perform MRI in all of the specimens prior to embedding, it was not possible to account for shrinkage that occurs during the processing and embedding, which MRI comparisons have shown to be in the range of 30-40%[60]. While the physical dimensions reported here were not corrected for shrinkage, this has no impact on relative density and fiber orientation measurements.

Microscopic visual inspection of the ON sheath disclosed two layers that differed conspicuously in: density, weave, and dispersion of collagen fibers, and color: the inner layer (IL) closest to the ON, and the outer layer (OL). Moreover, in some specimens, a physical gap separated the two layers. In sections stained with EVG (Fig. 1B), contrast threshold filters were set in Adobe Photoshop to identify pixels occupied by elastin, and thus all visible black elastin fibers. Five random microscope fields that included both the IL and OL of the ON sheath were analyzed in each of three sections in each specimen. Masked layers containing the selected fibers were analyzed with the particle analysis tool of *ImageJ* to enumerate them. Data from three sections was averaged for each eye. Color thresholds were used to determine the total area occupied by the ON sheath in each section. Elastin area fraction was defined as area stained for elastin divided by total area, and was operationally computed as the number of black pixels in the region divided by the total number of all pixels in within that region.

Each elastin fiber profile was sorted into one of three orientation categories: circumferential (CF), diagonal (DF), and longitudinal (LF). In coronally sectioned specimens, CF had focal depth that was uniform within histological sections transverse to the length of the ON sheath, these fibers appeared as curved segments longer than 30 μm. In transverse histological sections, DF had measured focal depth that varied from one end to the other within the section, reflecting an oblique orientation to the section; these typically crisscrossed at oblique angles and exhibited apparent medium lengths of 10-25 μm, although it is recognized that longer oblique fibers would appear truncated due to the limiting effect of histological slice thickness. The LF were oriented along the length of the ON had the smallest profile in coronal images, less than 8 μm, consistent with sectioning nearly perpendicular to their long dimensions. Using the *ImageJ* particle morphometry tool, the relative abundance of each fiber orientation was quantified for the IL and OL.

Fibers not oriented parallel or orthogonal to the coronal plane of sectioning were considered to be DF. These fibers approached the plane of sectioning at oblique angles. To ascertain the oblique angle, we varied microscope focus depth and followed each fiber along its length through the 10μm tissue section thickness. Noting the 2-D distance variation required to change the fiber's focus plane from one end of the fiber to the other end, we determined the angle (α) between each fiber and the tangent to the ONS circumference, and angle (β) between the fiber and the longitudinal axis of the ONS (Fig. 2).

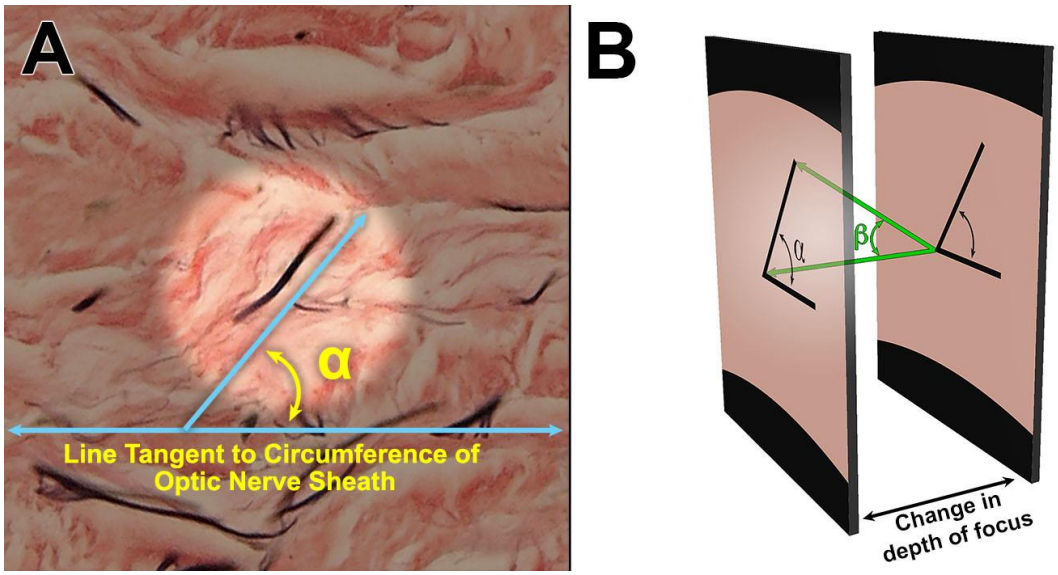

Figure. 2. A. Angle α measures the angle that a fiber makes with a line tangent to the ONS circumference. B. Angle β is between the diagonal fiber and the ON sheath longitudinal axis, determined in part from change in local focal depth.

ON sheath thickness was measured only in the whole orbits because only these maintained rotational orientation to orbital landmarks. To account for tissue shrinkage during processing, images were rescaled to match ON sheath dimensions determined from MRI prior to tissue dehydration and exenteration. Three sections spaced at 2mm intervals starting 1.5mm posterior to the globe-ON junction were analyzed per orbit. The ON sheath was divided into superior inferior, medial, and lateral quadrants, within each of which we measured its thickness every 8° for a total of 10 measurements per quadrant. These 10 measurements were averaged to estimate the overall thickness in each quadrant.

1.1.4 Results

In specimens stained with MT, the ON sheath exhibited two layers distinct due to the thicker and more densely woven collagen bundles in the IL (Fig. 3). In some specimens, a fissure separated the two layers. In other specimens, the collagen weave abruptly changed at the otherwise continuous interface between the IL and OL.

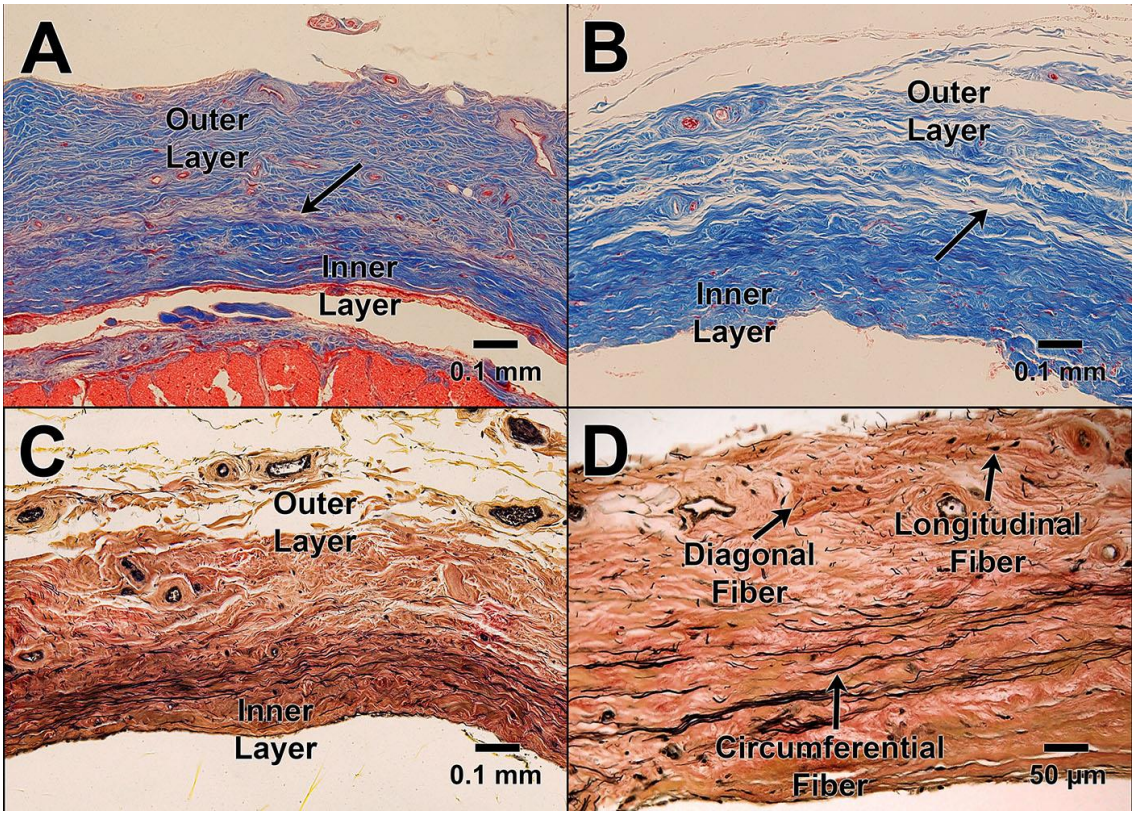

Figure. 3. A and B Masson trichrome, with arrows indicating boundary between inner (IL) and outer layers (OL) of optic nerve (ON) sheath. A. 57 year old specimen 23 mm posterior to corneal surface. B. 80-year-old specimen. Collagen of the OL is less dense than in the IL. C. and D. van Gieson elastin stain. C. 59 year old specimen. Collagen of the IL is darker than the OL. D. 64 year old specimen. Circumferential fibers predominate in the IL while longitudinal and diagonal fibers similarly populate both layers.

Elastin fibers appeared black within the salmon-colored collagen matrix. Elastin fibers in the IL were more tightly packed than in the OL, and the surrounding collagen matrix appeared denser (Fig. 4). This is also seen in high magnification in Fig. 5. Low-

power microscopic views were notable for distinct EVG staining: the IL was darker due to greater abundance of thin dark elastin fibrils and darker stained collagen matrix (Fig. 3C). Elastin area fraction defined by percentage of total area was significantly higher in the IL at 6.0±0.4% (SEM) than in the OL at 3.6±0.4% ($P<10^{-5}$). The IL was dominated by large black elastin fibers >30 μm long, and around 2.4 μm thick.

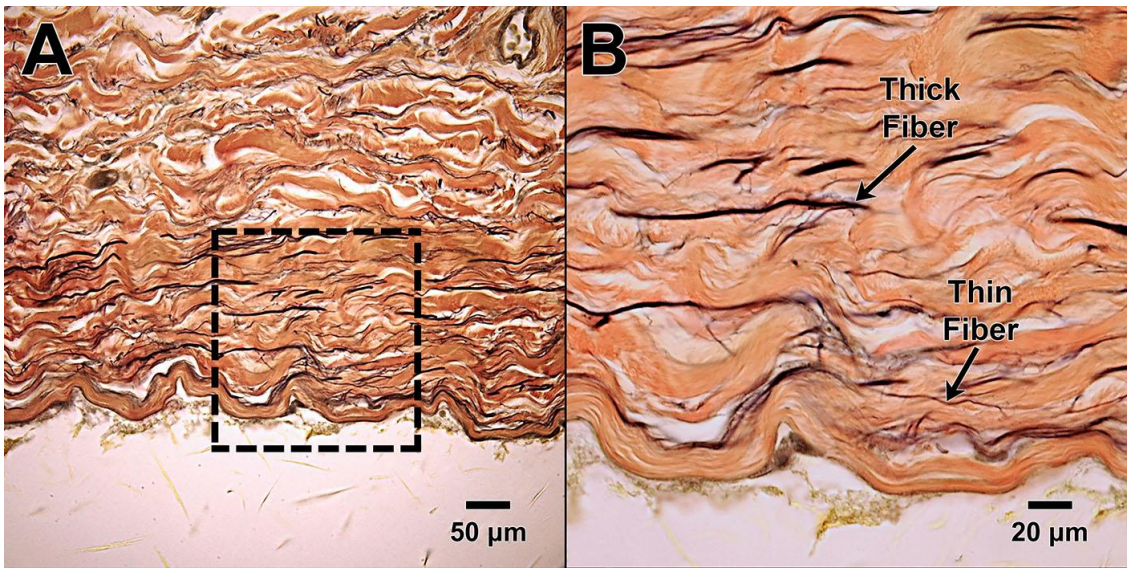

Figure. 4. A. van Gieson stained 93 year old optic nerve sheath. Elastin fibers of two different thicknesses are evident. B. Magnified view at (100X, oil immersion) reveals thick fibers measuring 2.4 μm and thin fibers 0.7 μm in transverse dimension.

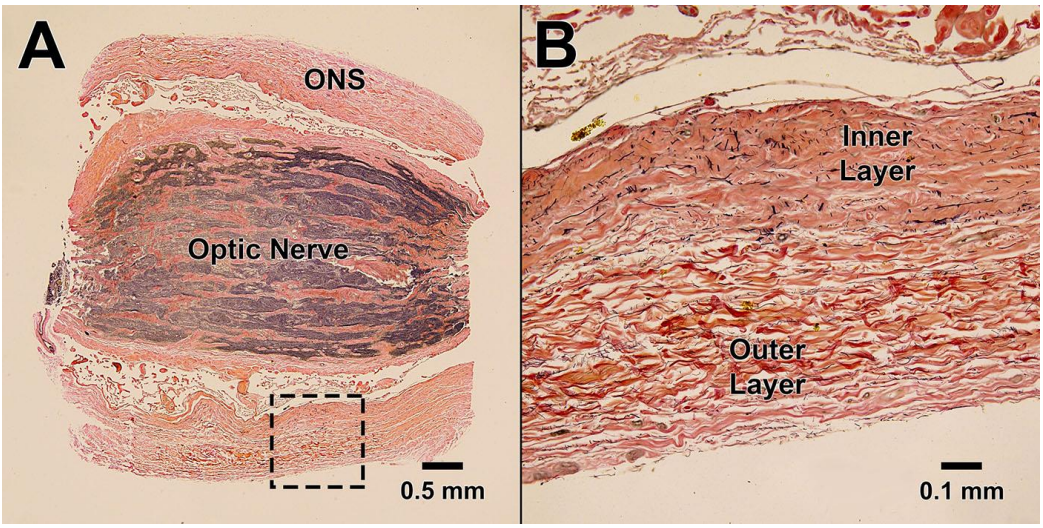

Figure. 5. A. van Gieson stained 69 year old optic nerve (ON) sheath sectioned longitudinally. B. Magnified view of the outlined box in A. IL and OL collagen have different weave patterns.

The distribution of elastin fiber orientations is plotted in Fig. 6. We considered these elastin fibers with long profiles that lie within the coronal plane of sectioning to be CF, since they form concentric rings around the ON sheath. Of the total CF, 63±4.7% were in the IL, and 37±4.7% in the OL ($P<10^{-4}$). Medium length elastin fibers, interpreted as DF, varied from 10-25 μm in length; these were uniformly distributed in both sheath layers. Small, short elastin profiles <8 μm in diameter were considered to represent LF whose lengths cannot be determined from this approach, since they are oriented transverse to the plane of sectioning; these LF were also uniformly distributed in both layers. A 2-way analysis of variance showed no significant differences among fiber types within the IL ($P>0.4$). On average, the OL exhibited similar preponderance of LF at 41.1±1.9% and DF at 36.4±1.9% ($P>0.13$). There were significantly fewer CF in the OL than the other two fiber types at 22.4±1.9% ($P<10^{-4}$). Of the total elastin fibers per coronal section in the entire sheath (including both IL and OL), LF were most abundant (4,094±885 fibers) followed by DF (3,716±813 fibers), and lastly CF (2,746±547 fibers).

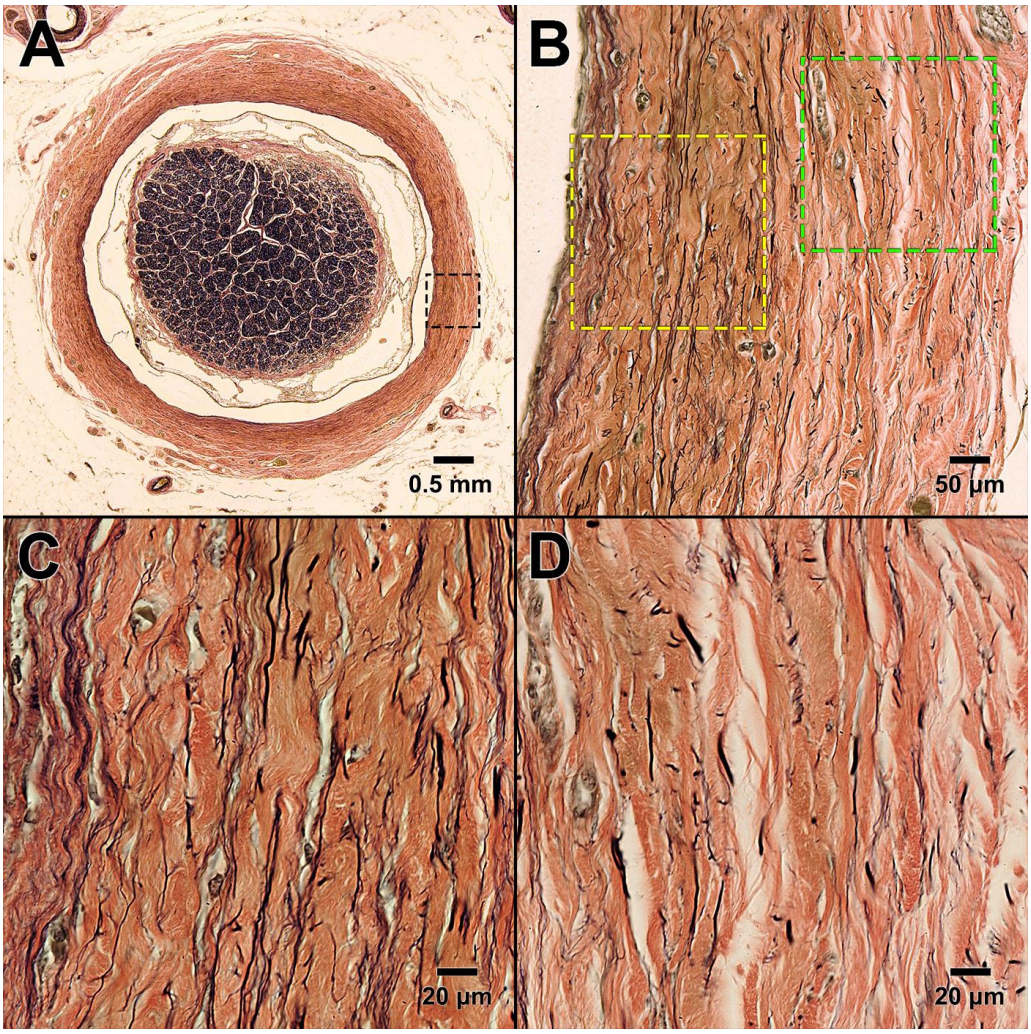

Figure. 6. A. van Gieson stained 65 year old optic nerve sheath. B. Magnified view from the boxed outline in A. IL on the left has more circumferential fibers. High magnification (oil immersion) of yellow box in B. Elastin fibers are more abundant and compact in the IL (C) in a comparable view of the OL (D) corresponding to the green box in B.

The DFs intersect obliquely with the coronal plane of sectioning that is transverse to the long dimension of the ON. To characterize 3-D orientation of DF, we measured two angles: angle α is the angle within the coronal plane between the fiber and a line tangent to the sheath circumference. Angle β is the angle between the long axis of the fiber and the longitudinal ON sheath axis. Angle α was widely distributed but clustered at

30°, 60°, and 150°. Angle β ranged from 40° to 80°. We found no DF that extended radially across the boundary demarcating IL from OL.

Thickness of the ON sheath generally did not vary significantly among its quadrants, except that the medial quadrant was significantly thinner than the lateral quadrant (ANOVA, $P<10^{-3}$), Average thicknesses for the medial, lateral, inferior, and superior quadrants were 363±39, 474±63, 452±64, and 415±59 μm (SEM), respectively.

The ON sheaths of the two pediatric specimens aged 1.7 and 4 years had visible clefts between IL and OL in the region in the region a few mm posterior to the globe, but posterior to this, the two layers fused into a single layer with uniform collagen weave and density that exhibited sparse and comparatively uniform elastin fiber distribution.

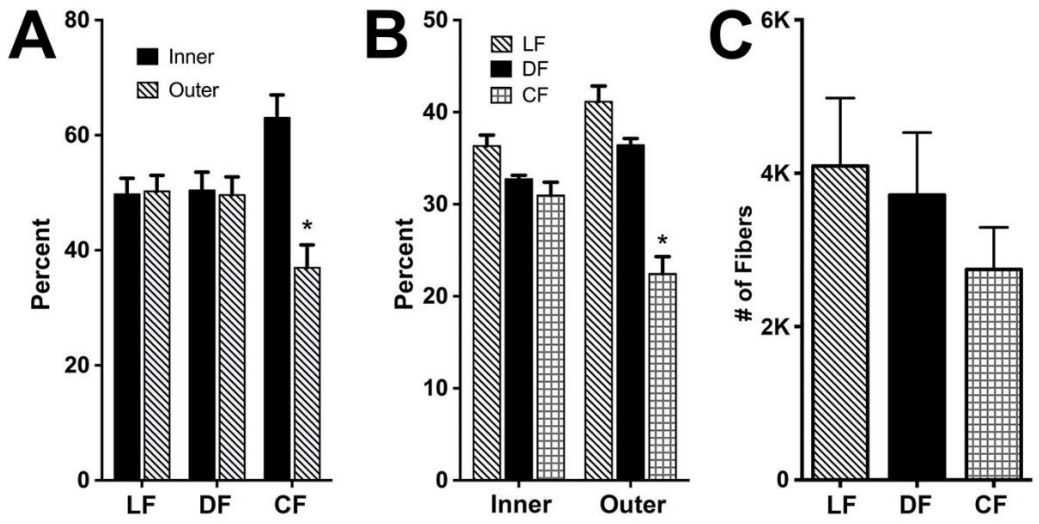

Figure 7. A. Longitudinal (LF) and diagonal fibers (DF) are evenly distributed in the optic nerve (ON) sheath. Most of the circumferential fibers (CF) lie in the inner layer (IL). B. The three fiber orientations have similar abundance in the IL, but CF are rarer than the other orientations in the outer layer. C. Longitudinal fibers (LF) were most abundant in the ON sheath as a whole. Least common were CF, with DF intermediate in abundance.

Total elastin area fraction in the ON sheath increased with age (Fig. 7A). While pediatric specimens had a 1.5±0.4% average total area fraction, the comparable value

for adult specimens was significantly higher at 4.7±0.3% ($P<10^{-3}$). Linear regression in 12 orbits showed that total elastin area fraction significantly increased with age by 0.04±0.01% per year ($P<10^{-3}$). Adult specimens had an average ON sheath thickness of 504±44 μm, which is significantly greater than corresponding thickness of pediatric specimens at 230±8 μm ($P<0.01$). Similar to the trend for total elastin area fraction, linear regression showed that sheath thickness also increased with age by 4.7±0.8 μm /yr ($P<10^{-5}$, Fig. 7B).

1.1.5 Discussion

The adult human ON sheath has two distinct layers differing in collagen density, and elastin fiber density and arrangement. The collagen matrix of the sheath IL appears densely compact in both MT and EVG stains. Collagen of the OL is more loosely arranged than in the IL. The IL has significantly higher elastin area fraction than the OL. These differences in anatomical structure correlate well with the different mechanical properties of each layer, as described in the companion paper that shows the IL to be stiffer and more viscous than the OL[61].

Elastin fibers in the ON sheath have three general orientations: circumferential, diagonal, and longitudinal (Fig. 8). In coronal sections, long CF are layered in concentric rings around the sheath to resist radial stress and deformation from the pressure of CSF. Medium length DF are juxtaposed at 40° - 80° angles relative to the LF, and crisscross within the collagen matrix. Elastin fibers running longitudinally (LF) appearing as small segments in coronal and long segments in longitudinal sections can resist tensile elongation. The widely varying orientations of the elastin fibers in the ONS provide an anatomical basis for its measured isotropic mechanical properties in the low strain regime[61].

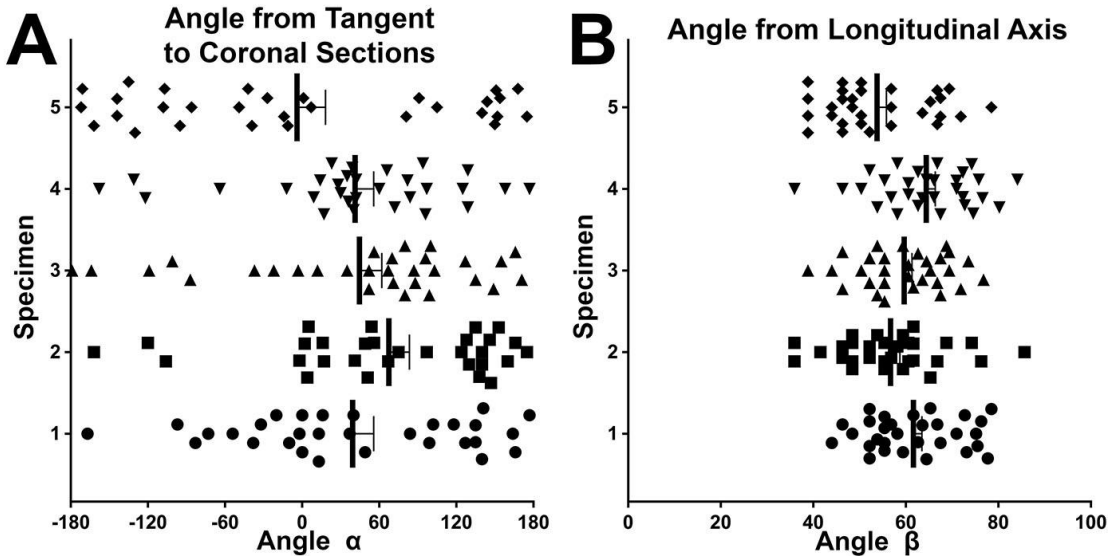

Figure 8. A. Elastin fiber orientation relative to the coronal plane. Angles varied widely but cluster around 60° and 150°. B. Elastin fiber orientation relative to the long optic nerve axis.

The majority (63%) of all CF in the ON sheath are in the IL, while LF and DF are equally abundant in the two layers. The IL contains approximately equal proportions of LF (36%), DF (33%), and CF (31%) organized in a 3-D isotropic mesh that can provide stiffness in all directions. The OL is contains a modestly greater predominance of LF (41%) and DF (37%) with a smaller contribution from CF (22%). However, the CF could be underestimated due to bias towards counting nearly every LF when sectioning the ON coronally, while only those CF lying in the plane of sectioning are included, missing CF in planes between the sections imaged. Thus, we think it likely that at least a sufficient representation of different fiber orientations exists in the ON sheath to support isotropic mechanical properties within layers.

Although many DFs extend radially at oblique angles, we found no radial elastin fibers crossing the boundary between the IL and OL. No underlying structure was evident to anchor the two layers together, implying that they are only loosely approximated. This lack of reinforcement allows the two layers in the adult to be easily

separated by gentle dissection in many cases. Each layer by itself is isotropically organized with elastin fibers of different orientation forming a reinforced mesh. The combination of elastin fiber orientations and the difference in elastin density between layers is consistent with to a bilayer structure having transverse isotropy.

Since the tissue was fixed post-mortem without physiological perfusion and intracranial pressure, the elastin fibers as studied resemble the relaxed state of a coiled spring[62]. Post-processing of the tissue could have degraded structures anchoring the elastin to the collagen matrix, thus allowing the elastin fibers to unwind. In living tissue, the elastin fibers are presumably under load and straighten from their curled conformation as they stretch under physiologic loading similarly to the porcine collagen fibers[63].

Burgoyne and Sigal have emphasized the important role of mechanically induced injury to the LC, peripapillary sclera, and neighboring structures in the pathogenesis of optic neuropathy[64, 65]. Eye movement may impose tractional force on the posterior eye, causing significant peripapillary stresses during adduction exceeding 26° where length redundancy of the ON has been exhausted, with consequent stretching of the taut ON sheath[1]. At the globe-ON junction, the IL, which is stiffer and rich in elastin, joins the sclera near the LC to which it can transfer the tractional force caused by adduction tethering. Finite element analysis suggests that ON traction in adduction concentrates stress at this junction[14], potentially exposing the transiting ON axons to damaging strain. Of course, MRI indicates that while ON sheath traction in adduction occurs even in healthy people[1, 2], so far only in patients with POAG does the adducting tethering retract the globe.

The current anatomical findings may explain why adduction tethering of the ON may be innocuous in most people, yet pathological in POAG. In brief, we propose that stiffening of the ON sheath can cause normal adduction eye movements to become progressively more damaging effectors of repetitive strain injury to the optic disc and peripapillary region. Elastin, responsible for tissue reversibility, is generally considered to dominate mechanical behavior at the “toe,” or low strain range, of the nonlinear stress-strain curve. This nonlinear behavior is important to understanding the role of elastin in ocular tissues. For example, in porcine medial collateral ligament, elastase digestion reduced the elastic modulus in the lower strain toe region (strain<8.7±0.1%), but did not affect the higher strain linear region or failure properties[66]. Thus, at low strains typical of those in ocular tissues that must maintain precise dimensions, more abundant elastin supports stiffer tissue. In porcine aortic valves, elastin digestion reduced tissue extensibility[67].

Elastin area fraction (Fig. 7A) and thickness (Fig. 7B) of the ON sheath both increased with age. When properly organized, the increased elastin can provide tissue resiliency. However, over time proteases can degrade elastin fibers, leading to fragmentation and disorganization of the elastin that alters mechanical behavior[68]. Increased expression of matrix metallo-protease has been linked to aortic aneurysm formation and increased arterial stiffness[69]. As senile elastin fibers degrade, newly synthesized elastin may not properly assemble, resulting in formation of large irregular deposits termed “elastosis.” Degradation of properly assembled elastin fibers and replacement with irregular aggregates of elastin could lead to a stiffer ON sheath that is more likely to transfer stress the globe during adduction tethering. Accumulation of these elastin deposits might be related to the increasing prevalence of POAG with age[70, 71]. Presumably, while the youthful ON and sheath are pliable enough to stretch harmlessly

during adducting tethering, thickening and elastosis of the sheath (and perhaps also the intrinsic connective tissue within the ON itself[11]) render these aging tissues stiffer, so that they transfer adducting tractional force to the relatively soft peripapillary region of the globe[14], which can only deform and retract in response. Some older people may develop greater stiffening of the normally pliable tissues than healthier people, and thus experience pathologically greater local stress concentrations in the ON and peripapillary region. Resulting repetitive strain during adduction might lead to structural remodeling of the ON head and gradual death of ON axons in individuals who have unfavorable combinations of high sheath stiffness and strong adduction tethering[2].

The present histological description of the ON sheath provides a basis for biomechanical modeling of the interaction between the sheath and peripapillary region. It is anatomically reasonable to expect that tensile properties of the sheath would be similar in all loading directions, but that the elastic modulus be greater in the IL than the OL. The absence of connective tissue fibers interconnecting IL and OL suggests little mutual mechanical coupling between the two layers. These observations should be helpful in finite element modeling of ON sheath behavior.

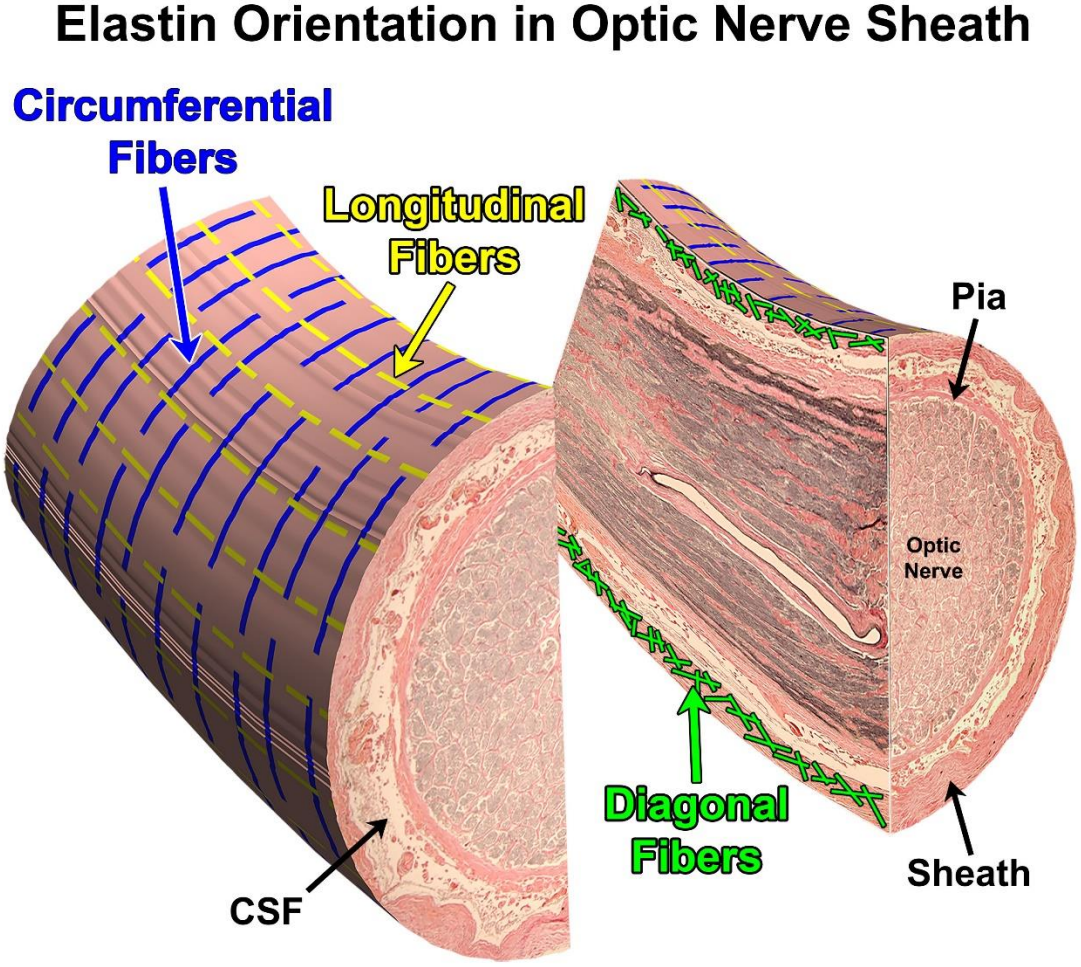

Figure 9. Three elastin fiber orientations in the optic nerve sheath create a 3-dimensional mesh including all general orientations and supporting isotropic properties. Illustration combines longitudinal and coronal sections stained with van Gieson's stain. CSF – cerebrospinal fluid.

We conclude that the ON sheath exhibits distinct inner and outer layers, with the former containing denser and more compact collagen and more elastin. In both layers, elastin fibers have longitudinal, diagonal, and circumferential orientations consistent with isotropic mechanical properties (Fig. 9). Elastin density and sheath thickness increase significantly with age. Differences in laminar elastin density and orientation may reflect greater tensile loading in the inner than outer layer.

1.1.6 References

1. Demer JL. Optic nerve sheath as a novel mechanical load on the globe in ocular duction. Invest Ophthalmol Vis Sci. 2016;57:1826-38.

2. Demer JL, Clark RA, Suh SY, et al. Magnetic resonance imaging of optic nerve traction during adduction in primary open-angle glaucoma with normal intraocular pressure. Invest Ophthalmol Vis Sci. 2017;58:4114-25.

3. Guitton D, Volle M. Gaze control in humans: eye-head coordination during orienting movements to targets within and beyond the oculomotor range. J Neurophysiol. 1987;58:427-59.

4. Anastasopoulos D, Ziavra N, Hollands M, Bronstein A. Gaze displacement and inter-segmental coordination during large whole body voluntary rotations. Exp Brain Res. 2009;193:323-36.

5. Chang MY, Shin A, Park J, et al. Deformation of optic nerve head and peripapillary tissues by horizontal duction. Am J Ophthalmol. 2017;174:85-94.

6. Suh SY, Le A, Shin A, et al. Progressive deformation of the optic nerve head and peripapillary structures by graded horizontal duction. Invest Ophthalmol Vis Sci. 2017;58:5015-21.

7. Epelboim J, Steinman RM, Kowler E, et al. Gaze-shift dynamics in two kinds of sequential looking tasks. Vision Res. 1997;37:2597-607.

8. Wu CC, Kowler E. Timing of saccadic eye movements during visual search for multiple targets. J Vis. 2013;13.

9. Robinson DA. Control of eye movements. In: Brooks VB, ed. The nervous system, handbook of physiology. Baltimore: Williams & Wilkins, 1981; v. II, pp. 1275-320.

10. Leclair-Visonneau L, Oudiette D, Gaymard B, et al. Do the eyes scan dream images during rapid eye movement sleep? Evidence from the rapid eye movement sleep behaviour disorder model. Brain. 2010;133:1737-46.

11. Karim S, Clark RA, Poukens V, Demer JL. Quantitative magnetic resonance imaging and histology demonstrates systematic variation in human intraorbital optic nerve size. Invest Ophthalmol Vis Sci. 2004;45:1047-51.

12. Shin A, Yoo L, Park J, Demer JL. Finite element biomechanics of optic nerve sheath traction in adduction. J Biomech Eng. 2017;139.

13. Goriely A, Geers MG, Holzapfel GA, et al. Mechanics of the brain: perspectives, challenges, and opportunities. Biomech Model Mechanobiol. 2015;14:931-65.

14. Shin A, Yoo L, Park C, Demer JL. Finite element biomechanics of optic nerve sheath traction in adduction. J Biomech Eng. 2017;139.

15. Park J, Shin A, Liu T, Demer JL. Sensitivity of mechanical strain in human peripapillary region to adduction tethering evaluated by hyperelastic characterization and finite element analysis (FEA). ARVO Abstracts. 2018;59:abstract 2029.

16. Ozawa H, Matsumoto T, Ohashi T, et al. Mechanical properties and function of the spinal pia mater. J Neurosurg Spine. 2004;1:122-7.

17. Saboori P, Sadegh A. On the properties of brain sub arachnoid space and biomechanics of head impacts leading to traumatic brain injury. Advances in Biomechanics and Applications,.1:253-67.

18. Kapetanakis VV, Chan MP, Foster PJ, et al. Global variations and time trends in the prevalence of primary open angle glaucoma (POAG): A systematic review and meta-analysis. Br J Ophthalmol. 2016;100:86-93.

19. Kingman S. Glaucoma is second leading cause of blindness globally. Bull World Health Organ. 2004;82:887-8.

20. Killer HE, Pircher A. Normal tension glaucoma: review of current understanding and mechanisms of the pathogenesis. Eye (Lond). 2018;32:924-30.

21. Chan MP, Grossi CM, Khawaja AP, et al. Associations with intraocular pressure in a large cohort: Results from the UK biobank. Ophthalmology. 2016;123:771-82.

22. Chang I, Caprioli J, Ou Y. Surgical management of pediatric glaucoma. Dev Ophthalmol. 2017;59:165-78.

23. Zhang X, Liu Y, Wang W, et al. Why does acute primary angle closure happen? Potential risk factors for acute primary angle closure. Surv Ophthalmol. 2017;62:635-47.

24. Tan AN, Cornelissen MF, Webers CAB, et al. Outcomes of severe uveitic glaucoma treated with Baerveldt implant: can blindness be prevented? Acta Ophthalmol. 2018;96:24-30.

25. Bai HQ, Yao L, Wang DB, et al. Causes and treatments of traumatic secondary glaucoma. Eur J Ophthalmol. 2009;19:201-6.

26. Kwong JM, Vo N, Quan A, et al. The dark phase intraocular pressure elevation and retinal ganglion cell degeneration in a rat model of experimental glaucoma. Exp Eye Res. 2013;112:21-8.

27. Samuels BC, Siegwart JT, Zhan W, et al. A novel tree shrew (Tupaia belangeri) model of glaucoma. Invest Ophthalmol Vis Sci. 2018;59:3136-43.

28. Guo C, Qu X, Rangaswamy N, et al. A murine glaucoma model induced by rapid in vivo photopolymerization of hyaluronic acid glycidyl methacrylate. PLoS One. 2018;13:e0196529.

29. Quigley HA. Use of animal models and techniques in glaucoma research: Introduction. Methods Mol Biol. 2018;1695:1-10.

30. Shi D, Funayama T, Mashima Y, et al. Association of HK2 and NCK2 with normal tension glaucoma in the Japanese population. PLoS One. 2013;8:e54115.

31. Iwase A, Suzuki Y, Araie M, et al. The prevalence of primary open-angle glaucoma in Japanese: the Tajimi Study. Ophthalmology. 2004;111:1641-8.

32. Kim CS, Seong GJ, Lee NH, et al. Prevalence of primary open-angle glaucoma in central South Korea the Namil study. Ophthalmology. 2011;118:1024-30.

33. Ha A, Kim YK, Jeoumg JW, et al. Association of angle width with progression of normal-tension glaucoma. A minimum 7-year follow-up study. JAMA Ophthalmol. 2019;137:13-20.

34. Zhao J, Solano MM, Oldenburg CE, et al. Prevalence of normal-tension glaucoma in the Chinese population: A systematic review and meta-analysis. Am J Ophthalmol. 2019;199:101-10.

35. Kim JA, Kim TW, Lee EJ, et al. Lamina Cribrosa Morphology in Glaucomatous Eyes with Hemifield Defect in a Korean Population. Ophthalmology. 2019;126:692-701.

36. Sommer A, Tielsch JM, Katz J, et al. Racial differences in the cause-specific prevalence of blindness in east Baltimore. N Engl J Med. 1991;325:1412-7.

37. Bonomi L, Marchini G, Marraffa M, et al. Prevalence of glaucoma and intraocular pressure distribution in a defined population. The Egna-Neumarkt Study. Ophthalmology. 1998;105:209-15.

38. Klein BE, Klein R, Sponsel WE, et al. Prevalence of glaucoma. The Beaver Dam Eye Study. Ophthalmology. 1992;99:1499-504.

39. Rotchford AP, Johnson GJ. Glaucoma in Zulus: A population-based cross-sectional survey in a rural district in South Africa. Arch Ophthalmol. 2002;120:471-8.

40. Seol BR, Kim SH, Kim DM, et al. Influence of intraocular pressure reduction on progression of normal-tension glaucoma with myopic tilted disc and associated risk factors. Jap J Ophthalmol. 2017;62:230-6.

41. Wang X, Fisher LK, Milea D, et al. Predictions of optic nerve traction forces and peripapillary tissue stresses following horizontal eye movements. Invest Ophthalmol Vis Sci. 2017;58:2044-53.

42. Wang YX, Jiang R, Wang NL, et al. Acute peripapillary retinal pigment epithelium changes associated with acute intraocular pressure elevation. Ophthalmology. 2015;122:2022-8.

43. Fortune B. Pulling and tugging on the retina: Mechanical impact of glaucoma beyond the optic nerve head. Inv Ophtalmol Vis Sci. 2019;60:26-35.

44. Apt L. An anatomical reevaluation of rectus muscle insertions. Trans Am Ophthalmol Soc. 1980;78:365-75.

45. Baldwin AK, Simpson A, Steer R, et al. Elastic fibres in health and disease. Expert Rev Mol Med. 2013;15:e8.

46. Daamen WF, Veerkamp JH, van Hest JC, van Kuppevelt TH. Elastin as a biomaterial for tissue engineering. Biomaterials. 2007;28:4378-98.

47. Kielty CM. Elastic fibres in health and disease. Expert Rev Mol Med. 2006;8:1-23.

48. Collins MJ, Eberth JF, Wilson E, Humphrey JD. Acute mechanical effects of elastase on the infrarenal mouse aorta: implications for models of aneurysms. J Biomech. 2012;45:660-5.

49. Jesudason R, Sato S, Parameswaran H, et al. Mechanical forces regulate elastase activity and binding site availability in lung elastin. Biophys J. 2010;99:3076-83.

50. Kono R, Poukens V, Demer JL. Quantitative analysis of the structure of the human extraocular muscle pulley system. Invest Ophthalmol Vis Sci. 2002;43:2923-32.

51. Dobrin PB, Canfield TR. Elastase, collagenase, and the biaxial elastic properties of dog carotid artery. Am J Physiol. 1984;247:H124-31.

52. Urban Z, Agapova O, Hucthagowder V, et al. Population differences in elastin maturation in optic nerve head tissue and astrocytes. Invest Ophthalmol Vis Sci. 2007;48:3209-15.

53. Pena JD, Roy S, Hernandez MR. Tropoelastin gene expression in optic nerve heads of normal and glaucomatous subjects. Matrix Biol. 1996;15:323-30.

54. Hernandez MR, Pena JD. The optic nerve head in glaucomatous optic neuropathy. Arch Ophthalmol. 1997;115:389-95.

55. Hernandez MR, Luo XX, Andrzejewska W, Neufeld AH. Age-related changes in the extracellular matrix of the human optic nerve head. Am J Ophthalmol. 1989;107:476-84.

56. Hernandez MR, Ye H. Glaucoma: changes in extracellular matrix in the optic nerve head. Ann Med. 1993;25:309-15.

57. Pena JD, Netland PA, Vidal I, et al. Elastosis of the lamina cribrosa in glaucomatous optic neuropathy. Exp Eye Res. 1998;67:517-24.

58. Park HL, Kim JH, Jung Y, Park CK. Racial Differences in the Extracellular Matrix and Histone Acetylation of the Lamina Cribrosa and Peripapillary Sclera. Invest Ophthalmol Vis Sci. 2017;58:4143-54.

59. Sheehan DC, Hrapchak BB. *Theory and Practice of Histotechnology*. St. Louis: Mosby, 1973; 95-116.

60. Kono R, Poukens V, Demer JL. Quantitative analysis of the structure of the human extraocular muscle pulley system. Invest Ophthalmol Vis Sci. 2002;43:2923-32.

61. Shin AS, Park J, Le A, et al. Bilaminar mechanics of the human optic nerve sheath. Cur Eye REs. 2019:(submitted).

62. Quigley HA, Dorman-Pease ME, Brown AE. Quantitative study of collagen and elastin of the optic nerve head and sclera in human and experimental monkey glaucoma. Curr Eye Res. 1991;10:877-88.

63. Raykin J, Forte TE, Wang R, et al. Characterization of the mechanical behavior of the optic nerve sheath and its role in spaceflight-induced ophthalmic changes. Biomech Model Mechanobiol. 2017;16:33-43.

64. Burgoyne CF, Downs JC, Bellezza AJ, et al. The optic nerve head as a biomechanical structure: a new paradigm for understanding the role of IOP-related stress and strain in the pathophysiology of glaucomatous optic nerve head damage. Prog Retin Eye Res. 2005;24:39-73.

65. Sigal IA, Ethier CR. Biomechanics of the optic nerve head. Exp Eye Res. 2009;88:799-807.

66. Henninger HB, Underwood CJ, Romney SJ, et al. Effect of elastin digestion on the quasi-static tensile response of medial collateral ligament. J Orthop Res. 2013;31:1226-33.

67. Lee TC, Midura RJ, Hascall VC, Vesely I. The effect of elastin damage on the mechanics of the aortic valve. J Biomech. 2001;34:203-10.

68. Wagenseil JE, Mecham RP. Elastin in large artery stiffness and hypertension. J Cardiovasc Transl Res. 2012;5:264-73.

69. Yasmin, McEniery CM, O'Shaughnessy KM, et al. Variation in the human matrix metalloproteinase-9 gene is associated with arterial stiffness in healthy individuals. Arterioscler Thromb Vasc Biol. 2006;26:1799-805.

70. Rudnicka AR, Mt-Isa S, Owen CG, et al. Variations in primary open-angle glaucoma prevalence by age, gender, and race: a Bayesian meta-analysis. Invest Ophthalmol Vis Sci. 2006;47:4254-61.

71. Doucette LP, Rasnitsyn A, Seifi M, Walter MA. The interactions of genes, age, and environment in glaucoma pathogenesis. Surv Ophthalmol. 2015;60:310-26.

1.2 Bilaminar Mechanics of the Human Optic Nerve Sheath

Andrew Shin[1, 6], Joseph Park[1, 2], Alan Le[1, 2], Vadims Poukens[1],

and Joseph L. Demer[1, 3-5]

[1]Department of Ophthalmology, Jules Stein Eye Institute; [2]Department of Bioengineering; [3]Biomedical Engineering Interdepartmental Program; [4]Neuroscience Interdepartmental Program; [5]Department of Neurology, University of California, Los Angeles.

[6]Wellman Center for Photomedicine, Harvard Medical School & Massachusetts General Hospital, Boston.

1.2.1 Abstract

Purpose: The adult human optic nerve sheath has recently been recognized to be bilaminar, consisting of inner and outer layers. Since the optic nerve and sheath exert tension on the globe in large angle adduction as these structures transmit reaction force of the medial rectus muscle to the globe, this study investigated the laminar biomechanics of the human optic nerve sheath.

Methods: Biomechanical characterization was performed in optic nerve sheath specimens from 12 pairs of fresh, post-mortem adult eyes. Some optic nerve sheath specimens were tested whole, while others were separated into inner and outer layers. Uniaxial tensile loading under physiological temperature and humidity was used to characterize a linear approximation as Young's modulus, and hyperelastic non-linear behavior using the formulation of Ogden. Micro-indentation was performed by imposing small compressive deformations with small, hard spheres. Specimens of the same sheaths were paraffin embedded, sectioned at 10 μm thickness, and stained with van Gieson's stain for anatomical correlation.

Results: Mean (± standard error of the mean, SEM) tensile Young's modulus of the inner sheath at 19.8±1.6 MPa significantly exceeded that for outer layer at 9.7±1.2 MPa; the whole sheath showed intermediate modulus of 15.4±1.1 MPa. Under compression, the inner sheath was stiffer (7.9±0.5 vs 5.2±0.5 kPa) and more viscous (150.8±10.6 vs 75.6±6 $\mathrm{kPa} \cdot \mathrm{s}$) than outer sheath. The inner sheath had denser elastin fibers than outer sheath, correlating with greater stiffness.

Conclusions: We conclude that maximum tensile stiffness occurs in the elastin-rich optic nerve sheath inner layer that inserts near the lamina cribrosa where tension in the

sheath exerted during adduction tethering may be concentrated adjacent the optic nerve head.

1.2.2 Introduction

Although previously neglected as a mechanical factor, it has recently been recognized that the optic nerve (ON) and its sheath contribute to mechanical loading on both extraocular muscles and the ocular globe[1]. We recently demonstrated by magnetic resonance imaging (MRI) that ON length is insufficient to avoid tethering the globe when, for normal subjects, adduction exceeds about 26°[2]. Further adduction approaching the much greater limit of the oculomotor range requires strains in the orbital tissues, including translation of the whole globe. This translation in adduction is mainly in the nasal direction in healthy people, but the globe retracts posteriorly in primary open angle glaucoma[3]. While MR force acts across a broad tendon insertion[4], reaction force to it is concentrated on the smaller ON canal and peripapillary sclera. Optical coherence tomography (OCT) shows that deformations of the ON head and Bruch's membrane produced by adduction exceed many-fold those resulting from extreme intraocular pressure (IOP) elevation[5], or IOP-related deformations recently proposed as pathological to retina[6]. Sibony et al. used OCT to show in patients with elevated intracranial pressure that adduction induces folds extending from the optic disc to the retinal macula[7].

Eye movements occur as often as several times per second[8] during wakefulness[9], but persist even during sleep[10]. Rapid eye movements called saccades that change gaze direction by 25-45° frequently occur when the head and body are both free to move naturally[11]. Typical gaze shifts that occur during everyday head movement include eye movements averaging about 30˚ [12, 13]. This means that the optic disc and peripapillary retina and sclera experience relentless, transient mechanical loadings by the ON. It has even been proposed that that many cases of primary open angle

glaucoma may represent repetitive stress injury to the optic disc induced by tractional force exerted as the ON and its sheath become tethered during large adduction movements[3]. Finite element modeling based upon bovine tissue properties suggests that reaction force to MR contraction is concentrated in the temporal peripapillary region and lamina cribrosa, sites of early damage in glaucoma[14]. It is evident form such modeling that the mechanical consequences of adduction tethering depend to a large extent on the local mechanical properties of the ON, its enclosing dural sheath, and the posterior sclera. The term “ON sheath” is widely used in the clinical and surgical literature for this mobile connective tissue structure, where it is preferred to the anatomically synonymous term “optic nerve dura mater,” probably because all other dura mater is tightly constrained by anchoring bone or intervertebral discs[15].

While biomechanical characterization has been performed of the lamina cribrosa[16, 17], and sclera, especially peripapillary sclera[18, 19], the ON and its enclosing sheath have been comparatively neglected. Consequently, prominent finite element models (FEMs) have either omitted the sheath entirely [20], or parameterized the human ON sheath as identical to the dura mater of brain[21]. The biomechanical properties of the ON sheath have recently been characterized in mammals such as cow[14] and pig[22, 23]. Based on measured mechanical properties of ocular tissues, FEM has been performed to predict stress and strain distribution around ONH due to eye movement [22] [14]. Although the foregoing studies have consistently suggested that the stress and strain are induced near the ONH by eye movement, the accuracy of such FEM simulations is questionable since mechanical properties of the non-human ON sheath were employed.

Biomechanical measurement of the human ON sheath is clearly warranted to make accurate inferences about the role of eye movements in human ON sheath biomechanics. Moreover, it has recently been found that the adult human ON sheath

consists of distinct inner (IL) and outer layers (OL), with the IL containing more dense collagen and abundant elastin, and the OL containing less of each of these important structural proteins [24]. The differing composition of the two ON sheath layers leads to the obvious supposition that they might have differing intrinsic mechanical properties. Therefore, current study aimed to investigate the laminar mechanical properties of the human ON sheath by employing some standard biomechanical characterization methods compared with histological evaluation of connective tissue composition in the same specimens.

1.2.3 Methods

Twelve pairs of whole human globes with long attached ONs were obtained from eye banks within three days of death. Average donor age was 66±15 (standard deviation, SD) years, and gender was equally balanced. Due to variations in technique by eye bank tissue harvesters, lengths of ON specimens varied so that it was impossible to perform every experimental test on each specimen. In the laboratory, the whole ON sheath was dissected from the ON, and then where possible the sheath was carefully separated into IL and OL using fine forceps, as illustrated in Fig. 1. When grossly distinct, only mild dissecting force was necessary to separate two layers because in suitable cases there was a weak boundary or spontaneous separation between the layers. In other cases where the two layers were strongly adherent, laminar separation was impossible. An industrial optical coherence tomography (OCT) scanner (OCS1300SS, Thorlabs Inc., Newton, NJ) was used to measure the cross-sectional dimensions of specimens that averaged 0.67±0.08, 0.49±0.04, and 0.92±0.14 mm, respectively, for IL, OL, and whole sheath specimens.

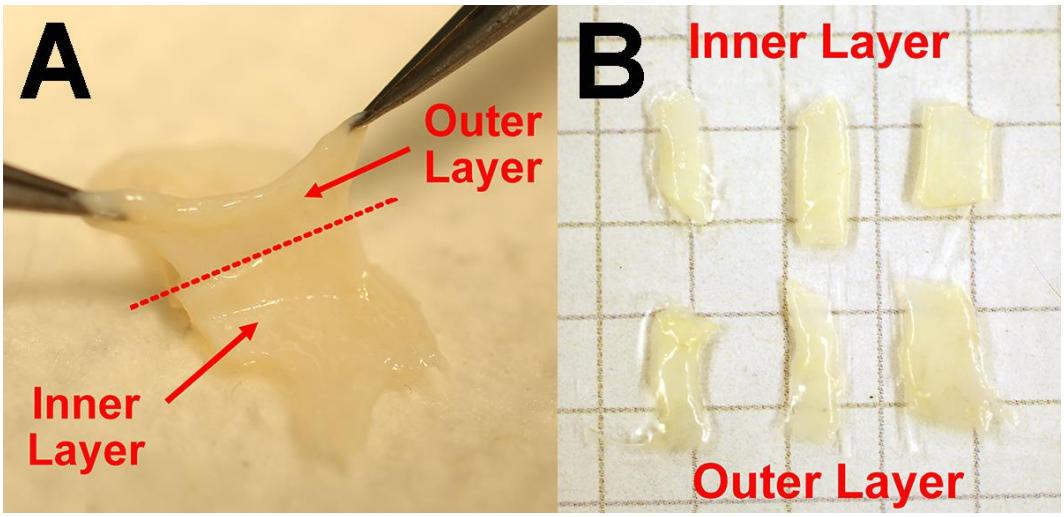

Figure 1. Laminar separation of optic nerve (ON) sheath for tensile testing. Prior to this photo, the cylindrical sheath was incised longitudinally to form a flat sheet. A. ON sheath was separated into inner and outer layers via forceps distraction when the boundary between the two layers was weak. B. Three pairs of inner and outer layers from whole ON sheath prepared for tensile experiments. 1 cm calibration grid.

Specimen dimensions were constrained by lengths of ONs obtainable by the eye banks even when harvesters were instructed to maximize specimen length. Each ON sheath was cut into 2 x 6 mm (width x length) rectangular shape for tensile testing including 1 mm clamping margin from each end; thus, aspect ratio was maintained at 2:1 in order to avoid experimental artifact due to aspect ratio variation [25]. Cross sectional dimensions of specimens were measured by OCT immediately after applying pre-loading for each tensile test. For micro-indentation, the whole sheath was trimmed to approximately 6-7 mm square shape for indentation at 4-5 widely-spaced locations.

A horizontal tensile loads cell was constructed, incorporating a linear motor (Ibex Engineering, Newbury Park, CA) having 100 mm/s maximum speed, a quadrature optical position encoder having 1 nm resolution, and a sensitive force sensor (LSB200, FUTEK, Irvine, CA) having 5 mN resolution. Via a frictionless air bearing, the linear motor shaft was coupled to an environmental chamber maintaining the tested specimens

in approximately physiological temperature and humidity. Details of the load cell are published elsewhere[26]. Specimens were glued using cyanoacrylate between 5 mm long layers of thin cardboard that was anchored in serrated clamps to prevent slip. Pre-loading of 0.05 N was applied by fine incremental elongation to avoid slackness, after which a constant elongation rate (0.01 mm/s) was imposed until failure as tensile force was recorded to characterize stress-strain behavior. Preliminary experiments were conducted with specimens preconditioned by cyclic loading up to 5% strain, but since tensile data obtained after this preconditioning did not differ significantly from data without preconditioning [14]. Preconditioning was thereafter omitted as unnecessary.

Specimens were loaded to failure, although of course with failure often at nonphysiologic strains. Full data sets with loading to failure are nevertheless presented with this understanding. In order to examine the possible anisotropic mechanical behavior, tensile loading in orthogonal longitudinal and circumferential loading directions was performed in separate specimens. Three different type of specimens were tested as available from each donated eye: 1) IL only; 2) OL only; and 3) the whole ON sheath consisting of both layers. Numbers of each type of specimen are reported in Results section 3.

While it is recognized that the relationship between stress and strain in most biological materials is non-linear, much of the existing literature and many published simulations of ocular biomechanics have approximated tensile properties using Young's modulus (YM), a linear relationship between stress and strain. For convenient comparison with the literature, we identified in every tensile stress-strain curve for each of the three ON sheath specimen types a linear region midway between the low strain "toe" and the failure region whose slope was considered to be YM. The reporting of YM values below should not be interpreted as a claim for linear behavior of the ON sheath,

nor as contradiction to our additional reporting of better-fitting non-linear material laws. In addition to the computation of YM, we also performed non-linear fitting to the Ogden hyperelastic model that gives excellent agreement with experimental data for brain and fat tissues [27], and that fit the current data better than alternative hyperelastic models. The hyperelastic model of Ogden [28] was employed having the strain energy potential form:

$$W = \sum_{i=1}^{N} \frac{2\mu_i}{{\alpha_i}^2}\left(\overline{\lambda_1}^{\alpha_i} + \overline{\lambda_2}^{\alpha_i} + \overline{\lambda_3}^{\alpha_i} - 3\right) + \sum_{i=1}^{N} \frac{1}{D_i}(J^{el} - 1)^{2i} \qquad \text{Eq. 1}$$

where $\overline{\lambda_i}$ are the deviatoric principal stretches, J^{el} is elastic volume ratio, N is number of terms in Material parameters from each layer were extracted by curve fitting of tensile data under the assumption of incompressibility.

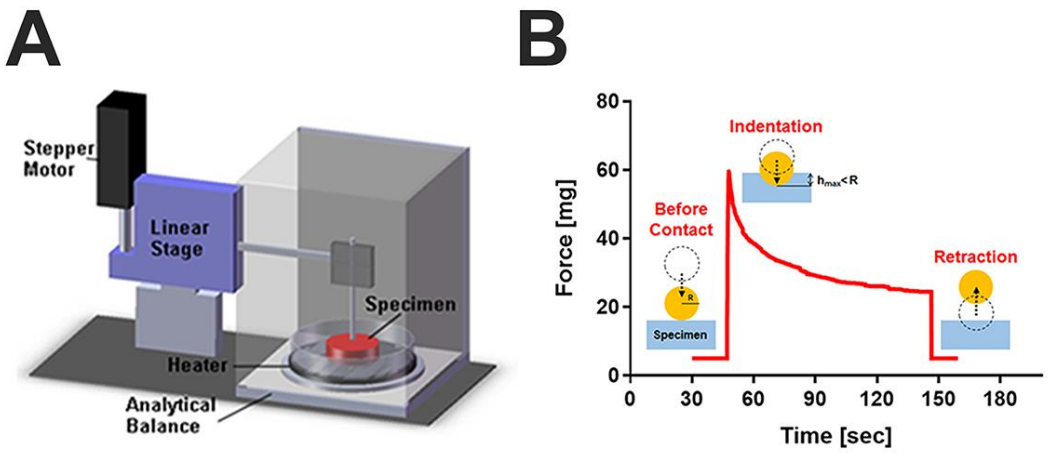

Figure 2. Micro-indentation compressive load cell. A 100 nm precision stepper motor was synchronized with a digital analytical balance whose pan was maintained in constant position by electromechanical feedback. B. Typical relaxation data by micro-indentation. After the spherical tip contacts the specimen surface, force rapidly increases due to the indentation that is smaller than the indenter radius. Force relaxation occurs during maintained deformation, after which then the indenter was lifted from the specimen.

Micro-indentation is a method of locally indenting the surface of a material with a probe of known shape to a depth that is small in relationship to overall specimen thickness. Provided that the specimen in relatively thick in comparison to the indentation depth, the result of microindentation is independent of total specimen thickness, and of whatever material may lie on the material's opposite side. Thus, for example, with a sufficiently small indenter, the IL or OL of the ON sheath could be tested by indentation of each respective surface without separating the two layers. A displacement-controlled indentation load cell (Fig. 2A) was constructed by synchronizing a linear stepper motor (LNR50 Series, Thorlabs, Newton, NJ) and analytical balance (ML54, Mettler-Toledo, Columbus, OH)[29]. Specimens were immersed in Ringer's lactate solution in a Petri dish placed on the pan of the analytical balance. The apparatus is sufficiently sensitive to detect the changing weight due to evaporation of water from the Petri dish. In order to minimize changes in load due to evaporation of water from the Petri dish, the load cell was surrounded by a glass chamber closed on all sides except for a small slit through which passed the indenter shaft. Downward indentation was created by a linear motor displacement having 100 nm precision, as force measurement was performed by analytical balance with 100 µg-force resolution, so loading could be recorded in a time series. Position of the balance pan was maintained by a servo within the balance, so that indenter position was equal to indenter depth. A 1 mm in diameter stainless steel sphere was used to indent samples to 50 µm depth. Because indentation depth was small relative to layer thickness, this method thus permitted local measurement of the properties of only the layer in direct with the indenter. In most cases the whole ON sheath specimen was simply placed in a Petri dish on the balance pan with the OL upward facing the indenter probe sphere to test the OL, or the specimen was inverted to

test the IL. It was not possible to interpret microindentation of the whole ON sheath, because the technique only evaluates the one surface layer contacting the indenter.

For each indentation, surface tension of the liquid layer on the specimen transiently created tractional (negative) force upon initial probe contact. Further incremental indentation was then applied to generate about 100~200 μg compressive (positive) force, indicating onset of contact with the specimen itself. Following contact, the probe was accelerated at 0.5 mm/s^2 to a speed of 1 mm/s until 50 μm indentation was achieved, after which the indenter was maintained in that fixed position as the specimen relaxed for approximately 80 seconds during applied force measurement. Figure 2B illustrates the stress relaxation testing procedure.

The Hertzian linear viscoelastic model was chosen for microindentation data analysis since a spherical-tip micro-indenter was used, a previous study successfully characterized bovine ocular tissues using this model [29], and insufficient data could be collected to characterize a nonlinear model in these tissues.

We show in a companion paper that the ON sheath contains collagen and abundant embedded elastin fibers [24]. A general rule of mixture provides a reasonable estimate the YM of a composite material composed of parallel fibers of uniform direction embedded in a matrix [30]. There are two extreme cases: the upper-bound modulus corresponding to loading parallel to the fibers, and lower-bound corresponding to loading transverse to the embedded fibers. The rule of mixture was applied to the two layers of the ON sheath as follows:

$$E_{w,upper} = fE_i + (1-f)E_0 \qquad \text{Eq. 2}$$

$$E_{w,lower} = (\frac{f}{E_i} + \frac{1-f}{E_0})^{-1}$$ Eq. 3

where E_i, E_o, and E_w are YM's for IL, OL, and whole ON sheath, respectively, and f is the volume fraction of the IL in proportion to the whole ON sheath. The rule of mixtures was used to make an inference about isotropy based upon comparison of whole ON sheath YM, and corresponding individual values for the IL and OL.

The companion paper provides detailed anatomical data on multiple ON sheath specimens that were subjected to histological examination, but for which overall ON dimensions were insufficient for both anatomical and biomechanical study in the same eye. Histological analysis is reported here for two globes with long enough ONs that they could also be utilized for biomechanical study in the same eye. The donors had no known histories of glaucoma. In both cases, ONs were sufficiently long that a histological specimen of retrobulbar ON and its enclosing ON sheath of approximately 2-3 mm length could be excised just anterior to a specimen sufficiently long for biomechanical testing. Histological specimens were processed as described elsewhere [24]. Briefly, specimens were fixed in 10% neutral buffered formalin, dehydrated in graded alcohol solutions, embedded in paraffin, and sectioned at 10 μm thickness before staining with van Gieson's elastin stain. Elastin density, defined as the number of pixels in an image occupied by black elastin fibers divided by the total number of pixels occupied by the ON sheath [24] in each IL and OL was determined for comparison with tensile and micro-indentation data in the same specimens.

To account for possible interocular correlation between the two eyes of each subject, statistical analysis was performed using generalized estimating equations (GEE) implemented in SPSS software (Version 24.0. Armonk, New York, USA: IBM

Corporation). This was considered more rigorous than parametric statistical approaches such as analysis of variance that might be confounded by intrasubject correlations.

1.2.4 Results

Specimens were loaded to failure, which occurred above 30% strain. While this extremely high ultimate strain is obviously nonphysiologic, complete stress-strain curves are illustrated in Fig. 43 for completeness. As a measure of approximate linear behavior and for convenient comparison to the literature, YM was determined in the range of about 10 - 15% strain for all specimen types (Table 1). The YM of the IL was about twice that of the OL (P<0.001, GEE), with the whole sheath YM intermediate between the two but not significantly different from the IL (P>0.2) but greater than the OL (P<0.001, GEE).

Table 1. Young's Modulus for the Human Optic Nerve Sheath

		Inner Layer	Outer Layer	Whole
Subject N		6	5	6
Specimen N		13	7	35
Young's Modulus (MPa)	Mean	**19.4**	**9.7**	**15.4**
	SEM	1.6	1.1	0.8
P Value	Inner - Outer	**< 0.01**		
	Outer - Whole	**< 0.07**		
	Inner - Whole	**> 0.10**		

To investigate possible anisotropy, whole ON sheath specimens were elongated in longitudinal (N=16) vs. circumferential (N=15) directions, for which YM values were 15.2±1.2 MPa and 15.1±2.1 MPa, respectively (P>0.94, GEE). This similarity indicates

that the sheath may be regarded as approximately isotropic with respect to the longitudinal and circumferential directions.

In order to obtain nonlinear characterizations, mean stress values at each corresponding strain were plotted for both layers, and for the whole ON sheath. Mean stress-strain plots averaging data for all specimens in Table 1 are shown in Fig. 3A. Whole ON sheath behavior was similar to the IL (P>0.38), but different from the OL (P<0.02), consistent with YM behavior in the linear region. Nonlinear curve fitting was performed for each layer, achieving an excellent match to the data (Fig. 3B).

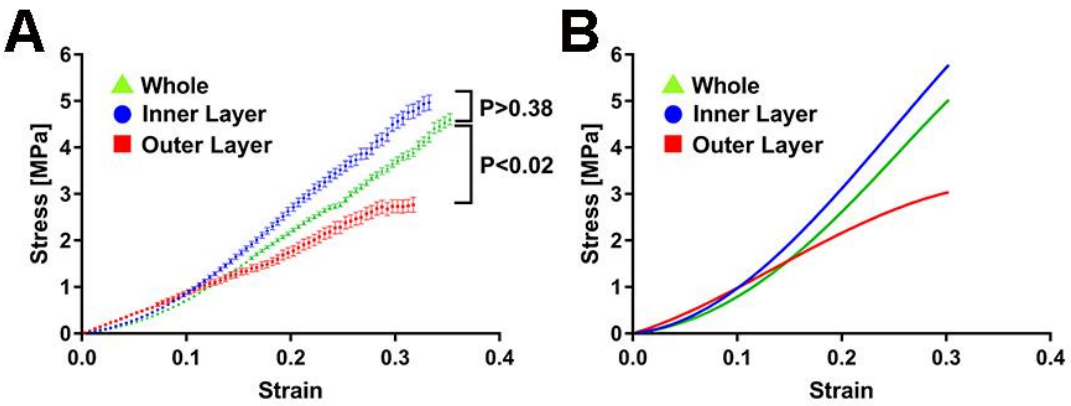

Figure 3. Nonlinear mechanical behavior of the human optic nerve sheath. A. Mean uniaxial tensile data. Behavior of the inner layer did not differ significantly from the whole sheath (P>0.38), but significantly differed from the outer layer. (P<0.02) The number of specimens and globes is indicated in Table 1. B. Three-parameter Ogden hyperelastic model closely fits the data in A.

Resulting parameters are illustrated in Table 2. Ogden functions with three strain energy terms (N=3) adequately described each layer's mechanical behavior within the entire strain range, including both the physiological lower part and the extremely high part approaching failure, thus providing quantitative descriptors that can be directly implemented in FEM.

Table 2. Ogden (N=3) Hyperelastic Parameters for Optic Nerve Sheath.

	μ_1 (MPa)	μ_2 (MPa)	μ_3 (MPa)	α_1	α_2	α_3
Inner Layer	445.65	-188.30	-256.60	3.09	4.12	1.92
Whole ONS	40.65	-9.60	-20.21	6.01	7.81	1.07
Outer Layer	45.52	-19.10	-24.20	1.89	3.91	-2.10

The rule of mixtures was used to estimate theoretically the combined properties of the whole ON sheath based upon measured YM for each layer, by this comparison to make an inference about predominant orientation of connective tissue fibers embedded in the sheath. In Equations 2 and 3, the mean f was calculated as 0.57 from OCT cross sectional measurements assuming constant thickness throughout the specimen length. By employing measured YM (E_i=19.8 MPa for IL, and E_o=9.7 MPa for OL), the rule of mixture predicts for whole sheath YM an upper bound of 15.5 MPa for parallel fiber loading and a lower bound of 13.7 MPa for transverse fiber loading, nicely matching the measured whole sheath YM of 15.4 MPa that corresponds to parallel loading. Approximately 10% less transverse stiffness suggests the weaker boundary between IL and OL.

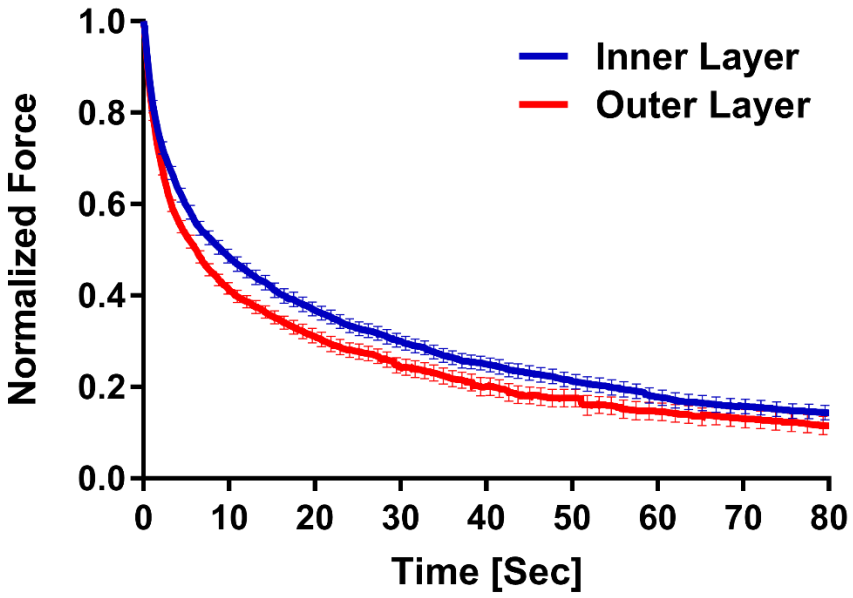

Figure 4. Mean relaxation behavior of inner (IL, 58 samples from 10 subjects) and outer layer (OL, 44 samples from 10 subjects) of the optic nerve sheath. The IL exhibited longer time constant (19.4 sec) than the OL (14.6 sec) corresponding to greater IL viscosity.

For every indentation, stress relaxation data was fitted to the Hertzian linear viscoelastic formulation (averaged in Fig. 4), from which instantaneous stiffness (analogous to YM), viscosity, and time constants were calculated. Table 1 shows averaged results for the IL and OL. Results showed the IL to be stiffer than the OL, and the IL about twice as viscous with about a 30% a longer time constant ($P<0.001$, GEE for all three comparisons).

Two globes with very long attached ONs were used to explore a possible relationship between mechanical properties and histology suggested by differences in laminar anatomical characteristics of the ON sheath. It was seldom possible to perform both anatomical and biomechanical analyses in the same sheaths, since both types of tests are destructive and only occasionally was overall ON length sufficient to provide samples for both analyses. For one such long specimen, micro-indentation was

performed to obtain local stiffness and viscosity of the two ON sheath layers. For this specimen (66 year old female), the IL was about 30% stiffer (12.6 vs 8.9 kPa) and about three-fold more viscous (296 vs 109 $\mathrm{kPa} \cdot \mathrm{s}$) than the OL. This may be compared with about 40% higher elastin density in the IL than OL (9.8 vs 7.2%) of this same sheath. Uniaxial tensile loading was performed for the second specimen (26 year old female). The IL exhibited about five-fold greater YM (8.1 vs 2.9 MPa) and about 60% greater elastin density (8.8 vs 5.5%) than the OL in this specimen, as illustrated in Fig. 5.

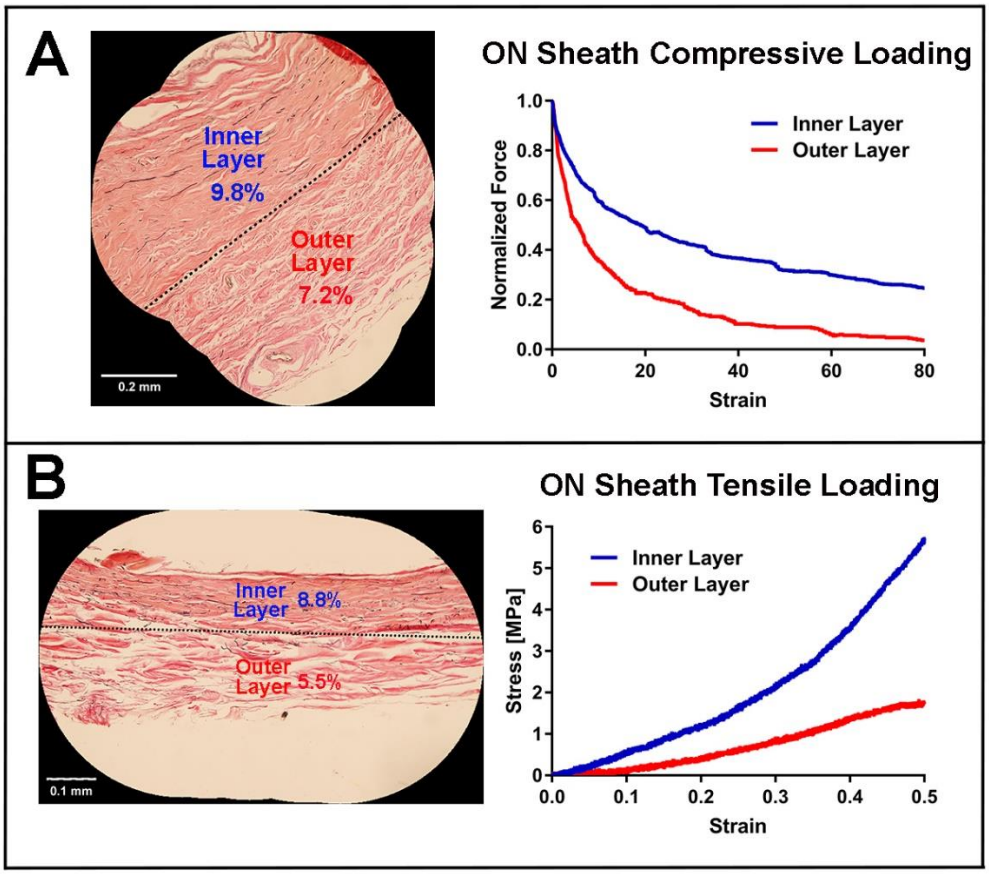

Figure 5. Mechanical properties of the ON sheath compared with elastin density in the same specimens. A. Compressive testing in one specimen aged 66 years. The inner layer (IL) had higher elastin density (9.8%) than the outer layer (OL, 7.2%), corresponding greater stiffness (12.6 vs 8.9 kPa) and viscosity (296 vs 109 kPa·s). B. Tensile testing of a different specimen aged 26 years. Young's modulus was 8.1 MPa for the IL and 2.9 MPa for the OL, which may be compared with 8.8% and 5.5% elastin density in the two layers, respectively.

1.2.5 Discussion

The current study demonstrated that inner (IL) and outer (OL) layers of the adult human ON sheath, comprising the dural investiture of the ON, have distinct tensile and compressive mechanical properties. In both tension and compression, the IL is stiffer, and its tensile modulus dominates behavior of the sheath as a whole. Local micro-indentation demonstrated that ON sheath IL is significantly stiffer and more viscous than the OL.

The ON sheath exhibited similar mechanical behavior under both longitudinal and circumferential tensile loading, and this similarity is supported by application of the rules of mixtures to compare the YM of the whole sheath with YM values of each of its readily-separable layers. Therefore, it is reasonable to regard the ON sheath as a transverse isotropic material (Fig. 6), a special case of orthotropic material, that is symmetric about an axis normal to the plane of isotropy [31], along the radial axis of the ON and sheath. Transverse isotropy is common in geophysics and biological membranes, wherein the properties in the plane of the membrane differ from those perpendicular to it.

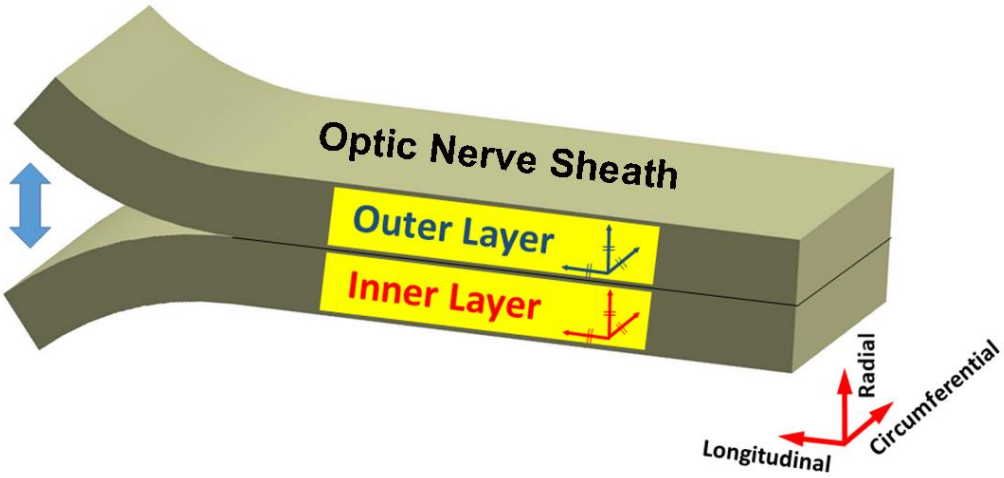

Figure 6. Transverse isotropy of optic nerve (ON) sheath that consists of inner and outer layers weakly attached along the radial boundary, so that the whole sheath has isotropic properties in the longitudinal and circumferential directions.

Examination of mechanical and anatomical characteristics in two of the same specimens suggests that the IL might stiffer, at least in part, because it has denser elastin. Elastin is a protein with reversible extensibility preventing dynamic tissue creep and permitting tissues to resume their shapes after loading [32]. Elastin is abundant in artery, lung, elastic ligament, cartilage, and skin [33, 34], as well as in the lamina cribrosa [35-37], the peripapillary scleral ring [36], and the connective pulley tissue system of the orbit at sites of concentrated mechanical stress [38]. Elastin resists tissue deformation and has a memory permitting it to return to its undeformed shape after low stress loading [32, 39]. Elastin and collagen fibers comprise parallel mechanical elements when tissue undergoes strain: at low strain, collagen fibers extend easily with most of the load borne by elastic fibers, but at high strain, collagen fibers become limiting [40]. For example, in rat aorta, collagen digestion has little effect on stress levels at up to about 30% strain, implicating a major role for elastin in this loading regime [41] that is most relevant to the

strains used in the current paper. We describe in greater detail elsewhere the laminar differences in elastin abundance and fiber orientation in the human ON sheath [24]. Cross linking and absence of elastin turnover with age leads to tissue stiffening [40]. The higher elastin density in the ON sheath IL is consistent with its stiffer mechanical properties than the OL.

The biomechanical properties of the human ON sheath are important to understanding of the mechanical loads on the ON and its critical juncture with the globe at the elastic fiber ring that borders the lamina cribrosa (LC) [42]. Finite element models of this mechanical behavior were first developed to clarify the effects of IOP and intracranial pressure on the LC and surrounding ocular tissues [43, 44], but have recently been expanded to include effects of eye movements [14, 22, 45]. Since MRI demonstrates that the ON and sheath exhaust their redundancy and tether the globe against the medial rectus muscle in adduction[1] in a manner that correlates with OCT evidence of peripapillary deformation [22, 46, 47], ON sheath mechanical behavior has become of particular interest. It has recently been proposed that eye movement, particularly adduction, may produce repetitive strain injury to the ON and thus constitute an IOP-independent mechanism of optic neuropathy in glaucoma [3, 22]. This has been proposed to be a major contributor to so-called “normal tension glaucoma” that now represents the most prevalent form of primary open angle glaucoma worldwide [3].

We have elsewhere reported the anatomical finding that the adult (although not child) human ON sheath is distinctly bilaminar. In this context, the present findings that the ON sheath is transversely isotropic with a stiffer and more viscous IL, have important implications for understanding the role of the ON sheath in glaucoma. No prior finite element model has represented the bilaminar nature of the ON sheath, even though the

IL inserts closest to the LC and scleral canal through which the ON axons traverse into the eye. There is published data on the biomechanical properties of the ON sheath only for pig, whose sheath is much thinner than that of human [23]. In the absence of measured data on the human ON sheath, commonly published FEMs have assumed that it identical to the ON sheath of the cow at 45 MPa [14] (three-fold greater than measured here for human), or fitted a Yeoh model to porcine data resulting in an approximate YM of about 4 MPa [23] (about one fourth that than measured here for human). It is obvious that neither of the foregoing values of YM accurately represents human ON sheath, determined here to be about 15 MPa overall, but 19 MPa in the relatively critical IL, about twice that of 10 MPa in the less critical OL. It is possible that the relatively-low 2:1 specimen aspect ratio employed in the current experiments out of anatomical necessity might have caused a modest under-estimation of YM. It is known that aspect ratio is positively correlated with tensile stiffness, so that as a specimen aspect ratio increases from 1 to 5, stiffness increases by 36% [25]. While aspect ratio might account for as much as 30% differences in YM, it seems unlikely to account for the three- to four-fold differences between the current values for human, and those published for pig.

No prior model has considered ON sheath viscosity, which should eventually be considered to account for human eye saccadic eye movements typically reaching hundreds of deg/s [9] and occur about 180,000 times daily [8]. Greater IL stiffness might concentrate the stress generated by ON sheath tethering in adduction into the critical ONH area [1]. Further FEM incorporating all these aspects would provide more precise predictions of the mechanical behavior of the posterior eye, both as influenced by IOP and by eye movement.

In general, younger people may have more compliant peripapillary tissues than older people because of age-related stiffening in sclera[48-50] and Bruch's membrane [51]. Elastosis of the lamina cribrosa progresses with age[52-55], particularly people who have open angle glaucoma [40, 56, 57]. Elastin density in the human ON sheath increases significantly with age [24]. Although specimens in the current study lacked sufficient age variation to address this question, it would of course be important to determine the relative laminar effects of age-related elastosis on the ON sheath, as sheath elastosis with advancing has been proposed as a likely etiologic factor in primary open angle glaucoma without elevated IOP [3]. The current study had a paucity of specimens available for concurrent biomechanical and anatomical study, limiting quantitative interpretation of anatomic-mechanical correlations. Future studies would benefit from performing such correlative studies in additional specimens with sufficiently long optic nerves, and preferably in donors both affected and unaffected by glaucoma.

1.2.6 Conclusions

Under tensile loading, the stiffness of the inner layer of the human optic nerve sheath is greater than that of the outer layer, with the sheath as a whole exhibiting an overall stiffness intermediate between the two layers. Under compression, the inner layer of the human optic nerve sheath is stiffer and more viscous than outer layer. The inner layer contains denser elastin than the outer sheath. The greater stiffness and viscosity of the elastin-rich inner layer of the optic nerve sheath may be important in concentrating mechanical stress near the lamina cribrosa when the sheath is under tension during eye movement.

1.2.7 References

1. Demer JL. Optic nerve sheath as a novel mechanical load on the globe in ocular duction. Invest Ophthalmol Vis Sci. 2016;57:1826-38.

2. Suh SY, Le A, Shin A, et al. Progressive deformation of the optic nerve head and peripapillary structures by graded horizontal duction. Invest Ophthalmol Vis Sci. 2017;58:5015-21.

3. Demer JL, Clark RA, Suh SY, et al. Magnetic resonance imaging of optic nerve traction during adduction in primary open-angle glaucoma with normal intraocular pressure. Invest Ophthalmol Vis Sci. 2017;58:4114-25.

4. Apt L. An anatomical reevaluation of rectus muscle insertions. Trans Am Ophthalmol Soc. 1980;78:365-75.

5. Wang YX, Jiang R, Wang NL, et al. Acute peripapillary retinal pigment epithelium changes associated with acute intraocular pressure elevation. Ophthalmology. 2015;122:2022-8.

6. Fortune B. Pulling and tugging on the retina: Mechanical impact of glaucoma beyond the optic nerve head. Inv Ophtalmol Vis Sci. 2019;60:26-35.

7. Sibony PA, Hou W. Adduction-Induced deformations evoke peripapillary folds in papilledema. Ophthalmology. 2019;126:912-4.

8. Robinson DA. Control of eye movements. In: Brooks VB, ed. The nervous system, handbook of physiology. Baltimore: Williams & Wilkins, 1981; v. II, pp. 1275-320.

9. Wu CC, Kowler E. Timing of saccadic eye movements during visual search for multiple targets. J Vis. 2013;13.

10. Leclair-Visonneau L, Oudiette D, Gaymard B, et al. Do the eyes scan dream images during rapid eye movement sleep? Evidence from the rapid eye movement sleep behaviour disorder model. Brain. 2010;133:1737-46.

11. Anastasopoulos D, Ziavra N, Hollands M, Bronstein A. Gaze displacement and inter-segmental coordination during large whole body voluntary rotations. Exp Brain Res. 2009;193:323-36.

12. Tomlinson RD, Bahra PS. Combined eye-head gaze shifts in the primate. II. Interaction between saccades and the vestibuloocular reflex. J Neurophysiol. 1986;56:1558-70.

13. Tomlinson RD, Bahra PS. Combined eye-head gaze shifts in the primate. I. Metrics. J Neurophysiol. 1986;56:1542-57.

14. Shin A, Yoo L, Park J, Demer JL. Finite element biomechanics of optic nerve sheath traction in adduction. J Biomech Eng. 2017;139.

15. Garrity JA. What is the current status of optic nerve sheath fenestration? J Neuroophthalmol. 2016;36:231-4.

16. Elkington AR, Inman CB, Steart PV, Weller RO. The structure of the lamina cribrosa of the human eye: an immunocytochemical and electron microscopical study. Eye (Lond). 1990;4 (Pt 1):42-57.

17. Spoerl E, Boehm AG, Pillunat LE. The influence of various substances on the biomechanical behavior of lamina cribrosa and peripapillary sclera. Invest Ophthalmol Vis Sci. 2005;46:1286-90.

18. Downs JC, Suh JK, Thomas KA, et al. Viscoelastic characterization of peripapillary sclera: material properties by quadrant in rabbit and monkey eyes. J Biomech Eng. 2003;125:124-31.

19. Downs JC, Suh JK, Thomas KA, et al. Viscoelastic material properties of the peripapillary sclera in normal and early-glaucoma monkey eyes. Invest Ophthalmol Vis Sci. 2005;46:540-6.

20. Sigal IA, Flanagan JG, Ethier CR. Factors influencing optic nerve head biomechanics. Invest Ophthalmol Vis Sci. 2005;46:4189-99.

21. Feola AJ, Myers JG, Raykin J, et al. Finite element modeling of factors influencing optic nerve head deformation due to intracranial pressure. Invest Ophthalmol Vis Sci. 2016;57:1901-11.

22. Wang X, Rumpel H, Lim WE, et al. Finite element analysis predicts large optic nerve strains heads during horizontal eye movements. Invest Ophthalmol Vis Sci. 2016;57:2452-62.

23. Raykin J, Forte TE, Wang R, et al. Characterization of the mechanical behavior of the optic nerve sheath and its role in spaceflight-induced ophthalmic changes. Biomech Model Mechanobiol. 2017;16:33-43.

24. Le A, Baig A, Shin A, et al. Bilaminar structure of the human optic nerve sheath. Curr Eye Res. 2017;(submitted).

25. Carew EO, Patel J, Garg A, et al. Effect of specimen size and aspect ratio on the tensile properties of porcine aortic valve tissues. Ann Biomed Eng. 2003;31:526-35.

26. Shin A, Yoo L, Demer JL. Independent active contraction of extraocular muscle compartments. Inv Ophtalmol Vis Sci. 2015;56:199-206.

27. Mihai LA, Chin L, Janmey PA, Goriely A. A comparison of hyperelastic constitutive models applicable to brain and fat tissues. J R Soc Interface. 2015;12:0486.

28. Ogden RW. Large deformation isotropic elasticity - Correlation of theory and Eeperiment for incompressible rubberlike solids. Proceedings of the Royal Society of London Series a-Mathematical and Physical Sciences. 1972;326:565-&.

29. Yoo L, Reed J, Shin A, et al. Characterization of ocular tissues using microindentation and hertzian viscoelastic models. Invest Ophthalmol Vis Sci. 2011;52:3475-82.

30. Askeland DR, Fulay PP, Wright WJ. *The Science and Engineering of Materials*, 6 ed. Boston: Cengage Learning, 2010.

31. Thomsen L. Weak Elastic-Anisotropy. Geophysics. 1986;51:1954-66.

32. Patel A, Fine B, Sandig M, Mequanint K. Elastin biosynthesis: The missing link in tissue-engineered blood vessels. Cardiovasc Res. 2006;71:40-9.

33. Debelle L, Alix AJ. The structures of elastins and their function. Biochimie. 1999;81:981-94.

34. Daamen WF, Veerkamp JH, van Hest JC, van Kuppevelt TH. Elastin as a biomaterial for tissue engineering. Biomaterials. 2007;28:4378-98.

35. Quigley HA, Dorman-Pease ME, Brown AE. Quantitative study of collagen and elastin of the optic nerve head and sclera in human and experimental monkey glaucoma. Curr Eye Res. 1991;10:877-88.

36. Quigley HA, Brown A, Dorman-Pease ME. Alterations in elastin of the optic nerve head in human and experimental glaucoma. Br J Ophthalmol. 1991;75:552-7.

37. Oyama T, Abe H, Ushiki T. The connective tissue and glial framework in the optic nerve head of the normal human eye: light and scanning electron microscopic studies. Arch Histol Cytol. 2006;69:341-56.

38. Kono R, Poukens V, Demer JL. Quantitative analysis of the structure of the human extraocular muscle pulley system. Invest Ophthalmol Vis Sci. 2002;43:2923-32.

39. Oxlund H, Manschot J, Viidik A. The role of elastin in the mechanical properties of skin. J Biomech. 1988;21:213-8.

40. Hernandez MR. Ultrastructural immunocytochemical analysis of elastin in the human lamina cribrosa. Changes in elastic fibers in primary open-angle glaucoma. Invest Ophthalmol Vis Sci. 1992;33:2891-903.

41. Oxlund H, Andreassen TT. The roles of hyaluronic acid, collagen and elastin in the mechanical properties of connective tissues. J Anat. 1980;131:611-20.

42. Tektas OY, Lutjen-Drecoll E, Scholz M. Qualitative and quantitative morphologic changes in the vasculature and extracellular matrix of the prelaminar optic nerve head in eyes with POAG. Invest Ophthalmol Vis Sci. 2010;51:5083-91.

43. Burgoyne CF, Downs JC, Bellezza AJ, et al. The optic nerve head as a biomechanical structure: a new paradigm for understanding the role of IOP-related stress and strain in the pathophysiology of glaucomatous optic nerve head damage. Prog Retin Eye Res. 2005;24:39-73.

44. Sigal IA, Ethier CR. Biomechanics of the optic nerve head. Exp Eye Res. 2009;88:799-807.

45. Wang X, Fisher LK, Milea D, et al. Predictions of optic nerve traction forces and peripapillary tissue stresses following horizontal eye movements. Invest Ophthalmol Vis Sci. 2017;58:2044-53.

46. Chang MY, Shin A, Park J, et al. Deformation of optic nerve head and peripapillary tissues by horizontal duction. Am J Ophthalmol. 2017;174:85-94.

47. Sibony PA. Gaze-evoked deformations of the peripapillary retina and papilledema and ischemic optic neuropathy. Inv Ophtalmol Vis Sci. 2016;57:4979-87.

48. Geraghty B, Jones SW, Rama P, et al. Age-related variations in the biomechanical properties of human sclera. J Mech Behav Biomed Mater. 2012;16:181-91.

49. Coudrillier B, Tian J, Alexander S, et al. Biomechanics of the human posterior sclera: age- and glaucoma-related changes measured using inflation testing. Invest Ophthalmol Vis Sci. 2012;53:1714-28.

50. Avetisov ES, Savitskaya NF, Vinetskaya MI, Iomdina EN. A study of biochemical and biomechanical qualities of normal and myopic eye sclera in humans of different age groups. Metab Pediatr Syst Ophthalmol. 1983;7:183-8.

51. Booij JC, Baas DC, Beisekeeva J, et al. The dynamic nature of Bruch's membrane. Prog Retin Eye Res. 2010;29:1-18.

52. Albon J, Karwatowski WS, Easty DL, et al. Age related changes in the non-collagenous components of the extracellular matrix of the human lamina cribrosa. Br J Ophthalmol. 2000;84:311-7.

53. Albon J, Karwatowski WS, Avery N, et al. Changes in the collagenous matrix of the aging human lamina cribrosa. Br J Ophthalmol. 1995;79:368-75.

54. Albon J, Purslow PP, Karwatowski WS, Easty DL. Age related compliance of the lamina cribrosa in human eyes. Br J Ophthalmol. 2000;84:318-23.

55. Leung LK, Ko MW, Lam DC. Effect of age-stiffening tissues and intraocular pressure on optic nerve damages. Mol Cell Biomech. 2012;9:157-73.

56. Pena JD, Netland PA, Vidal I, et al. Elastosis of the lamina cribrosa in glaucomatous optic neuropathy. Exp Eye Res. 1998;67:517-24.

57. Netland PA, Ye H, Streeten BW, Hernandez MR. Elastosis of the lamina cribrosa in pseudoexfoliation syndrome with glaucoma. Ophthalmology. 1995;102:878-86.

58. Lee EH, Radok JRM. The contact problem for viscoelastic bodies. J Appl Mech. 1960;27:438-44.

59. Mattice J, Lau A, Oyem M, Kent R. Spherical indentation load-relaxation of soft biological tissues. J Mater Res. 2006;21:2003-10.

60. Johnson KL. *Contact Mechanics*. Cambridge, UK: Cambridge University Press, 1985.

61. Oyen ML. Sopherical indentation creep following ramp loading. J Mater Res. 2005;20:2094-100.

62. Roylance D. *Engineering Viscoelasticity*. Cambridge, CA: Department of Materials Science and Engineering - Massachusetts Institute of Technology, 2001.

1.3 Elastin Reinforced Lamina Cribrosa

Presentation at The Association for Research in Vision and Ophthalmology (ARVO) Conference 2017

Addie Ferguson[2], Alan Le[1,2] , Milind Vasudev[2], Vadims Poukens[2], and Joseph L. Demer[1-6]

[1]Department of Bioengineering, [2]Department of Ophthalmology and Stein Eye Institute, [3]Department of Neurology, [4]Neuroscience and [5]Bioengineering Interdepartmental Programs, [6]David Geffen Medical School at University of California, Los Angeles.

1.3.1 Abstract

Purpose: Demer et. al, has previously shown optic nerve (ON) tethering and stretching during extreme adduction. The mechanical overload at the globe-optic nerve junction may cause a form of neuropathy independent of intraocular pressure. We are interested in studying elastin structures within the lamina cribrosa (LC) to help elucidate its role in glaucomatous optic neuropathy.

Methods: Seven human ONs, aged 64-93 years old, were fixed in formalin, embedded in paraffin, transversely sectioned at 10 microns thickness, and stained for light microscopy with the elastin van Gieson method. With Adobe Photoshop and ImageJ, we identified in micrographs the elastin fibers to determine elastin density within the LC, LC beam structure, and characterize the elastin ring structure at the anterior circumference of the LC.

Results: Elastin beams have hourglass structures, with wide bases joined by thinner connecting bridges. The ratio of wide base to thinnest center is 2.78 ± 0.04 (SEM). Anterior to the LC, elastin fibers circumferentially form a dense ring around the ON 33.8 ± 1.0 (SEM) μm thick. The LC is anchored to surrounding sclera by projections containing both collagen and elastin. There are 3.93 ± 0.15 (SEM) projections per arc length 525 μm along LC circumference.

Conclusions: The LC is reinforced with elastin fibrils, presumably allowing it to withstand repetitive mechanical stress. There is a dense elastin ring encircling the ON at the anterior end of the LC and multiple elastin embedded collagen projections, which anchors the LC to the surrounding circumferential peripapillary sclera (CPS).

1.3.2 Results

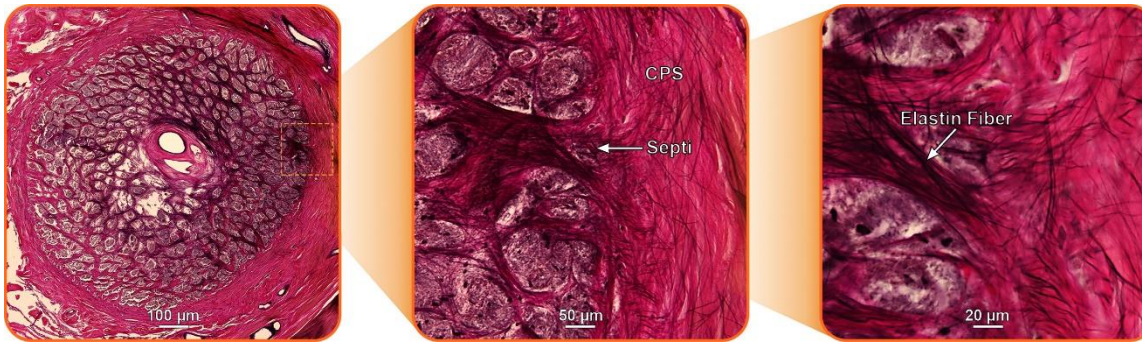

Figure 1. Lamina cribrosa is anchored by projects containing collagen and elastin. Each laminar beam is heavily reinforced with elastin.

1.3.3 Discussion

According to recent studies by Demer, et. al, during large adduction, there is force concentration at the surrounding CPS and underlying regions including the LC. Elastin reinforces the LC and CPS and may protect against ON tethering and stretching during repetitive, large adduction. Therefore, changes in elastin structures within the LC and CPS may contribute to damage at these areas. In agreement with Quigley's studies, there is a dense elastin ring at the immediate insertion zone of the. This ring completely surrounds the optic nerve and acts as an anchoring point between the LC insertion zone and surrounding CPS. Septi containing elastin and collagen also anchor the LC to the CPS and provide more reinforcement. Elastin fibers stretch and appear rigid, giving the laminar beams a structure of wide bases and a thin center, similar to an hourglass shape. Moreover, better understanding of these structures within the LC and CPS improves our knowledge of the biomechanical mechanisms that causes glaucomatous neuropathy independent of intraocular pressure.

1.3.4 Conclusion

A ring of dense elastin surrounds optic nerve at lamina cribrosa insertion zone. Septi containing elastin and collagen anchor the lamina cribrosa to the circumferential peripapillary sclera. Laminar beams are hourglass shaped with thin centers and wide bases.

1.4 Focal Circumpapillary Scleral Elastosis

Presentation at The Association for Research in Vision and Ophthalmology (ARVO) Conference 2018

Alan Le[1,2], Ayesha Baig[2,4], Joseph Park[1,2], Vadims Poukens[2], and Joseph L. Demer[1-6]

[1]Department of Bioengineering, [2]Department of Ophthalmology and Stein Eye Institute, [3]Department of Neurology, [4]Neuroscience and [5]Bioengineering Interdepartmental Programs, [6]David Geffen Medical School at University of California, Los Angeles.

1.4.1 Introduction

Magnetic resonance imaging shows that the optic nerve (ON) sheath tethers the globe in adduction, possibly causing repetitive strain injury and optic neuropathy after many accumulated eye movements. Tension in the straightened ON sheath acts on the peripapillary sclera causing local deformation. Elastin and collagen fibers reinforce the tissues at the globe ON junction to enhance structural integrity. The ON dural sheath contains a three-dimensional weave of elastin fibers protecting the nerve bundles within, while a dense elastin ring encircling the lamina cribrosa and fine elastin fibers circumferential to the peripapillary sclera have been described. However, little is known about development and distribution of elastin deposits (ED) in the posterior sclera more remote from the ON head that may be important to the biomechanics of optic neuropathy. This study characterized such ED in the human posterior sclera.

1.4.2 Methods

Slide Preparation

Samples of fresh eye bank circumpapillary tissue were cut with a trephine blade 7.5mm in diameter centered on the globe-optic nerve junction. These specimens and whole orbits were embedded in paraffin and serially sectioned traverse to the long orbital axis at 10 microns thickness. Van Gieson's stain was used to identify elastin fibers.

Image Processing

Color and contrast thresholding selected the dark elastin fibers. We measured local density of elastin fibers, size and location of elastin deposits.

1.4.3 Results

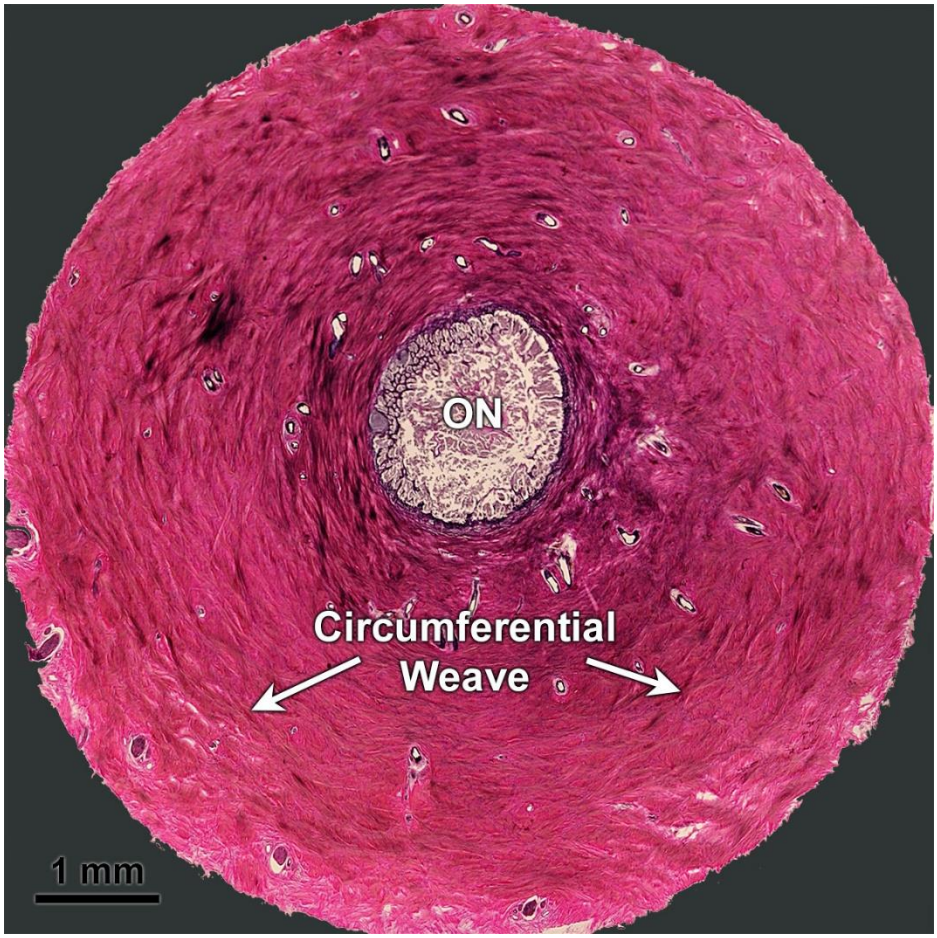

Figure 1. 74 year old adult. Broad circumferential bands encircle the optic nerve. Elastin deposits are scattered in the peripapillary sclera.

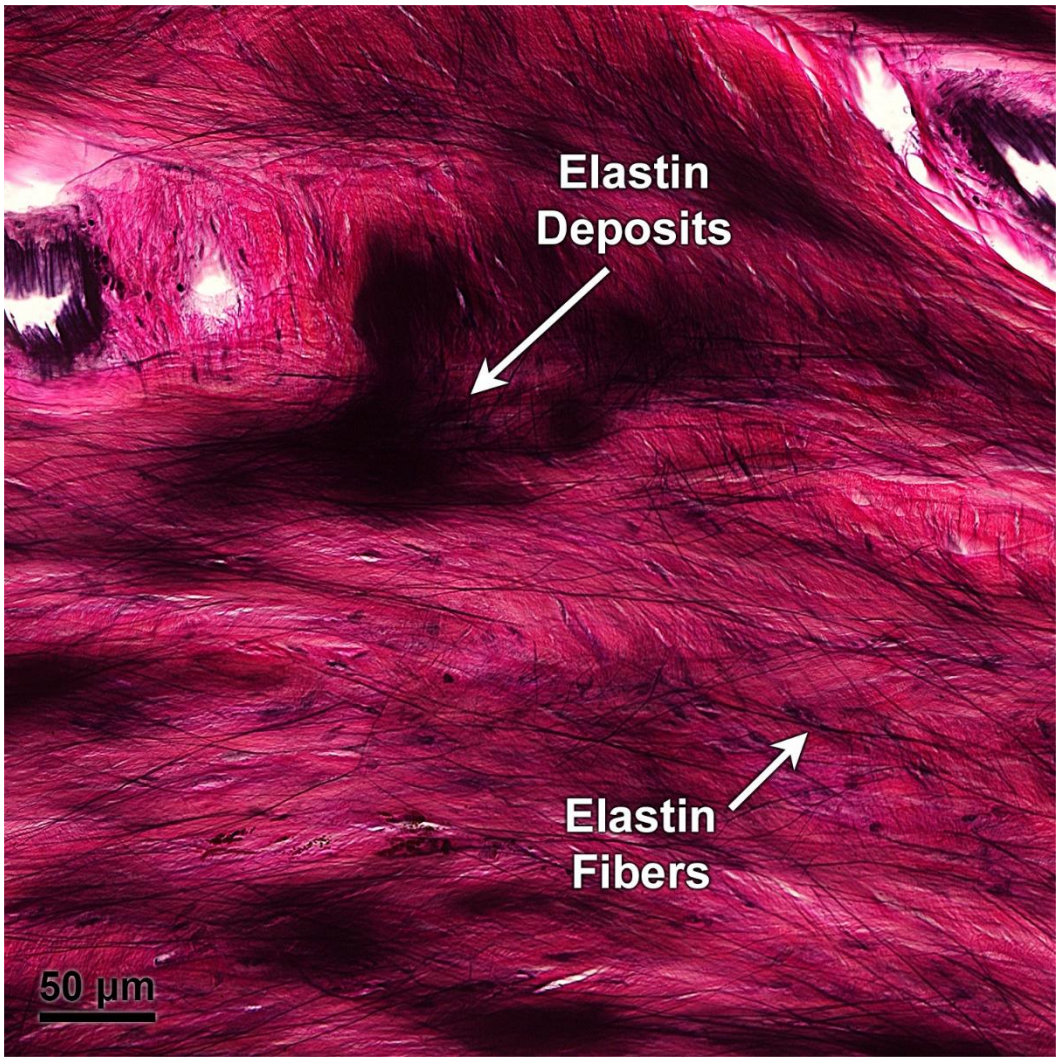

Figure 2. At high magnification, we can see that elastin deposits are composed of extremely fine disorganized elastin fibers clumping together.

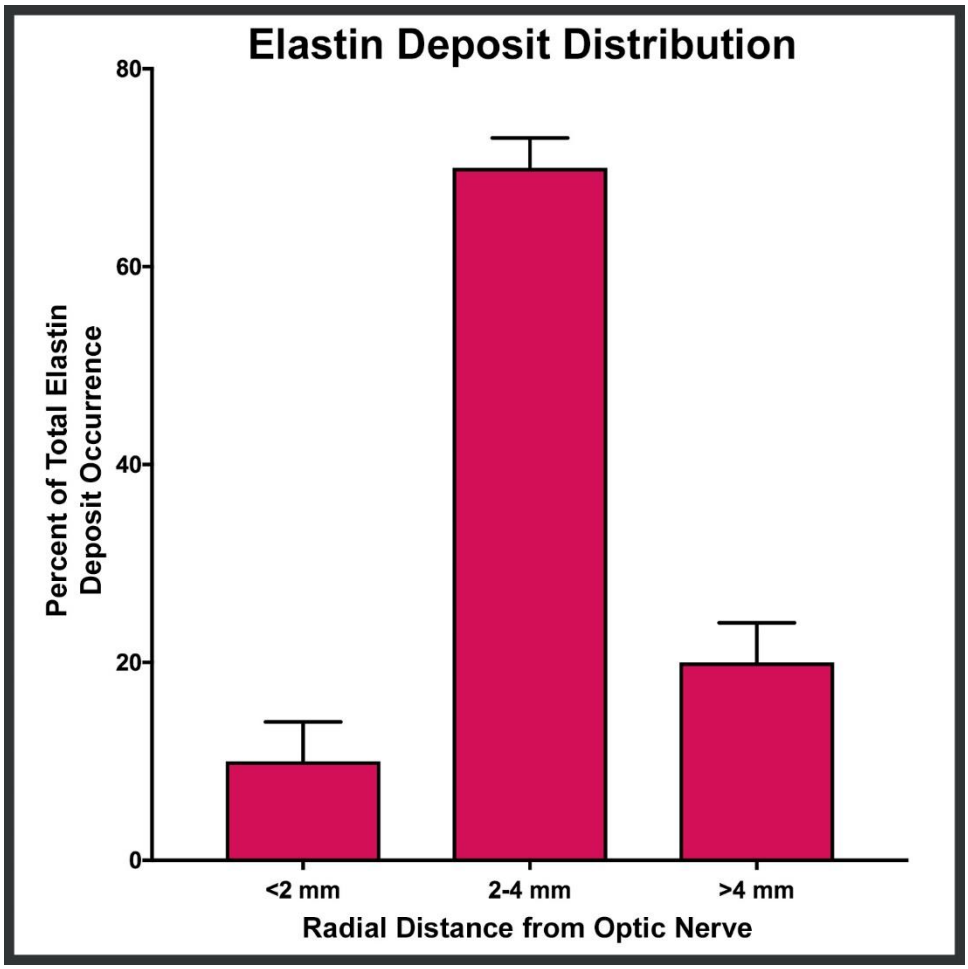

Figure 3. Elastin deposits with areas ranging from 0.003-0.044 mm^2 were widely dispersed 0.3 to beyond 8 mm from the globe-ON junction. The majority of elastin deposits were found 2-4 mm from the junction.

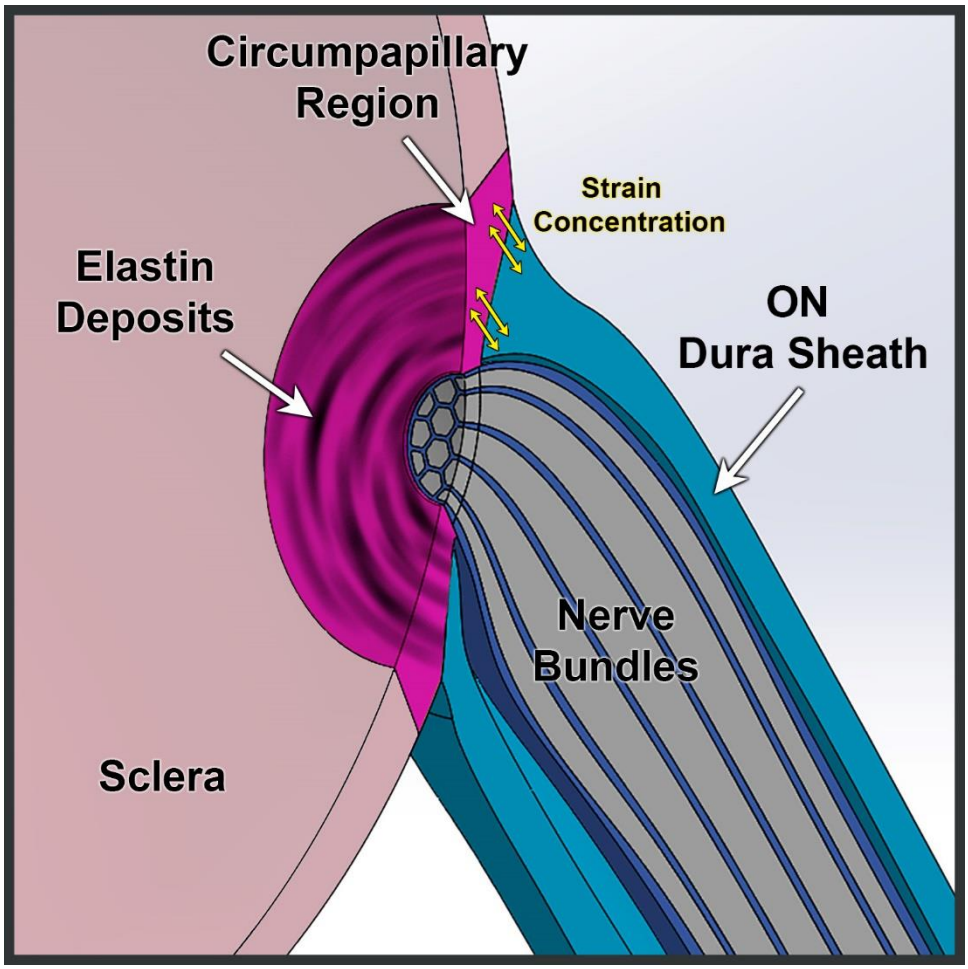

Figure 4. Tightening of the optic nerve dura sheath during large angle adduction can cause strain concentration at the peripapillary sclera where the dense elastin deposits are found. These deposits may have resulted from repetitive strain.

1.4.4 Discussion

Past studies have noted rings of the circumferential elastin fibers embedded in the posterior sclera and a dense elastin ring at the board of the lamina cribrosa. In this study, we confirm this circular weave of elastin fibers but also found dense deposits of elastin fibers in all adult specimens that were non-uniformly distributed around the circumpapillary sclera. Unlike the elastin in the optic nerve dura sheath reported to have uniform laminar circumferential, diagonal, and longitudinal arrangement of the fibers that crisscross to form a mesh, these deposits appear to be extremely fine elastin aggregated in an irregular dense orientation. Elastin deposits were not observed in children, leading us to conclude that these elastin deposits are probably acquired over a lifetime of eye rotations. The elastin deposits could be pathologic results of remodeling at the globe optic nerve junction in response to repetitive mechanical strain. Cyclic stretching of the circumpapillary sclera and the surrounding tissue could disrupt the regular circumferential orientation of elastin fibers, leading to large, disorganized, scattered clumps that we observed. Elastin deposits might alternatively have developed as a protective mechanism resisting repetitive strain, and thus fortify the tissue against further deformation that could worsen neuropathy.

1.4.5 Conclusion

Dense, focal masses of elastin develop in the PPS after childhood. Elastin deposits are embedded in the adult sclera around the optic nerve head just peripheral to the elastic ring around the lamina cribrosa. Elastin deposits may alter the biomechanical properties of the circumpapillary and posterior sclera and might be induced by repetitive strain in this normally mechanically pliable region when subjected to optic nerve traction during eye rotation.

Chapter 2: Clinical Studies with OCT and cSLO

Heidelberg Spectralis Swept-Source OCT imaging machine was used to observe optic nerve deformation during large angle eye rotations. Here, five papers are presented showing evidence of tissue deformation at and around the optic nerve head during static eye adduction. The first two utilizes OCT B-scans while the latter three relies on *enface* cSLO images taken concurrently with OCT B-scans. Paper 1 measures the Burch's membrane shift while paper 2 focuses on the choroidal changes during adduction. Papers 3-5 use blood vessel fiducials on the retina surface to quantify the deformation caused by adduction. Younger subjects had the most deformation to their retina and optic nerve head surface while subjects with glaucoma had the least.

Publications included in this chapter by Candidate:

Published Journal Papers

1. Suh SY, **Le A**, Shin A, Park J, Demer JL. Progressive deformation of the optic nerve head and peripapillary structures by graded horizontal duction. Invest Ophthalmol Vis Sci. 2017;58:5015-21.
2. Chen JY, **Le A**, De Andrade LM, Goseki T, Demer JL. Compression of the Choroid by Horizontal Duction. Invest Ophthalmol Vis Sci. 2019 Oct 1;60(13):4285-4291. doi:10.1167/iovs.19-27522.
3. **Le A**, Chen J, Lesgart M, Gawargious BA, Suh SY, Demer JL. Age-dependent Deformation of the Optic Nerve Head and Peripapillary Retina by Horizontal Duction. Am J Ophthalmol. 2020 Jan;209:107-116. doi:10.1016/j.ajo.2019.08.017. Epub 2019 Aug 29.

Journal Manuscripts under Review

4. **Le A**, Chen JY, Caprioli J, Giaconi JA, Nouri-Mahdavi K, Law SK, Bonelli L, Coleman AL, Demer JL. Adduction Deformation of Optic Disc and Peripapillary Region in Primary Open Angle Glaucoma with Normal Intraocular Pressure. Summited to *Current Eye Research*, 2020.
5. **Le A**, Chen JY, Caprioli J, Giaconi JA, Nouri-Mahdavi K, Law SK, Bonelli L, Coleman AL, Demer JL. Peripapillary Atrophy and Optic Disc Stiffening in

Primary Open Angle Glaucoma at Normal Intraocular Pressure. Summited to *Current Eye Research*, 2020.

2.1 Progressive Deformation of the Optic Nerve Head and Peripapillary Structures by Graded Horizontal Duction

Soh Youn Suh[1], Alan Le[1,4,5], Andrew Shin[1], Joseph Park[1,5], Joseph L. Demer[1-6]

[1]Department of Ophthalmology and [2]Stein Eye Institute, [3]Department of Neurology, [4]Neuroscience and [5]Bioengineering Interdepartmental Programs, [6]David Geffen Medical School at University of California, Los Angeles.

2.1.1 Abstract

Purpose: We investigated the effect of graded range of horizontal duction on the shape of the peripapillary Bruch's membrane (ppBM) and optic nerve head (ONH).

Methods: In 30 eyes of 15 normal subjects, the ONH and peripapillary retina were imaged by optical coherence tomography (OCT) in central gaze and incremental angles of both adduction and abduction. Displacements of the Bruch's membrane opening (BMO), optic cup (OC), and change in ONH angle in eccentric gazes were compared with those of central gaze, in both adduction and abduction.

Results: With increasing duction, the nasal BMO (nBMO) shifted progressively anteriorly in adduction and posteriorly in abduction, while the temporal BMO (tBMO) shifted posteriorly in adduction and anteriorly in abduction. The summed nBMO and tBMO displacements from 25° to 35° adduction was significantly larger than those in comparable angles of abduction ($P < 0.05$). ONH progressively tilted temporally in adduction and nasally in abduction; absolute ONH tilt in adduction was significantly greater than in abduction for ductions of 25°, 30° and 35°($P < 0.05$ for all). Both BMO displacement and ONH tilt in adduction exhibited bilinear behavior, with greater effects for both at angles exceeding 22°. The OC shifted significantly farther anteriorly in abduction than adduction at every angle from 10° to 35°.

Conclusion: Horizontal duction deforms the ONH and ppBM, but more in adduction than in abduction, and increasingly so for angles exceeding 22°. This behavior is consistent with optic nerve sheath tethering for adduction exceeding 22°.

2.1.2 Introduction

Magnetic resonance imaging (MRI) has recently demonstrated that the optic nerve (ON) and its sheath tether the globe during large angle ocular adduction[1]. The path of ON and sheath gets straightened in adduction, While the ON and sheath are generally sinuous and redundant in central gaze and abduction, these structures straighten to minimum path length at a threshold adduction angle, after which further adduction requires a combination of ON elongation and globe displacement, including retraction. These effects imply that tractional force is exerted on the globe by the ON and sheath at angles exceeding the tethering threshold estimated from MRI to be about 20°. MRI provides evidence that this traction force induced by ON sheath tethering in adduction is mainly focused on the temporal ONH and peripapillary tissue, which correlates with the location of the peripapillary atrophy (PPA) frequently found in glaucoma patients.[2-4] This mechanical force has therefore been suggested as a possible intraocular pressure (IOP)-independent mechanism of glaucomatous optic neuropathy.

This novel concept of ON tethering in adduction has been further supported by biomechanical studies using finite element analysis of the mechanical stress (force/cross-sectional area) and strain (local deformation caused by stress) in the ONH during horizontal eye movement,[5, 6] particularly in adduction. While most prior biomechanical studies focused on the effects of IOP changes on ONH,[7-11] these recent studies showed that deformation of the ONH caused by ON sheath traction in adduction is comparable or even greater than induced by significant IOP elevation.

Biomechanical effects of horizontal duction on the ONH and peripapillary tissue have also been demonstrated in vivo by optical coherence tomography (OCT) studies.[12-14] Sibony used fixed angles of add- and abduction to demonstrate gaze-evoked

deformation of the nasal and temporal peripapillary basement membranes in normal subjects that were greatly exaggerated in patients with papilledema.[12] Wang *et al*.[13] demonstrated by OCT that fixed angles of both moderate add- and abduction produce significant ONH strains in normal subjects. However, these OCT studies did not parameterize the angles of ocular duction, and thus could not evaluate possible gradual or threshold effects of graded amounts of eye movement.

In our earlier OCT study, we reported progressive tilting of the ONH with displacement of peripapillary retina during a graded range of add- and abduction in 10° increments nominally up to a maximum of 30°.[14] However, the nominal central position for this study was relative to the craniotopic straight-ahead position, and did not account for an offset of as much as 17° of the internal fixation target in the OCT scanner that biased fixation toward the nasal direction. It is now recognized that this internal target position offset caused overestimation of adduction angles, and underestimation of abduction angles. This adduction bias of central target position may be the reason that the earlier OCT study both failed to demonstrate significant ONH deformation during abduction, and did not demonstrate a threshold effect during adduction.

The foregoing evidence supports the supposition that there may be two mechanisms of horizontal duction-related ONH deformation: 1) a small angle mechanism acting similarly in both add- and abduction; and 2) a threshold mechanism acting only after ON and sheath tethering occur in large angle adduction. Using a wider range of both horizontal ductions in finer increments centered on an unbiased, straight-ahead eye position, the current study aimed to investigate the graded effect of horizontal eye movement on ONH and peripapillary retina and determine the possible threshold point of the tethering force exerted by the ON in adduction.

2.1.3 Methods

Subjects

Fifteen volunteers (10 male and 5 female) of the mean age 33.4 ± 15.9 (SD, range 18-63) years free from ocular disorder other than refractive error were recruited by advertising for this study. Subjects provided written, informed consent prior to participation according to a protocol approved by the University of California, Los Angeles Institutional Review Board conforming to the tenets of the Declaration of Helsinki. Comprehensive eye examinations were performed for each subject and all had normal corrected visual acuity, normal intraocular pressure (< 21mmHg) and normal binocular alignment. All 30 eyes were included for analysis. Mean spherical equivalent refractive error was -2.4 ± 2.6 (standard deviation, SD; range, 0.25 to -7.50) diopters.

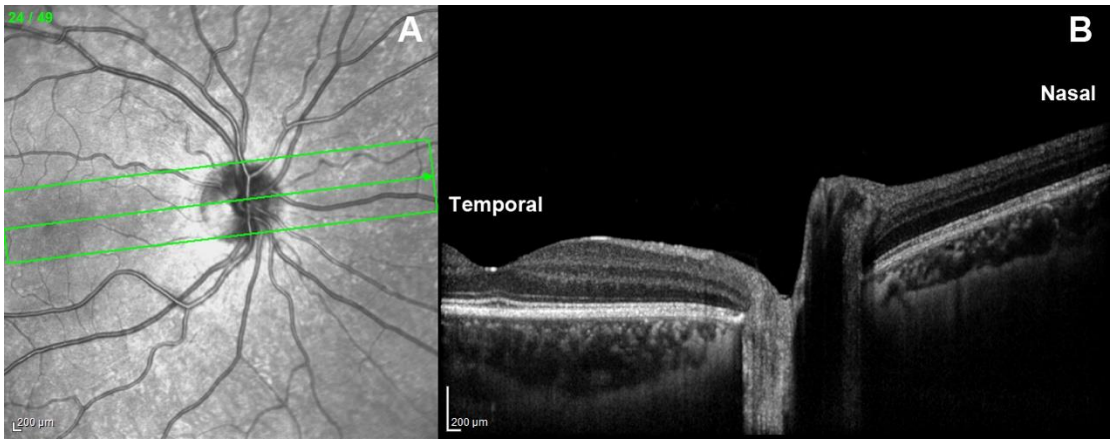

Figure 1. En face scanning laser ophthalmoscopy (A) and B-scan optical coherence tomography (B) of optic nerve head (ONH) and peripapillary retina. The middle scan including the ONH center and fovea was analyzed.

Optical Coherence Tomography

A spectral domain OCT (Spectralis, Heidelberg Engineering, Heidelberg, Germany) was used for imaging after pupillary dilation using phenylephrine-HCl 2.5% drops. A retinal nerve fiber layer (RNFL) circular scan was first performed to verify normal RNFL thickness in each eye. Then, wide-field volume scans of the ONH and

peripapillary retina were performed in both eyes in central gaze, adduction (10°, 20°, 25°, 30°, 35°, and 40° (when available) and abduction (10°, 20°, 25°, 30°, and 35°) sequentially. The enhanced depth imaging (EDI) consisted of 49 horizontal B-scans covering 30° x 5° rectangular region of ONH and peripapillary retina, vertically spaced at 30μm. The raster was rotated to align the center of the ONH with the fovea before each scan (Fig. 1). To scan the eye in eccentric gazes, the OCT device was incrementally rotated in yaw to angles marked with a goniometric scale on its vertically-oriented pivot. Subjects were instructed to fix on the internal scanner target with head fixed in central position using cushions and straps. The scanner is designed to offset its internal fixation target nasally to scan the ONH. The angle of this offset was determined in preliminary scans in which subjects fixated a target about 3 m distant with the non-imaged fellow eye. Since this viewing condition is not associated with convergence, it was possible to iteratively position the horizontal location of the distant target until the fovea was centered in the OCT scan. This demonstrated that the internal target was offset by 12° nasally. This offset was then applied to the goniometer scale attached to the scanner pivot, and employed for all subjects. Adduction angle of 40° was obtainable in only a minority of subjects (n=10) with favorable facial anatomy, since in the remainder the subject's nose collided with the lens of OCT scanner. Abduction was limited to of 35° due to a mechanical limit in the scanner pivot.

Image Analysis

Among the 49 scans obtained for each eye in each gaze position, the scan including the center of the ONH and fovea was analyzed. These selected images were exported as TIFF files and processed using Adobe Photoshop (Adobe Systems, San Jose, CA, USA). After correction of the aspect ratio that is vertically exaggerated in raw scanner images, images in central gaze and eccentric gazes were colored differently in

red or green for comparison in superimposable layers. Using reduced image opacity, scans in central and each eccentric gaze were then superimposed at both the far nasal and temporal peripheries of Bruch's membrane (BM, Figure 2, top). While no absolute reference for ONH deformation is available, this approach provided a reference for displacement of the peripapillary region relative to relatively remote retinal locations presumed to be least likely to experience local deformation transmitted from the ONH. The remote nasal and temporal peripheral locations were both used as reference points since the direction of peripapillary retina displacement would otherwise depend on the choice of the reference.[14]

We analyzed three parameters for the scan in each eccentric gaze relative to central gaze: (1) displacement of the nasal and temporal Bruch's membrane opening (nBMO and tBMO); (2) change in ONH tilt angle as measured by the angle of a line connecting the nBMO and tBMO; and (3) displacement of the optic cup (OC) measured by the vertical distance from the deepest point of the OC to the line connecting nBMO and tBMO. The BMO, the termination of Bruch's membrane at the ONH, was chosen for the analysis because it is easily identified by SD-OCT and is an important anatomical structure through which the retinal nerve fibers pass.[15]

Statistical Analysis

Displacement from central gaze of the nBMO and tBMO, the change of the ONH tilt angle, and the displacement of the OC were compared using paired t-tests. To account for interocular correlation in the two eyes of each subject, repeated analysis was performed using generalized estimating equations (GEE) with SPSS software (Version 24.0. Armonk, New York, USA: IBM Corporation). For data sets that seemed monotonically bilinear, we summed coefficients of determination for linear fits to each data segment for all possible ranges of each fit, and considered the optimum transition

point between fits to be that transition point resulting in the maximum summed coefficient of determination. The intersection of the two regression lines having the greatest summed coefficients of determination was considered to be the best estimate of the transition point between bilinear fits.

2.1.4 Results

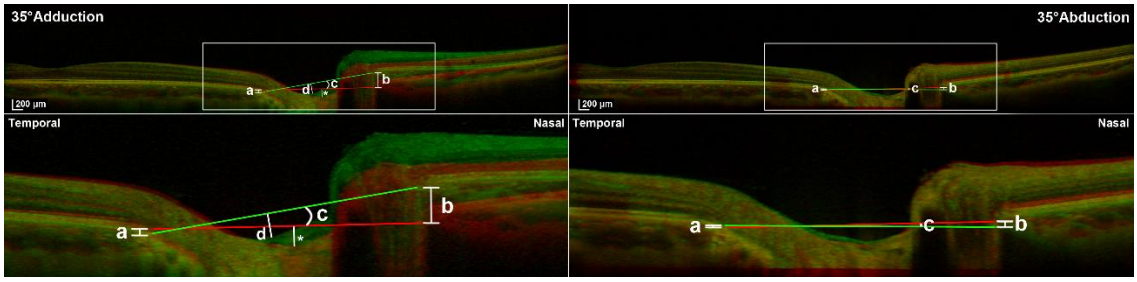

Figure 2. Superimposed optical coherence tomography (OCT) images of a right eye in central gaze (red reference image in all cases), 35° adduction (green, left column), and 35° abduction (green, right column). (Top row) Ten mm-wide OCT scans. Red (central gaze) and green lines (eccentric gaze) connect nasal (nBMO) and temporal edges of Bruch's membrane opening (tBMO). (Bottom row) Magnified views of rectangular area in upper panels. (Left column) In adduction, tBMO shifts posteriorly (a), nBMO shifts anteriorly (b), and optic nerve head (ONH) tilts temporally (c). Vertical distance from the BMO connecting line to the bottom of the optic cup (OC) was measured in central gaze (*) and in adduction (d) to determine the OC displacement. (Right column) In abduction, tBMO shifts anteriorly (a), nBMO shifts posteriorly (b), and ONH tilts nasally (c). Note that the absolute BMO displacements and ONH tilt angles are greater in 35° adduction than in 35° abduction.

Bruch's membrane opening displacements

Deformation of the peripapillary region was consistently demonstrated by OCT in both add- and abduction (Fig. 2). In adduction**,** nBMO shifted anteriorly and tBMO shifted posteriorly continuously with increasing angle (Fig. 3). Conversely, in abduction, nBMO shifted posteriorly and tBMO shifted anteriorly relative to central gaze (Fig. 3). Since nBMO and tBMO shifted in opposite directions, the sum of the absolute values of nBMO and tBMO displacement was compared between abduction and adduction. Total BMO displacement in adduction was significantly greater than in abduction for angles of 25°, 30°, and 35° (P= 0.02, P = 0.001, and P = 0.001, respectively, GEE). The summed

amount of nBMO and tBMO displacements were 90 ± 13μm (mean ± standard error of mean, SEM) and 133 ± 25 μm in 35° and 40° adduction, respectively, but only 52 ± 9 μm in 35° abduction.

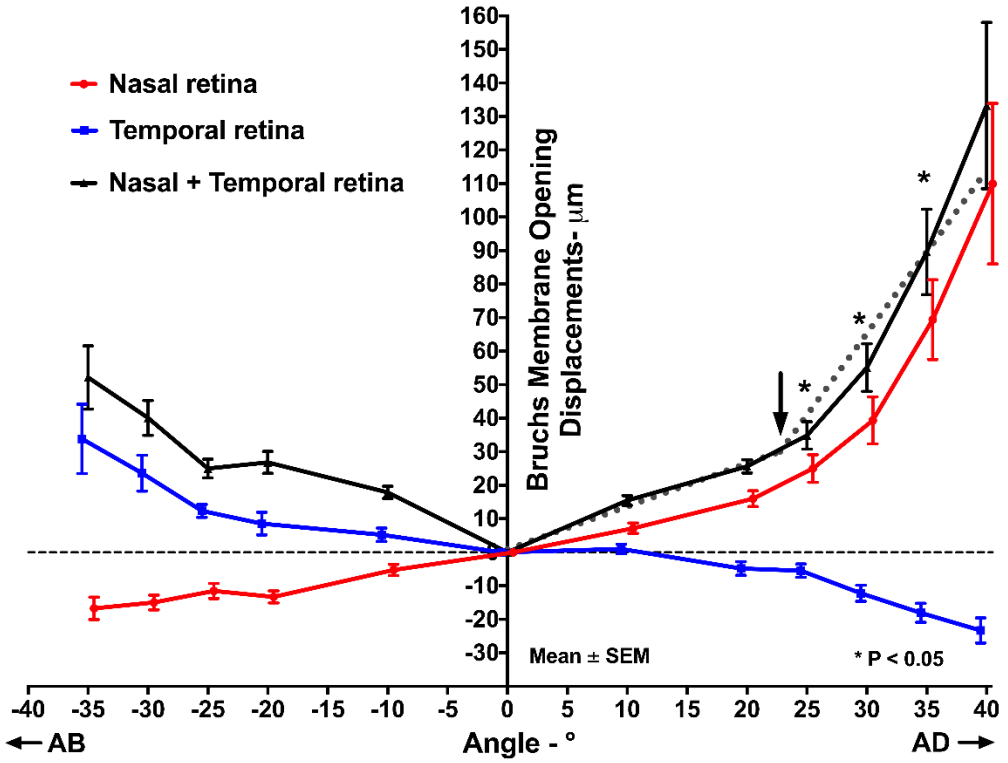

Figure 3. Mean displacements of nasal (nBMO) and temporal Bruch's membrane opening (tBMO) in adduction and abduction. The summed absolute nBMO and tBMO displacements were greater in adduction than in abduction at 25°, 30°, and 35°. Intersection of the two best bilinear fits regarding summed BMO displacements in adduction occurred at 22.8° (black arrow).

The plots of BMO displacement in adduction illustrated in Fig. 3 suggest bilinear phenomena, with a low rate of change in BMO displacement with gaze angle up to about 20°, and a higher rate of change for larger angles where displacements in adduction significantly exceeded those in the same angles of abduction (Fig. 3). This suggestion was tested quantitatively by bilinear regression as described above. The intersection of the two best bilinear fits occurred at 22.8° adduction, suggesting this angle as a threshold for behavioral transition.

Optic nerve head tilt angle

The ONH progressively tilted temporally in increasing adduction and reached 3.7 ± 0.7° in 40° adduction (Fig. 4). In abduction, ONH tilted nasally and the tilted angle measured 1.3 ± 0.2° in 35° abduction (Fig. 4). Similar to the pattern of BMO displacement, the absolute value of ONH tilt was significantly larger in 25°, 30° and 35° adduction than in comparable abduction ($P = 0.048$, $P < 0.001$, and $P < 0.001$, respectively, GEE). Bi-linear regression indicated a transition point of 22.1° in adduction, which is similar to the threshold for BMO displacement.

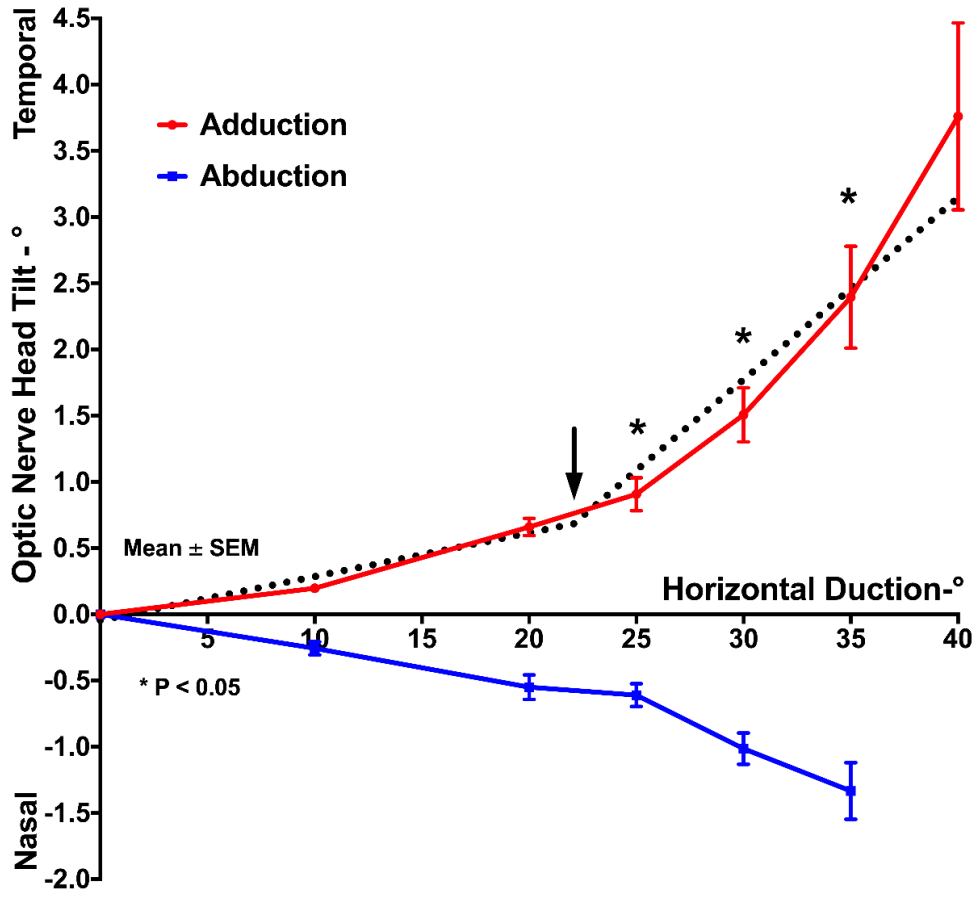

Figure 4. Mean optic nerve head (ONH) tilt in adduction and abduction. The absolute tilt at 25°, 30°, and 35° adduction was significantly greater than in comparable abduction. Bi-linear regression of ONH tilt angle in adduction indicated a transition point of 22.1° (black arrow).

Optic cup displacement

The direction of the OC displacement in eccentric gazes corresponded to the dominant direction of the ppBM displacement. Thus, we considered that measuring the vertical distance from the line connecting nasal and temporal BMO points with the bottom of the OC would reflect the relative movement of the OC independently of shifts in the BMO. Position of the OC position varied widely, particularly for large ductions, but there was a trend toward anterior OC displacement in abduction and slight posterior displacement in adduction (Fig. 5). The difference in OC position between abduction and adduction was statistically significant at every angle from 10° to 35° ($P < 0.04$, GEE).

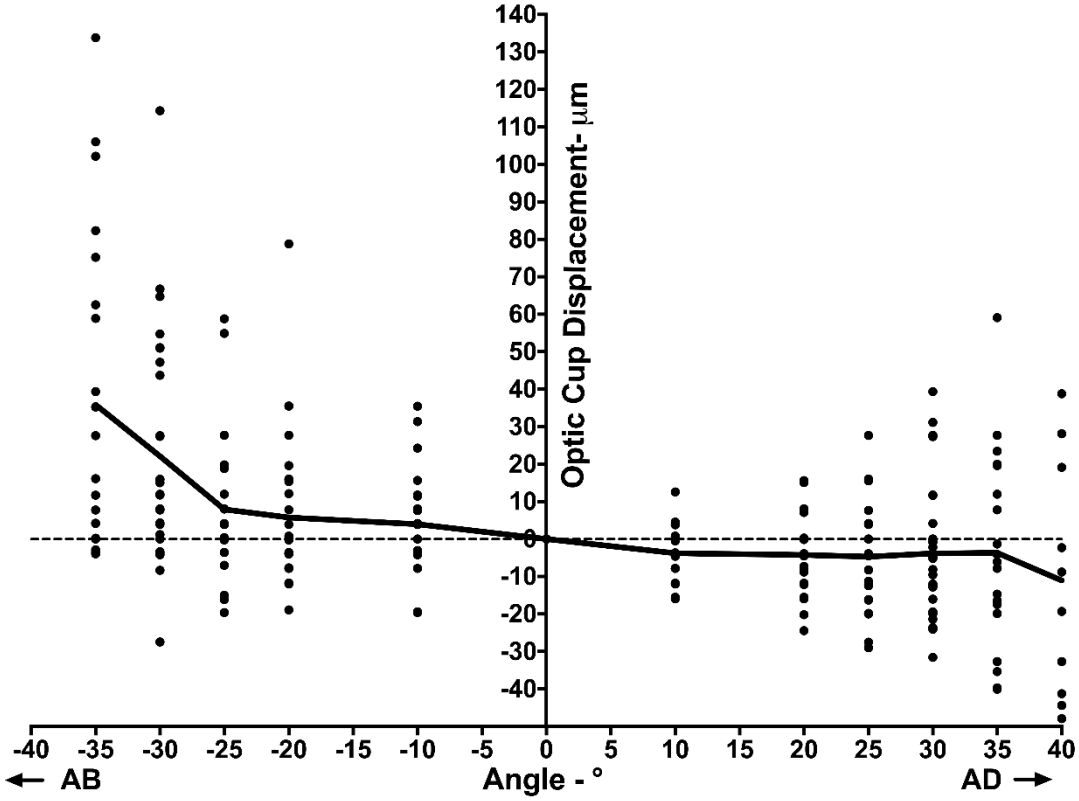

Figure 5. Optic cup (OC) displacements in adduction and abduction. Although displacements of OC largely varied among individuals, the tendency showed that OC displaces anteriorly in abduction, while slightly posteriorly in adduction.

2.1.5 Discussion

This study confirms and extends the findings of earlier OCT studies[12-14] that horizontal eye movement significantly deforms the ONH and peripapillary tissues. Adduction shifted the nBMO anteriorly, the tBMO posteriorly, and tilted the ONH temporally, while abduction caused converse behavior of each in the fashion described by Sibony as "see-saw." [12] While the displacement pattern of the OC during horizontal duction varied widely among subjects, but the OC generally shifted anteriorly in abduction and slightly posteriorly in adduction. This see-saw behavior had a roughly linear behavior with respect to gaze angle and was directionally symmetrical for add- and abduction. However, beyond about 22° of adduction only, there was a significantly greater rate of BMO displacement and ONH tilt with further adduction, a phenomenon not evident for larger angles of abduction. This threshold for greater BMO displacement and ONH tilt beyond 22° adduction is consistent with adduction tethering by the ON and ON sheath demonstrated by MRI to occur at about this angle.[1]

The "seesaw-like" shape deformation of the BMO and ONH observed here might be explained by the stiffness of ON sheath, as pressurized by cerebrospinal fluid within it[12]. Elastin fibers embedded in the dense collagen matrix of the ON sheath have a mesh-like orientation providing high mechanical stiffness (Le A, et al. IOVS 2017;:ARVO E-Abstract.1736). The inner layer of the ON sheath that inserts on the sclera canal even has denser collagen and more elastin than the outer layer (Baig A, et al. IOVS 2017;:ARVO E-Abstract 1738). Given that ON sheath is much stiffer than the peripapillary sclera (Shin A, et al. IOVS 2016;57:ARVO E-Abstract 3563),[5, 6] during horizontal duction the ON sheath would compress the peripapillary sclera on the side ipsilateral to the gaze direction, forcing the overlying ppBM anteriorly, while the ON sheath on the side contralateral to the gaze direction simultaneously exerts traction to

drag the overlying ppBM posteriorly. These effects may be augmented by hydrostatic pressure of CSF stiffening the ON sheath. MRI demonstrates that CSF within the ON sheath shifts to the nasal side of the retrobulbar ON in adduction[1], a shift that could compress the nasal peripapillary retina anteriorly. The foregoing is only one aspect of hydraulic stiffening of the ON sheath during horizontal duction, a concept further supported by the finding that the gaze-evoked seesaw deformations of the peripapillary region in papilledema are reduced after normalization of pathologically elevated intracranial pressure.[12] However, both of these effects should be similar in add- and abduction. For angles of 25° or more, neither ON sheath stiffness or localized CSF pressure can explain the greater BM displacement and ONH tilting observed in adduction abduction.

Both BM displacement and ONH tilt angle during graded range of adduction showed bilinear patterns suggesting existence of an alternative or supplemental mechanism of deformation beyond the threshold of 22°, and this mechanism is most likely ON and sheath tethering in adduction. Such tethering has been demonstrated by MRI. Once the ON and its sheath lose redundancy and become straightened in adduction,[1] additional adduction causes the globe to retract, an effect especially prominent in axial high myopia.[1] More recently, medial globe translation has also been demonstrated by MRI in adduction (Demer, et al. IOVS 2017;58:ARVO E-Abstract 2455). With the straightened ON sheath exerting traction on the temporal side of the ON and the globe simultaneously shifting postero-nasally, the globe's rotational center shifts postero-temporally as eye adducts, causing larger progressive displacements in nasal than in temporal peripapillary region. The sharply angulated anterior shifting of the nasal peripapillary retina in large adduction termed "nasal buckling' observed in our earlier study[14] was indeed not a rare finding here, but rather a general phenomenon in the

current study. Our result suggests that the threshold of ON sheath tethering and possibly the globe translation occurs around 22°-23° in adduction, which matched to where the ON straightening was observed in normal controls by MRI.[1]

Significant temporal tilt of the ONH in adduction was again confirmed in the current study. Temporal ONH tilting along with temporal PPA is commonly seen in myopia, [16-20] which is a well-known risk factor of glaucoma.[21-23] Recent studies have shown that presence of temporal ONH tilting and PPA are both better associated with visual field defects and progression than the refractive error itself, implying that it is the structural change associated with myopia that leads to glaucoma.[24, 25] Although axial elongation of the globe has been suggested to cause both ONH tilt and PPA,[20, 26] there is no good explanation for why the tilting of the ONH and PPA dominantly occurs "temporally" in myopia and glaucoma. Our current finding suggests that ON sheath traction might be the primary cause of temporal ONH tilt considering that the pulling force induced by the tethered ON in adduction is mainly exerted on the temporal ONH and peripapillary tissue.[1] Biomechanical modeling has predicted that ONH sheath tractional force in adduction is greatest at the temporal edge of the ON (Shin A, et al. IOVS 2016;57:ARVO E-Abstract 3563), which is the region where PPA generally occurs.

One might ask whether the reversible gaze-induced tiling of the ONH or the displacements of peripapillary BM presented in our study could lead to permanent deformations, and thus significantly damage these structures. As predicted by biomechanical modeling, ONH strain induced by horizontal duction can greatly exceed that induced by marked IOP elevation.[5, 6] When this significant amount of strain occurs repetitively throughout the lifetime, repetitive strain injury might occur analogous to injury observed in peripheral neuropathy or musculoskeletal disorders related to repetitive tasks.[27] As saccadic eye movements are reported to occur approximately 3 times per

second[28], it is plausible that these frequent saccades especially when accompanied by ONH tethering could cause remodeling of ONH and peripapillary region and irreversibly damage these tissues.

A few limitations deserve consideration in the current study. In the earlier study, we noticed that the directions of the peripapillary retinal pigment epithelium and OC displacements depended on the chosen reference point when a single reference structure was used. In adduction, for example, the temporal RPE and OC shifted posteriorly when alignment to nasal BM was used as a reference, but anteriorly when alignment to temporal Bruch's membrane was used. The current study avoided the effect of an arbitrary choice of reference by employing both the far nasal and temporal peripheral BM were used as dual reference points to investigate the directions of the ppBM and OC displacements in eccentric gazes. However, even these remote reference points are still within a 10-mm wide region of the posterior retina that might also have been deformed by horizontal duction. Gaze-related deformation of even the remote nasal and temporal BM reference points would cause the current data to underestimate the reported effects. This limitation appears unavoidable at present, since available OCT scanners can at maximum image only a field of 10 mm. While MRI can image the entire globe, its spatial resolution in the range of 300 mm within 2 mm thick planes is probably insufficient for reliable measurement of ONH and peripapillary deformations in the range of tens of microns.

Although EDI-OCT was performed in the current study, high-speed mode that slightly compromised resolution in order to minimize the scanning time as necessary to repetitively scan in numerous eccentric gazes. Deeper structures such as LC or choroid were not well visualized in every case, so those structures were not included for the analysis. Recently, posterior displacement of LC and its reversal after IOP reduction has

been demonstrated in OCT studies of glaucoma.[29-32] In future studies evaluating the possibility that ON tethering might constitute an IOP independent mechanism of glaucomatous optic neuropathy, it would be useful to investigate whether horizontal eye movements deform the LC.

In conclusion, horizontal duction deforms the ONH and peripapillary region, significantly more so in adduction than in abduction. The displacement of ppBM and temporal tilting of the ONH substantially increases beyond about 22° in adduction, corresponding to the presumed the threshold angle at which the ON sheath becomes tethered. Further studies are needed to investigate whether these gaze-induced deformations of ONH and peripapillary tissue are abnormally great in glaucoma, which would test the novel hypothesis that ON sheath tethering occurring in adduction constitutes an IOP-independent mechanism of ON damage.

2.1.6 References

1. Demer JL. Optic nerve sheath as a novel mechanical load on the globe in ocular duction. *Invest Ophthalmol Vis Sci.* 2016;57:1826-1838.

2. Park KH, Tomita G, Liou SY, Kitazawa Y. Correlation between peripapillary atrophy and optic nerve damage in normal-tension glaucoma. *Ophthalmology.* 1996;103:1899-1906.

3. Uchida H, Ugurlu S, Caprioli J. Increasing peripapillary atrophy is associated with progressive glaucoma. *Ophthalmology.* 1998;105:1541-1545.

4. Jonas JB. Clinical implications of peripapillary atrophy in glaucoma. *Curr Opin Ophthalmol.* 2005;16:84-88.

5. Wang X, Rumpel H, Lim WE, et al. Finite element analysis predicts large optic nerve head strains during horizontal eye movements. *Invest Ophthalmol Vis Sci.* 2016;57:2452-2462.

6. Wang X, Fisher LK, Milea D, Jonas JB, Girard MJ. Predictions of optic nerve traction forces and peripapillary tissue stresses following horizontal eye movements. *Invest Ophthalmol Vis Sci.* 2017;58:2044-2053.

7. Burgoyne CF, Downs JC, Bellezza AJ, Suh JK, Hart RT. The optic nerve head as a biomechanical structure: a new paradigm for understanding the role of IOP-related stress and strain in the pathophysiology of glaucomatous optic nerve head damage. *Prog Retin Eye Res.* 2005;24:39-73.

8. Burgoyne CF, Downs JC. Premise and prediction-how optic nerve head biomechanics underlies the susceptibility and clinical behavior of the aged optic nerve head. *J Glaucoma.* 2008;17:318-328.

9. Sigal IA, Ethier CR. Biomechanics of the optic nerve head. *Exp Eye Res.* 2009;88:799-807.

10. Burgoyne CF. A biomechanical paradigm for axonal insult within the optic nerve head in aging and glaucoma. *Exp Eye Res.* 2011;93:120-132.

11. Nguyen TD, Ethier CR. Biomechanical assessment in models of glaucomatous optic neuropathy. *Exp Eye Res.* 2015;141:125-138.

12. Sibony PA. Gaze evoked deformations of the peripapillary retina in papilledema and ischemic optic neuropathy. *Invest Ophthalmol Vis Sci.* 2016;57:4979-4987.

13. Wang X, Beotra MR, Tun TA, et al. In vivo 3-Dimensional strain mapping confirms large optic nerve head deformations following horizontal eye movements. *Invest Ophthalmol Vis Sci.* 2016;57:5825-5833.

14. Chang MY, Shin A, Park J, et al. Deformation of optic nerve head and peripapillary tissues by horizontal duction. *Am J Ophthalmol.* 2017;174:85-94.

15. Chauhan BC, Burgoyne CF. From clinical examination of the optic disc to clinical assessment of the optic nerve head: a paradigm change. *Am J Ophthalmol.* 2013;156:218-227 e212.

16. Vongphanit J, Mitchell P, Wang JJ. Population prevalence of tilted optic disks and the relationship of this sign to refractive error. *Am J Ophthalmol.* 2002;133:679-685.

17. Tay E, Seah SK, Chan SP, et al. Optic disk ovality as an index of tilt and its relationship to myopia and perimetry. *Am J Ophthalmol.* 2005;139:247-252.

18. Samarawickrama C, Mitchell P, Tong L, et al. Myopia-related optic disc and retinal changes in adolescent children from singapore. *Ophthalmology.* 2011;118:2050-2057.

19. You QS, Xu L, Jonas JB. Tilted optic discs: The Beijing Eye Study. *Eye.* 2008;22:728-729.

20. Kim TW, Kim M, Weinreb RN, Woo SJ, Park KH, Hwang JM. Optic disc change with incipient myopia of childhood. *Ophthalmology.* 2012;119:21-26 e21-23.

21. Marcus MW, de Vries MM, Junoy Montolio FG, Jansonius NM. Myopia as a risk factor for open-angle glaucoma: a systematic review and meta-analysis. *Ophthalmology.* 2011;118:1989-1994 e1982.

22. Mitchell P, Hourihan F, Sandbach J, Wang JJ. The relationship between glaucoma and myopia: the Blue Mountains Eye Study. *Ophthalmology.* 1999;106:2010-2015.

23. Wong TY, Klein BE, Klein R, Knudtson M, Lee KE. Refractive errors, intraocular pressure, and glaucoma in a white population. *Ophthalmology.* 2003;110:211-217.

24. Sawada Y, Hangai M, Ishikawa M, Yoshitomi T. Association of myopic optic disc deformation with visual field defects in paired eyes with open-angle glaucoma: a cross-sectional study. *PloS one.* 2016;11:e0161961.

25. Sawada Y, Hangai M, Ishikawa M, Yoshitomi T. Association of myopic deformation of optic disc with visual field progression in paired eyes with open-angle glaucoma. *PloS one.* 2017;12:e0170733.

26. Jonas JB, Weber P, Nagaoka N, Ohno-Matsui K. Glaucoma in high myopia and parapapillary delta zone. *PloS one.* 2017;12:e0175120.

27. Barr AE, Barbe MF. Pathophysiological tissue changes associated with repetitive movement: a review of the evidence. *Phys Ther.* 2002;82:173-187.

28. Wu CC, Kowler E. Timing of saccadic eye movements during visual search for multiple targets. *J Vis.* 2013;13.

29. Lee EJ, Kim TW, Weinreb RN. Reversal of lamina cribrosa displacement and thickness after trabeculectomy in glaucoma. *Ophthalmology.* 2012;119:1359-1366.

30. Lee EJ, Kim TW, Weinreb RN, Kim H. Reversal of lamina cribrosa displacement after intraocular pressure reduction in open-angle glaucoma. *Ophthalmology.* 2013;120:553-559.

31. Barrancos C, Rebolleda G, Oblanca N, Cabarga C, Munoz-Negrete FJ. Changes in lamina cribrosa and prelaminar tissue after deep sclerectomy. *Eye.* 2014;28:58-65.

32. Lee EJ, Kim TW. Lamina cribrosa reversal after trabeculectomy and the rate of progressive retinal nerve fiber layer thinning. *Ophthalmology.* 2015;122:2234-2242.

2.2 Compression of the Choroid by Horizontal Duction

Jessica Y. Chen[1], Alan Le[2-4], Lindsay M. De Andrade[2,4],

Toshiaki Goseki[2,4], and Joseph L. Demer[2-6]

[1]Computational and Systems Biology Interdepartmental Program; [2]Department of Ophthalmology; [3]Bioengineering Interdepartmental Program; [4]Stein Eye Institute; [5]Department of Neurology; [6]David Geffen Medical School of the University of California, Los Angeles.

2.2.1 Abstract

Purpose: The optic nerve becomes tethered in adduction in most people, which deforms the disc. We investigated the effect of horizontal ocular duction and subject age on choroidal volume at the macular side of the optic disc.

Methods: In 25 younger (18-33 years) and 15 older (50-73 years) normal subjects, the disc and the peripapillary choroid were imaged with optical coherence tomography (OCT) in central gaze and 35° add- and abduction. The choroid temporal to the optic disc underlying the region between the Bruch's membrane opening and fovea was segmented into regions that were multiples of the disc radius for determination of local choroidal thickness. Regional volume changes from central gaze were determined in add- and abduction.

Results: In adduction, regional choroidal volume decreased by 42.4±3.4 nanoliters (nil) (SEM) in younger ($P < 0.0001$) and 6.2±2.6nL in older ($P < 0.02$) subjects. Relative volume reduction in adduction was 7.5±0.6% in younger ($P < 0.001$) and 1.3±0.6% in older ($P < 0.02$) subjects. Volume reduction was greatest near the disc and significant up to 3 disc radii from it in younger, and 1 radius in older subjects, but was insignificant in abduction.

Conclusions: Horizontal duction compresses the temporal peripapillary choroid, more in adduction than in abduction, and more in younger than older subjects. This reflects duction-related peripapillary tissue deformation probably related at least in part to optic nerve tethering in adduction.

2.2.2 Introduction

When the human eye rotates into a large angle adduction, we have shown by magnetic resonance imaging (MRI) that the optic nerve (ON) and its sheath tether the globe and exert tractional force on the optic disc.[1,2] We have also demonstrated by optical coherence tomography (OCT) that adduction deforms the peripapillary Bruch's membrane (ppBM) and tilts the ONH anterposteriorly.[3] The deformation is exaggerated at a threshold of approximately 26° adduction, the angle at which the limited ON length necessitates the onset of tethering.[3,4] While some reversal of the see-saw tilting of the disc also occurs in abduction, the greater deformation in adduction than abduction is probably due to ON tethering.

Finite element analysis (FEA) has been employed to simulate mechanical stress and strain in the ONH and the peripapillary retina during horizontal eye rotation[5,6] and we have shown this to be especially the case in adduction.[7] Those simulations suggest that ON tethering force is concentrated on the temporal disc and peripapillary tissue, in the typical location where peripapillary atrophy occurs in patients with primary open angle glaucoma (POAG).[8-10] Simulations further suggest that adduction tethering can deform the optic disc more than extreme, acute intraocular pressure (IOP) elevation, providing a possible explanation, at least in part, for the many cases of POAG where there is glaucomatous optic neuropathy without abnormally elevated IOP.[11-13] It has been speculated that horizontal eye movements that repetitively deform the optic disc and peripapillary retina may contribute to the peripapillary chorioretinal atrophy common in glaucoma.[10] In addition, choroidal microvascular dropout in regions of peripapillary atrophy occurs in POAG where it is associated with advanced visual field defects.[14]

Our earlier OCT studies showed that horizontal duction deforms peripapillary Bruch's membrane and the superficial ON vasculature.[3,15-17] We have not previously investigated the effect of gaze direction on choroidal volume, nor the effect of subject age on such changes. This current study sought evidence of possible deformation of the peripapillary choroid (ppC). The ppC has been reported to thin during both adduction and abduction.[4] We sought to extend the investigation to choroidal volume. Choroidal thinning due to loss of inner choroidal vessels is linked to POAG[18] and normal tension glaucoma (NTG).[19-21] Older people typically have thinner choroids[22-26] and thus choroidal volume and deformation has been proposed to be associated with other age-related ocular diseases.[26] In this study, we examined choroidal deformation in different age groups by quantifying the choroidal volume change resultant from horizontal duction.

2.2.3 Methods

Subjects

Forty volunteers (19 males and 21 females; mean age, 37±20 [standard deviation, SD] yrs; range 18-73) were recruited for the study. Subjects, who had not previously participated in research of this sort, were separated into a younger group of 25 (15 male and 10 female; mean age 24±5; range 18-33) and an older group of 15 volunteers (4 male and 11 female; mean age 62±8 yrs; range 50-73). Subjects gave written informed consent before participating according to a protocol approved by the University of California, Los Angeles Institutional Review Board and compliant with the Declaration of Helsinki. Ophthalmic evaluations were performed of all subjects to confirm normal corrected visual acuity and absence of any ocular abnormalities besides refractive error and pseudophakia. Subjects had normal IOP (<21 mm Hg), normal

binocular alignment, and normal optic nerves. The mean spherical equivalent refractive error where determined was -1.5±2.9 (SD; range, +2 to -8.3), although refractive error was not ascertained for 24 volunteers.

Optical Coherence Tomography

A spectral domain OCT scanner (Spectralis; Heidelberg Engineering, Heidelberg, Germany) was used to image the choroid with enhanced depth imaging. Volume scans of both eyes in central gaze, abduction (35°), and adduction (35°) were performed sequentially. Imaging consisted of 25 horizontal B-scans covering a 30° x 5° rectangular region centered between the fovea and disc at vertical increments of approximately 62μm, depending on the focal depth. To scan in the eccentric gazes, the OCT imager was pivoted in yaw to angles set by goniometric scale placed on the instrument's gimbal. For standardization, the raster was rotated for every scan to align the center of the disc with the fovea. This rotation compensated for ocular torsion, which according to Listing's Law varies systematically with gaze direction, but typically by different amounts in each eye of the same individual, and differently among individuals.[27,28] Torsional correction of the OCT scan raster thus cancelled the effect of ocular torsion and rendered otherwise superimposable the sets of images obtained in multiple gaze positions.

Axial tilt of the B-scans was maintained because the scanning light beam always entered the eye at the same angle relative to the visual direction. The axial tilt of the B-scans was held constant because when the scanner head rotated, the eye rotated with it maintain fixation on the scanner's internal target. Thus, the angle of beam entrance into the eye did not change with gaze direction. Subjects' heads were fixed straight ahead with straps and cushions. Subjects were instructed to maintain this head position as they fixated the scanner's internal target that was measured to be offset 12° nasally from

straight ahead.[3] Rotation of the OCT imager was mechanically limited to 35° by its design.

Image Analysis

Images were processed with Adobe Photoshop (Adobe Systems, San Jose, CA, USA) as TIFF files. The scans were cropped, scaled, and if necessary rotated, correcting aspect ratio, so that peripheral retinal features were in precise alignment for all gaze positions for the same eye. Images were converted to a volumetric stack in Materialise Mimics (Materialise, Leuven, Flemish Brabant, Belgium) with the slices in original scaling (3.87μm/pixel horizontally, an average of 11.6μm/pixel in depth, and an average of 62.1μm/slice vertically [distance between B-scans]). For each stack, the middle 12 slices of the 25 acquired were all analyzed in order to evaluate the ppC, as these 12 slices consistently straddled the central optic disc. Tracing of the choroid was temporally bounded nasally by the Bruch's membrane opening (BMO). The ppC was then segmented into three contiguous regions with horizontal dimensions equal to the BMO radius, beginning at the temporal edge of the BMO (Fig. 1). For each eye in each subject, a three-dimensional representation of the temporal ppC was rendered from 12 traced cross-sections, with the distance between B-scans as the interval with which the summed areas were multiplied to generate the volume. Each eye was treated as a separate sample in the analyses.

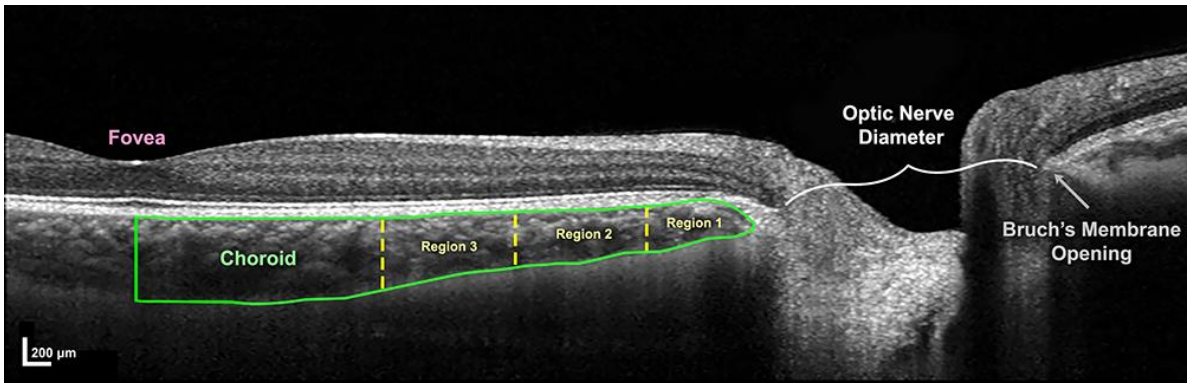

Figure 1. The choroid was outlined (green) from the temporal edge of Bruch's membrane to the fovea, and then separated into 3 contiguous regions (yellow) each equal to the Bruch's membrane opening (BMO) radius beginning at the temporal margin of the BMO.

We analyzed two parameters for the scans in each eccentric gaze relative to central gaze: (1) change in volume of the choroid within the three total regions; and (2) variation among the three segmented regions. These changes were then compared between younger and older age groups.

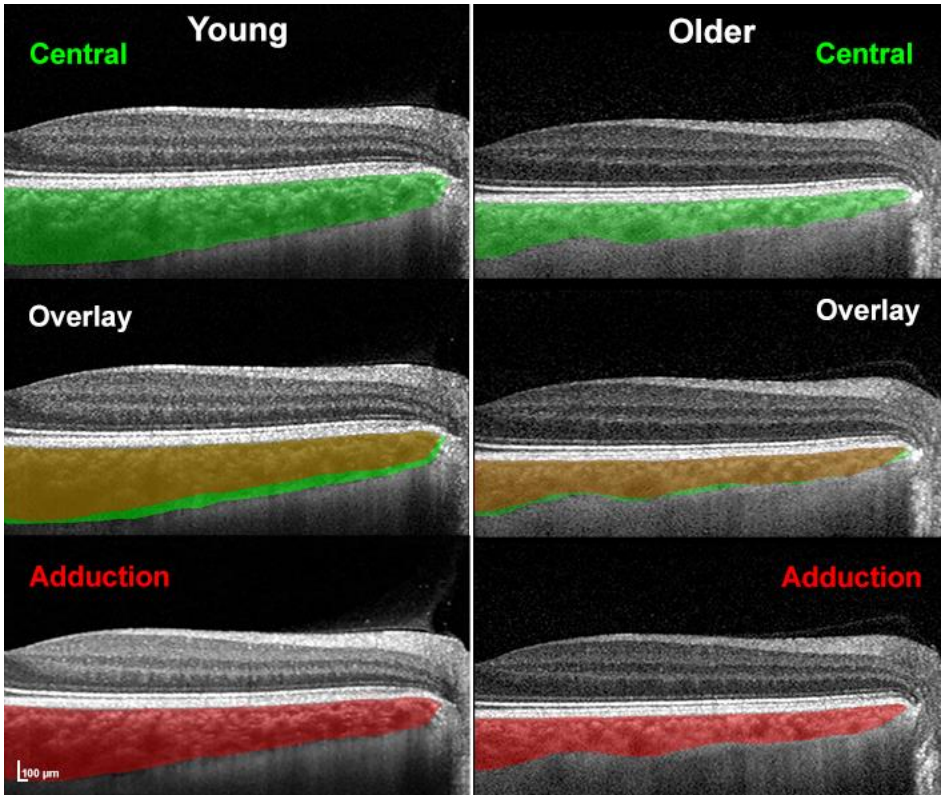

Figure 2. Optical coherence tomography of choroid between temporal edge of optic disc (right) and foveola (left) color in a young (left column) and an older subject (right column). Upper row: central gaze. Bottom row: adduction. The central row overlays images in central gaze and adduction, so that overlapping choroidal regions appear yellow-brown, but areas of choroidal thinning in adduction appear green. Note greater choroidal thinning in adduction in the young subject.

Statistical Analysis

In order to account for possible interocular correlation between the two eyes of the same subject, and among choroidal regions in the same eye, statistical analysis was executed utilizing generalized estimating equations (GEE) with SPSS software (Version 24.0; IBM Corp., Armonk, NY, USA) with eye and choroidal region as nested, within-subject variables. The statistical package reports significant values to only three decimal places based upon a chi-square distribution, but this is not a simple chi-square test of simple proportions. Where the SPSS package reported significance at “P = 0.000,” we

also note the chi-square value and number of degrees of freedom for the reader's interest, since probabilities of the random significant differences for the findings reported here could never be exactly zero.

2.2.4 Results

Choroidal Volume in Younger and Older Subjects

Images in Fig. 2 illustrate the decrease in choroid volume reduction when gaze shifts from central to adduction, in example and younger and older subjects. The choroid typically appeared thicker in younger than older subjects, supported measurements showing 556±25 nanoliters (nL) (SEM) average choroidal volume in central gaze in younger subjects, but only 460±21nL in older subjects ($P < 0.01$, Fig. 4). Choroidal volume was also greater in younger than older subjects in eccentric horizontal gazes, but was always less in adduction than in central gaze in both groups. In adduction, choroidal volume in younger subjects decreased to 514±24nL, but in older subjects decreased less so to 454±21nL, reducing to statistical insignificance the difference between groups. In abduction, choroidal volume of younger subjects increased insignificantly to 559±26nL and that of the older group remained 460±21nL, so that the difference between groups again became significant ($P < 0.01$).

Test-Retest Variability

Test-retest variability was evaluated by repeating the experiment on different days in 10 eyes of 5 young subjects using identical data collection and analysis to compute choroidal volume in both central gaze and adduction. As shown in Figure 3, a Bland-Altman analysis of test-retest agreement was performed, demonstrating for central gaze a mean choroidal volume of 562nL, with bias of 5nL (<0.9%) in the repeat

measurement relative to the first measurement. For central gaze, the 95% limits of agreement were from -34 to 45nL, representing a maximum of 8% for individual measurements. In adduction, the comparable values were 514nL, with bias of 4nL (<0.8%). The 95% limits of agreement were from -27 to 36nL, representing a maximum of 7% for individual measurements. This implies that test-retest variability would account for no more than 0.9% difference in average measurements. The first and second sets of measurements in each eye, in both central gaze and adduction, were also compared using linear regression for difference from the null hypothesis of unity slope, the ideal value if both sets of measurements were identical in every eye. For both primary gaze and adduction choroidal volumes, neither regression slope differed significantly from unity (P > 0.75), indicating that the repeat experiments yielded statistically similar results to the initial experiments.

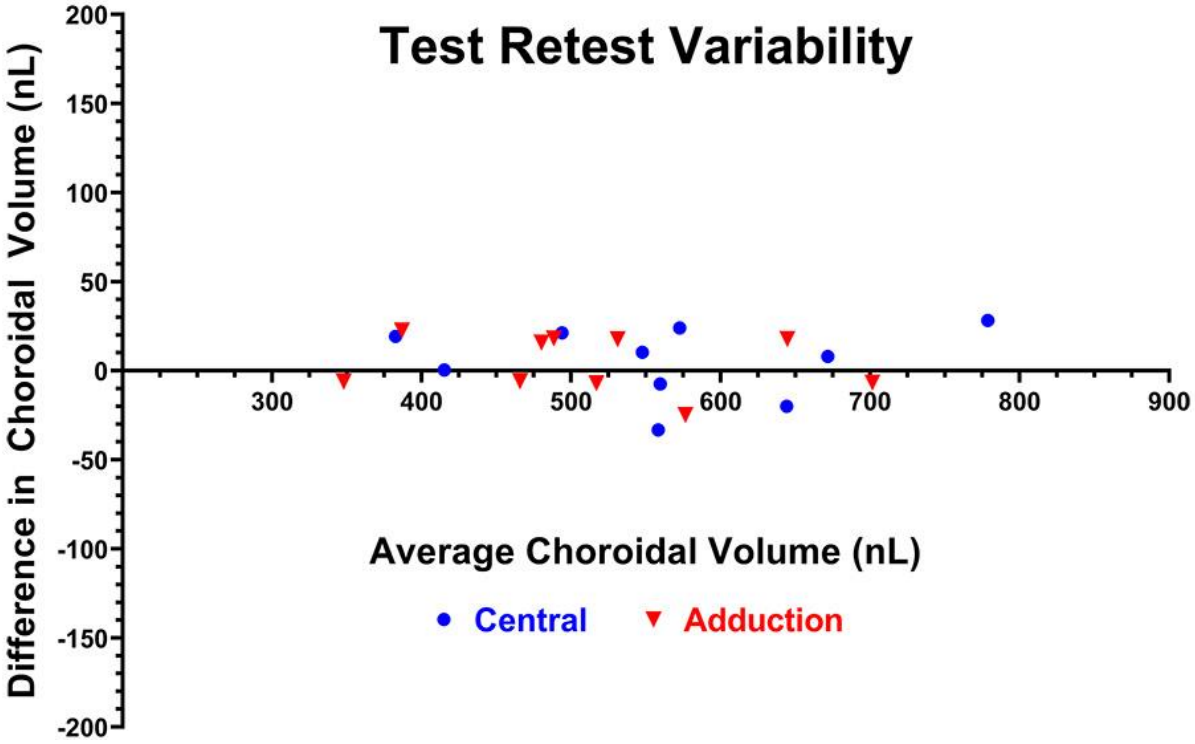

Figure 3. Bland Altman analysis of test retest variability in 10 eyes of 5 young subjects who were tested twice.

Change in Choroidal Volume with Gaze

Choroidal volume change from central gaze was significantly related to gaze position as a factor (P = 0.000, GEE X^2 = 47, 2 d.f.). In both younger (Fig. 2) and older subjects, choroidal volume consistently decreased in adduction, but did not change much in abduction (Fig. 4). In younger subjects, mean choroidal volume decreased in adduction by 42±3nL (P < 0.0001), a value about 8-fold greater than test-retest variability. Choroidal volume insignificantly increased by 2±3nL in abduction. In older subjects, choroidal volume decreased by 6±3nL in adduction (*P* < 0.02) and increased insignificantly by 1±4nL in abduction. There was a significant interaction of gaze position with age (P = 0.000, GEE X^2 = 17, 2 d.f.).

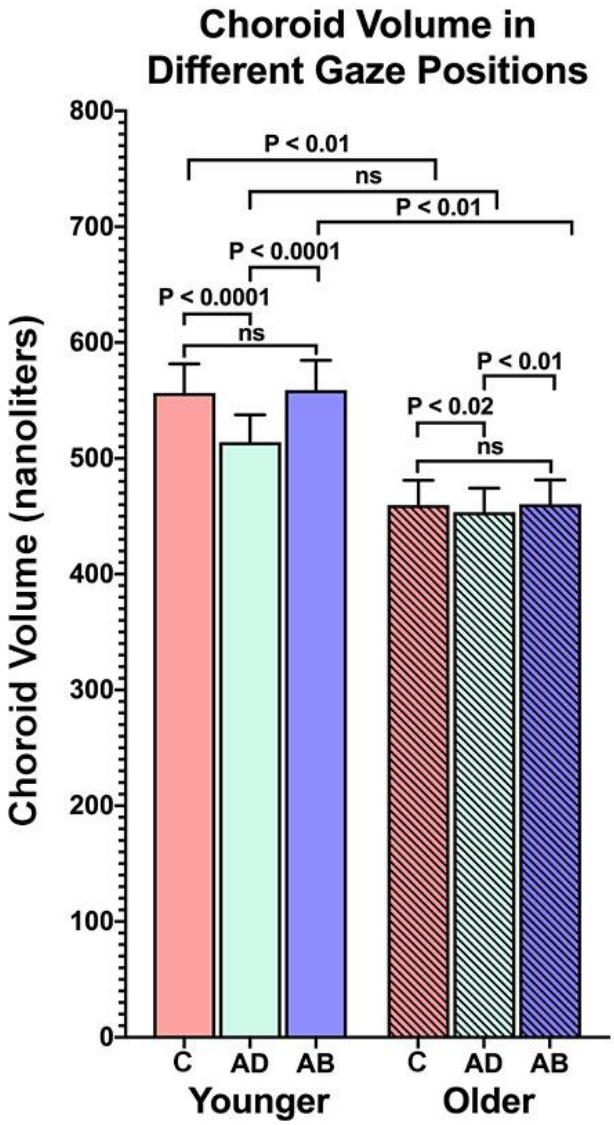

Figure. 4. Temporal peripapillary choroidal volume in central gaze (C), adduction (AD), and abduction (AB) for younger and older subjects. Choroidal volume was less in adduction than in central gaze in both younger and older subjects, but did not change in abduction. C - central gaze. AD - adduction. AB - abduction. Solid colored bars indicate data of 50 eyes of younger subjects. Hatched bars indicate data of 30 eyes of older subjects. 95% confidence limits.

It is informative to evaluate change in choroidal volume relative to central gaze. In the younger subjects, adduction was associated with 7.5±0.6% mean decrease in choroidal volume ($P < 0.001$), while in abduction, there was insignificant 0.4±0.4% increase in volume. In the older subjects, adduction was associated with 1.3±0.6% mean decrease in choroidal volume ($P < 0.02$), while in abduction there was insignificant 0.2±0.7% increase in volume.

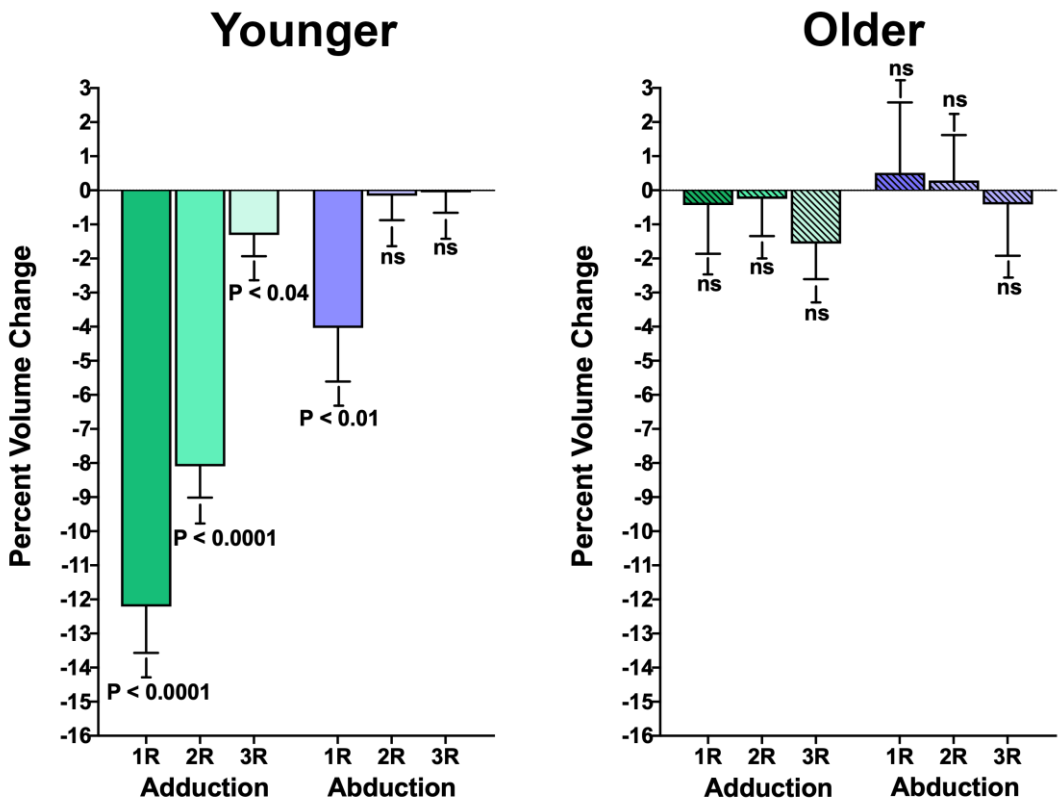

Figure 5. Volume change in the temporal papillary choroid, relative to central gaze, was greater in regions nearest the optic disc in younger subjects. Data is from 50 eyes of younger and 30 eyes of older subjects. Brackets mark 95% confidence intervals. R – disc radius, as defined in the text.

In younger subjects, relative choroidal volume change in adduction was greatest in the immediate peripapillary zone, and decreased progressively with distance from the disc margin ($X^2 = 19$). As shown in Fig. 5, In younger subjects during adduction, choroidal volume within one radius of the disc decreased 12±1%, between one and two radii decreased 2±1%, and between two and three radii decreased 1±1%. In these younger subjects, the relative volume decrease in abduction was significant only within one disc radius of the disc margin (1R, $P < 0.01$). In older subjects, relative choroidal volume did not change significantly in adduction or abduction in any region.

2.2.5 Discussion

Previous studies have shown that horizontal duction, particularly adduction, deforms the optic disc and surrounding peripapillary tissues.[4,15-17] This deformation in adduction includes temporal shifting of the nasal part of the disc, anteroposterior displacement of the ppBM, and tilting of the disc. The current demonstrates that temporal peripapillary choroidal volume decreases more in adduction than in abduction, extending prior findings that adduction deforms the peripapillary retina. Most of the compression of the temporal choroid during horizontal duction occurs near the disc, suggesting that the deformation is due to force transmission by the ON or its sheath during eye movements.

Compression of the temporal choroid is associated with deformation of the peripapillary retina and ON fibers. The temporal choroid is compressed during adduction in both younger and older subjects, but approximately 15-fold more so in adduction than in abduction in younger subjects. This greater compression in adduction than abduction is consistent with optical imaging showing greater deformation of the disc and peripapillary retina in these duction directions,[15] and the observation by MRI imaging of ON tethering only in adduction.[3,4,29] Compression of the temporal choroid is also consistent with observed temporal displacement of peripapillary vessels[15] and the overall temporalward compression of optic disc tissue during ON tethering in adduction.[2] The situation in abduction is quite different, being associated with only minimal choroidal compression, less ON and peripapillary deformations in young adults but none in older subjects.[15] This difference between ad- and abduction is also consistent with MRI studies showing that the ON is usually slack during abduction.[2]

In general, younger people may have more compliant peripapillary tissues than older people because of age-related stiffening in sclera,[30-32] Bruch's membrane,[33] and

lamina cribrosa.[34-37] As such, peripapillary choroidal deformation would be expected to be less in older people who have stiffer tissues surrounding the choroid. Older people generally have thinner choroids,[22-26] perhaps accounting for relatively smaller change in choroidal volume in the eccentric gaze positions in older people. Subjects with normal tension glaucoma (NTG) have significantly thinner choroids than normal in the inferonasal, inferior, and inferotemporal regions.[18] Choroids of subjects with both NTG and high myopia average significantly thinner than normal at the fovea, superior, superotemporal, temporal, and inferotemporal regions than at the optic nerve head.[21] In light of the correlation between decreasing choroidal thickness and age-related ocular neuropathies, choroidal thinning might be a cause or effect of glaucomatous optic neuropathy, since choroidal thickness is subnormal in both ordinary NTG[20,38,39] and highly myopic NTG.[21]

During adduction, the disc and the peripapillary retina shift and tilt, signifying that this entire region undergoes mechanical strain. Some of the blood supply to the ON arises from the choroid.[40,41,42] Compression of the ppC in adduction might interfere with some of the blood supply to the ON,[40] which may eventually damage these tissues in situations where there is also compromise to the posterior ciliary circulation. Choroidal vascular insufficiency might thus contribute to optic neuropathies such as glaucoma.[41,42] There are conflicting reports regarding the relationship between choroidal thickness and glaucoma, with some histological and in vivo studies showing a thinner ppC in glaucomatous eyes,[18,19,43] but other studies finding no association.[44-49] However, the present study provides in vivo evidence that adduction instantaneously compresses the ppC. As this study only includes healthy subjects, future research could investigate possible gaze-evoked changes in choroidal volume of patients with glaucoma to clarify a possible relationship between choroidal deformation and glaucoma.

There may be pathological implication to the lesser choroidal compression in adduction observed here in older than younger subjects. This might be the consequence of remodeling induced by accumulation of strains during adduction eye movements. The thinner elderly choroids are probably also sclerotic, containing proportionately more rigid connective tissue than younger choroids. If so, choroidal volume reduction in adduction would be diminished by greater resistance to mechanical strain imposed by the tethering ON. Our MRI studies have demonstrated that the ON becomes tethered when adduction exceeds 26° in people of all ages, [3,4] so that reaction force to the powerful medial rectus muscle must in everyone deform or displace the globe to permit further adduction. Limited ON length makes local deformation in the eye or orbit geometrically inevitable. Healthy deformation – “strain” in mechanical terminology – would ideally occur only in compliant tissues that are not functionally compromised by deformation, and so dissipate the mechanical force harmlessly. We propose that the choroid is among the tissues that safely absorb mechanical strain during adduction. Choroidal deformation normally acts like a cushion to avert transfer of mechanical strain to critical tissues such as the lamina cribrosa and optic nerve. Sclerosis of the choroid and other peripapillary tissues would defeat the cushioning function and transfer potentially damaging strain to critical tissues such as the ON. A relatively thin and poorly compressible peripapillary choroid would then be a pathogenic factor in optic neuropathy, including glaucoma.

This study was limited to imaging of the temporal peripapillary region. While more remote areas of the choroid could not be evaluated, absence of significant eye movement related changes in choroidal volume beyond three disc radii from the border of the BMO is highly suggestive that the effects of eye movement are limited to this region, but the current study cannot verify this directly. This study did not include graded duction angles and thus cannot determine if a threshold exists for gaze-evoked choroidal

deformation as has been shown in Bruch's membrane deformation.[3] The current study did not measure choroidal blood flow.

2.2.6 References

1. Demer JL, Clark RA, Suh SY, et al. Magnetic resonance imaging of optic nerve traction during adduction in primary open-angle glaucoma with normal intraocular pressure. *Invest Ophthalmol Vis Sci* 2017;58:4114-4125.

2. Demer JL. Optic nerve sheath as a novel mechanical load on the globe in ocular duction. *Invest Ophthalmol Vis Sci* 2016;57:1826-1838.

3. Suh SY, Le A, Shin A, Park J, Demer JL. Progressive deformation of the optic nerve head and peripapillary structures by graded horizontal duction. *Invest Ophthalmol Vis Sci* 2017;58:5015-5021.

4. Chang MY, Shin A, Park J, et al. Deformation of optic nerve head and peripapillary tissues by horizontal duction. *Am J Ophthalmol* 2017;174:85-94.

5. Wang X, Rumpel H, Lim WE, et al. Finite element analysis predicts large optic nerve head strains during horizontal eye movements. *Invest Ophthalmol Vis Sci* 2016;57:2452-2462.

6. Wang X, Fisher LK, Milea D, Jonas JB, Girard MJ. Predictions of optic nerve traction forces and peripapillary tissue stresses following horizontal eye movements. *Invest Ophthalmol Vis Sci* 2017;58:2044-2053.

7. Shin A, Yoo L, Park J, Demer JL. Finite element biomechanics of optic nerve sheath traction in adduction. *J Biomech Eng* 2017;139.

8. Uchida H, Ugurlu S, Caprioli J. Increasing peripapillary atrophy is associated with progressive glaucoma. *Ophthalmology* 1998;105:1541-1545.

9. Park KH, Tomita G, Liou SY, Kitazawa Y. Correlation between peripapillary atrophy and optic nerve damage in normal-tension glaucoma. *Ophthalmology* 1996;103:1899-1906.

10. Jonas JB. Clinical implications of peripapillary atrophy in glaucoma. *Curr Opin Ophthalmol* 2005;16:84-88.

11. Zhao J, Solano MM, Oldenburg CE, et al. Prevalence of normal-tension glaucoma in the chinese population: A systematic review and meta-analysis. *Am J Ophthalmol* 2019;199:101-110.

12. Iwase A, Suzuki Y, Araie M, et al. The prevalence of primary open-angle glaucoma in japanese: The tajimi study. *Ophthalmology* 2004;111:1641-1648.

13. Kim JH, Kang SY, Kim NR, et al. Prevalence and characteristics of glaucoma among korean adults. *Korean J Ophthalmol* 2011;25:110-115.

14. Rao HL, Sreenivasaiah S, Riyazuddin M, et al. Choroidal microvascular dropout in primary angle closure glaucoma. *Am J Ophthalmol* 2019;199:184-192.

15. Le A, Chen J, Lesgart M, Gawargious BA, Suh SY, Demer JL. Age-dependent deformation of the optic nerve head and peripapillary retina by horizontal duction. *Am J Ophthalmol* 2019.

16. Sibony PA. Gaze evoked deformations of the peripapillary retina in papilledema and ischemic optic neuropathy. *Invest Ophthalmol Vis Sci* 2016;57:4979-4987.

17. Wang X, Beotra MR, Tun TA, et al. In vivo 3-dimensional strain mapping confirms large optic nerve head deformations following horizontal eye movements. *Invest Ophthalmol Vis Sci* 2016;57:5825-5833.

18. Yin ZQ, Vaegan, Millar TJ, Beaumont P, Sarks S. Widespread choroidal insufficiency in primary open-angle glaucoma. *J Glaucoma* 1997;6:23-32.

19. Park HY, Lee NY, Shin HY, Park CK. Analysis of macular and peripapillary choroidal thickness in glaucoma patients by enhanced depth imaging optical coherence tomography. *J Glaucoma* 2014;23:225-231.

20. Hirooka K, Tenkumo K, Fujiwara A, Baba T, Sato S, Shiraga F. Evaluation of peripapillary choroidal thickness in patients with normal-tension glaucoma. *BMC Ophthalmol* 2012;12:29.

21. Usui S, Ikuno Y, Miki A, Matsushita K, Yasuno Y, Nishida K. Evaluation of the choroidal thickness using high-penetration optical coherence tomography with long wavelength in highly myopic normal-tension glaucoma. *Am J Ophthalmol* 2012;153:10-16 e11.

22. Rhodes LA, Huisingh C, Johnstone J, et al. Peripapillary choroidal thickness variation with age and race in normal eyes. *Invest Ophthalmol Vis Sci* 2015;56:1872-1879.

23. Huang W, Wang W, Zhou M, et al. Peripapillary choroidal thickness in healthy chinese subjects. *BMC Ophthalmol* 2013;13:23.

24. Johnstone J, Fazio M, Rojananuangnit K, et al. Variation of the axial location of bruch's membrane opening with age, choroidal thickness, and race. *Invest Ophthalmol Vis Sci* 2014;55:2004-2009.

25. Huang W, Wang W, Gao X, et al. Choroidal thickness in the subtypes of angle closure: An edi-oct study. *Invest Ophthalmol Vis Sci* 2013;54:7849-7853.

26. Margolis R, Spaide RF. A pilot study of enhanced depth imaging optical coherence tomography of the choroid in normal eyes. *Am J Ophthalmol* 2009;147:811-815.

27. Demer JL. Pivotal role of orbital connective tissues in binocular alignment and strabismus: The friedenwald lecture. *Invest Ophthalmol Vis Sci* 2004;45:729-738; 728.

28. Demer JL. Current concepts of mechanical and neural factors in ocular motility. *Curr Opin Neurol* 2006;19:4-13.

29. Suh SY, Clark RA, Demer JL. Optic nerve sheath tethering in adduction occurs in esotropia and hypertropia, but not in exotropia. *Invest Ophthalmol Vis Sci* 2018;59:2899-2904.

30. Geraghty B, Jones SW, Rama P, Akhtar R, Elsheikh A. Age-related variations in the biomechanical properties of human sclera. *J Mech Behav Biomed Mater* 2012;16:181-191.

31. Coudrillier B, Tian J, Alexander S, Myers KM, Quigley HA, Nguyen TD. Biomechanics of the human posterior sclera: Age- and glaucoma-related changes measured using inflation testing. *Invest Ophthalmol Vis Sci* 2012;53:1714-1728.

32. Avetisov ES, Savitskaya NF, Vinetskaya MI, Iomdina EN. A study of biochemical and biomechanical qualities of normal and myopic eye sclera in humans of different age groups. *Metab Pediatr Syst Ophthalmol* 1983;7:183-188.

33. Booij JC, Baas DC, Beisekeeva J, Gorgels TG, Bergen AA. The dynamic nature of bruch's membrane. *Prog Retin Eye Res* 2010;29:1-18.

34. Albon J, Karwatowski WS, Easty DL, Sims TJ, Duance VC. Age related changes in the non-collagenous components of the extracellular matrix of the human lamina cribrosa. *Br J Ophthalmol* 2000;84:311-317.

35. Albon J, Karwatowski WS, Avery N, Easty DL, Duance VC. Changes in the collagenous matrix of the aging human lamina cribrosa. *Br J Ophthalmol* 1995;79:368-375.

36. Albon J, Purslow PP, Karwatowski WS, Easty DL. Age related compliance of the lamina cribrosa in human eyes. *Br J Ophthalmol* 2000;84:318-323.

37. Leung LK, Ko MW, Lam DC. Effect of age-stiffening tissues and intraocular pressure on optic nerve damages. *Mol Cell Biomech* 2012;9:157-173.

38. Hirooka K, Fujiwara A, Shiragami C, Baba T, Shiraga F. Relationship between progression of visual field damage and choroidal thickness in eyes with normal-tension glaucoma. *Clin Exp Ophthalmol* 2012;40:576-582.

39. Park JH, Yoo C, Kim YY. Peripapillary choroidal thickness in untreated normal-tension glaucoma eyes with a single-hemifield retinal nerve fiber layer defect. *Medicine (Baltimore)* 2018;97:e11001.

40. Hayreh SS. The blood supply of the optic nerve head and the evaluation of it - myth and reality. *Prog Retin Eye Res* 2001;20:563-593.

41. Hayreh SS. Blood supply of the optic nerve head and its role in optic atrophy, glaucoma, and oedema of the optic disc. *Br J Ophthalmol* 1969;53:721-748.

42. Hayreh SS, Revie IH, Edwards J. Vasogenic origin of visual field defects and optic nerve changes in glaucoma. *Br J Ophthalmol* 1970;54:461-472.

43. Kubota T, Jonas JB, Naumann GO. Decreased choroidal thickness in eyes with secondary angle closure glaucoma. An aetiological factor for deep retinal changes in glaucoma? *Br J Ophthalmol* 1993;77:430-432.

44. Ehrlich JR, Peterson J, Parlitsis G, Kay KY, Kiss S, Radcliffe NM. Peripapillary choroidal thickness in glaucoma measured with optical coherence tomography. *Exp Eye Res* 2011;92:189-194.

45. Li L, Bian A, Zhou Q, Mao J. Peripapillary choroidal thickness in both eyes of glaucoma patients with unilateral visual field loss. *Am J Ophthalmol* 2013;156:1277-1284 e1271.

46. Mwanza JC, Hochberg JT, Banitt MR, Feuer WJ, Budenz DL. Lack of association between glaucoma and macular choroidal thickness measured with enhanced depth-imaging optical coherence tomography. *Invest Ophthalmol Vis Sci* 2011;52:3430-3435.

47. Suh W, Cho HK, Kee C. Evaluation of peripapillary choroidal thickness in unilateral normal-tension glaucoma. *Jpn J Ophthalmol* 2014;58:62-67.

48. Maul EA, Friedman DS, Chang DS, et al. Choroidal thickness measured by spectral domain optical coherence tomography: Factors affecting thickness in glaucoma patients. *Ophthalmology* 2011;118:1571-1579.

49. Lee S, Han SX, Young M, Beg MF, Sarunic MV, Mackenzie PJ. Optic nerve head and peripapillary morphometrics in myopic glaucoma. *Invest Ophthalmol Vis Sci* 2014;55:4378-4393.

2.3 Age-dependent Deformation of the Optic Nerve Head and Peripapillary Retina by Horizontal Duction

Alan Le[1-3], Jessica Chen Michael Lesgart[4], Bola A. Gawargious[5],

Soh Youn Suh[1,2,7], Joseph L. Demer[1,2,3,6,7]

[1]Department of Ophthalmology and [2]Stein Eye Institute, [3]Bioengineering Interdepartmental Programs, [4]Department of Psychology, [5]Department of Integrative Biology and Physiology, [6]Department of Neurology, [7]David Geffen Medical School at University of California, Los Angeles.

2.3.1 Introduction

When the human eye rotates into large angle adduction, magnetic resonance imaging (MRI) demonstrates that the optic nerve (ON) and the optic nerve dural sheath (ONS) straighten, become tethered, and exert traction on the posterior globe.[1,2] Resulting anteroposterior deformations of posterior ocular tissues during horizontal duction have been demonstrated by two-dimensional optical coherence tomography (OCT), including anteroposterior tilting of the ON head (ONH) and peripapillary Bruch's membrane.[2,3,4] The nasal side of the ONH moves anteriorly while the temporal side moves posteriorly.[2,5] The effect is greatly enhanced with adduction exceeding a threshold of about 26°. 25-45° Saccades are common during everyday eye movement and can rotate the eyes beyond this threshold. Gaze shifts with head rotation includes eye movements averaging ~30°. In abduction, the ONH also exhibits see-saw motion directionally inverse to abduction.[3, 6] While both abduction and adduction can deform the ONH, the effect is greater for adduction, presumably due to ON tethering. This is likely why our previous MRI study found no optic nerve tethering in exotropia, but higher occurrence in esotropia.

Biomechanical studies of stress and strain in the posterior eye using finite element analysis have focused on the structural properties of the ONH, peripapillary sclera and lamina cribrosa to suggest possible mechanisms of glaucoma independent of intraocular pressure (IOP).[7-10] Elevated IOP can of course produce mechanical stress in the ONH,[7,11,12] yet IOP alone cannot alone explain glaucomatous optic neuropathy in many patients with normal or subnormal IOP that accounts for a majority of glaucoma cases in Asian populations.[13,14] It has been proposed that force concentration in peripapillary sclera due to eye movements may be an IOP-independent mechanism for ONH deformation leading to glaucomatous optic neuropathy,[15] since by this mechanism,

strain is concentrated on the temporal side of the ONH where peripapillary atrophy most commonly occurs, as does the earliest damage in glaucoma.[16]

Although peripapillary mechanical deformation is greatly exaggerated in adduction where the ON becomes tethered, eye rotation also deforms this region during smaller ductions. In papilledema, Sibony showed distortion of the peripapillary basement membrane during horizontal duction even without ON tethering.[6] Wang *et al*. demonstrated by OCT in normal subjects that there are ONH strains during even moderate abduction and adduction.[17]

Previous OCT studies of horizontal duction examined anteroposterior shifts and tilts of the ONH, but did not investigate possible horizontal and vertical deformations. Examination of the ONH by OCT is often confounded by shadows cast by epipapillary blood vessels (BVs) obscuring much of the underlining tissue. We have explored an alternative approach of *en face* imaging that exploits these same BVs as fiducial landmarks to study local horizontal and vertical displacements in the ONH and surrounding retina produced by gaze changes. Local deformations of the ONH and retinal surface can be deduced from differential translational shifts in local features. In the current study, we tracked large BVs on the retinal and ONH surfaces as markers of local deformation of the underlying tissues. We investigated whether horizontal ductions differently displace BVs in subjects of different ages.

2.3.2 Methods

Subjects

Twenty healthy young adult volunteers (11 males, 9 females) of mean age 23.9±3.9 (SD, range 19-32) years and 20 healthy older volunteers (7 males, 13 females)

of mean age 61.4±9.3 (range 48-79) years were recruited by advertising and examined to verify absence of ocular disorders besides correctable refractive error. Subjects were provided written, informed consent prior to participation according to a protocol approved by the University of California, Los Angeles Institutional Review Board compliant with the Declaration of Helsinki. All subjects underwent comprehensive eye examinations to confirm normal corrected visual acuity, normal binocular alignment, and normal IOP (<21mmHg) without evidence of glaucomatous optic neuropathy. Only the right eye of each subject was analyzed. There were no high myopes or high hyperopes, defined as having more than 5 D spherical equivalent refractive error. Of the total 40 subjects studied, 26 had uncorrected visual acuity at least 20/20, and so represent emmetropes or low hyperopes.

Of the younger volunteers, 10 were Caucasian and 2 each of African American, East Asians, South Asians, Middle Easterners, and Hispanics. The older group included 8 Caucasians, 4 African American, 1 East Asian, 3 Middle Eastern, and 4 Hispanics.

En face Infrared Imaging

The infrared scanning laser ophthalmoscope mode of a Heidelberg Spectralis scanner (Heidelberg Engineering, Heidelberg, Germany) was used to image the ONH and adjacent retina. A retinal nerve fiber layer (RNFL) circular scan was first performed to verify normal thickness. Each right eye was then imaged in central gaze, 35° abduction, and 35° adduction sequentially by rotating the imager camera to calibrated angles on its azimuth pivot, including central gaze and 35° ab- and adduction. The scanner rotated along with the eye thus maintaining a constant angle relative to the line of sight. The subject's head was stabilized to the scanner headrest using cushions and straps to prevent head rotation. To obtain images centered on the ONH, subjects fixated the scanner's internal target that, by manufacturer's design, is offset 12° nasally from

straight-ahead; this offset was compensated by a custom goniometric scale to set desired ductions. During eccentric gaze imaging in some subjects, the camera was also translated towards the subject to obtain the desired gaze angle to clear the nose and other facial features. This anteroposterior camera translation changed image magnification slightly but this was corrected during analysis. En face images were exported at 5.85μm/pixel.

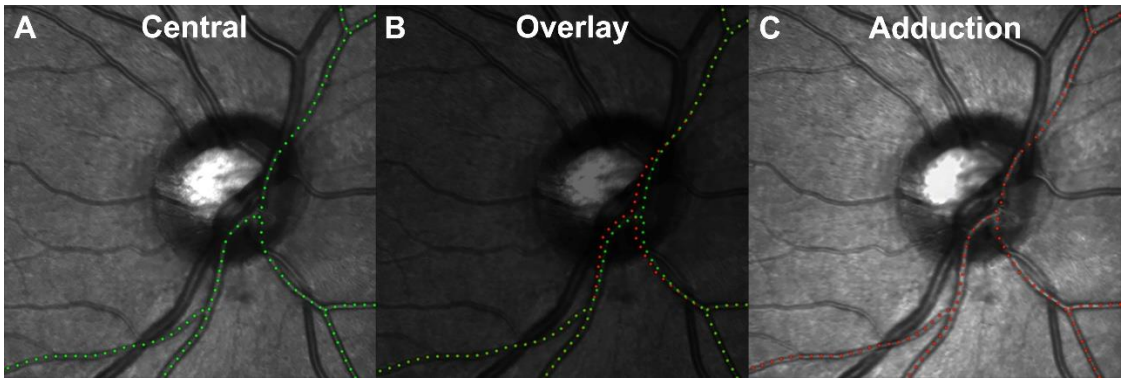

Figure 1. Images obtained in central gaze (A) and 35° adduction (C) in which a large blood vessel has been marked with green and red dots, respectively. Vessel displacements due to gaze change indicate deformation of the underlying retina, and were determined by image superimposition (B). Temporal shifting of vessel on the ONH is evident.

Large BVs on the retinal and ON surface were used as fiducials to track local deformations of the underlying tissues to which they are attached. Figure 1 shows a major BV branch traced during central gaze (1A green) and adduction (1C red). Figure 1B superimpose the green and red paths, highlighting relative displacement between gazes. Dotted green and red paths in the figure are shown for representation of major BV displacement.

B-Scan OCT

Subjects were imaged using in the OCT mode with enhanced depth imaging of the ONH and peripapillary retina (PPR). The B-scans were assessed for vitreous attachment.

Image Analysis

Images were exported as tagged image file format (TIFF) files and processed using Adobe Photoshop (Adobe Systems, San Jose, CA, USA). In subjects who required translation of the OCT camera to focus the retina, magnifications of images obtained in ab- and adduction were isotropically scaled to match the size of the central gaze image. In all cases, the resulting three images for each eye were superimposed in a digital stack for analysis. Images obtained in ab- and adduction were rotated and translated to match the central gaze image using BVs remote from the ONH as anchor fiducials; this approach compensates for physiologic ocular torsion in eccentric gazes resulting from Listing's Law [18]. A circular grid (Fig. 2) with 5 concentric rings divided radially into 8 sectors was overlaid on the image stack. The center ring had diameter equal to the ONH, and each successive ring had an integer multiple of the center diameter, dividing the retina into concentric regions. Region 0 represented the ONH. Region 1 enclosed the area 1 disc radius beyond the ONH border. Region 2 extended an additional disc radius from Region 1, Region 3 the next disc radius, and Region 4 extended a further disc radius beyond Region 3 to a maximum of 4 disc radii from the ONH. Each of the five regions was divided into 8 equal sectors numbered clockwise from the top as shown in Fig. 2.

Whenever one or more BV intersections or branch points were present in each of the 40 zones, a marker was placed on each feature, thus demarcating fiducials that permitted robust tracking of underlying retinal displacements associated with changes in

gaze direction. By alternating the opacity of images obtained in abduction and adduction superimposed on the central gaze image, displacements caused by the gaze change were tracked for each marker.

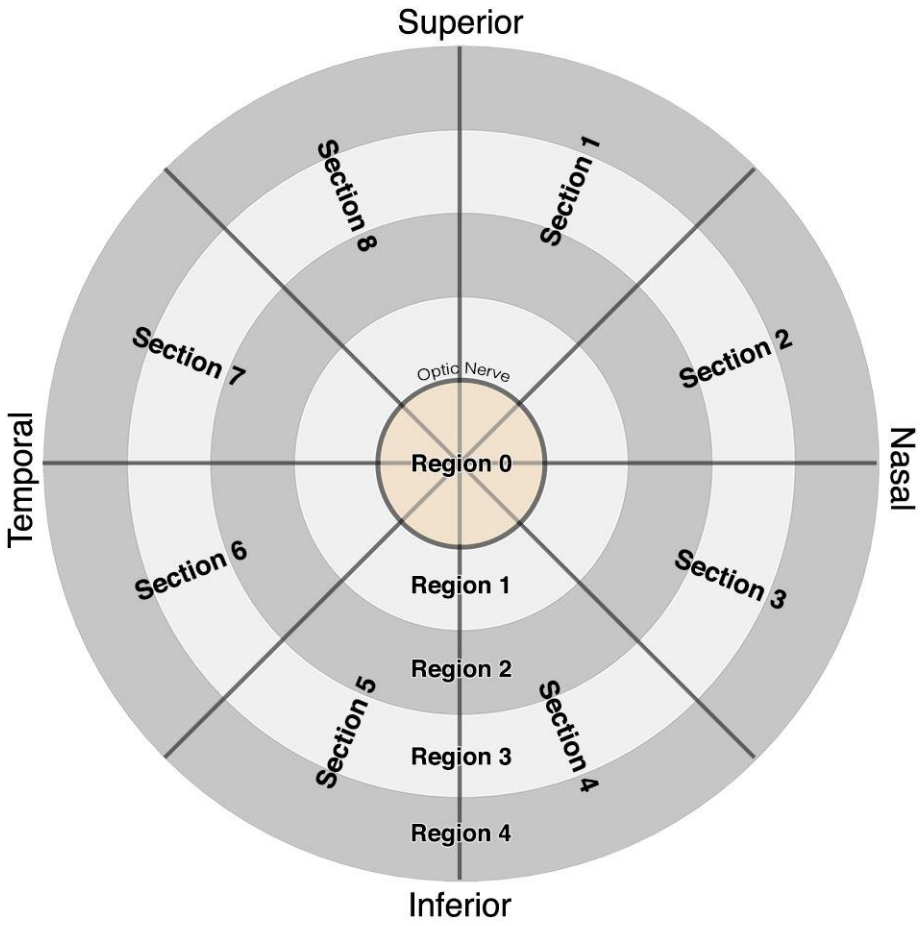

Figure 2. For analysis, images were divided into 40 different zones using a circular grid. Region 0 represented the ONH itself. Each concentric region was a multiple of ONH diameter, and divided into 8 sections at 45° each. Sections 1-4 and Sections 5-8 represented the nasal and temporal halves of the ONH, respectively.

Each of the three image layers had associated marker fiducial layers that represented BV intersections or branch points in each sector containing such features (Fig. 3). *ImageJ64* (W. Rasband, National Institutes of Health, Bethesda, Maryland, USA; http://rsb.info.nih.gov/ij/, 1997-2018, in public domain) was used to compensate

magnification variations, and to determine the location of each fiducial. Custom programs then calculated horizontal and vertical displacements of fiducials for each gaze position. Software written in the MATLAB (MathWorks, Inc, Natick, Massachusetts) software suite was used to plot heatmaps of the displacements.

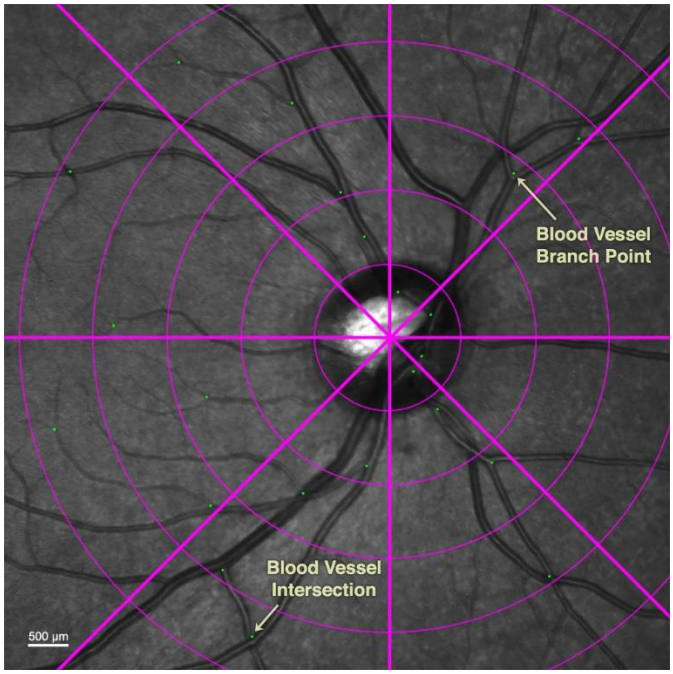

Figure 3. Green dot fiducials were placed at vascular branches and intersections

Statistical Analysis

Using GraphPad Prism (GraphPad Software, San Diego, CA), horizontal and vertical displacements of fiducials from central to 35° ab- and adduction were compared using paired t-tests in each circular region and section to determine significant differences from zero and between age groups at the 95% confidence level. All measurements were repeated by a second analyst. Results by the two analysts did not differ significantly.

2.3.3 Results

Horizontal Displacements

Adduction of 35° temporally shifted vessels intrinsic to the ONH in both young and elderly subjects, indicting displacement of the ONH itself. In young subjects (Fig. 4), all sections (1-8) overlying the ONH (Region 0) exhibited significant temporal displacement ($P<0.0001$) with the largest displacement in Section 2 (41.7±5.8μm SEM), which is the superonasal disc. The entire nasal half (Sections 1-4) of the ONH were displaced more on average than the temporal half (Sections 5-8) at 4.1±2.1μm ($P<0.001$). The PPR (Region 1) extending one disc radius from the ONH was significantly displaced temporally in all sections but Sections 6 and 7, averaging 7.6±1.6μm (Figs. 4 and 5). There was less displacement farther than one disc radius from the ON center; in Region 2, only Section 8 was significantly displaced in adduction. There were no significant horizontal displacements in the more distal Regions 3 and 4. Abduction shifted vessels in and near the ONH nasally, but less than in adduction; there were no displacements beyond the ON border (Regions 1-4) in abduction.

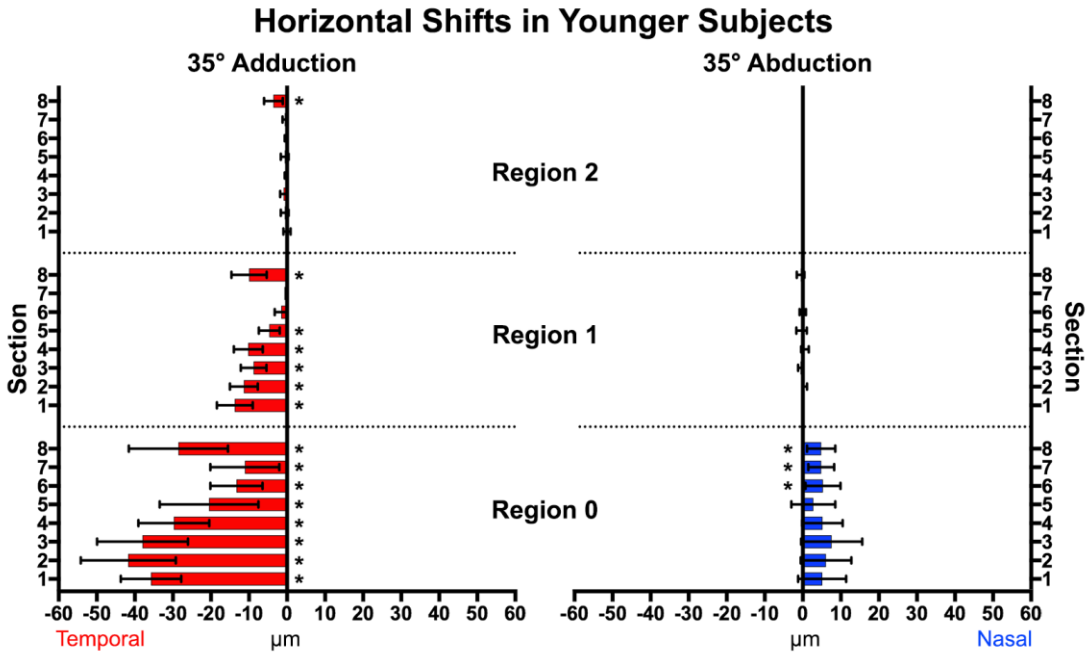

Figure 4. Vessel displacement during 35° horizontal duction of younger subjects. All sections within the optic nerve head (Region 0) and the majority of Region 1 showed significant temporal shifts in adduction (left), with fewer and smaller shifts nasally in abduction. * represents significant non-zero displacements. Brackets mark 95% confidence intervals.

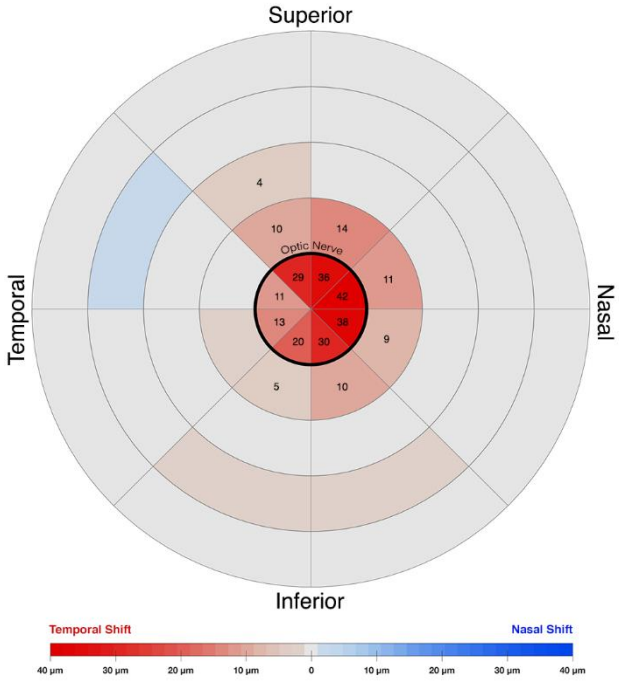

Figure 5. Horizontal displacement heatmap during adduction in younger subjects. The center circle represents the optic nerve head. Temporal shifts are colored red, nasal shifts blue. Numbers denote zones exhibiting significant displacement during adduction. The nasal half of the nerve head showed the greatest temporal deformation.

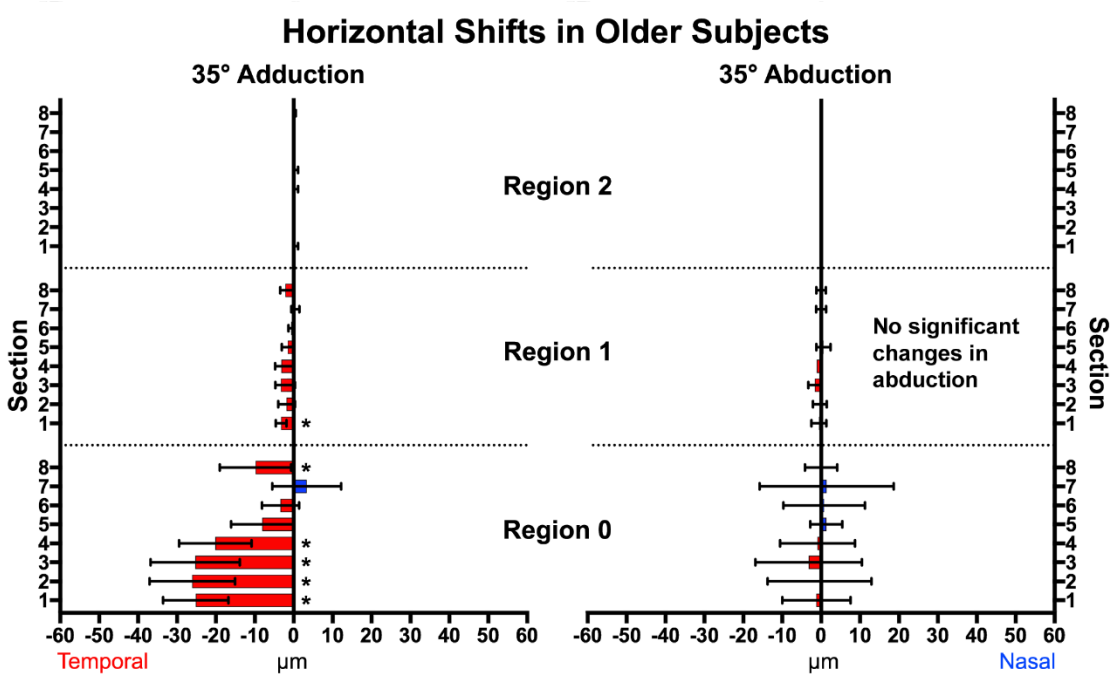

Figure 6. Horizontal displacement in older subjects during adduction (left) and abduction (right). In adduction, the nasal half (Sections 1-4) of the optic nerve head (Region 0) exhibited greatest temporal shift while there were smaller temporal displacements in Region 1. There were no significant displacements in abduction. * signifies non-zero displacements. Brackets mark 95% confidence intervals.

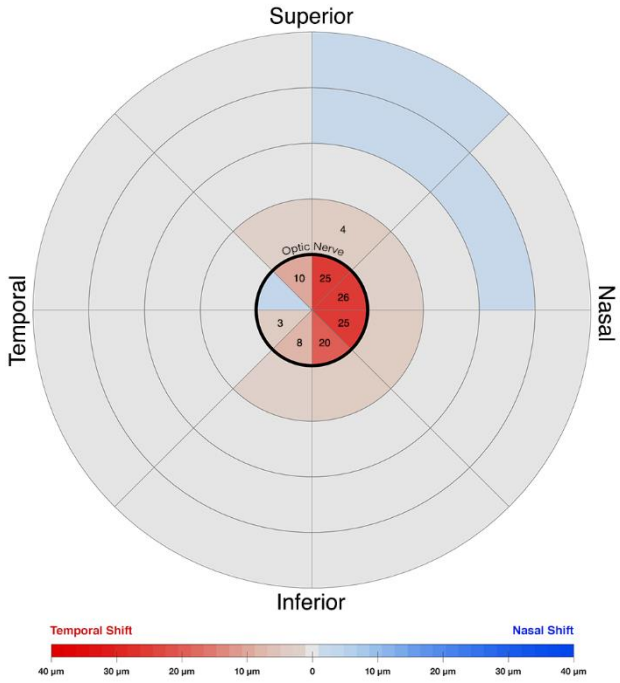

Figure 7. Horizontal displacement heatmap for adduction in older subjects. The center circle represents the optic nerve head. Temporal shifts are colored red. Nasal shifts are colored blue. Numbers on the map denote zones that had a significant change during adduction. The nasal half of the nerve head exhibited more temporal deformation. There was less overall deformation than in younger subjects.

In older subjects (Figs. 6 and 7), 5 of the 8 sectors within the ONH exhibited significant temporal displacement in adduction but not in abduction. In adduction, the nasal half sections of the ONH shifted more on average at 24.5±1.3µm than the temporal half sections at 4.4±2.1µm ($P<0.001$). While there were no displacements in Regions 2 – 4, four sections adjacent to the ON (Region 1) significantly shifted temporally by an average 2.0±0.4µm during adduction. No significant displacements in abduction occurred anywhere in older subjects.

Vertical Displacements

Adduction to 35° caused much smaller vertical than horizontal displacements in both young and older subjects ($P<0.001$, Figs. 8 and 9). In younger subjects there were

4 zones exhibiting deformation: Region 0, Section 4, and Region 2 Sections 5 and 8 shifted superiorly, while Region 1, Section 1shifted inferiorly. Abduction produced small inferior shifts in the ONH and three zones of Region 1. The superior half of the ONH in older subjects (Fig. 9) shifted inferiorly in adduction, although only two zones exhibited small vertical displacement (<3.2μm) during abduction. All vertical displacements were smaller than horizontal displacements.

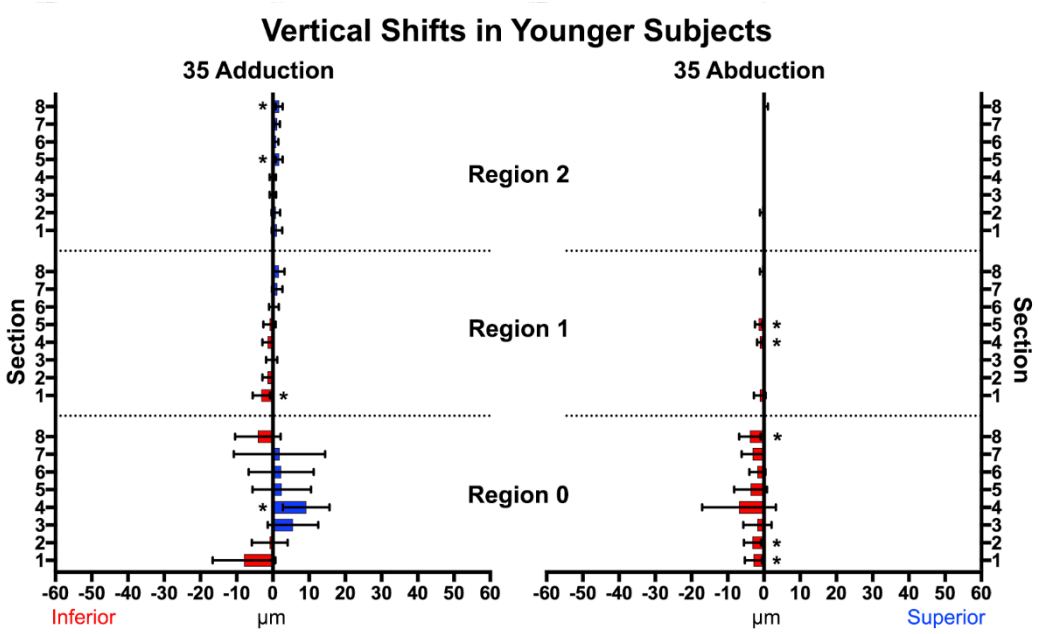

Figure 8. In younger subjects, neither adduction not abduction caused major vertical displacements of the optic nerve head or papillary retina. * represents statistically significant (P<0.02) but mechanically trivial displacements. Brackets mark 95% confidence intervals.

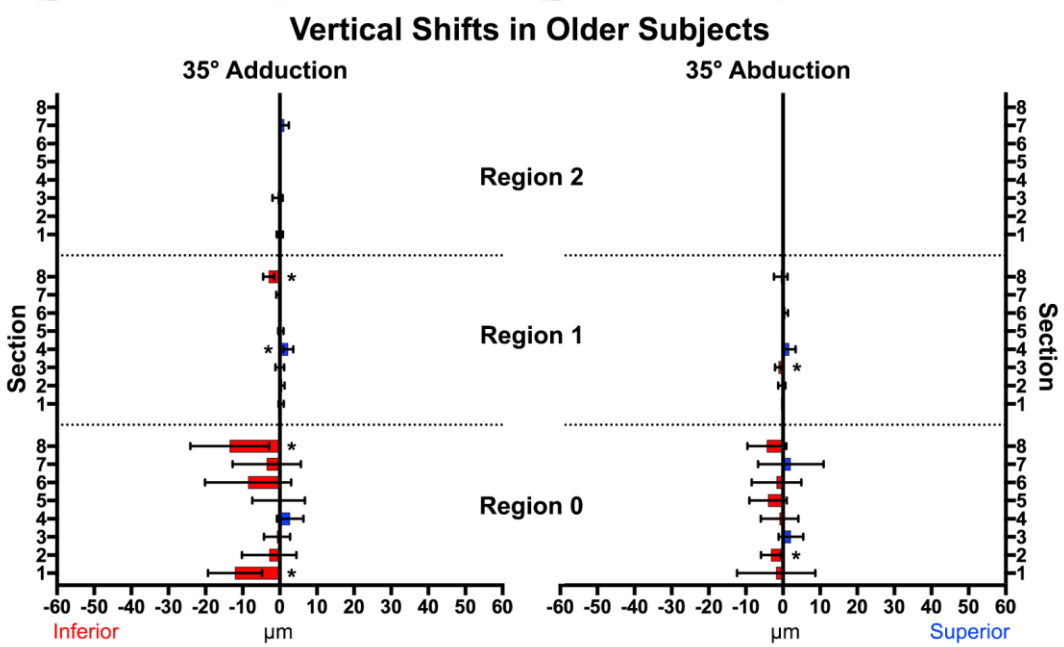

Figure 9. In older subjects, the superior half of the ONH shifted inferiorly in adduction. * represents significant (P<0.02) non-zero displacements. Brackets mark 95% confidence intervals.

Effect of Posterior Vitreous Detachment (PVD)

Standard B-scan OCT was employed to examine the relationship of the vitreous body to ON and peripapillary displacements during horizontal duction. Of the 20 older subjects, 12 had complete PVD and 8 had partial PVD. Displacements during horizontal duction were similar regardless of vitreous attachment. Vitreous detachment was not significantly associated with horizontal and vertical displacement in ab- or adduction (P> 0.6).

Vascular Pulsatility

Pulsating vessels on the ONH were observed in six of the younger subjects in *en face* imaging. Movement of superficial BV due to pulsatility was confined to the ONH surface, was only in the anteroposterior direction, and had very small magnitude (<10

μm). No significant horizontal and vertical fiducial shifts resulted from vascular pulsatility. No vascular pulsatility was observed in older subjects.

2.3.4 Discussion

Deformation of the ONH has been linked to reduction in RNFL thickness and gradual visual loss in glaucoma.[19-23] While many studies focus on elevated IOP as a cause of short term ONH deformation, some recent studies have demonstrated that eye movements can also deform the ONH, and so may represent a pathological process when repeated many times during the very large number of everyday eye movements.[1] The current study provides further evidence that horizontal ductions not only deform the superficial ONH but also the surrounding PPR. Whereas prior OCT studies measured anteroposterior movement of Bruch's membrane[3] and ONH tilt angle[2], our current study quantified local horizontal and vertical translational shifts of large blood vessels embedded in the ONH and retinal surface. Extending previous OCT studies,[2,3] the current *en face* imaging shows that the nasal half of the ONH moves temporally in addition to what was already known to be anteriorly, during adduction, and conversely the nasal half of the ONH moves slightly nasally in addition to what was already known to be posteriorly during abduction. The nasal half of the ONH is thus compressed during adduction more than during abduction.

The blood vessels tracked in this study were embedded in or adherent to the ONH and PPR with which they are intimately associated. Movements of papillary and peripapillary retinal blood vessels indicate movements of these neural tissues: blood vessels marking neural tissue of the ONH shift temporally during 35° adduction in both young and older subjects, and nasally in abduction for younger individuals. In younger

subjects, the temporal displacement in adduction was more than four-fold greater than the nasal shift in abduction. The greater magnitude of displacement in ad- in comparison with abduction is consistent with MRI findings that ON tethering occurs only in adduction[2,3,5]. However, one might have reasoned that if the ON sheath were to become tethered in adduction, resulting traction exerted on the globe-optic nerve junction would displace the ONH nasally relative to the retina. Instead, we observed a temporal shift in ONH vessels. This seemingly counter-intuitive finding likely resulted from "nasal buckling"[2] at the nasal edge of the globe-optic nerve junction where in large adduction, an acute angle formed between the ON and sclera compresses the surrounding tissue to force the ONH anteriorly and temporally. The ON neural tissue shifts temporally relative to the sclera and ON sheath during ON tethering in adduction, as directly demonstrated by MRI.[24] Nasal buckling may also explain why in adduction the nasal half of the ONH and surrounding nasal PPR shift farther temporally than the temporal half does. There may be less if any buckling in abduction, which may explain why only minor displacements are observed there in young adults, and none in older subjects. This again is consistent with MRI findings in abduction, where the slack ON generally remains centered within the ON sheath.

The ONH of young adults shifted more during both abduction and adduction than in older subjects. Young adults may have more compliant ONH tissue than older individuals who accumulate structural changes and stiffening. Young adults generally have vitreous attached to the posterior retina, while elderly subjects often undergo vitreous liquefaction commonly resulting in PVD.[25] Nevertheless, individuals with complete PVD had ON and peripapillary deformation in adduction statistically similar to those with partial PVD. Literature suggests that aging is associated with tissue stiffening in the trabecular meshwork[26], lamina cribrosa[27-30], sclera[31-33], Bruch's membrane[34], and

cornea[35]. The ONH can undergo extracellular matrix remodeling by altering the interplay between collagen and elastin fibers, changing the composition and concentration of matrix components, and by post-translational modifications (glycosylation, trans-glutamination, and crosslinking).[36] Additionally, older adults may have less orbital fat[37] that might allow the globe to retract more posteriorly into the orbit. This may increase ON sinuosity and decrease the path length that the ON must traverse during horizontal duction, and may attenuate ON tethering in adduction. Horizontal duction can generate strain at the ONH exceeding that caused by elevated IOP.[4,9] If adduction tethering does produce sufficient strain to cause optic neuropathy as predicted by biomechanical models,[9,15] then reduction of orbital fat to gain greater ON sinuosity might alleviate the strains during large adduction.

Differential shifts between adjacent zones in and around the ONH indicate that areas of the retina and ONH tissue are undergoing tensile or compressive shear in adduction. Among younger subjects, we observed an 18.3μm differential during adduction between the average horizontal shifts of the nasal and temporal halves of the ONH. This implies that the ONH is compressed while the nasal PPR is stretched. Compression of the ONH during adduction might impede capillary blood flow and damage the surrounding tissues. However, while the current study measured retinal blood vessel movements due to horizontal ductions, the study did not quantify blood flow. Future studies using techniques such as OCT angiography[38] could help elucidate whether large horizontal gaze duction hinder circulation in the ONH and retina.

Six of the current subjects exhibited pulsating ONH vessels due to the cardiac cycle. Previous literature has quantified the effect of vascular pulsatility in normal subjects and patients with glaucoma. The axial distance between the PPR and base of the normal optic disc cup (ADRC) reportedly fluctuates by 10.7±2.1μm and 11.6±1.8μm for the

nasal and temporal sides of the ONH, respectively.[39] In patients with glaucoma, significantly higher ADRC fluctuations have been reported at 14.9±5.6μm and 14.0±4.9μm on nasal and temporal sides, respectively. Pulsatile displacements of approximately 10 μm may be innocuous to the ONH, so abduction-induced small nasal shifts are presumably undamaging. In adduction, however, the ONH is deformed four-fold as in abduction. Temporal deformations of the nasal half of the ONH in the current study were as high as 42μm, averaging 36.5μm, well beyond the ADRC fluctuations observed in glaucoma. This observation supports the notion that repetitive strain from large adduction and adducting saccadic movements[40] occurring over a lifetime might cause gradual remodeling of the ONH leading to optic neuropathy. Further investigation may determine whether horizontal gaze evoked ONH deformations are exaggerated in patients with glaucoma.

The present study was limited to detection of local vascular shifts relative to points of reference at the remote corners of the *en face* images that were assumed to be undeformed. All displacements reported here should be interpreted as local deformations of the ON and retina relative to the fixed reference points beyond 4 disc radii from its rim. Horizontal duction-induced translational changes to the whole posterior retina surface exceeding the imaging boundaries cannot be detected. Thus, if horizontal duction were to translate the entire globe, our method would not detect such changes. The current method is also insensitive to displacements in the anteroposterior direction that are observable by OCT. A previous OCT study identified 26° adduction as a threshold for marked gaze-evoked deformation of Bruch's membrane.[3] The current study did not include graded degrees of duction and thus cannot determine if any threshold exists for the observed displacements. Future studies could investigate whether such a threshold exists and may also explore effects of axial myopia and staphyloma on ONH

deformations resulting from gaze shift. It could be predicted that duction-related ON and peripapillary deformations could be larger in high myopia, because globe axial elongation is associated with greater adduction tethering and prominent peripapillary atrophy and temporal ONH tilt.[41] Simple geometry suggests that an elongated globe necessitates a longer ON path length change during duction, and could amplify the effect of ON tethering to create greater ONH deformation during adduction. Future studies could also analyze tissue deformations in all 3 dimensions simultaneously from volumetric OCT angiography, although such an endeavor would be complicated by occlusions of multiple layers of vessels at the ONH.

In conclusion, 35° adduction displaces the nasal half of the ON and adjacent PPR temporally. This displacement is greater in younger than older adults, and reflects deformation of the underlying retinal and neural tissue. Abduction causes a smaller but oppositely directed deformation observable only in young subjects. These shearing displacements in the ONH and adjacent PPR indicate tissue compression of the ONH.

2.3.5 References

1. Demer JL, Clark RA, Suh SY, et al. Magnetic resonance imaging of optic nerve traction during adduction in primary open-angle glaucoma with normal intraocular pressure. Invest Ophthalmol Vis Sci 2017;58(10):4114-25.

2. Chang MY, Shin A, Park J, et al. Deformation of optic nerve head and peripapillary tissues by horizontal duction. Am J Ophthalmol 2017;174:85-94.

3. Suh SY, Le A, Shin A, et al. Progressive deformation of the optic nerve head and peripapillary structures by graded horizontal duction. Invest Ophthalmol Vis Sci 2017;58(12):5015-21.

4. Wang X, Fisher LK, Milea D, et al. Predictions of optic nerve traction forces and peripapillary tissue stresses following horizontal eye movements. Invest Ophthalmol Vis Sci 2017;58(4):2044-53.

5. Suh SY, Clark RA, Demer JL. Optic nerve sheath tethering in adduction occurs in esotropia and hypertropia, but not in exotropia. Invest Ophthalmol Vis Sci 2018;59(7):2899-904.

6. Sibony PA. Gaze evoked deformations of the peripapillary retina in papilledema and ischemic optic neuropathy. Invest Ophthalmol Vis Sci 2016;57(11):4979-87.

7. Burgoyne CF, Downs JC, Bellezza AJ, et al. The optic nerve head as a biomechanical structure: A new paradigm for understanding the role of iop-related stress and strain in the pathophysiology of glaucomatous optic nerve head damage. Prog Retin Eye Res 2005;24(1):39-73.

8. Burgoyne CF, Downs JC. Premise and prediction-how optic nerve head biomechanics underlies the susceptibility and clinical behavior of the aged optic nerve head. J Glaucoma 2008;17(4):318-28.

9. Wang X, Rumpel H, Lim WE, et al. Finite element analysis predicts large optic nerve head strains during horizontal eye movements. Invest Ophthalmol Vis Sci 2016;57(6):2452-62.

10. Sigal IA, Ethier CR. Biomechanics of the optic nerve head. Exp Eye Res 2009;88(4):799-807.

11. Lee EJ, Kim TW, Weinreb RN. Reversal of lamina cribrosa displacement and thickness after trabeculectomy in glaucoma. Ophthalmology 2012;119(7):1359-66.

12. Lee EJ, Kim TW, Weinreb RN, Kim H. Reversal of lamina cribrosa displacement after intraocular pressure reduction in open-angle glaucoma. Ophthalmology 2013;120(3):553-9.

13. Iwase A, Suzuki Y, Araie M, et al. The prevalence of primary open-angle glaucoma in japanese: The tajimi study. Ophthalmology 2004;111(9):1641-8.

14. Kim JH, Kang SY, Kim NR, et al. Prevalence and characteristics of glaucoma among korean adults. Korean J Ophthalmol 2011;25(2):110-5.

15. Shin A, Yoo L, Park J, Demer JL. Finite element biomechanics of optic nerve sheath traction in adduction. J Biomech Eng 2017;139(10).

16. Jonas JB. Clinical implications of peripapillary atrophy in glaucoma. Curr Opin Ophthalmol 2005;16(2):84-8.

17. Wang X, Beotra MR, Tun TA, et al. In vivo 3-dimensional strain mapping confirms large optic nerve head deformations following horizontal eye movements. Invest Ophthalmol Vis Sci 2016;57(13):5825-33.

18. Ruete C. Ocular physiology. Strabismus 1999; 7:43-60.

19. Leung CK, Chan WM, Hui YL, et al. Analysis of retinal nerve fiber layer and optic nerve head in glaucoma with different reference plane offsets, using optical coherence tomography. Invest Ophthalmol Vis Sci 2005;46(3):891-9.

20. Strouthidis NG, Fortune B, Yang H, et al. Longitudinal change detected by spectral domain optical coherence tomography in the optic nerve head and peripapillary retina in experimental glaucoma. Invest Ophthalmol Vis Sci 2011;52(3):1206-19.

21. Fortune B, Burgoyne CF, Cull GA, et al. Structural and functional abnormalities of retinal ganglion cells measured in vivo at the onset of optic nerve head surface change in experimental glaucoma. Invest Ophthalmol Vis Sci 2012;53(7):3939-50.

22. Fortune B, Reynaud J, Wang L, Burgoyne CF. Does optic nerve head surface topography change prior to loss of retinal nerve fiber layer thickness: A test of the site of injury hypothesis in experimental glaucoma. PLoS One 2013;8(10):e77831.

23. Medeiros FA, Alencar LM, Zangwill LM, et al. Prediction of functional loss in glaucoma from progressive optic disc damage. Arch Ophthalmol 2009;127(10):1250-6.

24. Demer JL. Optic nerve sheath as a novel mechanical load on the globe in ocular ductionoptic nerve sheath constrains duction. Invest Ophthalmol Vis Sci 2016;57(4):1826-38.

25. Sebag J. Structure, function, and age-related changes of the human vitreous. Bull Soc Belge Ophtalmol 1987;223 Pt 1:37-57.

26. Tektas OY, Lutjen-Drecoll E. Structural changes of the trabecular meshwork in different kinds of glaucoma. Exp Eye Res 2009;88(4):769-75.

27. Albon J, Karwatowski WS, Avery N, et al. Changes in the collagenous matrix of the aging human lamina cribrosa. Br J Ophthalmol 1995;79(4):368-75.

28. Albon J, Karwatowski WS, Easty DL, et al. Age related changes in the non-collagenous components of the extracellular matrix of the human lamina cribrosa. Br J Ophthalmol 2000;84(3):311-7.

29. Albon J, Purslow PP, Karwatowski WS, Easty DL. Age related compliance of the lamina cribrosa in human eyes. Br J Ophthalmol 2000;84(3):318-23.

30. Leung LK, Ko MW, Lam DC. Effect of age-stiffening tissues and intraocular pressure on optic nerve damages. Mol Cell Biomech 2012;9(2):157-73.

31. Avetisov ES, Savitskaya NF, Vinetskaya MI, Iomdina EN. A study of biochemical and biomechanical qualities of normal and myopic eye sclera in humans of different age groups. Metab Pediatr Syst Ophthalmol 1983;7(4):183-8.

32. Geraghty B, Jones SW, Rama P, et al. Age-related variations in the biomechanical properties of human sclera. J Mech Behav Biomed Mater 2012;16:181-91.

33. Coudrillier B, Tian J, Alexander S, et al. Biomechanics of the human posterior sclera: Age- and glaucoma-related changes measured using inflation testing. Invest Ophthalmol Vis Sci 2012;53(4):1714-28.

34. Booij JC, Baas DC, Beisekeeva J, et al. The dynamic nature of bruch's membrane. Prog Retin Eye Res 2010;29(1):1-18.

35. Malik NS, Moss SJ, Ahmed N, et al. Ageing of the human corneal stroma: Structural and biochemical changes. Biochim Biophys Acta 1992;1138(3):222-8.

36. Liu B, McNally S, Kilpatrick JI, et al. Aging and ocular tissue stiffness in glaucoma. Surv Ophthalmol 2018;63(1):56-74.

37. Salvi SM, Akhtar S, Currie Z. Ageing changes in the eye. Postgrad Med J 2006;82(971):581-7.

38. Mansoori T, Sivaswamy J, Gamalapati JS, et al. Measurement of radial peripapillary capillary density in the normal human retina using optical coherence tomography angiography. J Glaucoma 2017;26(3):241-6.

39. Singh K, Dion C, Godin AG, et al. Pulsatile movement of the optic nerve head and the peripapillary retina in normal subjects and in glaucoma. Invest Ophthalmol Vis Sci 2012;53(12):7819-24.

40. Wu CC, Kowler E. Timing of saccadic eye movements during visual search for multiple targets. J Vis 2013;13(11).

41. Kim TW, Kim M, Weinreb RN, et al. Optic disc change with incipient myopia of childhood. Ophthalmology 2012;119(1):21-6 e1-3.

2.4 Adduction Deformation of Optic Disc and Peripapillary Region in Primary Open Angle Glaucoma with Normal Intraocular Pressure

Alan Le[1-3], Jessica Chen[4], JoAnn A. Giaconi[1,2], Kouros Nouri-Mahdavi[1,2],

Simon K. Law[1,2], Laura Bonelli[1,2], Anne L. Coleman[1,2],

Joseph Caprioli[1,2], and Joseph L. Demer[1,2,3,5,6]

[1]Department of Ophthalmology and [2]Stein Eye Institute, [3]Bioengineering Interdepartmental Programs, [4]Computational and Systems Biology Interdepartmental Program, [5]Department of Neurology, [6]David Geffen Medical School at University of California, Los Angeles.

2.4.1 Abstract

Purpose: Local tissue shearing in the optic disc and peripapillary retina (PPR) occurs during horizontal duction in normal subjects. We investigated if this tissue deformation is similar in patients who have primary open angle glaucoma (POAG) at intraocular pressure (IOP) never exceeding the normal range.

Methods:

Study Population: Both eyes of 15 patients with POAG in whom untreated or treated IOP never exceeded the normal range of 21 mmHg, and 15 age-matched normal subjects.

Observational Procedure: The ONH and PPR were imaged using infrared scanning laser ophthalmoscopy.

Main Outcome Measure: Displacements of blood vessel fiducials on and around the disc in 35° adduction and in 35° abduction.

Results: In control subjects of average age 62±9 years (standard deviation, SD), epipapillary fiducials shifted temporally during adduction, more so in the nasal half of the disc at 22.7±5.1 µm (standard error of mean, SEM) and less at 16.6±4.1 µm in the temporal half ($P<0.001$). In patients with POAG averaging 65±14 years old, epipapillary fiducials shifted less than controls during adduction ($P=0.025$): 15.2±4.1 µm in the nasal hemidisc, and 12.6±2.9 µm in the temporal hemidisc. There were no significant epipapillary shifts in abduction in either patients with POAGs or controls.

Conclusion: Adduction but not abduction deforms the optic disc less in patients with POAG than in normal subjects. This may be due to tissue stiffening in POAG. Peripapillary deformation in adduction, detectable using widely-available clinical ophthalmic imaging equipment, may represent a risk factor or biomarker for glaucomatous optic neuropathy.

2.4.2 Introduction

It has been recently demonstrated by magnetic resonance imaging (MRI) that optic nerve (ON) length is insufficient to avoid tethering the globe when the eye adducts beyond about 26°.[1] Since the ON is relatively stiff, further adduction within the roughly 40° oculomotor range requires that the globe also shift linearly. This globe shift is nasally in healthy subjects, but the globe retracts posteriorly in subjects who have primary open angle glaucoma (POAG).[2] Adduction tethering concentrates the reaction force of extraocular muscles against the optic disc, peripapillary retina (PPR), and sclera. Studies employing optical coherence tomography (OCT) and *en face* scanning laser ophthalmoscopic imaging have shown that this tethering locally deforms these visually critical tissues.[3] When exaggerated by ON sheath distention in papilledema, peripapillary folds induced by adduction can even extend from the disc into the macula.[4]

Glaucoma is a leading cause of visual impairment and blindness, affecting over 60 million people worldwide.[5] It has been proposed that eye-movement related mechanical stress on the optic disc might be another mechanical etiology for optic neuropathy in POAG, operating alternatively or in addition to IOP.[2, 6-8] Consistent with adduction tethering, OCT demonstrates in normal subjects that large angle adduction produces more anteroposterior displacement of the peripapillary Bruch's membrane than does abduction,[1] and even moderate ad- and adduction also induce ONH strains.[9]

However, the study of ONH and PPR contour by B-scan OCT is problematic due to curvature distortions inherent in tomographic image reconstruction, thus degrading reliability for lateral measurements. Complex reconstruction is not necessary for *en face* images. In the present study, we compared horizontal gaze-evoked deformation in patients with POAG at normal IOP to that of age-matched control subjects. We utilize *en face* infrared imaging of intersections and branch points of large blood vessels (BV)

embedded in the retina and ONH as fiducials to deduce local horizontal and vertical tissue deformations.

2.4.3 Methods

Subjects

Prior to participation, all participants gave written, informed consent according to a protocol approved by the University of California, Los Angeles Institutional Review Board conforming to the tenets of the Declaration of Helsinki. From an academic glaucoma practice, we recruited 25 patients with POAG (13 males, 12 females) of mean age 65±14 (SD, range 27-83) years. These patients were recruited from a multi-physician academic glaucoma practice and had been diagnosed with POAG based upon the following inclusion criteria: applanation IOP never exceeding 21 mmHg, with or without treatment, on multiple clinical examinations; and ophthalmoscopic examinations, disc photography, and OCT evidence of disc and nerve fiber layer features that correlated with typical glaucomatous visual field defects on Humphry automated perimetry. Patients were excluded if they had previously undergone incisional ocular surgeries besides those for cataract, glaucoma, or refractive error, or if they had cause for optic neuropathy or visual field defects besides glaucoma.

By advertising we also recruited 19 normal volunteers (8 males, 11 females) of similar mean age 62±9 (range 52-79) years. None had ocular disorders other than refractive error less than 5 D spherical equivalent myopia or hyperopia. Normal subjects underwent comprehensive eye examinations to confirm normal corrected visual acuity, normal binocular alignment, and normal intraocular pressure (<21mmHg) without evidence of glaucomatous optic neuropathy.

En Face Imaging

The confocal scanning laser ophthalmoscope mode of a Spectralis scanner (Heidelberg Engineering, Heidelberg, Germany) was used to obtain infrared images of the optic disc and PPR. Each eye was imaged in central gaze, 35° abduction, and 35° adduction sequentially. The subject's head was stabilized to the headrest using cushions and straps to avoid head rotation. For eccentric gazes, the OCT camera was rotated on its azimuth pivot to 35° ab- and adduction angles marked by a goniometric scale on the scanner gimbal. The subject fixated the internal target that was offset 12° nasally from straight-ahead in order to center the image on the optic disc. This 12° nasal shift of the target was incorporated into calibration of the goniometric scale. It was necessary in some subjects to translate the OCT imager forward towards the subject to obtain the desired gaze eccentricity due to mechanical limitation of the scanner pivot and the subject's facial anatomy. This forward translation of the imaging module influenced image magnification, but this effect was that was later compensated during image processing.

B-Scan OCT

Enhanced depth imaging (EDI) was performed using the spectral-domain (SD)-OCT mode of the scanner to obtain views of the ONH and PPR. A retinal nerve fiber layer (RNFL) circular scan was performed to verify normal RNFL thickness in control subjects.

Image Analysis

En face images covering approximately 9x9mm of the posterior eye, centered on the optic nerve, were exported as TIFF files and processed using Adobe Photoshop (Adobe Systems, San Jose, CA, USA). In subjects who required translation of the OCT

imager, the varying magnifications of images acquired in central gaze, ab- and adduction were isotropically scaled to match the central gaze image size. To account for physiological ocular torsion that is the kinematic consequence of horizontal duction, images obtained in eccentric gazes were rotated and translated to superimpose BVs remote from the ONH with these corresponding fiducials in the central gaze image. This superimposition assumes absence of retinal deformation in regions remote from the disc. A grid with 4 concentric rings divided radially into 8 slices was superimposed over the *en face* images quantizing the retinal surface into 40 sections. The innermost circle enclosed the disc, with each successive concentric ring spanning 1 disc radius radially. Region 0 comprised the entire optic disc. Region 1 extended 1 disc radius beyond the disc margin, with each subsequent region incorporating an additional disc radius to a maximum of 3 radii. Figure 1 displays the arrangement of the 8 slices and 4 regions dividing the disc and PPR into 40 sections.

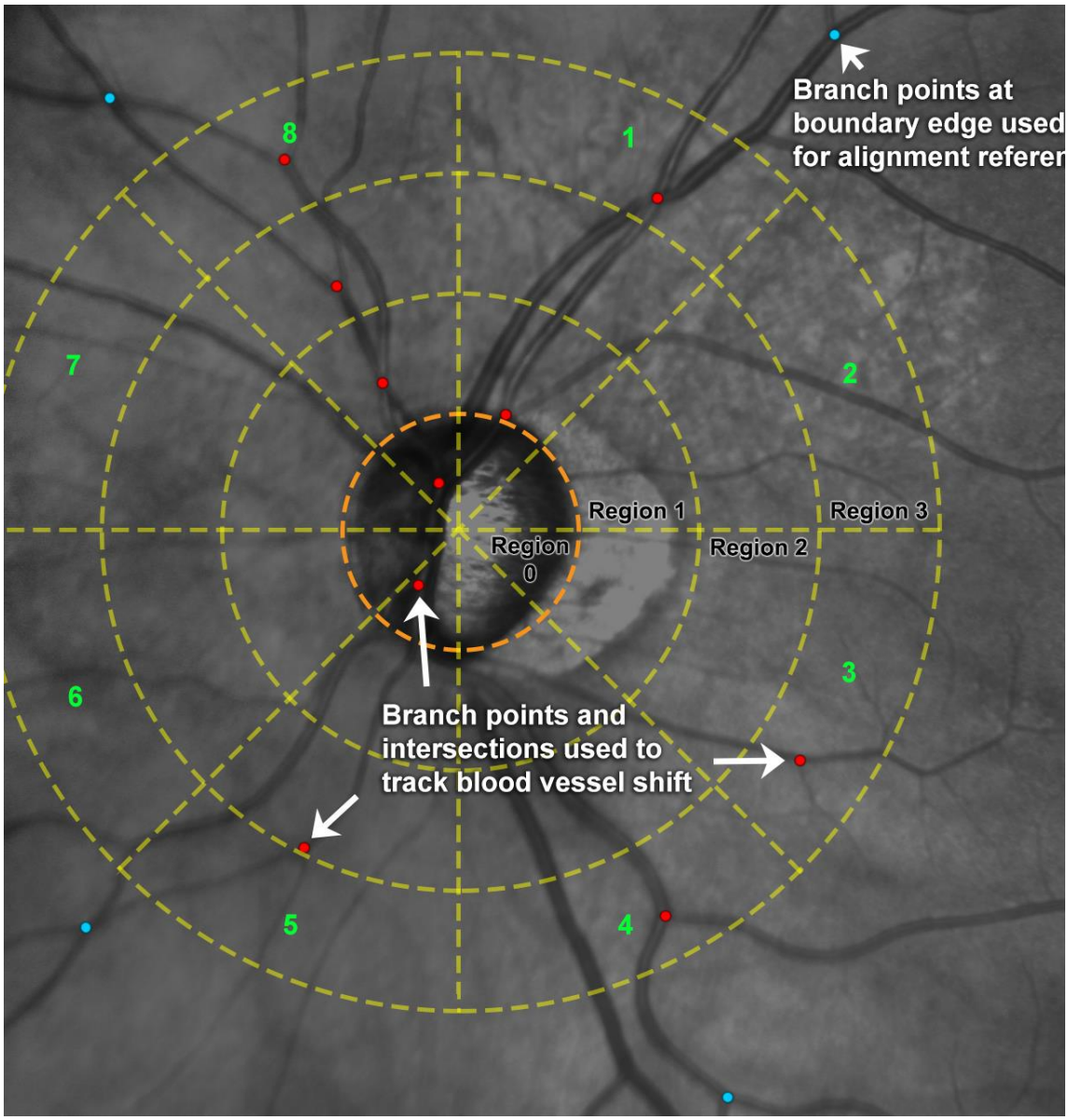

Figure 1. A circular grid divided the optic disc and peripapillary retina into 8 slices (labeled in green) and 4 regions. Region 0 is the disc (orange). Each region spanned 1 disc radius. Red dots mark identifiable blood vessel intersection and branch points. One dot was placed in each section where a fiducial feature was present. Fiducials remote to the disc at the boundary edges were used as anchor points (blue dots) to align images.

Since BVs are embedded in the underlying disc and retina, we used BV intersection and branching points as fiducial markers to track displacements resulting from eye movement. For each of the 40 sections in central gaze, a dot was marked on a

BV intersection or branch point if present, as shown in Figure 1. The fiducial points were tracked in eccentric gaze images.

Figure 2 shows *en face* images in central gaze (Fig. 2A) and adduction (Fig. 2C), magnified in Figs. 2B and 2D to show temporal displacement of fiducials in adduction. The program *ImageJ64* (W. Rasband, National Institutes of Health, Bethesda, Maryland, USA; http://rsb.info.nih.gov/ij/, 1997-2018, in public domain) was used to track the location of each fiducial, and custom MS Excel spreadsheets then calculated displacement vectors for each gaze position. Software written in the MATLAB (MathWorks, Inc, Natick, Massachusetts) software generated heatmaps summarizing displacements in ab- and adduction.

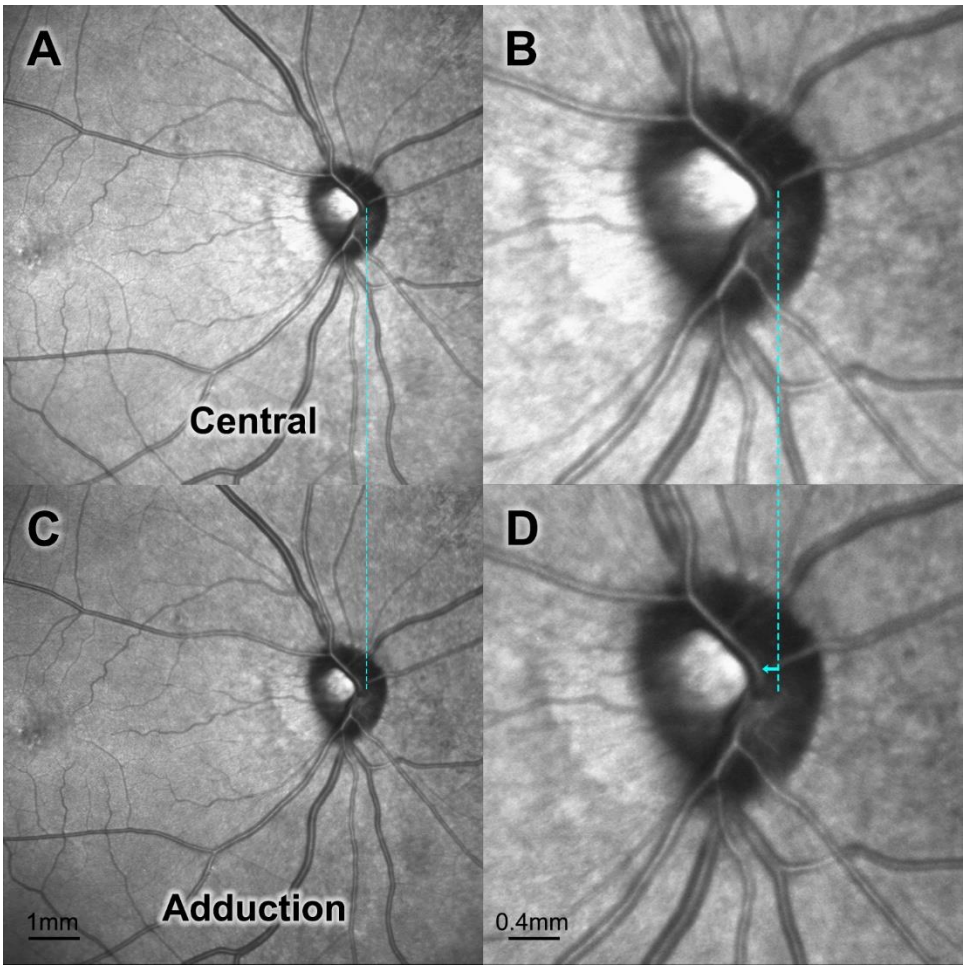

Figure 2. *En face* images of the ONH and PPR in central gaze (A) and adduction (C). BVs within the ONH shift temporally during adduction, denoted by the blue arrow overlaying magnified views of the ONH during central (B) and adduction (D).

Statistical Analysis

We used generalized estimating equations (GEE, IBM SPSS), which has type 1 error characteristics superior to t-testing for our samples,[10] to determine the statistical significance of displacements from eccentric gazes and compensate for possible inter-eye correlations within individual subjects. In multivariate analyses, we compared regions, nasal and temporal halves, and between normal and POAG groups.

2.4.4 Results

Horizontal Displacements

Displacements of disc and peripapillary fiducials can be represented as vectors whose tails are positions in central gaze, and heads are positions of the same fiducials in eccentric gaze. The length of each vector represents the distance of the displacement in the direction of the vector. Figure 3 is a composite displacement of all such vectors from 15 control subjects in adduction, showing the majority of displacements, and the largest ones, were within the ONH and particularly in its nasal half. Most displacement vectors were directed temporally, although some were circumferentially tangent to the disc with an overall flow from the nasal to the temporal side.

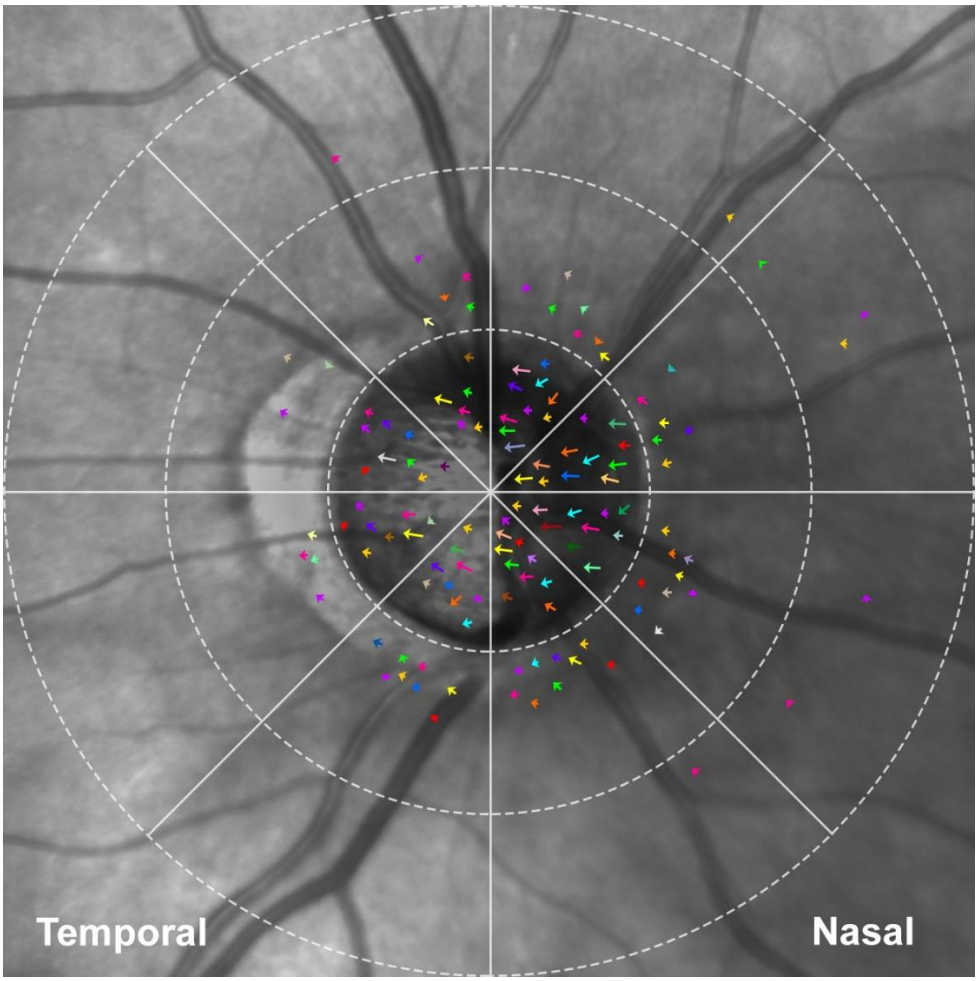

Figure 3. Composite of all displacement vectors for adduction in 15 control subjects (each labeled a different color). The majority of larger displacements were within the nasal disc.

Fiducial displacements in adduction by control subjects were only in the temporal direction and statistically significant only within the disc, not in the PPR. Significant deformation in the disc was evident in 5 of 8 slices (Figs. 4 and 5), particularly in the nasal half (Slices 1-4) of the disc, which was displaced significantly more temporally (averaging 19.9 µm displacement) than in the temporal half (Slices 5-8) where only one slice had significant shifts ($P<0.001$).

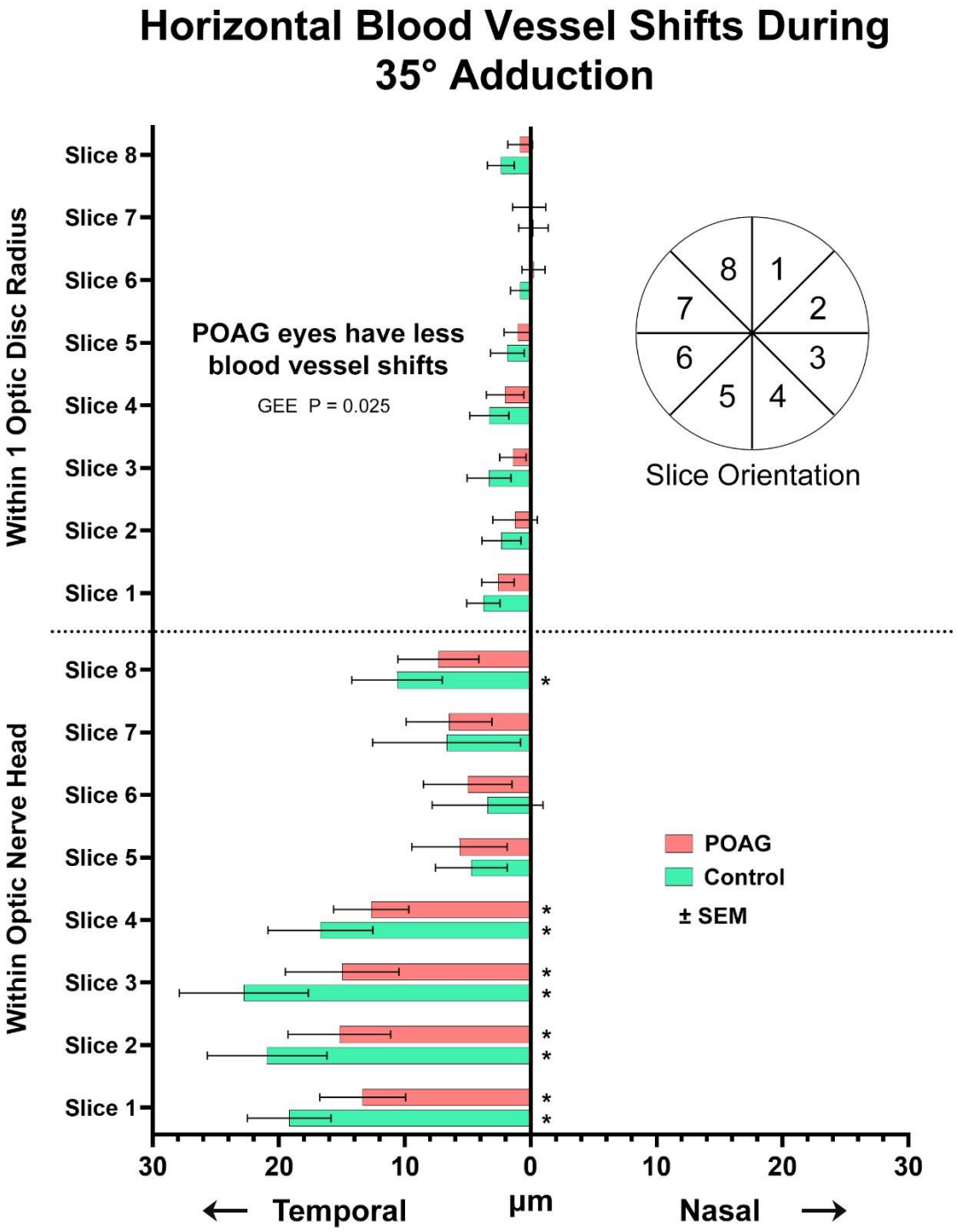

Figure 4. Horizontal blood vessel displacements in control subjects and subjects with POAG from central gaze to 35° adduction. The nasal half (Slices 1-4) of the disc exhibited more temporal shift than the temporal half (Slices 5-8) in both groups (P <0.002). There were no significant displacements outside of the disc. Generalized estimating equations showed that controls had greater displacements than subjects with POAG (P=0.025).

Subjects with POAG experienced less deformation in adduction than in age-matched controls (P=0.025, Figs. 4, 5, and 6). Significant deformation was present in 4 of 8 slices in these subjects. The nasal disc exhibited displacement ranging from 15.2±4.1 µm to 12.6±2.9 µm temporally, while the temporal half exhibited no significant displacement.

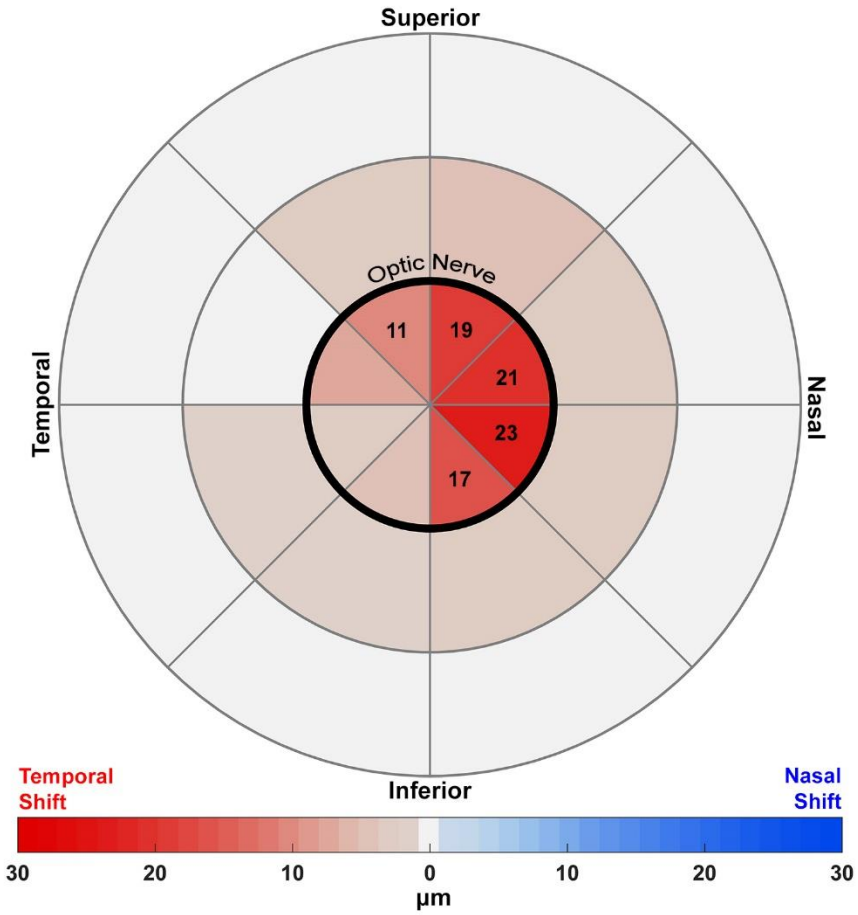

Figure 5. Horizontal displacement heatmap of control subjects from central gaze to 35° adduction. Numbers indicate sector with significant deformations. Most deformations occurred in the nasal disc.

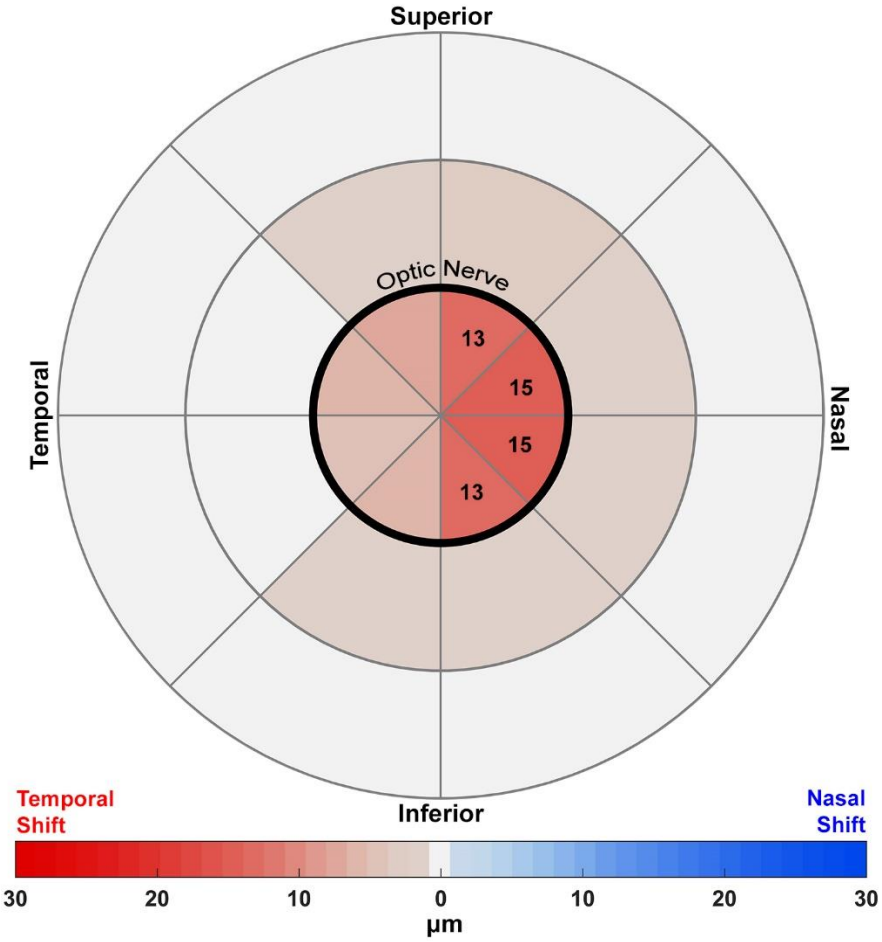

Figure 6. Horizontal displacements heatmap of subjects with POAG from central gaze to 35° adduction. Numbers indicate sectors with significant deformations, which were present in the nasal half of the disc.

There were no significant displacements of BVs during abduction in subjects with POAG or controls (Fig. 7).

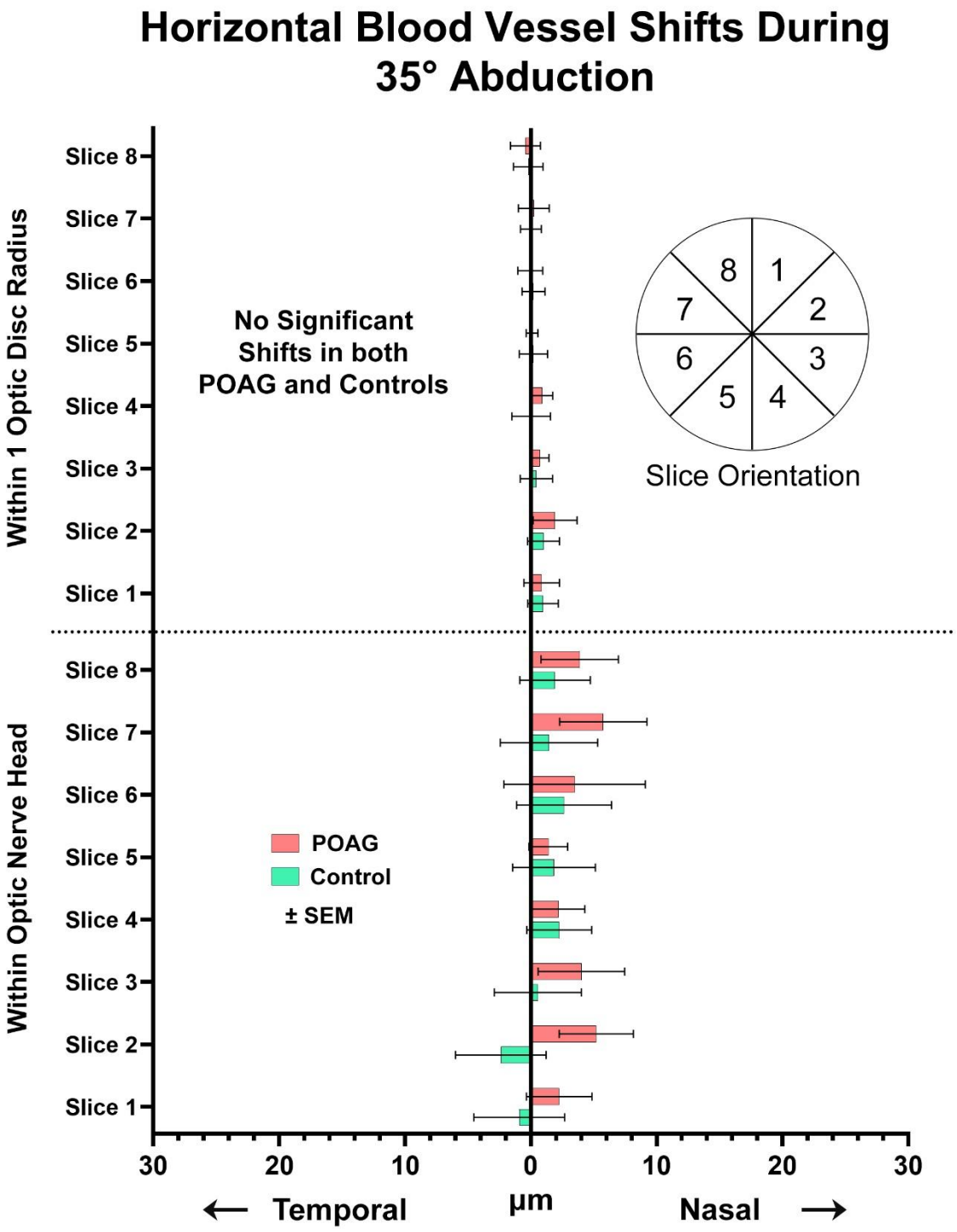

Figure 7. Horizontal blood vessel displacements in POAG and control subjects from central gaze to 35° abduction. There were no significant displacements in either group.

Vertical Displacements

There were no significant vertical displacements of fiducials during horizontal ductions in either the POAG or control groups (P=0.48 and P=0.37, respectively).

2.4.5 Discussion

Consistent with previous OCT[1, 3] and MRI observations,[2, 11] we observed greater mechanical deformation of the optic disc and peripapillary region during 35° adduction than abduction. This was the case in both normal subjects and in patients with POAG, both of whom were similarly aged in the early to mid-60 years. The nasal half of the optic disc, and to a lesser extent the adjacent PPR, shifted temporally during adduction. Since the temporal half of the disc underwent little or no temporal displacement, this implies compression of the nasal half of the optic disc against the temporal hemidisc. A similar pattern, albeit of larger magnitude, is evident in normal younger adults in the second or third decade of life.[12] This finding is consistent with adduction tethering of the ON, which becomes taut and restrains the posterior sclera during large adduction.[11] During adduction tethering, the contracting medial rectus muscle compresses the sclera posterior to its insertion, forcing the sclera against the restraining optic nerve and compressing the scleral canal and lamina cribrosa through which the optic nerve axons pass. This mechanical behavior has been quantitatively simulated using the engineering technique of finite element analysis.[13] In contrast, 35° abduction does not tether the ON, consistent with the current finding that abduction does not deform the disc or PPR in either group.

Patients with POAG exhibited significantly less average deformation within the disc than did normal control subjects. The nasal side half of the disc shifted an average

of 14 µm temporally in POAG, but 19.9 µm in controls, without deformation in the temporal half. The lesser disc deformation in adduction in POAG suggests that the disc and peripapillary tissues may be mechanically stiffer than those of normal controls. Stiffening could be due to tissue remodeling in POAG, similar to the way age-related stiffening is presumed to result in less such deformation during adduction in older subjects.[12] Many studies have suggested that ocular tissue stiffens with increasing age.[14-18] A plethora of evidence implicates age-related stiffening of sclera,[16, 19-22] lamina cribrosa,[23-25] trabecular meshwork,[26, 27] Bruch's membrane,[28] cornea,[29] vascular tissues,[30] extracellular matrix of the optic disc,[31] and collagen fibers generally.[32] Analogous to "hardening of the arteries" in arteriosclerosis, stiffening of the disc and peripapillary tissues could be a factor contributing to glaucomatous optic neuropathy, and explain in part why glaucoma is increasingly prevalent with age.[16] Tissue remodeling that increases overall ocular stiffness could increase susceptibility to glaucomatous damage,[18] for example by decreasing ocular compliance to changes in IOP due to vascular pulsations. Fazio *et al*. have suggested that peripapillary scleral stiffening could account for higher glaucoma prevalence in the elderly and people of African descent.[22] While stiffer tissue properties help resist mechanical deformation in the stiffened tissue itself, the force exerted by a tethered optic nerve in adduction must inevitably be dissipated by some combination of deformation or displacement of other ocular tissues. It is possible that stiffer disc and peripapillary tissues in glaucoma might shift the mechanical stress and strain resulting from adduction tethering to more vulnerable sites such as retrolaminar ON axon bundles, BVs, or lamina cribrosa beams. Other studies have investigated changes to ocular tissue during glaucoma progression and found loss of fiber-forming collagen types,[33, 34] and decline and disorganization of elastin content during ECM remodeling.[35, 36] Injury to the ONH can initiate fibrosis that would further

stiffen the tissue. Repetitive mechanical strain from adductions accumulated over many years might thus induce detrimental remodeling of the optic disc, making it more susceptible to the mechanical effects of both IOP and further cycles of adduction.

Alternatively, the stiffer disc and peripapillary region might merely be a biomarker of previous glaucomatous damage, which is known to induce an increase in type-IV collagen in areas affected by retinal ganglion cells loss.[37, 38] As the axon nerve fibers die during the progression of glaucoma, they are replaced by stiffer fibrotic tissue. A stiffer optic disc in POAG may explain the decreased deformation observed here in adduction. Thus, reduced disc deformation in adduction might be considered to represent either a risk factor for development of glaucomatous optic neuropathy, an indicator that damage has occurred, or perhaps both.

This study was limited by the relatively small number of participating subjects. Study conclusions are limited to patients with POAG who had never experienced statistically abnormally elevated IOP, since patients with secondary glaucoma and elevated IOP were excluded. Deformations reported here were indicated by displacement of intrinsic anatomical fiducials that were not uniformly distributed throughout the disc and PPR, and not identically distributed in all subjects. As a result, deformations in anatomic regions sparse in fiducial features might have gone undetected.

In conclusion, large adduction by healthy subjects forces the nasal optic disc and peripapillary tissues temporally, compressing the optic disc. This disc deformation, which is mechanically explainable by tethering of the ON in adduction, is significantly subnormal in patients with POAG who have never experienced elevated IOP. Reduced disc and peripapillary deformation in adduction suggest that the disc and peripapillary

tissues become stiffened in POAG despite the absence of statistically abnormal IOP. Peripapillary deformation in adduction, detectable using widely-available clinical ophthalmic imaging equipment, may represent a risk factor or biomarker for glaucomatous optic neuropathy.

2.4.6 References

1. Suh SY, Le A, Shin A, et al. Progressive deformation of the optic nerve head and peripapillary structures by graded horizontal duction. Invest Ophthalmol Vis Sci 2017;58(12):5015-21.

2. Demer JL, Clark RA, Suh SY, et al. Magnetic resonance imaging of optic nerve traction during adduction in primary open-angle glaucoma with normal intraocular pressure. Invest Ophthalmol Vis Sci 2017;58(10):4114-25.

3. Chang MY, Shin A, Park J, et al. Deformation of optic nerve head and peripapillary tissues by horizontal duction. Am J Ophthalmol 2017;174:85-94.

4. Sibony PA, Hou W. Adduction-induced deformations evoke peripapillary folds in papilledema. Ophthalmology 2019;126(6):912-4.

5. Quigley HA, Broman AT. The number of people with glaucoma worldwide in 2010 and 2020. Br J Ophthalmol 2006;90(3):262-7.

6. Demer JL. Optic nerve sheath as a novel mechanical load on the globe in ocular duction. Invest Ophthalmol Vis Sci 2016;57(4):1826-38.

7. Wang X, Fisher LK, Milea D, et al. Predictions of optic nerve traction forces and peripapillary tissue stresses following horizontal eye movements. Invest Ophthalmol Vis Sci 2017;58(4):2044-53.

8. Shin A, Yoo L, Park C, Demer JL. Finite element biomechanics of optic nerve sheath traction in adduction. J Biomech Eng 2017;139(10).

9. Wang X, Beotra MR, Tun TA, et al. In vivo 3-dimensional strain mapping confirms large optic nerve head deformations following horizontal eye movements. Invest Ophthalmol Vis Sci 2016;57(13):5825-33.

10. Huang J, Huang J, Chen Y, Ying GS. Evaluation of approaches to analyzing continuous correlated eye data when sample size is small. Ophthalmic Epidemiol 2018;25(1):45-54.

11. Demer JL. Optic nerve sheath as a novel mechanical load on the globe in ocular ductionoptic nerve sheath constrains duction. Investigative Ophthalmology & Visual Science 2016;57(4):1826-38.

12. Le A, Chen J, Lesgart M, et al. Age-dependent deformation of the optic nerve head and peripapillary retina by horizontal duction. American Journal of Ophthalmology 2019.

13. Shin A, Yoo L, Park J, Demer JL. Finite element biomechanics of optic nerve sheath traction in adduction. J Biomech Eng 2017;139(10).

14. Albon J, Karwatowski WS, Easty DL, et al. Age related changes in the non-collagenous components of the extracellular matrix of the human lamina cribrosa. Br J Ophthalmol 2000;84(3):311-7.

15. Kida T, Liu JH, Weinreb RN. Effects of aging on corneal biomechanical properties and their impact on 24-hour measurement of intraocular pressure. Am J Ophthalmol 2008;146(4):567-72.

16. Coudrillier B, Tian J, Alexander S, et al. Biomechanics of the human posterior sclera: Age- and glaucoma-related changes measured using inflation testing. Invest Ophthalmol Vis Sci 2012;53(4):1714-28.

17. Leung LK, Ko MW, Lam DC. Effect of age-stiffening tissues and intraocular pressure on optic nerve damages. Mol Cell Biomech 2012;9(2):157-73.

18. Liu B, McNally S, Kilpatrick JI, et al. Aging and ocular tissue stiffness in glaucoma. Surv Ophthalmol 2018;63(1):56-74.

19. Brown CT, Vural M, Johnson M, Trinkaus-Randall V. Age-related changes of scleral hydration and sulfated glycosaminoglycans. Mech Ageing Dev 1994;77(2):97-107.

20. Avetisov ES, Savitskaya NF, Vinetskaya MI, Iomdina EN. A study of biochemical and biomechanical qualities of normal and myopic eye sclera in humans of different age groups. Metab Pediatr Syst Ophthalmol 1983;7(4):183-8.

21. Coudrillier B, Pijanka J, Jefferys J, et al. Effects of age and diabetes on scleral stiffness. J Biomech Eng 2015;137(7).

22. Fazio MA, Grytz R, Morris JS, et al. Human scleral structural stiffness increases more rapidly with age in donors of african descent compared to donors of european descent. Invest Ophthalmol Vis Sci 2014;55(11):7189-98.

23. Morrison JC, Jerdan JA, Dorman ME, Quigley HA. Structural proteins of the neonatal and adult lamina cribrosa. Arch Ophthalmol 1989;107(8):1220-4.

24. Albon J, Karwatowski WS, Avery N, et al. Changes in the collagenous matrix of the aging human lamina cribrosa. Br J Ophthalmol 1995;79(4):368-75.

25. Albon J, Purslow PP, Karwatowski WS, Easty DL. Age related compliance of the lamina cribrosa in human eyes. Br J Ophthalmol 2000;84(3):318-23.

26. Tektas OY, Lutjen-Drecoll E. Structural changes of the trabecular meshwork in different kinds of glaucoma. Exp Eye Res 2009;88(4):769-75.

27. Pattabiraman PP, Rao PV. Mechanistic basis of rho gtpase-induced extracellular matrix synthesis in trabecular meshwork cells. Am J Physiol Cell Physiol 2010;298(3):C749-63.

28. Booij JC, Baas DC, Beisekeeva J, et al. The dynamic nature of bruch's membrane. Prog Retin Eye Res 2010;29(1):1-18.

29. Malik NS, Moss SJ, Ahmed N, et al. Ageing of the human corneal stroma: Structural and biochemical changes. Biochim Biophys Acta 1992;1138(3):222-8.

30. Kohn JC, Lampi MC, Reinhart-King CA. Age-related vascular stiffening: Causes and consequences. Front Genet 2015;6:112.

31. Hernandez MR, Luo XX, Andrzejewska W, Neufeld AH. Age-related changes in the extracellular matrix of the human optic nerve head. Am J Ophthalmol 1989;107(5):476-84.

32. Bailey AJ, Paul RG, Knott L. Mechanisms of maturation and ageing of collagen. Mech Ageing Dev 1998;106(1-2):1-56.

33. Quigley HA, Brown A, Dorman-Pease ME. Alterations in elastin of the optic nerve head in human and experimental glaucoma. Br J Ophthalmol 1991;75(9):552-7.

34. Hernandez MR. Ultrastructural immunocytochemical analysis of elastin in the human lamina cribrosa. Changes in elastic fibers in primary open-angle glaucoma. Invest Ophthalmol Vis Sci 1992;33(10):2891-903.

35. Hernandez MR, Andrzejewska WM, Neufeld AH. Changes in the extracellular matrix of the human optic nerve head in primary open-angle glaucoma. Am J Ophthalmol 1990;109(2):180-8.

36. Quigley HA, Dorman-Pease ME, Brown AE. Quantitative study of collagen and elastin of the optic nerve head and sclera in human and experimental monkey glaucoma. Curr Eye Res 1991;10(9):877-88.

37. Fukuchi T, Sawaguchi S, Hara H, et al. Extracellular matrix changes of the optic nerve lamina cribrosa in monkey eyes with experimentally chronic glaucoma. Graefes Arch Clin Exp Ophthalmol 1992;230(5):421-7.

38. Morrison JC, Dorman-Pease ME, Dunkelberger GR, Quigley HA. Optic nerve head extracellular matrix in primary optic atrophy and experimental glaucoma. Arch Ophthalmol 1990;108(7):1020-4.

2.5 Peripapillary Atrophy and Optic Disc Stiffening in Primary Open Angle Glaucoma at Normal Intraocular Pressure

Alan Le[1-3], Jessica Y. Chen[4], Joseph Caprioli[1,2], JoAnn A. Giaconi[1,2],

Kouros Nouri-Mahdavi[1,2], Simon K. Law[1,2], Laura Bonelli[1,2],

Anne L. Coleman[1,2], and Joseph L. Demer[1,2,3,5,6]

[1]Department of Ophthalmology and [2]Stein Eye Institute, [3]Bioengineering Interdepartmental Programs, [4]Computational and Systems Biology Interdepartmental Program, [5]Department of Neurology, [6]David Geffen Medical School at the University of California, Los Angeles.

2.5.1 Abstract

Purpose: We investigated, as a biomarker of optic disc mechanical stiffness, the relationship between adduction-induced disc deformations and β-zone peripapillary atrophy (PPA) in patients who have primary open angle glaucoma (POAG) with normal intraocular pressure (IOP).

Materials and Methods: We studied both eyes of 23 patients with POAG (mean age 65±13 (standard deviation, SD) years in whom IOP never measured to exceed the normal range of up to 21 mmHg, and 19 age-matched normal subjects (age 62±9 years). The optic disc and peripapillary retina were imaged using infrared scanning laser ophthalmoscopy in both central gaze, and 35° adduction. Deformations of the optic disc and peripapillary retina, and location and extent of PPA were evaluated.

Results: During adduction, the nasal side of the optic disc was less compressed in the temporal direction in patients with POAG than in controls ($P<0.001$). In POAG, the β–zone PPA extended an average of one-half disc radius from the disc margin, and was most common in the inferotemporal quadrant where it was present in 71% of eyes; PPA was present in only 13% of controls. PPA was typically located opposite the disc region exhibiting the largest deformation during adduction, and its extent was inverse to the magnitude of disc deformation ($P<0.001$).

Conclusions: The lesser optic disc deformation during large angle adduction in patients with POAG may have potential as a clinically practical biomarker for pathological stiffening of disc and peripapillary tissues associated with glaucomatous optic neuropathy.

2.5.2 Introduction

Biomarkers for glaucoma risk are of vital importance to this disorder that is the world's leading cause of irreversible blindness[1]. While abnormally high intraocular pressure (IOP) was once considered a reliable biomarker and even an etiologic mechanism, and IOP remains the only known modifiable risk factor, it is now neither considered the cause of primary open angle glaucoma (POAG) and nor regarded as an essential diagnostic criterion. Glaucomatous damage may progress even with low normal IOP. For example, over five years follow-up, two thirds of Japanese patients with untreated IOP that remained an average of 12 mmHg and had normal diastolic blood pressure nevertheless suffered progressive glaucomatous optic neuropathy[2], as did 25% of myopic Korean patients who maintained 15 mmHg average IOP[3].

While untreated IOP has not proven a reliable predictor of glaucoma progression, there are suggestions that peripapillary atrophy (PPA) may be associated with progression of glaucomatous visual field loss[4-6]. By convention, PPA has been partitioned into α and β-zones, with the α-zone characterized by irregular retinal pigment epithelium pigmentation more peripherally, and the β-zone characterized by marked atrophy of the retinal pigment epithelium and choriocapillaris revealing the sclera more proximally to the optic disc[7, 8]. Multiple studies have noted that extent and prevalence of β-zone atrophy is associated with progressive glaucoma stages[5, 7-13]. In POAG without elevated IOP, the area of PPA is positively associated with greater visual defects and optic nerve damage[5, 6]. The β-zone PPA atrophy demonstrable in confocal scanning laser ophthalmoscope (cSLO) images corresponds to that observed in cross-sectional optical coherence tomography (OCT) B-scans[14]. Remarkably in light of the widespread prevalence and numerous observations concerning clinical associations of PPA, there is almost no theory or even speculation as to its etiology.

During adduction exceeding a threshold of 26º, the peripapillary retina (PPR) and the optic nerve head (ONH) undergo especially great deformation[15, 16]. Suh *et al*. used OCT to demonstrate that these tissues deform as the optic disc tilts temporally and the temporal edge of Bruch's membrane opening is displaced anteroposteriorly during adduction[15]. Even moderate angles of ad- and abduction can induce strains in the lamina cribrosa and ONH[17], and that deformation in peripapillary Bruch's membrane occurs even without an extreme adduction angle[18]. Confocal scanning laser ophthalmoscope (cSLO) imaging that uses infrared illumination without need for tomographic reconstruction also demonstrates significant deformation of the PPR and disc during large adduction, particularly in younger adults[19]. Mechanical stress on the disc and peripapillary tissues during adduction may therefore be considered a physiological perturbation during normal eye movement.

Post-mortem studies have demonstrated that peripapillary tissues stiffen with advancing age. Younger people generally have more elastic peripapillary tissues, including Bruch's membrane[20], the lamina cribrosa[21, 22], and sclera[23, 24]. Calcification of elastin and increased cross-linked collagen in Bruch's membrane are both progressive with age[20]. Mechanical compliance of the lamina cribrosa declines with age[22], so that older sclera is stiffer than younger adult sclera[23]. Optical imaging has been consistent with these in vitro biomechanical findings insofar as younger subjects exhibit more disc and peripapillary deformation during adduction than older subjects[19]. The optic disc and peripapillary tissues also stiffen in glaucoma[25, 26].

In order to clarify the pathogenesis of glaucoma, it would be desirable to have biomarkers for the mechanical properties of the disc and peripapillary tissues. Short of inducing substantial IOP elevation[27], it has heretofore been impractical to deliver a mechanical perturbation allowing assessment of the stiffness of the disc and

peripapillary tissues in vivo. The present study sought to exploit the mechanical effect of optic nerve traction in adduction as a physiologic source of tissue strain to probe stiffness of the ON and peripapillary tissues in vivo. In doing so, we considered the significance of this deformation in relationship to the topography and extent of β-zone PPA in patients with POAG.

2.5.3 Methods

Prior to participation, all subjects gave written, informed consent according to a protocol approved by the Institutional Review Board of the University of California, Los Angeles, and conforming to the tenets of the Declaration of Helsinki. From a multi-physician academic glaucoma practice, 23 patients with POAG (13 males, 10 females) of mean age 65 (13 standard deviation, SD, range 27-83) years were recruited who had been diagnosed with POAG based upon the following inclusion criteria: ophthalmoscopic examinations, disc photography, and OCT evidence of disc and nerve fiber layer features that correlated with typical glaucomatous visual field defects on Humphry automated perimetry; and applanation IOP never measured to exceed 21 mmHg, with or without treatment, on multiple clinical examinations. Patients were excluded if they had previously undergone ocular surgeries besides those for cataract, glaucoma, refractive error, or if they had cause for optic neuropathy or visual field defects besides glaucoma. Patients with POAG had average refractive error of -2.78±3.37 D, range -9.00 to +2.00 D.

By advertising we also recruited 19 normal controls (8 men, 11 women) of similar mean age 62±9 (range 52-79) years. Normal subjects underwent comprehensive eye examinations to confirm normal corrected visual acuity, normal binocular alignment, and

normal IOP (<21mmHg) without evidence of glaucomatous optic neuropathy. Average refractive error in the control group was -1.71±1.87 D, range -4.75 to +2.75 D and not significantly different from that of POAG (P=0.09).

Infrared images of the optic disc and PPR were acquired with the cSLO mode of a Spectralis scanner (Heidelberg Engineering, Heidelberg, Germany). Each eye was imaged in central gaze and 35° adduction while the subject's head was fixed to the headrest frame using cushions and straps to avoid head rotation. The imaging camera was rotated on its azimuth pivot to 35° adduction as marked by an affixed goniometric scale. The subject fixated the internal target that was offset 12° nasally from straight-ahead in order to center the image on the optic disc. This 12° nasal shift of the target was incorporated into the goniometric calibration. Due to limitation on the range of elevation of the Spectralis scanner, imaging was only performed straight ahead and during horizontal duction.

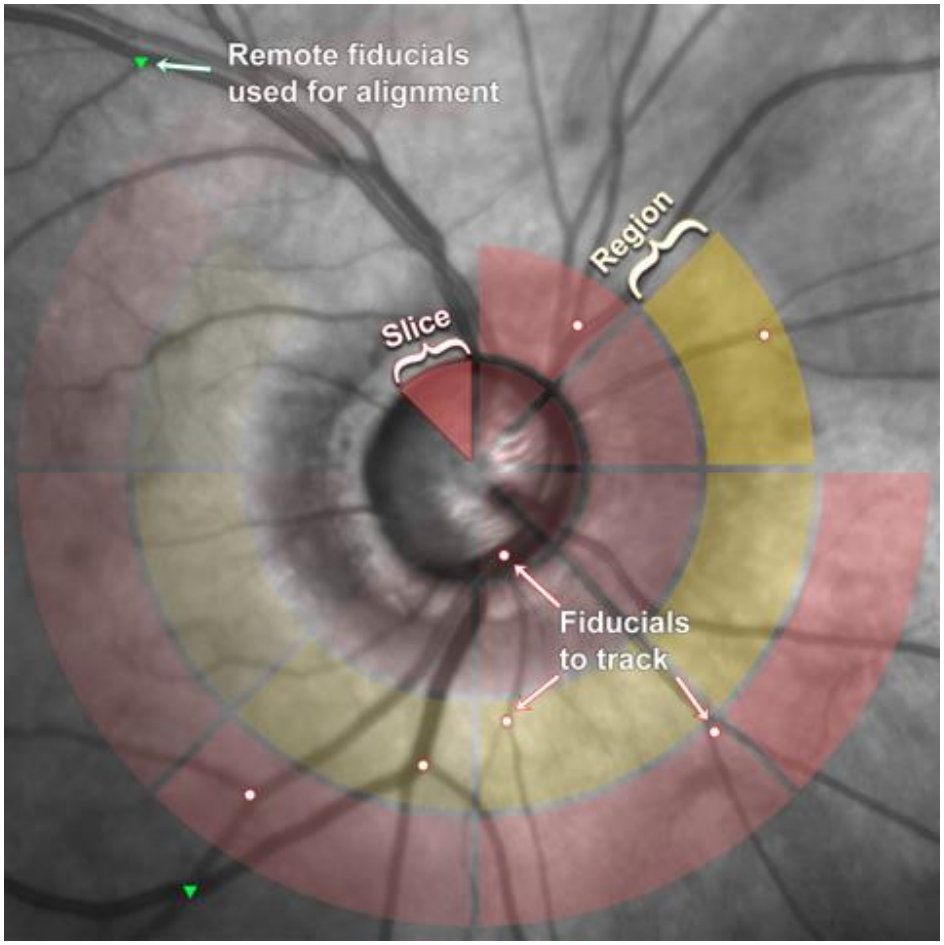

Figure 1. Scanning laser ophthalmoscopy image of right eye of a representative patient with POAG. For analysis, images were divided into 4 concentric regions and 8 slices.

Enhanced depth imaging was performed using the spectral-domain, B-scan OCT mode of the scanner to obtain views of the ONH and PPR. A retinal nerve fiber layer (RNFL) circular scan was performed to verify normal RNFL thickness for control subjects.

Images obtained by cSLO were exported from the scanner in tagged image file format (TIFF). As described in detail elsewhere, prominent blood vessel (BV) bifurcations and intersections were used as trackable fiducials that corresponded to retina surface deformation[19]. Using Adobe Photoshop (Adobe Systems, San Jose, CA,

USA), images obtained in eccentric gaze were rotated and translated to align remote fiducial points with corresponding features in central gaze images. This compensated for ocular torsion resulting from horizontal duction. Images were divided into 4 regions in each of three concentric rings surrounding an inner circle scaled to the size of the optic disc. Each region was divided into 8 slices to form a total of 32 different sections (Fig. 1). Any trackable fiducial feature that was present was tagged with a colored dot in both central and eccentric gaze images, and the differences in these locations represented as displacement vectors. Since trackable fiducials did not occur in every section, displacement magnitudes from each eye of each subject were pooled to generate a deformation map for that subject group. Significant deformation was only observed within the optic disc[19]. The disc was sectioned into 8 slices and deformation magnitudes in each slice were averaged for comparison with PPA.

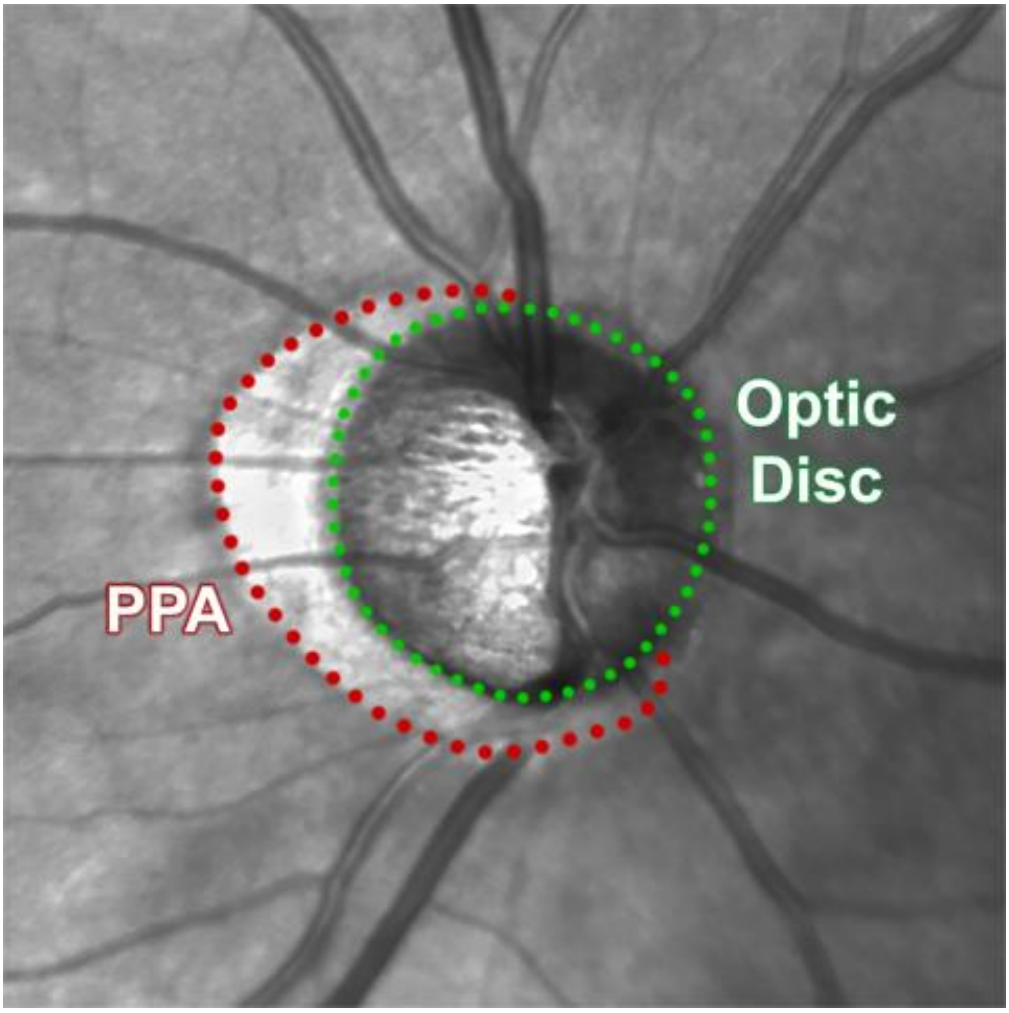

Figure 2. Optic disc margin (green) and β-zone of peripapillary atrophy (red) were manually demarcated.

Left eye images were digitally reflected to the orientation of right eyes for analysis. The optic disc and β-zone PPA were manually outlined by two independent observers, as shown in Fig. 2. The outlines were subdivided by a grid of 3 concentric rings, each spanning half an optic disc radius radially, and into circumferential 64 slices per ring for an overall total of 192 sections. Every section was surveyed occurrence of PPA, and averaged across all eyes in each subject group to generate heatmaps of PPA occurrence. The PPA extent from the optic disc margin was assessed along its entire

circumference by radially sampling 32 times at 11.25° intervals (Fig. 3). To compare PPA and adduction-induced deformation, the ratio of PPA area to optic disc area was used to normalize according for variations in optic disc size.

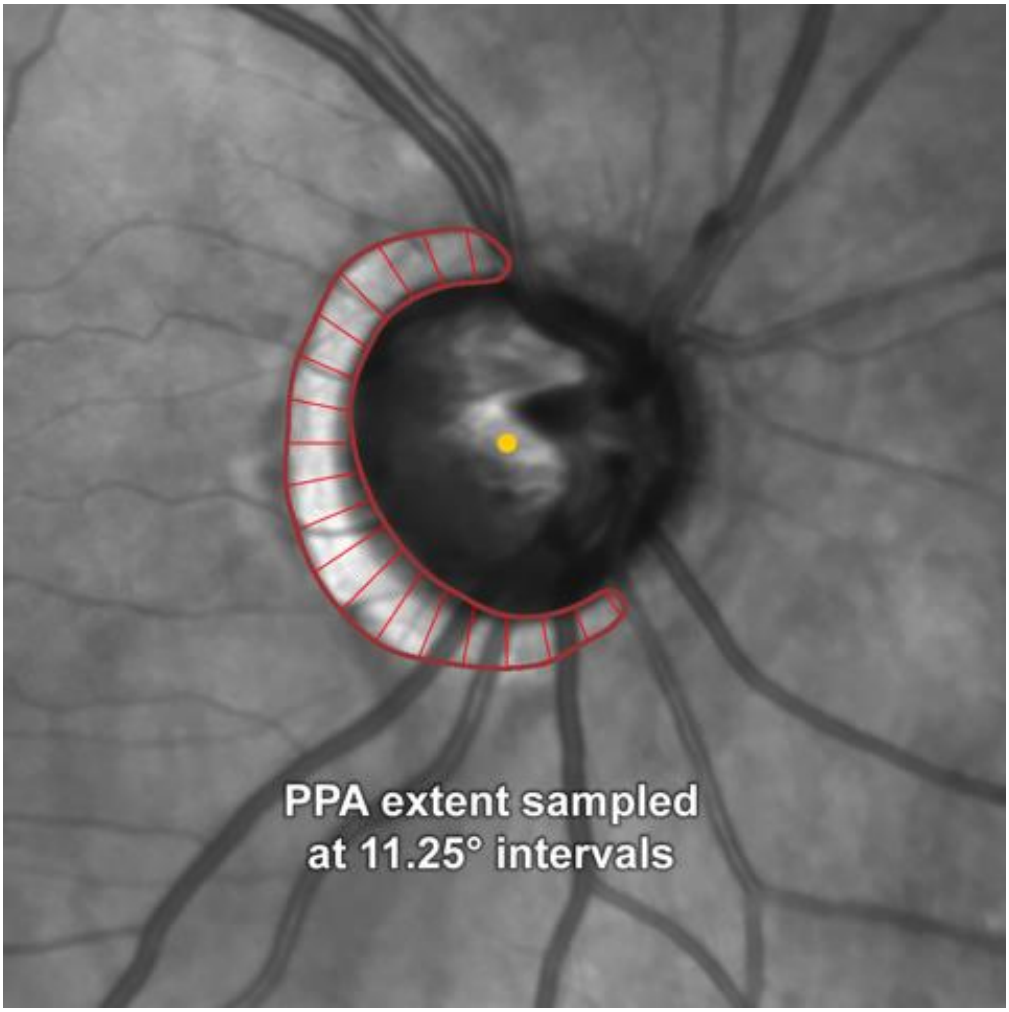

Figure 3. Extent of peripapillary atrophy from optic disc rim was measured 32 times at every 11.25° angle increment from the centroid of the optic disc (marked in yellow).

Data were analyzed using generalized estimating equations (GEE) implemented in SPSS software (Version 24.0; IBM Corp., Armonk, NY, USA), which has type 1 error characteristics superior to t-testing, to compensate for possible inter-eye correlations within individual subjects[28]. This enables valid statistical interpretation of both eyes of

each subject. Pearson's chi-square test was performed to determine significance of differences in frequency of PPA occurrence in each of 192 sections. Levels less than 0.05 were considered significant. Normalized PPA area was plotted against the magnitude of deformation and fitted with a two-phase decay curve.

2.5.4 Results

Deformation during Adduction.

Fiducial deformations were mainly within the nasal optic hemidisc for both control and POAG groups (Fig. 4), although there was less mean deformation in both hemidisc in subjects with POAG (22±14μm) than in controls (37±12μm, P=0.025). There were no significant deformations outside of the optic disc in either group.

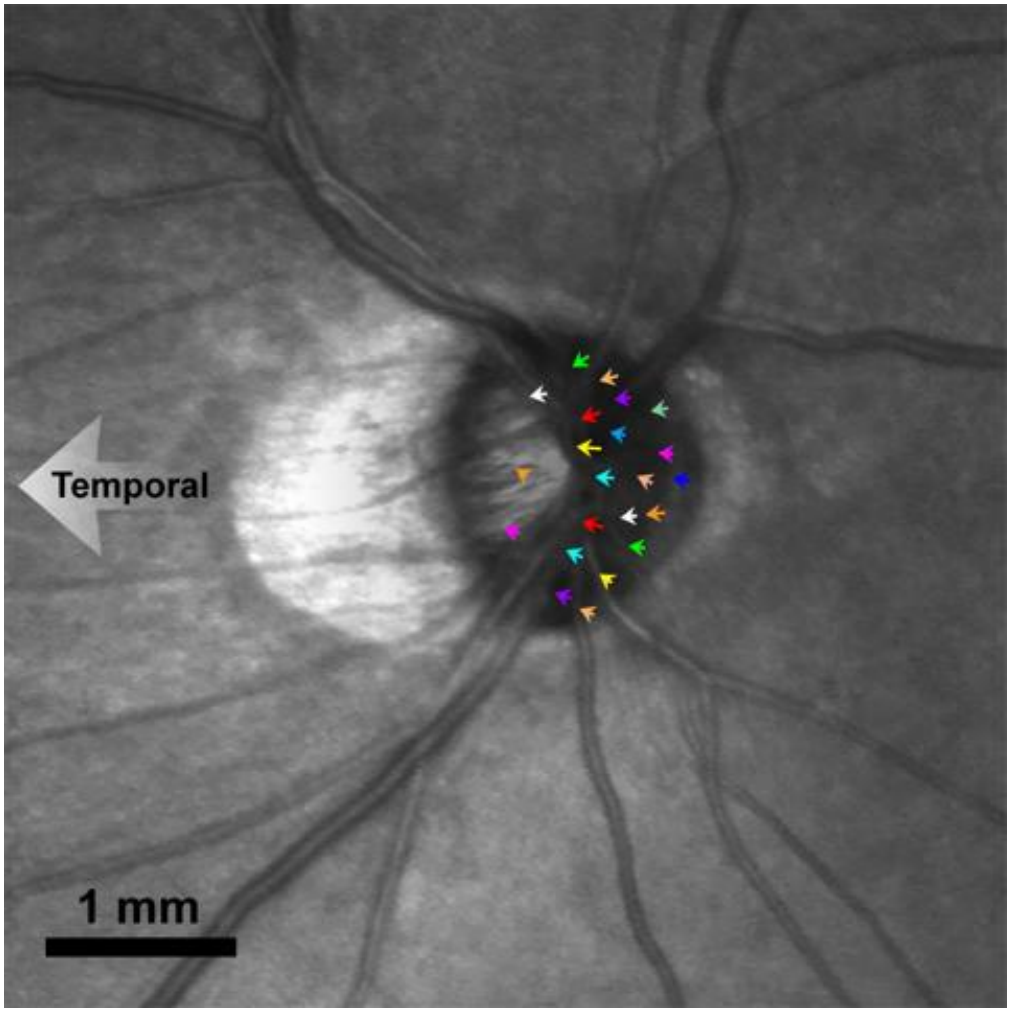

Figure 4. Pooled deformation vectors combined for multiple patients with primary open angle glaucoma. Displacements of fiducials in 35° adduction were significant only within the optic disc, mainly consisting of temporal shifts in its nasal half. Deformation vectors in age-matched controls were larger but in similar directions.

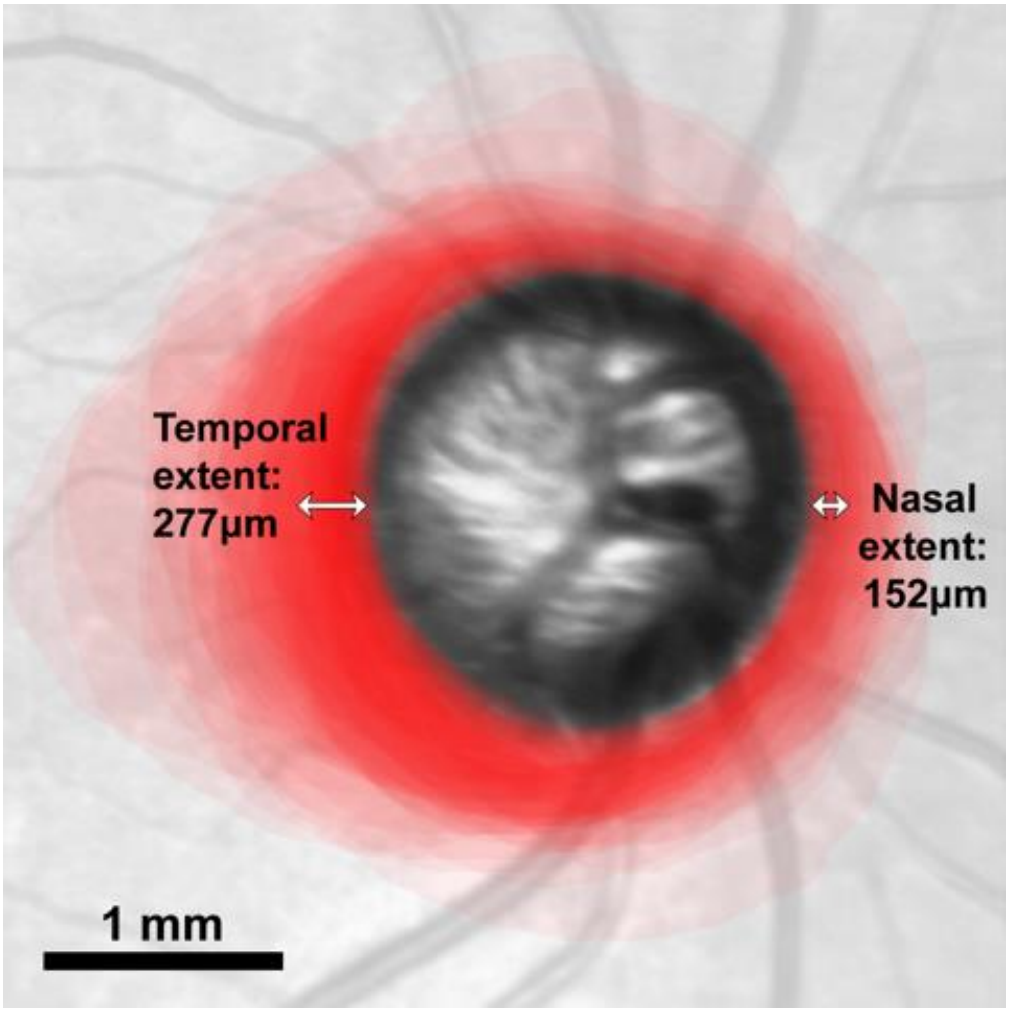

Figure 5. Outlines of β-zone peripapillary atrophy in all eyes of patients with primary open angle glaucoma have been normalized in size, and individually superimposed in red at 10% opacity on an example en face disc image. On average, the temporal margin of PPA extended 277µm from the disc rim, but 152µm nasally.

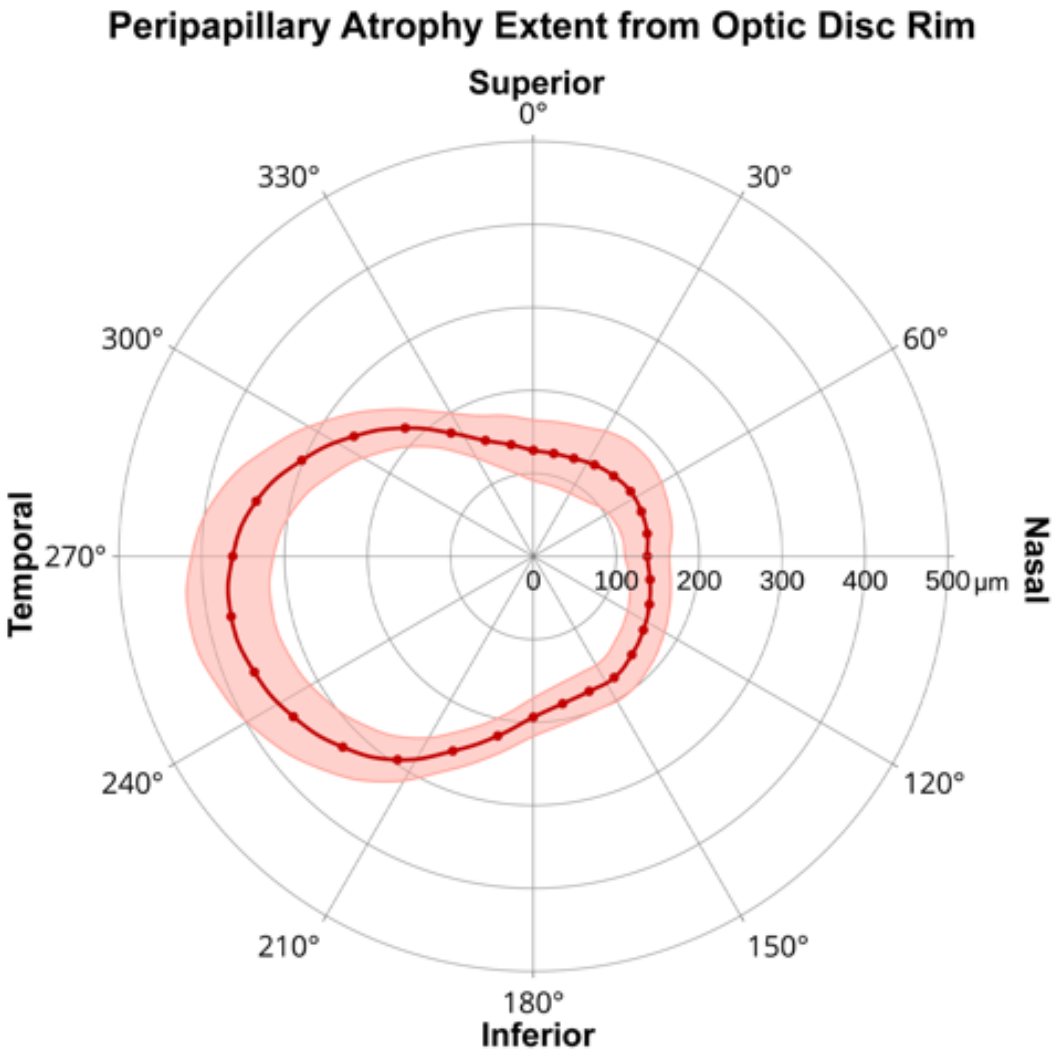

Figure 6. Polar plot of the radial extent of β-zone PPA in patients with POAG. Error bands indicate ± standard error of the mean.

Peripapillary Atrophy in POAG

The mean extent of PPA in patients with POAG was significantly greater at 277± 83µm on the temporal side than 152±20µm on the nasal side of the optic disc (P<0.01). This is illustrated in the color intensity map of PPA extent in Fig. 5 that pools results in all eyes of all patients with POAG and superimposes this on a representative *en face* disc image. Figure 6 is a polar plot of the average extent of PPA, showing a maximum located 258° clockwise from the superior pole, and thus on the slightly inferotemporal

side of the disc. The temporal side not only exhibited the greatest PPA extent, but is also the highest prevalence. Most PPA in subjects with POAG was confined to a half-disc radius of the disc margin. The most common site for PPA was the inferotemporal region, where it was present in 71% of eyes with POAG (χ^2 P<0.0001, Fig. 7A). Only 4 of 19 (16%) of control subjects had PPA, also most commonly in the temporal sections (Fig. 7B).

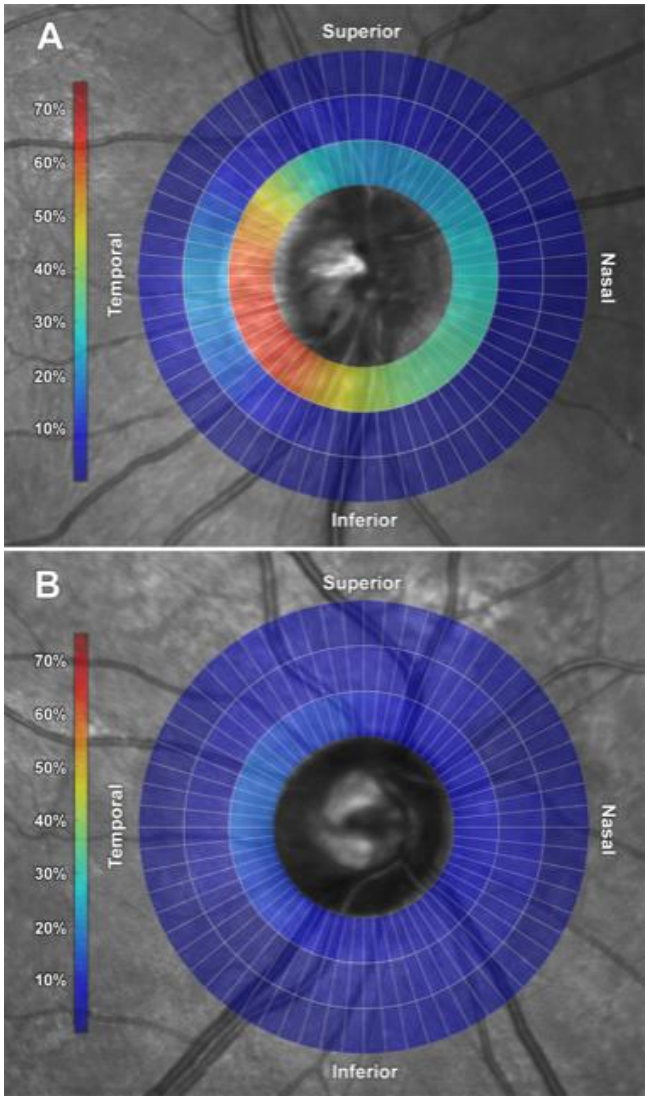

Figure 7. Heatmap of peripapillary atrophy prevalence. The peripapillary region was divided into 192 sections (3 concentric regions spanning half an optic disc radius, each divided into 64 slices). Color of each section represents prevalence in 48 eyes of patients with primary open angle glaucoma (A), and 42 eyes of controls (B).

There was a strong inverse correlation between the extent of normalized PPA and the magnitude of deformation in the optic disc during 35°adduction: eyes with more PPA had less deformation in both subject groups (GEE P<0.001, Fig. 8). On average, eyes with POAG having less than 10μm deformation in adduction had normalized PPA of 0.99±0.37 (SD) disc areas, while eyes with more than 30μm shifts in adduction had less PPA averaging only 0.16±0.15 disc areas (P<0.0001). Although only 5 control eyes exhibited any PPA, all but one of these exhibited less deformation than the remaining control subjects who had no PPA.

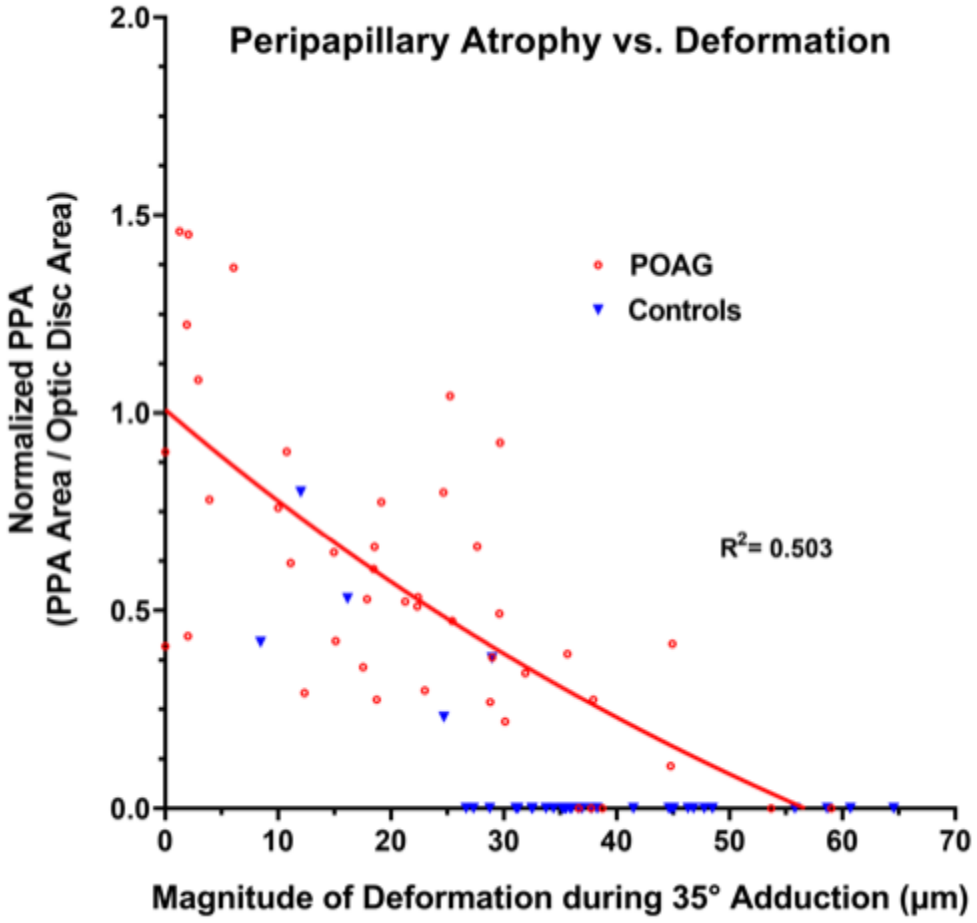

Figure 8. Peripapillary atrophy (PPA) area normalized to optic disc size was inversely correlated to deformation. Eyes with larger PPA had less deformation.

2.5.5 Discussion

The present study demonstrates a novel inverse correlation between extent of □-zone PPA, and optic disc deformation during large angle adduction that is known to exert mechanical stress on the disc by tethering the optic nerve. The threshold for adduction tethering has been established by OCT to be about 26° [15], and MRI has confirmed that the 35° adduction employed here tethers the optic nerves of both healthy subjects and patients with POAG, whether IOP has ever been elevated[29], or not been observed to have been elevated[30]. The current findings are consistent with our previous report showing marked displacement of retinal and optic nerve vascular fiducials during 35° adduction by both young and old healthy subjects, although deformation was greater in younger eyes[19]. It is thus highly likely that the deformations observed here during large adduction were due to ON tethering, and thus can serve as a mechanical perturbation for probing mechanical properties of the peripapillary tissues. The correlation between PPA and disc deformation was observed to be inverse in two different ways: first, PPA is most extensive on the temporal side of the disc, while deformation is most extensive in the nasal half of the disc. Second, the greater the disc deformation during adduction, the less probable and less extensive the PPA.

The current study used magnitude of fiducial displacement rather than previously-reported directional shifts[19] to assess the compliance of the optic disc and peripapillary sclera. Eyes with more PPA exhibited less deformation of fiducials in both POAG subjects and controls. Controls exhibited significantly less PPA than did subjects with POAG, as well as more overall deformation of the disc in adduction. Furthermore, PPA occurred predominantly at the nasal and temporal disc margins, not superior or inferior. Since ON tethering consistently occurs during adduction[30] but it is our impression that tethering is less during vertical duction, PPA may be particularly related

to horizontal duction. However, because it was not possible to study vertical duction here for technical reasons, this remains an open question.

Displacements of fiducials in cSLO images were measured under the assumption that fiducials remained within the imaging plane. Large tilts of any local retinal or optic nerve region out of the overall imaging plane would produce apparent position changes within the plane proportional to both the cosine of the tilt angle, and to the distance of the fiducial from the point at which the tilting originated. Using the same Spectralis OCT imager as employed in the current study but in the B-scan mode, Suh et al reported 2° mean optic disc tilt in the 35° adduction angle employed in the present study[15]. The cosine of 2° is approximately 0.06%. Under the worst-case assumption that the optic disc tilted at one nasal or temporal edge of a typical 1500 □m diameter disc, the projection error in horizontal position introduced by the tilt effect at the opposite side of the disc would be only 0.9 microns in young adult subjects. The tilt effect would at most be negligible in comparison with the much large in-plane deformations up to 65 □m illustrated in Fig. 8. It is therefore to be concluded that nearly all of the deformations reported here represent in-plane phenomena, and not artifacts of tilting of the tissue surface.

General stiffening of scleral tissue, either through age-related or artificial means, has been associated with glaucomatous damage[23, 31-35]. Kimball et al. found that stiffening the sclera by cross-linking exacerbates glaucoma damage in a mouse model[35]. Girard et al. reported that chronic IOP elevations stiffened the posterior sclera in a monkey glaucoma model[36]. In canine glaucoma, both control dogs and dogs having a mutation that exposed them to chronically high IOP had similar age-related posterior scleral stiffening[37]. While high IOP could be a cause of PPA in people who have IOP that is elevated above the statistically defined range measured in the healthy population, the

subjects with POAG included in the current study never had IOP exceeding that range, eliminating elevated IOP above the statistically normal range as a cause of tissue stiffening here. Stiffening of the cornea[38], Bruch's membrane[20], lamina cribrosa[21, 39, 40], and optic nerve extracellular matrix[41, 42] are all age-dependent. Ages of controls and subjects with POAG were similar by design in the current study, avoiding age as a confounding factor.

Finite element biomechanical models of the effects of adduction tethering of the optic nerve have predicted that strain during adduction tethering is concentrated at the temporal border of the optic disc corresponding to the location of typical PPA[43]. However, the current study did not find major deformation in the regions of PPA, but rather adjacent to the opposite hemidisc where contiguous PPA was absent. As such, it appears that tissue deformation in adduction is not substantial in the region of PPA itself. However, the distribution of deformations may be indicative of general remodeling of underlying tissue that could contribute to development of PPA, or be intrinsic to it. Regions exhibiting PPA may have become sclerotic due to tissue remodeling, and absence of deformation within the optic disc opposite them may be a biomarker for peripapillary sclerosis that might ultimately prove associated with optic nerve pathology. A stiffened and atrophic PPR is less resilient, while stress concentration within it is greater if the tissue cannot dissipate applied force through deformation (strain)[43]. Subjects with POAG are known to have less compliant tissue; conversely, more compliant tissue, as typical of youth, may protect against mechanical injury. Those with stiffer tissues may not have the ability to absorb such mechanical insults.

There is an extensive literature on corneal hysteresis (CH) in glaucoma, with emphasis on its role as a possible indirect biomarker of biomechanical characteristics of the sclera and lamina cribrosa[44]. For example, in patients with glaucoma, CH is

associated with increased deformation of the optic nerve surface during IOP elevation[45]. Lower CH is significantly associated with faster rates of visual field loss[46] and faster nerve fiber loss in patients with glaucoma[47]. Increased corneal stiffness and decreased corneal viscosity are the corneal mechanical factors that would decrease CH, and the former probably corresponds to increased stiffness underlying the decreased optic disc deformation in adduction observed in the current study. Since CH directly reflects the biomechanical properties of the cornea and anterior eye, measurement of CH can only indirectly correlate with biomechanics of the optic disc and peripapillary sclera that are remote from the cornea. The current approach of evaluating disc deformations associated with adduction tethering of the optic has the important advantage of directly assessing the biomechanics of the optic disc itself, and of doing so topographically in relationship to anatomic features of the peripapillary sclera. The eye movement-related disc deformations reported here can be imaged with widely-available clinical instrumentation at low cost, and so deserve further investigation of their possible role in glaucoma. Application of automated image processing will probably be required, however, for efficient processing of large numbers of such images.

Study Limitations

Although this study sampled a relatively small number of subjects, it is a strength of this hypothesis-driven study that the major findings were nevertheless highly statistically significant. This study relied on identification of vascular fiducials to quantify tissue deformation. If an area did not commonly have trackable fiducials, any deformation that occurred in that area could not have been detected. The PPA zone has few prominent vascular fiducials to track; however, deformation in this region was not likely to have been masked by the PPA since controls without PPA also exhibited no significant deformation in the area immediately outside the optic disc.

2.5.6 Conclusions

Large adduction is normally associated with temporal displacement of the nasal half of the optic disc that is opposite the typical location of β–zone PPA, if PPA is present at all. Patients with POAG in the absence of abnormally elevated IOP have significantly subnormal temporal displacement of the nasal half of the optic disc during large adduction, and the deformations that these patients do have are highly inversely correlated with the extent of PPA on the opposite side of the disc. The lesser optic disc deformation during large angle adduction in patients with POAG may have potential as a clinically-practical biomarker for pathological stiffening of disc and peripapillary tissues associated with glaucomatous optic neuropathy.

2.5.7 References

1. Kapetanakis VV, Chan MP, Foster PJ, Cook DG, Owen CG, Rudnicka AR. Global variations and time trends in the prevalence of primary open angle glaucoma (POAG): a systematic review and meta-analysis. Br J Ophthalmol. 2016;100:86-93.

2. Sakata R, Yoshitomi T, Iwase A, Matsumoto C, Higashide T, Shirakashi M, Aihara M, Sugiyama K, Araie M, Lower Normal Pressure Glaucoma Study Members in Japan Glaucoma S. Factors associated with progression of Japanese open-angle glaucoma with lower normal intraocular pressure. Ophthalmology. 2019;126:1107-16.

3. Han JC, Han SH, Park DY, Lee EJ, Kee C. Clinical course and risk factors for visual field progression in normal-tension glaucoma with myopia without glaucoma medications. Am J Ophthalmol. 2020;209:77-87.

4. Ernest PJ, Schouten JS, Beckers HJ, Hendrikse F, Prins MH, Webers CA. An evidence-based review of prognostic factors for glaucomatous visual field progression. Ophthalmology. 2013;120:512-9.

5. Araie M, Sekine M, Suzuki Y, Koseki N. Factors contributing to the progression of visual field damage in eyes with normal-tension glaucoma. Ophthalmology. 1994;101:1440-4.

6. Park KH, Tomita G, Liou SY, Kitazawa Y. Correlation between peripapillary atrophy and optic nerve damage in normal-tension glaucoma. Ophthalmology. 1996;103:1899-906.

7. Jonas JB, Nguyen XN, Gusek GC, Naumann GO. Parapapillary chorioretinal atrophy in normal and glaucoma eyes. I. Morphometric data. Invest Ophthalmol Vis Sci. 1989;30:908-18.

8. Jonas JB. Clinical implications of peripapillary atrophy in glaucoma. Curr Opin Ophthalmol. 2005;16:84-8.

9. Jonas JB, Naumann GO. Parapapillary chorioretinal atrophy in normal and glaucoma eyes. II. Correlations. Invest Ophthalmol Vis Sci. 1989;30:919-26.

10. Teng CC, De Moraes CG, Prata TS, Tello C, Ritch R, Liebmann JM. Beta-zone parapapillary atrophy and the velocity of glaucoma progression. Ophthalmology. 2010;117:909-15.

11. Uchida H, Ugurlu S, Caprioli J. Increasing peripapillary atrophy is associated with progressive glaucoma. Ophthalmology. 1998;105:1541-5.

12. Lee EJ, Kim TW, Weinreb RN, Park KH, Kim SH, Kim DM. Beta-zone parapapillary atrophy and the rate of retinal nerve fiber layer thinning in glaucoma. Invest Ophthalmol Vis Sci. 2011;52:4422-7.

13. Teng CC, De Moraes CG, Prata TS, Liebmann CA, Tello C, Ritch R, Liebmann JM. The region of largest beta-zone parapapillary atrophy area predicts the location of most rapid visual field progression. Ophthalmology. 2011;118:2409-13.

14. Na JH, Moon BG, Sung KR, Kook MS. Characterization of peripapillary atrophy using spectral domain optical coherence tomography. Korean J Ophthalmol. 2010;24:353-9.

15. Suh SY, Le A, Shin A, Park J, Demer JL. Progressive deformation of the optic nerve head and peripapillary structures by graded horizontal duction. Invest Ophthalmol Vis Sci. 2017;58:5015-21.

16. Chang MY, Shin A, Park J, Nagiel A, Lalane RA, Schwartz SD, Demer JL. Deformation of optic nerve head and peripapillary tissues by horizontal duction. Am J Ophthalmol. 2017;174:85-94.

17. Wang X, Beotra MR, Tun TA, Baskaran M, Perera S, Aung T, Strouthidis NG, Milea D, Girard MJ. In vivo 3-dimensional strain mapping confirms large optic nerve head deformations following horizontal eye movements. Invest Ophthalmol Vis Sci. 2016;57:5825-33.

18. Sibony PA. Gaze-evoked deformations of the peripapillary retina and papilledema and ischemic optic neuropathy. Invest Ophthalmol Vis Sci. 2016;57:4979-87.

19. Le A, Chen J, Lesgart M, Gawargious BA, Suh SY, Demer JL. Age-dependent deformation of the optic nerve head and peripapillary retina by horizontal duction. Am J Ophthalmol. 2020;209:107-16.

20. Booij JC, Baas DC, Beisekeeva J, Gorgels TG, Bergen AA. The dynamic nature of Bruch's membrane. Prog Retin Eye Res. 2010;29:1-18.

21. Albon J, Karwatowski WS, Avery N, Easty DL, Duance VC. Changes in the collagenous matrix of the aging human lamina cribrosa. Br J Ophthalmol. 1995;79:368-75.

22. Albon J, Karwatowski WS, Easty DL, Sims TJ, Duance VC. Age related changes in the non-collagenous components of the extracellular matrix of the human lamina cribrosa. Br J Ophthalmol. 2000;84:311-7.

23. Coudrillier B, Tian J, Alexander S, Myers KM, Quigley HA, Nguyen TD. Biomechanics of the human posterior sclera: age- and glaucoma-related changes measured using inflation testing. Invest Ophthalmol Vis Sci. 2012;53:1714-28.

24. Geraghty B, Jones SW, Rama P, Akhtar R, Elsheikh A. Age-related variations in the biomechanical properties of human sclera. J Mech Behav Biomed Mater. 2012;16:181-91.

25. Pena JD, Netland PA, Vidal I, Dorr DA, Rasky A, Hernandez MR. Elastosis of the lamina cribrosa in glaucomatous optic neuropathy. Exp Eye Res. 1998;67:517-24.

26. Netland PA, Ye H, Streeten BW, Hernandez MR. Elastosis of the lamina cribrosa in pseudoexfoliation syndrome with glaucoma. Ophthalmology. 1995;102:878-86.

27. Wang YX, Jiang R, Wang NL, Xu L, Jonas JB. Acute peripapillary retinal pigment epithelium changes associated with acute intraocular pressure elevation. Ophthalmology. 2015;122:2022-8.

28. Huang J, Huang JY, Chen Y, Ying GS. Evaluation of approaches to analyzing continuous correlated eye data when sample size Is small. Ophthalmic Epidemiol. 2018;25:45-54.

29. Demer JL, Clark RA, Suh SY, Giaconi JA, Nouri-Mahdavi K, Law SK, Bonelli L, Coleman AL, Caprioli J. Magnetic resonance imaging of optic nerve traction during adduction in primary open-angle glaucoma with normal intraocular pressure. Invest Ophthalmol Vis Sci. 2017;58:4114-25.

30. Demer JL, Clark RA, Suh SY, Giaconi JA, Nouri-Mahdavi K, Law SK, Bonelli L, Coleman AL, Caprioli J. Optic nerve traction during adduction in open angle glaucoma with normal versus elevated intraocular pressure. Curr Eye Res. 2020;45:199-210.

31. Fazio MA, Grytz R, Morris JS, Bruno L, Girkin CA, Downs JC. Human scleral structural stiffness increases more rapidly with age in donors of African descent compared to donors of European descent. Invest Ophthalmol Vis Sci. 2014;55:7189-98.

32. Avetisov ES, Savitskaya NF, Vinetskaya MI, Iomdina EN. A study of biochemical and biomechanical qualities of normal and myopic eye sclera in humans of different age groups. Metab Pediatr Syst Ophthalmol. 1983;7:183-8.

33. Brown CT, Vural M, Johnson M, Trinkaus-Randall V. Age-related changes of scleral hydration and sulfated glycosaminoglycans. Mech Ageing Dev. 1994;77:97-107.

34. Coudrillier B, Pijanka J, Jefferys J, Sorensen T, Quigley HA, Boote C, Nguyen TD. Effects of age and diabetes on scleral stiffness. J Biomech Eng. 2015;137.

35. Kimball EC, Nguyen C, Steinhart MR, Nguyen TD, Pease ME, Oglesby EN, Oveson BC, Quigley HA. Experimental scleral cross-linking increases glaucoma damage in a mouse model. Exp Eye Res. 2014;128:129-40.

36. Girard MJ, Suh JK, Bottlang M, Burgoyne CF, Downs JC. Biomechanical changes in the sclera of monkey eyes exposed to chronic IOP elevations. Invest Ophthalmol Vis Sci. 2011;52:5656-69.

37. Palko JR, Morris HJ, Pan X, Harman CD, Koehl KL, Gelatt KN, Plummer CE, Komaromy AM, Liu J. Influence of age on ocular biomechanical properties in a canine glaucoma model with ADAMTS10 mutation. PLoS One. 2016;11:e0156466.

38. Malik NS, Moss SJ, Ahmed N, Furth AJ, Wall RS, Meek KM. Ageing of the human corneal stroma: structural and biochemical changes. Biochim Biophys Acta. 1992;1138:222-8.

39. Morrison JC, Jerdan JA, Dorman ME, Quigley HA. Structural proteins of the neonatal and adult lamina cribrosa. Arch Ophthalmol. 1989;107:1220-4.

40. Albon J, Purslow PP, Karwatowski WS, Easty DL. Age related compliance of the lamina cribrosa in human eyes. Br J Ophthalmol. 2000;84:318-23.

41. Hernandez MR, Luo XX, Andrzejewska W, Neufeld AH. Age-related changes in the extracellular matrix of the human optic nerve head. Am J Ophthalmol. 1989;107:476-84.

42. Bailey AJ, Paul RG, Knott L. Mechanisms of maturation and ageing of collagen. Mech Ageing Dev. 1998;106:1-56.

43. Shin A, Yoo L, Park C, Demer JL. Finite element biomechanics of optic nerve sheath traction in adduction. J Biomech Eng. 2017;139.

44. Liang L, Zhang R, He LY. Corneal hysteresis and glaucoma. Int Ophthalmol. 2019;39:1909-16.

45. Wells AP, Garway-Heath DF, Poostchi A, Wong T, Chan KC, Sachdev N. Corneal hysteresis but not corneal thickness correlates with optic nerve surface compliance in glaucoma patients. Invest Ophthalmol Vis Sci. 2008;49:3262-8.

46. De Moraes CV, Hill V, Tello C, Liebmann JM, Ritch R. Lower corneal hysteresis is associated with more rapid glaucomatous visual field progression. J Glaucoma. 2012;21:209-13.

47. Zhang C, Tatham AJ, Abe RY, Diniz-Filho A, Zangwill LM, Weinreb RN, Medeiros FA. Corneal hysteresis and progressive retinal nerve fiber layer loss in glaucoma. Am J Ophthalmol. 2016;166:29-36.

Chapter 3: Possible Remedies to Optic Nerve Traction

Given the evidence that large adduction can deform the optic nerve head and could lead to glaucomatous damage, we surveyed two possible remedies that could mitigate injuries to the optic nerve: collagen cross-linking and prostaglandin agonist drugs. By cross-linking the sclera, areas that undergo high levels of mechanical stress can be fortified to protect from excessive mechanical force. The following study looks at the feasibility of using ultraviolet light and riboflavin to cross-link sclera tissue. A less invasive possibility could be to use prostaglandin agonists that are known to reduce orbital fat as a side effect in patients who have glaucoma. Treatment with prostaglandin agonists maybe be a feasible way to create extra slack in the optic nerve and prevent traction.

Publications included in this chapter by Candidate:

Published Journal Paper

1. Gawargious B, **Le A**, Lesgart M, Ugardar S, Demer JL. Differential Regional Stiffening of Sclera by Collagen Cross-linking. Curr Eye Res.10.1080/02713683.2019.1694157.

Journal Manuscripts under Review

2. Chen JY, **Le A**, Caprioli J, Giaconi JA, Nouri-Mahdavi K, Law SK, Bonelli L, Coleman AL, Demer JL. Orbital Fat Volume After Treatment with Topical Prostaglandin Agonists. Summited to *Current Eye Research*.

3.1 Differential Regional Stiffening of Sclera by Collagen Cross-linking

Bola A. Gawargious[1], Alan Le[2,3,4], Michael Lesgarte[5], Shoaib Ugradar[2,3], and Joseph L. Demer[2,3,4,6,7]

[1] Department of Integrative Biology and Physiology, [2]Department of Ophthalmology and [3]Stein Eye Institute, [4]Bioengineering Interdepartmental Programs, [5]Department of Psychology, [6]Department of Neurology, [7]David Geffen Medical School at University of California, Los Angeles.

3.1.1 Abstract

Purpose: Corneal collagen cross-linking by ultraviolet light activation of riboflavin has been used clinically to enhance corneal stiffness. We sought to determine if cross-linking differentially affects scleral regions.

Methods: Adjacent, parallel strips of sclera were cut from superolateral, superomedial, inferolateral, and inferomedial quadrants of posterior and equatorial sclera of 12 human cadaver eyes. One of each pair served as control while the other was cross-linked by immersion in 0.1% riboflavin and 365 nm exposure at 6 mW/cm2 irradiance for 30 min. Behavior of strips was characterized using a microtensile load cell. Preloaded strips were imaged using orthogonally mounted cameras and optical coherence tomography to determine specimen dimensions including cross-sectional area. Tension was measured during 0.1 mm/s constant rate elongation.

Results: Young's modulus (YM), the slope of the relationship relating tensile stress to strain, was calculated at 8% strain, and increased significantly after cross-linking ($P < .001$). In posterior sclera, mean (± standard error of mean, SEM) YM is increased in the superolateral, superomedial, inferolateral, and inferomedial quadrants by 46 ± 15%, 32 ± 11%, 67 ± 20%, and 53 ± 11%, respectively. In equatorial sclera, YM is increased by 139 ± 43%, 68 ± 27%, 143 ± 92%, and 68 ± 14%, respectively. The YM of pooled equatorial quadrants increased significantly more than that of the pooled posterior quadrants.

Conclusions: Scleral collagen cross-linking by ultraviolet activation of riboflavin differentially increases scleral YM more in the equatorial than posterior sclera, and most in the lateral, equatorial sclera. Crosslinking might be used to arrest progressive myopia or to prevent staphyloma formation.

3.1.2 Introduction

Myopia affects around 30% of the population in the United States and Europe, but up to 60% in Asian countries,[1,2] with myopic progressionoccurringinupto50%ofsuchcases.[3] Severe myopia, a leading cause of blindness worldwide, is associated with sight threatening consequences such as retinal detachment and macular choroidal degeneration.[4] Pathological scleral thinning and localized ectasia often occur in high myopia.[5] Because biomechanical properties of the sclera influence globe shape and size,[6] scleral thinning may permit further globe elongation and progressive refractive error. Pathological scleral thinning involves structural scleral abnormalities such as decreased collagen fiber diameter,[7] deficiencies in collagen fibrillogenesis,[8] and impairment of collagen cross-linking (CXL).[9] Reversing these abnormalities would beneficially change scleral biomechanical properties and might serve as a treatment for myopic progression.

Cross-linking induced by riboflavin and ultraviolet-A light (UVA) can increase corneal rigidity to treat keratoconus[10] and has emerged as the favored initial treatment.[11–14] Riboflavin serves as a photosensitizer in CXL, forming of intra- and interfibrillar covalent bonds between collagen fibers when activated byUVA.[15,16] The riboflavin also shields underlying tissues, such as the corneal endothelium and iris, from UV irradiation.[13] Cross-linking increases corneal Young's modulus (YM), a measure of stiffness, by about 4.5 fold and typically prevents progression of keratoconus.[17,18] Since human sclera contains approximately 50% collagen by weight, primarily type I collagen[19] much like cornea, CXL can also be used to increase scleral stiffness. Wollensak conducted CXL using riboflavin and UVA and noted a significant increase in the YM of porcine (145%) and human (31%) sclera in vitro,[20] as well as in rabbit sclera (465%) in vivo.[21] This study, however, did not consider possible regional variation as a result of

CXL. In a study by Wang, CXL of anteriorly to posteriorly oriented scleral strips in the equatorial and posterior regions produced 185% and 201% increases in YM, respectively.[22] However, since scleral thickness varies markedly between the equatorial and posterior regions,[23] scleral strips in this orientation necessarily have nonuniform thickness, and so cannot reflect likely regional variations in mechanical effects of CXL. In the present study, we investigated the effect of CXL on biomechanical strength and volume of circumferentially cut scleral strips in eight scleral regions.

3.1.3 Methods

Specimen preparation Institutional review board review is not required for the cadaveric material studied here that was obtained in conformity with applicable local laws. Two eyes were harvested by eye banks within 48 h of death and were obtained unfrozen but stored at just above 0°C. Ten eyes were obtained from cadavers donated to medical research and had been previously frozen. In all eyes, circumferentially oriented, parallel adjacent scleral strips measuring 2 × 8 mm^2 were trimmed by scalpel from the superolateral, superomedial, inferolateral, and inferomedial quadrants of the equatorial as well as posterior sclera. Equatorial strips were cut between the rectus muscle insertions, while posterior strips were cut 1 mm from edge of the optic nerve. The eye was initially hemisected sagitally, separating medial and lateral portions. Scleral strips were then excised from four different regions in each of the halves (Figure 1). One strip of each identically prepared parallel pair was used as a control while the other underwent CXL. The retina, choroid, and episcleral tissue were removed before other procedures.

Cross-linking Each treated strip was immersed in 0.1% dextran-free riboflavin for 30 min, and then exposed to 365 nm UVA light at 6 mW/cm^2 irradiance for 30 min using the LightLink CXL Corneal CrossLink System (LightMed, San Clemente, CA). Riboflavin was applied drop wise onto the specimens every 30 s during CXL. To avoid dehydration, treated and control strips were kept in Ringer's solution in petri dishes placed on ice until tensile testing.

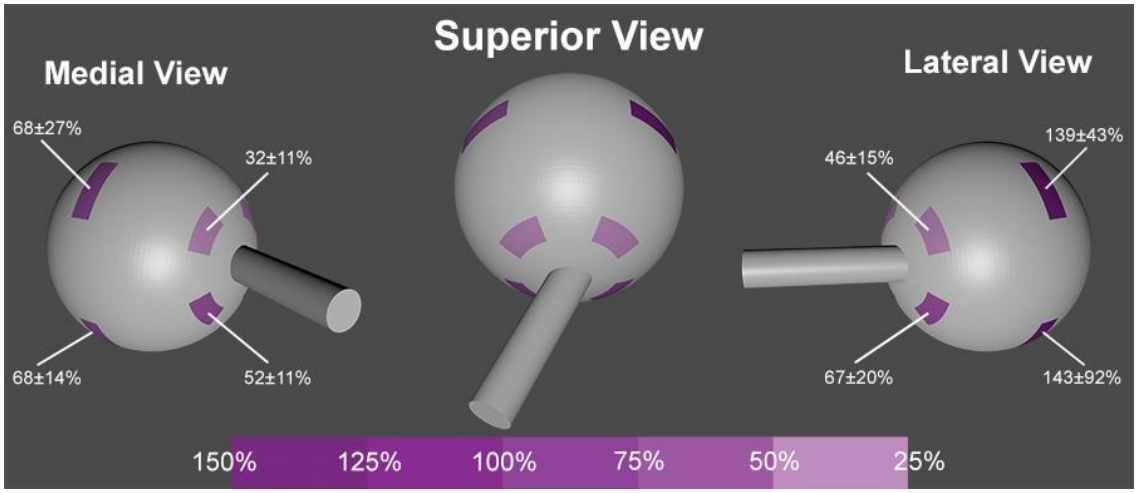

Figure 1. Scleral regions tested and mean percent increase in Young's modulus (± standard error of mean) following cross-linking.

Tensile testing Tensile testing was performed in a horizontally mounted load cell incorporating a precise train gauge (LSB200, FUTEK, Irvine, CA) with 5 mN force resolution attached to a linear motor (Ibex Engineering, Newbury Park, CA) having 20 nm distance resolution. Scleral strips were tested in an environmental chamber simulating physiological conditions at 36°C and 100% humidity for 5 min. Excess moisture was wiped away. Scleral strips were anchored in serrated clamps separated by 5 mm to set initial specimen length, and preloaded to 0.05 N tension to eliminate slack. Preloaded strips were photographed with two orthogonally mounted digital cameras (Canon 70D and Canon 5D) to determine specimen dimensions, and also imaged using

optical coherence tomography (OCT, Thorlabs Inc., Newton NJ) to measure cross-sectional area for stress calculation.

Young's modulus calculation Tensile force was divided by mean specimen cross-sectional area in four OCT images obtained at 0.5 mm intervals along the specimen length to calculate stress. The YM, the ratio of tensile force to stress, was analyzed at 8% strain. In each of the 8 scleral regions, 10 control, and 10 cross-linked samples were tested. Of the 12 specimens prepared for each region, two were typically damaged by ruptures due to preparation or clamping, so data from only the 10 specimens free of artifacts is included in the reported results. The sample size in the current study is similar to sample sizes in relevant literature.[20,21,24]

Cross-linking shrinkage analysis Twenty specimens, measuring approximately 3.5 × 3.5 mm^2, were excised from the posterior (10 specimens) and equatorial (10 specimens) regions. Excess moisture was removed, and the specimen equilibrated in the environmental chamber for 10 min prior to OCT imaging. The specimen was then immersed in 0.1% riboflavin for 30 min. Next, each specimen was placed on an inclined platform to prevent riboflavin pooling, and exposed to 365 nm UVA at 6 mW/cm^2 irradiance for 30 min to produce CXL, during which specimens were dropwise irrigated with riboflavin every 30 s. After CXL, specimens were placed in the environmental chamber for 10 min, and were re-imaged by OCT. Specimen thickness and volume were determined using OCT before and after CXL. The entire length of each specimen was cross-sectionally imaged at 125 μm intervals, requiring approximately 28 image planes in which specimen boundaries were then manually traced to determine cross-sectional areas. Summed areas were multiplied by 125 μm to calculate specimen volume. This current study only investigated CXL shrinkage in the posterior and equatorial sclera

because we lacked sufficient scleral tissue to study CXL shrinkage in all eight scleral regions individually.

Statistical analysis

In each region, paired t-tests were conducted for YM to compare control and cross-linked samples. An unpaired t-test was used to determine regional variation in YM. A secondary analysis was conducted to assess the effect of outlier values, with removal of all values more than 2 standard deviations (SD) from the mean. Since outlier removal did not change the overall conclusions, in the interest of rigor we report results of all data acquisitions that were free of obvious experimental artifacts.

3.1.4 Results

Stress–strain analysis

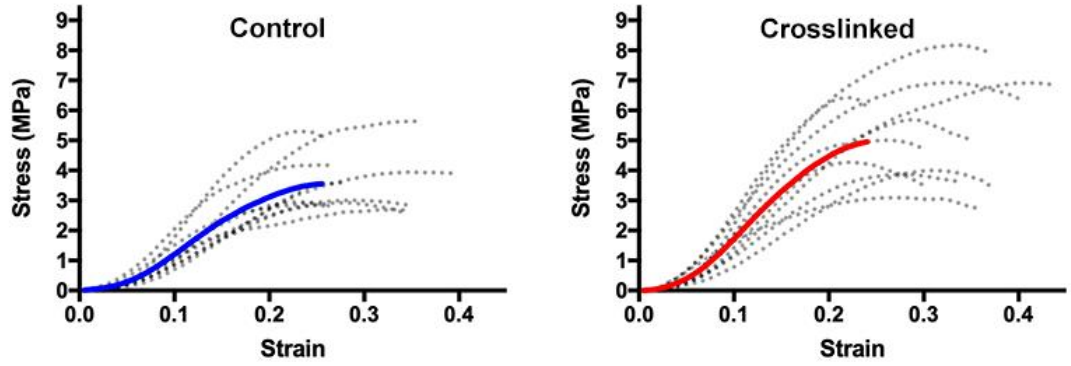

Figure 2. Individual stress–strain curves of 10 samples from the posterior superolateral sclera (dotted curves), with average curves solid. Note greater stress for crosslinked specimens

Significant increases in YM were evident after CXL in all eight scleral regions. Figure 2 shows example stress–strain curves of individual samples (dotted curves) and their overall average (solid curve) in the posterior superolateral region.

Average stress–strain curves for posterior sclera are shown in Figure 3. In posterior superolateral sclera, mean YM (± SEM) increased 46 ± 15% from 23.2 ± 2.5 MPa to 32.4 ± 2.9 MPa. In posterior superomedial sclera, YM increased 32 ± 11% from 26.2 ± 3.7 MPa to 34.7 ± 5.8 MPa. In posterior inferolateral sclera, YM increased 67 ± 20% from 22.1 ± 2.0 MPa to 34.6 ± 3.0 MPa, similar to the 53 ± 11% increase in posterior inferomedial sclera from 26 ± 4 MPa to 37 ± 5 MPa. Data are summarized in Table 1 and Figure 1.

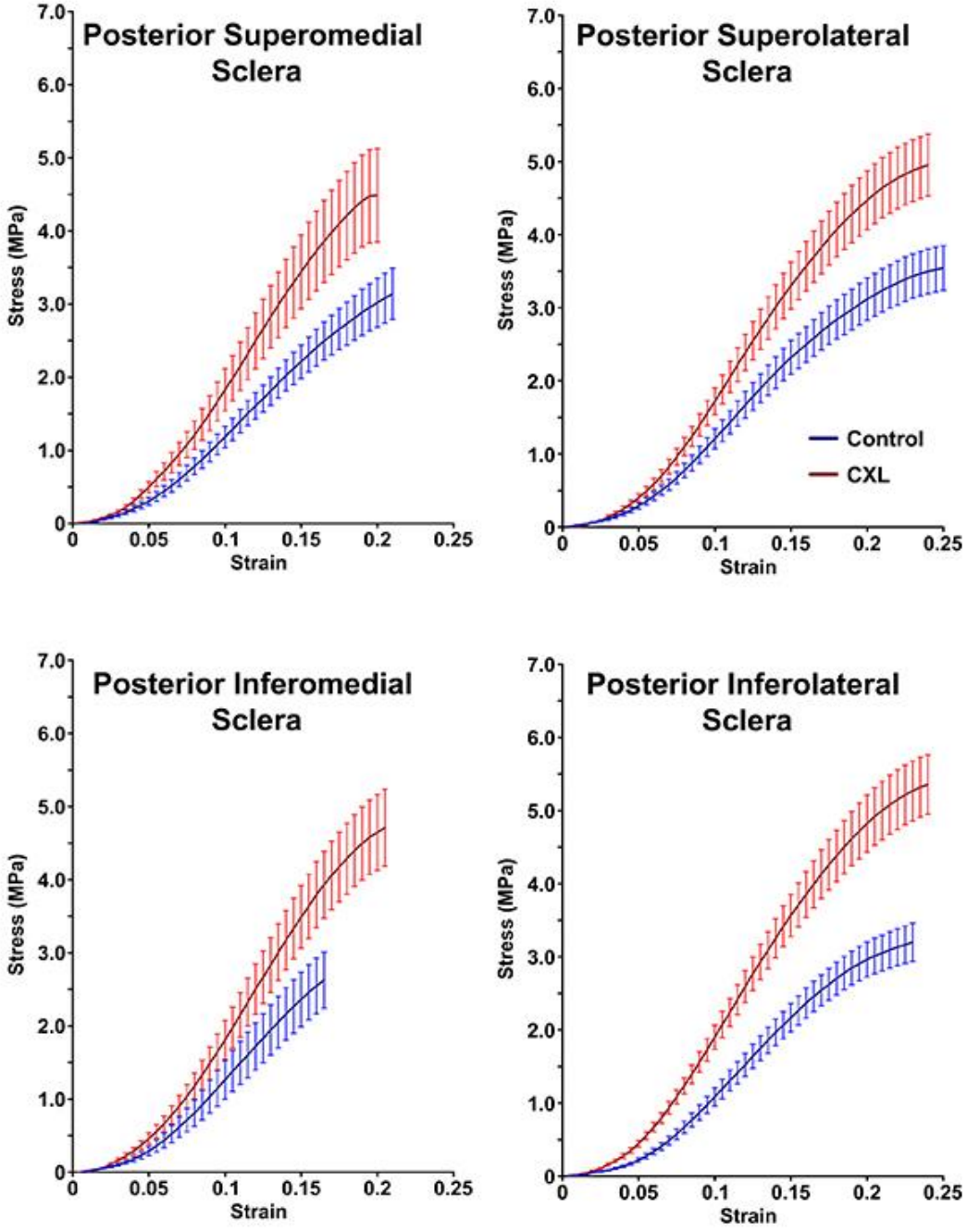

Figure 3. Stress–strain curves in posterior superomedial, superolateral, inferomedial and inferolateral sclera for control and cross-linked (CXL) specimens. Error bands ±standard error of mean.

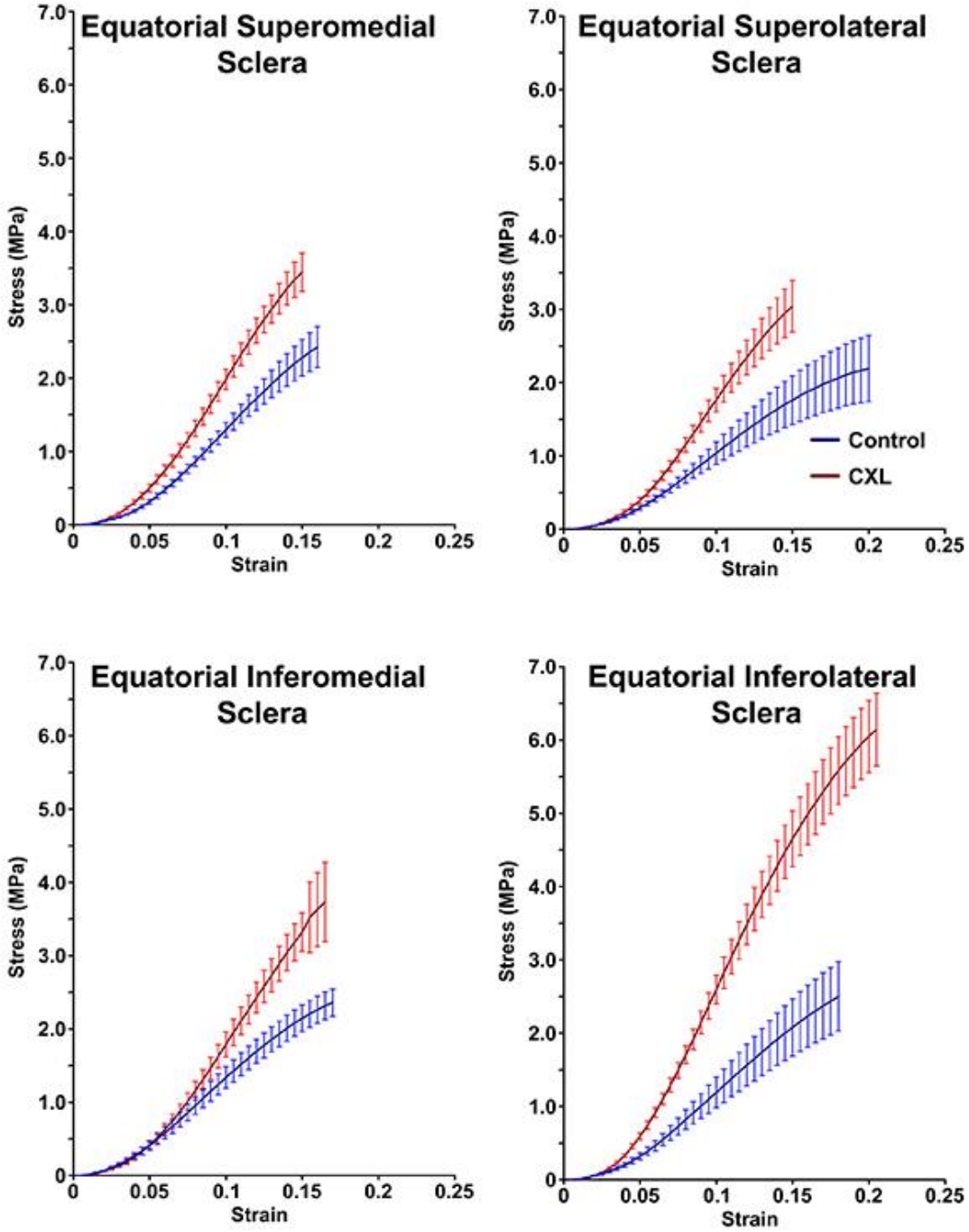

Figure 4. Stress–strain curves in equatorial sclera for control specimens and after cross-linking (CXL). Error bands ± standard error of mean.

Average stress–strain graphs for equatorial sclera are shown in Figure 4. The

YM of equatorial superolateral and equatorial inferolateral sclera was similarly increased

by CXL by 139 ± 43% and 143 ± 92%, respectively. The YM of equatorial superolateral sclera was increased by CXL from 17.1 ± 3.8 MPa to 30.8 ± 3.5 MPa, while that of equatorial inferolateral sclera increased from 23.3 ± 4.3 MPa to 44.3 ± 4.8 MPa. Likewise, CXL increased the YM of superomedial and equatorial inferomedial sclera similarly by 68 ± 27% and 68 ± 14%, respectively. The YM of equatorial superomedial sclera was increased by CXL from 23.3 ± 3.0 MPa to 34.7 ± 3.8 MPa, while that of equatorial inferomedial sclera increased from 21.4 ± 3.2 MPa to 32.8 ± 3.0 MPa. Data are summarized in Table 1 and Figure 5. Un-paired t-testing showed that the increase in YM produced by CXL was significantly greater in the pooled equatorial than in the pooled posterior regions ($P < .01$), and the increase in the pooled lateral regions was significantly greater than in the pooled medial regions ($P < .05$, Figure 5). However, CXL affected YM similarly in the pooled superior (71 ± 14% increase) and inferior regions (118 ± 29% increase) with $P = .14$.

Table 1. Effect of Cross-linking on Scleral Young's Modulus				
Regions	Control YM (MPa, SEM)	Cross-linked YM (MPa, SEM)	Percent Increase (SEM)	Significance
Posterior Superlateral	23.2±2.5	32.4±2.9	46±15%	0.01
Posterior Supermedial	26.2±3.7	34.7±5.8	32±11%	0.05
Posterior Inferolateral	22.1±2.0	34.6±3.0	67±20%	0.01
Posterior Inferomedial	25.7±4.5	36.6±5.1	53±11%	0.001
Equatorial Superlateral	17.1±3.8	30.8±3.5	139±43%	0.001
Equatorial Supermedial	23.3±3.0	34.7±3.8	68±27%	0.005
Equatorial Inferolateral	23.3±4.3	44.3±4.8	143±92%	0.001
Equatorial Inferomedial	21.4±3.2	32.8±3.0	68±14%	0.001

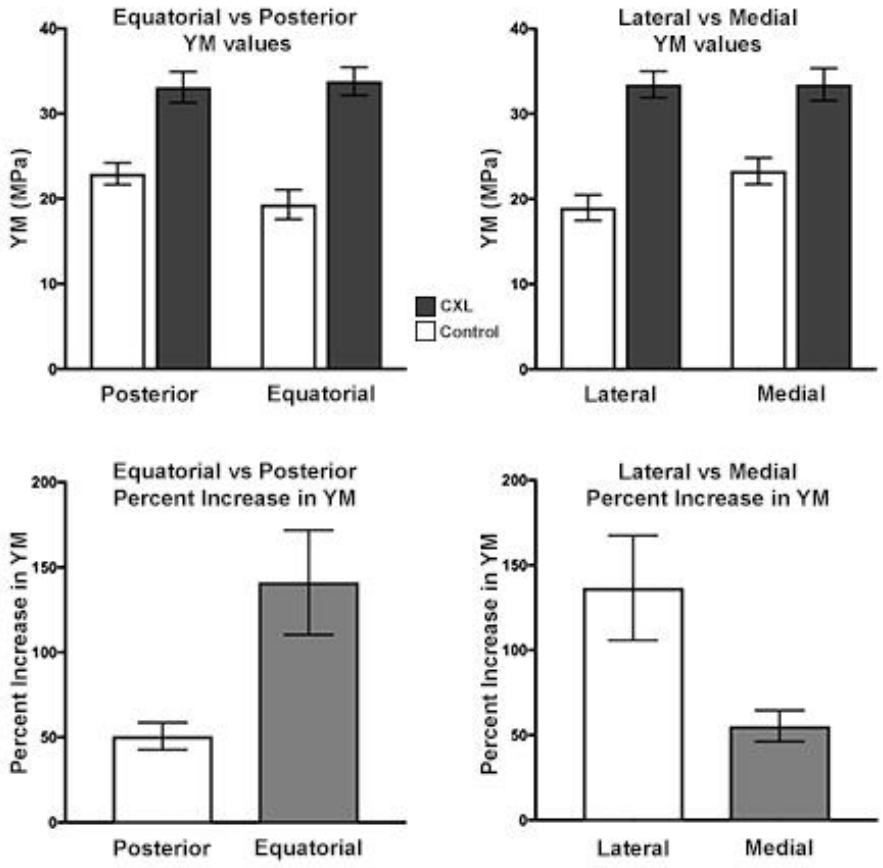

Figure 5. Top. Young's modulus (YM, top row) and its percentage increase (bottom row) in control specimens, and after cross-linking (CXL), in posterior, equatorial, lateral, and medial sclera. Error bars – standard error of mean.

Scleral shrinkage

Posterior sclera was on average significantly thicker at 1.00 ± 0.03 mm than equatorial sclera at 0.77 ± 0.03 mm prior to CXL ($P < .001$). Cross-linking generally reduced scleral thickness, as illustrated by the OCT cross section in Figure 6. Pooling all quadrants, CXL reduced scleral volume 17 ± 1% in the equatorial and 13 ± 1% in posterior sclera ($P < .001$). Figure 7 illustrates relative reduction of both thickness and volume in posterior and equatorial sclera. Correlation analysis indicated that 90% of the volume reduction was due to thickness reduction, with little change in length and width.

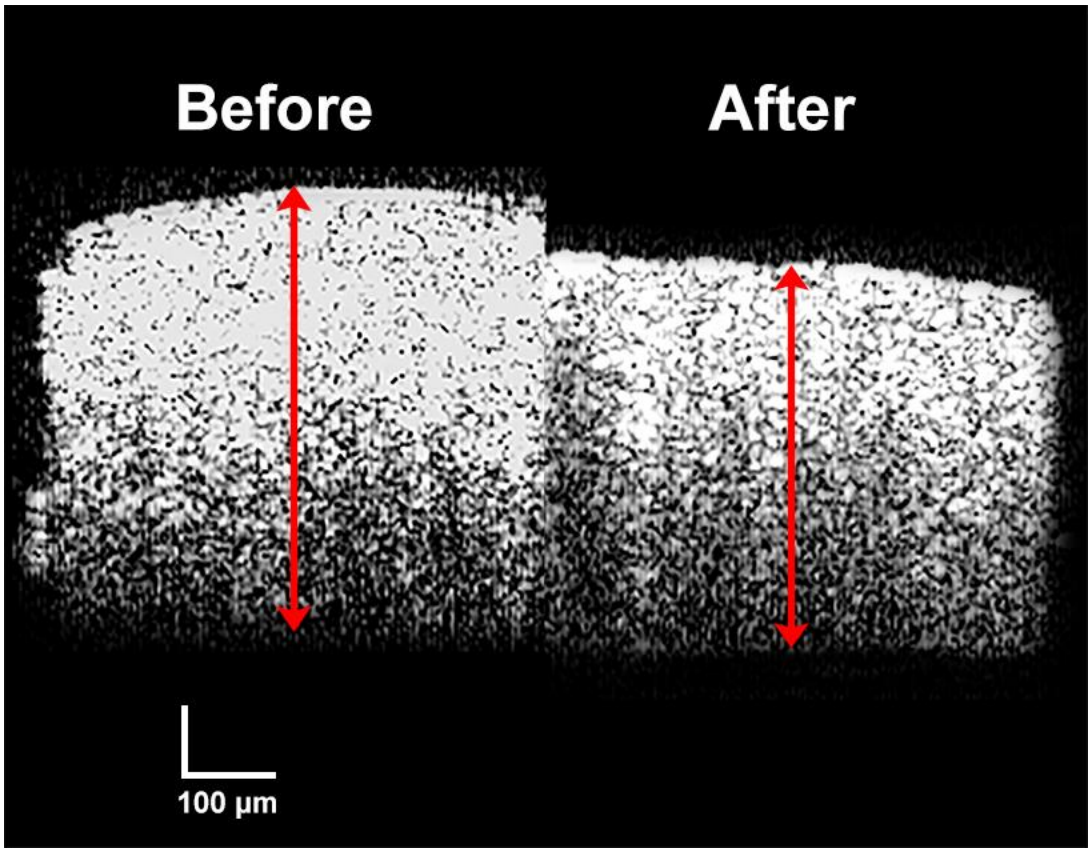

Figure 6. Cross sectional optical coherence tomography of the same scleral specimen before and after cross-linking.

Outliers

After removal of YM values lying more than ±2SD from the mean of all sample results before and after CXL, average SEM for the remaining values decreased by 16% in posterior and 21% in equatorial sclera. Nevertheless, after outlier removal, the increase in YM due to CXL remained significantly greater in equatorial than posterior sclera ($P < .01$), and greater in lateral than medial sclera ($P < .05$). These relative changes are the same as illustrated in Figure 5 when considering the entire date set, an approach that avoids possible bias and which is therefore the basis for the principal data reported here.

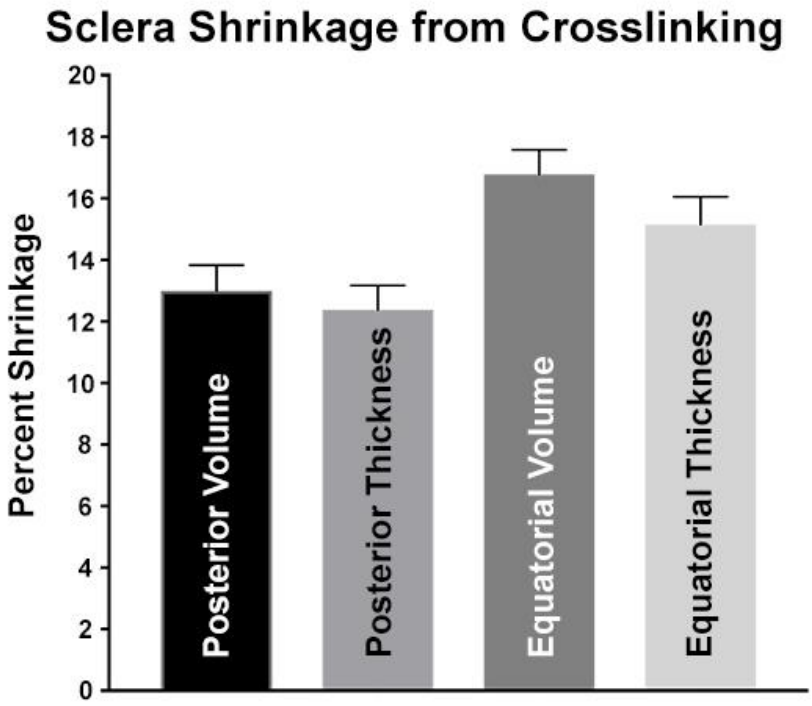

Figure 7. Shrinkage due to cross-linking in posterior and equatorial sclera

3.1.5 Discussion

Cross-linking using riboflavin and UVA increased YM significantly in all regions of human sclera. The effect was varied topographically, being relatively greater in the equatorial than posterior region (Figure 5). This difference is in part attributable to regional variation in scleral thickness. Consistent with previous studies,[23] we found that the average posterior sclera thickness at 1.00 mm to be significantly greater than the equatorial sclera thickness averaging at 0.77 mm. Limited to a fixed tissue depth, UVA illumination therefore cross-linked a greater percentage of the total thickness of the equatorial than posterior sclera, and thus produced a greater increase in relative stiffness. In addition, we found that CXL increases YM significantly more in the lateral than in medial sclera. It should be noted that the irradiance and time of UV exposure were chosen to provide a stronger scleral crosslinking effect than the standard Dresden protocol for corneal cross-linking. Since other dosages of UV exposure were not investigated, specific protocols for in vivo scleral CXL would likely require optimization. Another factor in differential regional effect of CXL may be a ceiling effect suggested by Figure 5. After CXL, mean pooled YM similarly averaged about 33 MPa in posterior, equatorial, lateral, and medial regions. The differential effect of CXL might also be understood as increasing scleral YM to a maximum value regardless of reginal variation in untreated YM. Thus, the lower the untreated YM, the greater the relative increase in YM due to CXL. Previous studies used calipers to measure volume changes post CXL.[21,22,24] In this study, we measured volume more accurately by OCT, showing that CXL significantly reduces equatorial and posterior sclera volume(Figures 6 and 7),almost entirely due to thinning similar to that of corneal CXL.[25] In vivo, corneal thickness returned to baseline after CXL treatment for keratoconus.[26] It is unknown if similar reversal of scleral thinning might occur after CXL in vivo. The current results differ

substantially from those of Wang et al.,[22] the only other study to evaluate regional variations in human sclera tissue due to CXL. Wang et al. study reported human YM in the quantitatively implausible range of 200–470 MPa,[22] roughly an order of magnitude greater than typically observed in sclera. Such unrealistic scleral values are more typical of muscle at approximately 480 MPa,[27,28] or tendon,

approximately 560 MPa.[28–31] Our study of sclera yielded a mean YM of 23 ± 1 (SEM) MPa, similar to the report of Wollensak, who did not investigate, however, possible regional variations.[20] Prior studies of scleral YM[20,22] applied loading to scleral strips that had been cut sagitally from anterior to posterior, a direction in which systematic variation in specimen thickness compromises accurate computation of YM. Consistent with the anatomical literature,[23] we found equatorial to be significantly thinner than posterior sclera.

Assuming that the thinnest cross-section is applicable to the entire specimen would exaggerate apparent YM by exaggerating computed stress, which is calculated as force divided by cross sectional area. Finally, in previous studies where CXL was performed in whole globes prior to specimen excision,[6,22] control specimens were obtained from different eyes, introducing intersubject variability. The present approach mitigated interindividual variability by using adjacent scleral strips in the same eye as controls. Diminished CXL is an important factor in the weakening process of myopic sclera[9] as in myopic human eyes that have significantly lower scleral YM.[32] There is a natural increase in CXL with advancing age[9] and in diabetics.[33] In older people, the natural increase in CXL is believed to slow myopic progression.[34] Similarly, the increase glycation-induced CXL in diabetic patients has been proposed to explain their reduced axial myopia.[33] It is therefore hypothesized that if natural CXL is associated with retardation of myopic progression, then artificially inducing CXL using UVA/riboflavin

might be used therapeutically to retard axial elongation and reduce the risk of blindness.35 Other treatment options exist, such as scleral reinforcement surgery,36 in which a strip of cadaveric sclera is wrapped around the globe to prevent further elongation.37,38 In one study, scleral reinforcement was usually successful in arresting the progression of myopia.39 However, such procedure is both highly invasive and relies on the availability of healthy scleral donor tissue, which is currently becoming scarcer with the increasing prevalence of myopia. Complications of high myopia, such staphylomata, may be sight-threatening. Staphylomata form as localized scleral ectasia having a radius of curvature less than the surrounding scleral curvature.40 Localized posterior scleral ectasia is an important component of several vision-threatening myopic maculopathies.41–43 It is theorized that the prevention of posterior staphyloma couldpreventfurthervisualimpairmentrelatedtomaculopathies.41 Because the formation of staphylomata involves localized scleral weakening, CXL might be a prophylactic measure to reinforce scleral tissue. The topographically differential effect of CXL might be useful as a treatment for staphylomata formation in various regions of the globe.

3.1.6 References

1. Saw SM, Shih-Yen EC, Koh A, Tan D. Interventions to retard myopia progression in children: an evidence-based update. *Ophthalmology* 2002;109:415-421; discussion 422-414; quiz 425-416, 443.

2. McBrien NA, Gentle A. Role of the sclera in the development and pathological complications of myopia. *Prog Retin Eye Res* 2003;22:307-338.

3. Bullimore MA, Jones LA, Moeschberger ML, Zadnik K, Payor RE. A retrospective study of myopia progression in adult contact lens wearers. *Invest Ophthalmol Vis Sci* 2002;43:2110-2113.

4. Young TL. Molecular genetics of human myopia: an update. *Optom Vis Sci* 2009;86:E8-E22.

5. Rada JA, Shelton S, Norton TT. The sclera and myopia. *Exp Eye Res* 2006;82:185-200.

6. Zhang M, Zou Y, Zhang F, Zhang X, Wang M. Efficacy of Blue-Light Cross-linking on Human Scleral Reinforcement. *Optom Vis Sci* 2015;92:873-878.

7. Curtin BJ, Iwamoto T, Renaldo DP. Normal and staphylomatous sclera of high myopia. An electron microscopic study. *Arch Ophthalmol* 1979;97:912-915.

8. Funata M, Tokoro T. Scleral change in experimentally myopic monkeys. *Graefes Arch Clin Exp Ophthalmol* 1990;228:174-179.

9. McBrien NA, Norton TT. Prevention of collagen crosslinking increases form-deprivation myopia in tree shrew. *Exp Eye Res* 1994;59:475-486.

10. Kennedy RH, Bourne WM, Dyer JA. A 48-year clinical and epidemiologic study of keratoconus. *Am J Ophthalmol* 1986;101:267-273.

11. Caporossi A, Baiocchi S, Mazzotta C, Traversi C, Caporossi T. Parasurgical therapy for keratoconus by riboflavin-ultraviolet type A rays induced cross-linking of corneal collagen: preliminary refractive results in an Italian study. *J Cataract Refract Surg* 2006;32:837-845.

12. Mazzotta C, Balestrazzi A, Traversi C, et al. Treatment of progressive keratoconus by riboflavin-UVA-induced cross-linking of corneal collagen: ultrastructural analysis by Heidelberg Retinal Tomograph II in vivo confocal microscopy in humans. *Cornea* 2007;26:390-397.

13. Spoerl E, Huhle M, Seiler T. Induction of cross-links in corneal tissue. *Exp Eye Res* 1998;66:97-103.

14. Wollensak G, Spoerl E, Seiler T. Riboflavin/ultraviolet-a-induced collagen crosslinking for the treatment of keratoconus. *Am J Ophthalmol* 2003;135:620-627.

15. Ziaei M, Barsam A, Shamie N, et al. Reshaping procedures for the surgical management of corneal ectasia. *J Cataract Refract Surg* 2015;41:842-872.

16. McCall AS, Kraft S, Edelhauser HF, et al. Mechanisms of corneal tissue cross-linking in response to treatment with topical riboflavin and long-wavelength ultraviolet radiation (UVA). *Invest Ophthalmol Vis Sci* 2010;51:129-138.

17. Wollensak G, Spoerl E, Seiler T. Stress-strain measurements of human and porcine corneas after riboflavin-ultraviolet-A-induced cross-linking. *J Cataract Refract Surg* 2003;29:1780-1785.

18. Henriquez MA, Villegas S, Rincon M, Maldonado C, Izquierdo L, Jr. Long-term efficacy and safety after corneal collagen crosslinking in pediatric patients: Three-year follow-up. *Eur J Ophthalmol* 2018;28:415-418.

19. Keeley FW, Morin JD, Vesely S. Characterization of collagen from normal human sclera. *Exp Eye Res* 1984;39:533-542.

20. Wollensak G, Spoerl E. Collagen crosslinking of human and porcine sclera. *J Cataract Refract Surg* 2004;30:689-695.

21. Wollensak G, Iomdina E, Dittert DD, Salamatina O, Stoltenburg G. Cross-linking of scleral collagen in the rabbit using riboflavin and UVA. *Acta Ophthalmol Scand* 2005;83:477-482.

22. Wang M, Zhang F, Qian X, Zhao X. Regional Biomechanical properties of human sclera after cross-linking by riboflavin/ultraviolet A. *J Refract Surg* 2012;28:723-728.

23. Vurgese S, Panda-Jonas S, Jonas JB. Scleral thickness in human eyes. *PLoS One* 2012;7:e29692.

24. Wollensak G, Iomdina E. Long-term biomechanical properties of rabbit sclera after collagen crosslinking using riboflavin and ultraviolet A (UVA). *Acta Ophthalmol* 2009;87:193-198.

25. Rosenblat E, Hersh PS. Intraoperative corneal thickness change and clinical outcomes after corneal collagen crosslinking: Standard crosslinking versus hypotonic riboflavin. *J Cataract Refract Surg* 2016;42:596-605.

26. Greenstein SA, Shah VP, Fry KL, Hersh PS. Corneal thickness changes after corneal collagen crosslinking for keratoconus and corneal ectasia: one-year results. *J Cataract Refract Surg* 2011;37:691-700.

27. Buchanan CI, Marsh RL. Effects of long-term exercise on the biomechanical properties of the Achilles tendon of guinea fowl. *J Appl Physiol (1985)* 2001;90:164-171.

28. McKee CT, Last JA, Russell P, Murphy CJ. Indentation versus tensile measurements of Young's modulus for soft biological tissues. *Tissue Eng Part B Rev* 2011;17:155-164.

29. Shadwick RE. Elastic energy storage in tendons: mechanical differences related to function and age. *J Appl Physiol (1985)* 1990;68:1033-1040.

30. Azizi E, Halenda GM, Roberts TJ. Mechanical properties of the gastrocnemius aponeurosis in wild turkeys. *Integr Comp Biol* 2009;49:51-58.

31. Wren TA, Yerby SA, Beaupre GS, Carter DR. Mechanical properties of the human achilles tendon. *Clin Biomech (Bristol, Avon)* 2001;16:245-251.

32. Awetissow ES. [The role of the sclera in the pathogenesis of progressive myopia (author's transl)]. *Klin Monbl Augenheilkd* 1980;176:777-781.

33. Logstrup N, Sjolie AK, Kyvik KO, Green A. Long-term influence of insulin dependent diabetes mellitus on refraction and its components: a population based twin study. *Br J Ophthalmol* 1997;81:343-349.

34. National Research Council (U.S.). Working Group on Myopia Prevalence and Progression. *Myopia : prevalence and progression*. Washington, D.C.: National Academy Press; 1989:xii, 113 p.

35. Elsheikh A, Phillips JR. Is scleral cross-linking a feasible treatment for myopia control? *Ophthalmic Physiol Opt* 2013;33:385-389.

36. Autrata R, Rehurek J. [Scleroplasty surgery in the treatment of progressive myopia in children]. *Cesk Slov Oftalmol* 1998;54:323-327.

37. Thompson FB. A simplified scleral reinforcement technique. *Am J Ophthalmol* 1978;86:782-790.

38. Snyder AA, Thompson FB. A simplified technique for surgical treatment of degenerative myopia. *Am J Ophthalmol* 1972;74:273-277.

39. Balashova NV, Ghaffariyeh A, Honarpisheh N. Scleroplasty in progressive myopia. *Eye (Lond)* 2010;24:1303.

40. Spaide RF, Ohno-Matsui K, Yannuzzi LA. *Pathologic myopia*. New York: Springer; 2014:xvii, 376 pages.

41. Hayashi K, Ohno-Matsui K, Shimada N, et al. Long-term pattern of progression of myopic maculopathy: a natural history study. *Ophthalmology* 2010;117:1595-1611, 1611 e1591-1594.

42. Ohno-Matsui K, Kawasaki R, Jonas JB, et al. International photographic classification and grading system for myopic maculopathy. *Am J Ophthalmol* 2015;159:877-883 e877.

43. Ohno-Matsui K, Lai TY, Lai CC, Cheung CM. Updates of pathologic myopia. *Prog Retin Eye Res* 2016;52:156-187.

3.2 Orbital Fat Volume After Treatment with Topical Prostaglandin Agonists

Jessica Chen[1], Alan Le[2-4], Joseph Caprioli[2,4], JoAnn A. Giaconi[2,4], Kouros Nouri-Mahdavi[2-4],Simon K. Law[1,2,4], Laura Bonelli[2,4], Anne L. Coleman[2,4,6], and Joseph L. Demer[2-5]

[1]Computational and Systems Biology Interdepartmental Program; [2]Department of Ophthalmology; [3]Bioengineering Interdepartmental Program; [4]Stein Eye Institute; [5]Department of Neurology; [6]Department of Epidemiology, Jonathan and Karin Fielding School of Public Health of the University of California, Los Angeles.

3.2.1 Abstract

Purpose. Topical prostaglandin analogs (PGAs) are common treatment for primary open angle glaucoma (POAG), but reportedly may cause adnexal fat atrophy. We asked if patients with POAG treated with PGAs have abnormalities in orbital fat volume (OFV).

Methods. We studied 23 subjects with POAG who had never experienced intraocular pressure (IOP) exceeding 21 mmHg, and were chronically treated with PGAs, in comparison with 21 age-matched controls. Orbital volume, non-fat orbital tissue volume, and OFV were measured using high resolution magnetic resonance imaging.

Results. Subjects with POAG had been treated with PGAs for 39±19 months (SD) and were all treated within the 4 months preceding study. In the region from trochlea to orbital apex, OFV in POAG was significantly less at 9.8±1.9mL than in the control subjects at 11.1±1.3mL (P=0.019). However, between the globe-optic nerve junction (GONJ) and trochlea, OFV was similar in both groups. Width and cross sectional area of the bony orbit were significantly smaller in POAG than in controls (P<0.0001). Posterior to the GONJ, the average orbital cross sectional area was 68.2mm^2 smaller, and the orbital width averaged 1.5mm smaller throughout the orbit, in patients with POAG than in controls.

Conclusions. Patients with POAG who have been treated with PGAs have lower overall OFV than controls, but OFV in the anterior orbit is similar in both groups. Lower overall OFV in POAG may be a primary association of this disorder with a horizontally narrower bony orbit, which may be a risk factor for POAG at non-elevated IOPs.

3.2.2 Introduction

Glaucoma is the leading cause of irreversible blindness.[1, 2] Prostaglandin analogs (PGAs) are a commonly applied topically to the eye as first line treatment for primary open angle glaucoma (POAG) because they reduce intraocular pressure (IOP) through facilitation of aqueous outflow[3-6] and are convenient and well-tolerated. However, topical PGA agents reportedly cause periorbital fat atrophy, deepening of the superior sulcus, ptosis,[7-9] and have been claimed to induce enophthalmos in some patients.[7, 10, 11] Recently, Higashiyama et al. used standard magnetic resonance imaging (MRI) to compare orbital fat volume (OFV) in 9 patients treated monocularly with brimatoprost for various secondary glaucoma for at least 11 months, reporting mean OFV to be significantly smaller in the treated than nontreated eye.[12] There is no comparable study of the effects of PGAs in POAG without abnormally elevated IOP.

The pathogenic role of IOP elevated well above the statistically normal range of up to 22mmHg is undisputed in congenital and juvenile glaucoma,[13] angle closure,[14] uveitic,[15] and traumatic glaucoma,[16] because IOP is typically highly elevated and progression of optic neuropathy is decisively attenuated when IOP is normalized in these disorders. Nevertheless, elevated IOP is no longer a diagnostic criterion for POAG, recognizing that many such patients, including the great majority of Asians,[17-22] do not exhibit abnormally high IOP[23] yet suffer progressive glaucomatous optic neuropathy even at lower IOPs.[24] Such observations mandate consideration of other as causes of POAG. Eye-movement related deformation of the optic nerve (ON) has been suggested as another possible mechanical etiology for optic neuropathy in POAG.[25-28] Adduction may be particularly pathogenic, because ON length is insufficient to avert tethering the globe in adduction.[25] Optical coherence tomography shows that when adduction exceeds 26°,[29] deformations of the ON head and Bruch's membrane greatly exceed

those during extreme IOP elevation,[30] or deformations recently proposed as pathological to retina.[31] These large eye movements occur often, as 25-45° saccades are frequent in daily life when the head and body are unrestrained.[32] When head movements combined with eye movements, gaze shifts average around 30°.[33] MRI has demonstrated significant globe retraction in adduction in patients who have POAG without elevated IOP, but not in controls.[27] This globe retraction suggests that adduction tethering induces mechanical strain on the globe's suspensory tissues, including the orbital fat. However, it is not clear if abnormally great globe retraction in adduction in POAG is due to abnormally great ON traction in such patients, versus more compliant retrobulbar tissues providing less mechanical resistance to normal ON traction in adduction. If topical PGAs do induce atrophy of retrobulbar orbital fat, the remaining tissues might become more compliant. Such a finding of orbital fat atrophy would then suggest that the observed globe retraction in adduction in POAG patients who have been treated with PGAs is merely an epiphenomenon of therapy, rather than related to the pathogenesis of the disease.

Another consideration in evaluating the possible effect of PGAs is the total volume of the orbit itself. Possible variations in the size and shape of the orbit have not been previously considered in relationship to PGA therapy.

In this study, we sought to clarify the foregoing questions through high resolution, surface coil MRI of OFV and orbital dimensions in patients with POAG without abnormally elevated IOP who had been treated with topical PGA drugs. We aimed to extend the literature beyond the small number of previously-reported patients who were monocularly-treated for secondary glaucoma,[12] and to evaluate the anatomical compartments where the orbital fat resides.

3.2.3 Methods

Subjects

This study was conducted according to a protocol approved by the Institutional Review Board for Protection of Human Subjects of the University of California, Los Angeles, and conformed to the tenets of the Declaration of Helsinki. Subjects gave written informed consent prior to participation.

Included were 23 patients (13 females, 10 males, average age 63±11 yrs (SD), range 52-83 yrs) diagnosed by a co-author who is a glaucoma specialist to have POAG, but who had never had an IOP exceeding 21 mmHg, with or without treatment. Subjects in the POAG group included 11 Asians, 11 Caucasians, and 1 African American. This distribution of ethnicity did not differ significantly from that of the control group (χ^2: P>0.1). All patients had been cumulatively treated with topical PGAs for an average of 39±19 months, and had been treated within the four months preceding the study. Six patients were treated with bimatoprost, 11 with latanoprost, 5 with tafluprost, 1 with travoprost. Most patients also received additional topical glaucoma medications. Patients were excluded if they had previously undergone intraocular surgeries besides those for cataract, glaucoma, refractive error; or if they had orbital disease, or if they had any other cause for optic neuropathy. Since patients with POAG at our institution are almost universally treated with topical PGAs, it was not possible to recruit a control group with POAG who were not exposed to these drugs.

A healthy control group without POAG was recruited through advertisement, consisting of 15 females and 6 males, with average age 62±10 yrs (range 47-78 yrs). Subjects in the control group included 2 Asians, 11 Caucasians, and 8 African Americans. Control subjects were required to have corrected visual acuity of 20/20 in

each eye, normal IOP, no history of ocular surgeries besides those for cataract or refractive error, no ocular trauma, and no other ocular disorder except for refractive error or lens opacity. None had been treated with PGAs or any other ocular hypotensive agents.

Magnetic Resonance Imaging

An author performed high resolution MRI using a 1.5T General Electric Signa scanner and custom surface coils (Medical Advances, Milwaukee, WI) with T2 fast spin echo pulse sequence as described.[34, 35] In order to minimize movement artifacts, subjects monocularly fixated an illuminated, fiber optic target in central gaze. Axial 2-mm thick images (100x100 mm field of view, 256x256 matrix) including both orbits were obtained to determine distances between the orbital apex, globe-optic nerve junction (GONJ), and trochlea. Quasi-coronal sets of 17–20, 2mm thick planes perpendicular to the long orbital axis were obtained separately for each orbit (field of view 80x80 mm, 256x256 matrix, resolution 312 microns).

Image Analysis

Quasi-coronal images were rotated as necessary to align the midline of the brain to vertical. Using the program *ImageJ64* (W. Rasband, National Institutes of Health, Bethesda, Maryland, USA; http://rsb.info.nih.gov/ij/, 1997-2018, in public domain), the extraocular muscles, ON, globe, orbit, blood vessels, and large nerves were manually traced in contiguous, quasi-coronal planes from the deep orbit to the trochlea (Fig. 1). Segmentation and measurements were performed independently by two graders to ascertain agreement. All subsequent measurements and calculations were automated through ImageJ macro scripts, ensuring rigor and reproducibility. Orbit volume (OV) was calculated by summing areas within the orbital borders in each image plane from the orbital apex to the trochlea, which was selected as an anatomical reference since it is

fixed to the medial orbital wall. The summed areas were then integrated through all image planes by multiplying by the 2mm image plane thickness to obtain the OV. We determined OFV by subtracting from the orbital areas, the cross-sectional areas of the other intraorbital tissues, including globe, muscles, nerves, and blood vessels (Fig. 1), then multiplying by the 2mm image plane thickness.

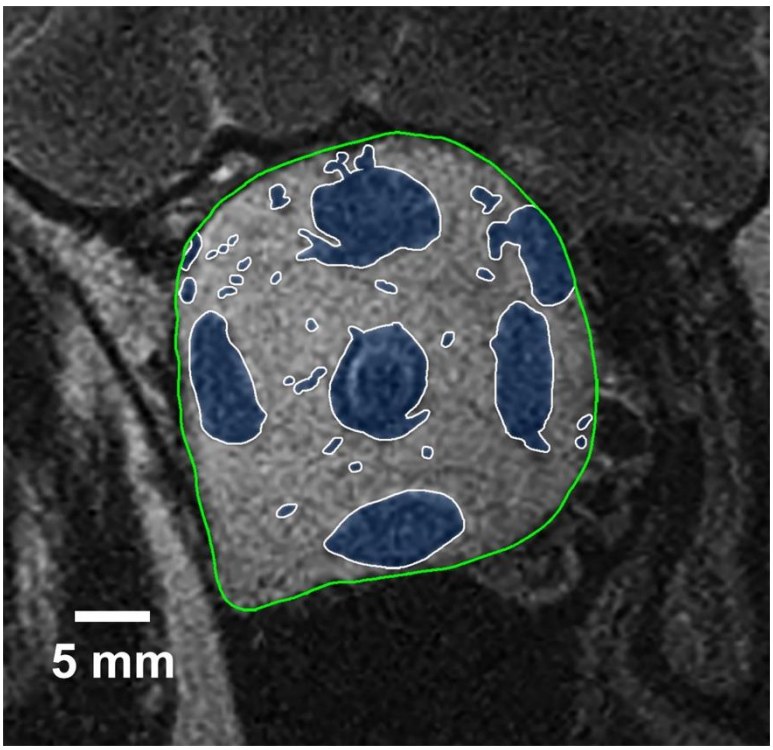

Figure 1. Quasi-coronal MRI in the mid-portion of a representative right orbit, whose bony walls are outlined in green. Intra-orbital structures including extraocular muscles, ON, and blood vessels, are outlined in white and shaded blue. Orbital fat represents the remaining orbital area excluding structures shaded in blue.

Axial images were used to measure Cartesian distances in three dimensions across multiple planes between the trochlea, GONJ, and orbital apex. The orbital apex was defined in axial planes by the intersection of lines running formed by the centers of the lateral and medial rectus muscles (Fig. 2).

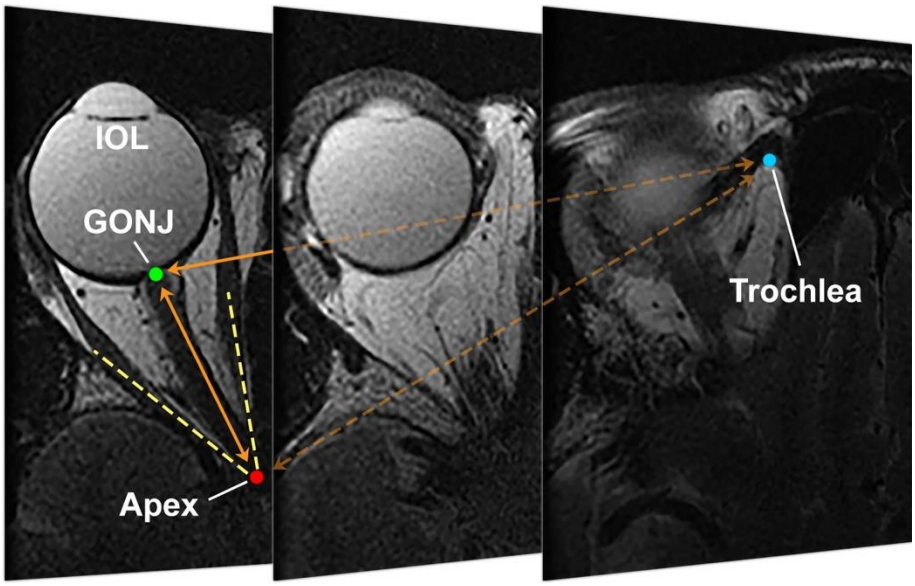

Figure 2. Axial MRI of representative orbit in pseudophakic subject, with contiguous 2 mm thick image planes arranged from inferior at mid-globe at left, to superior at right with the plane including the trochlea. GONJ – globe-optic nerve junction. IOL – intraocular lens.

The orbit does not have a regular shape amenable to simple geometric description. Therefore, the horizontal width of the orbit was determined by averaging its horizontal dimension within the central 60% of its vertical extent, as sampled at 15 equal intervals (Fig. 3). Horizontal width was averaged in each MRI plane from the GONJ to the trochlea in order to compute average orbital width. Using analogous parameters, average vertical height of the orbit was also obtained.

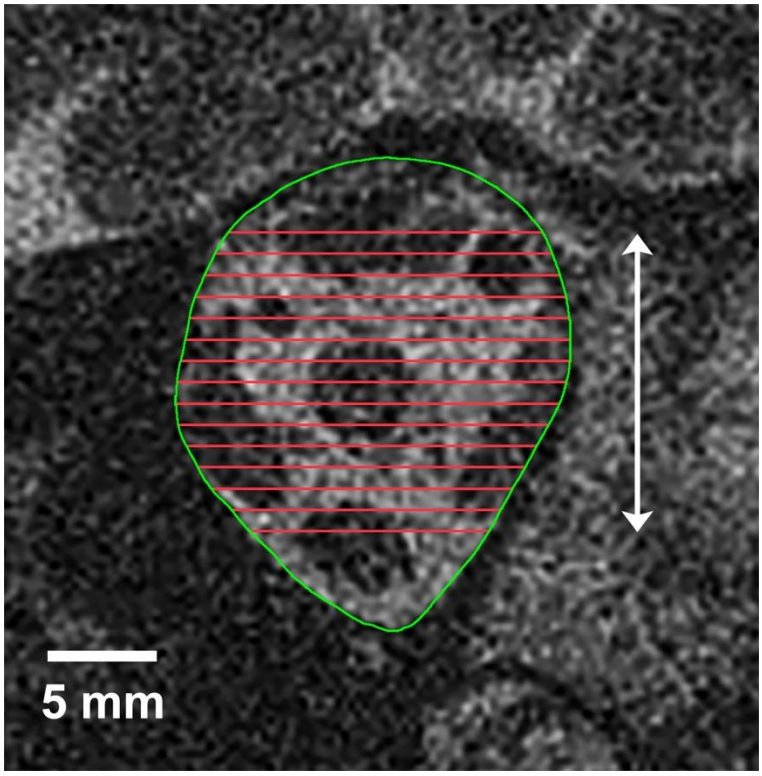

Figure 3. Horizontal width of each quasi-coronal image was sampled 15 times (red lines) at uniformly-spaced vertical intervals spanning the middle 60% of the vertical extend of the orbit (white arrow). These measurements were averaged to compute orbital width in each image plane.

Statistical Analysis

To account for possible intraocular correlation between eyes of the same subject, statistical analysis was conducted with generalized estimating equations (GEE) implemented in SPSS software (Version 24.0; IBM Corp., Armonk, NY, USA), designating the eye as a within-subject variable, and including effects of subject age and race as factors. Type 1 error characteristics of GEE are superior to t-testing for the data.[36] Statistical significance was defined as $P<0.05$. All measurements were independently duplicated by two authors, and subjected to Bland-Altman analysis to ascertain reproducibility.

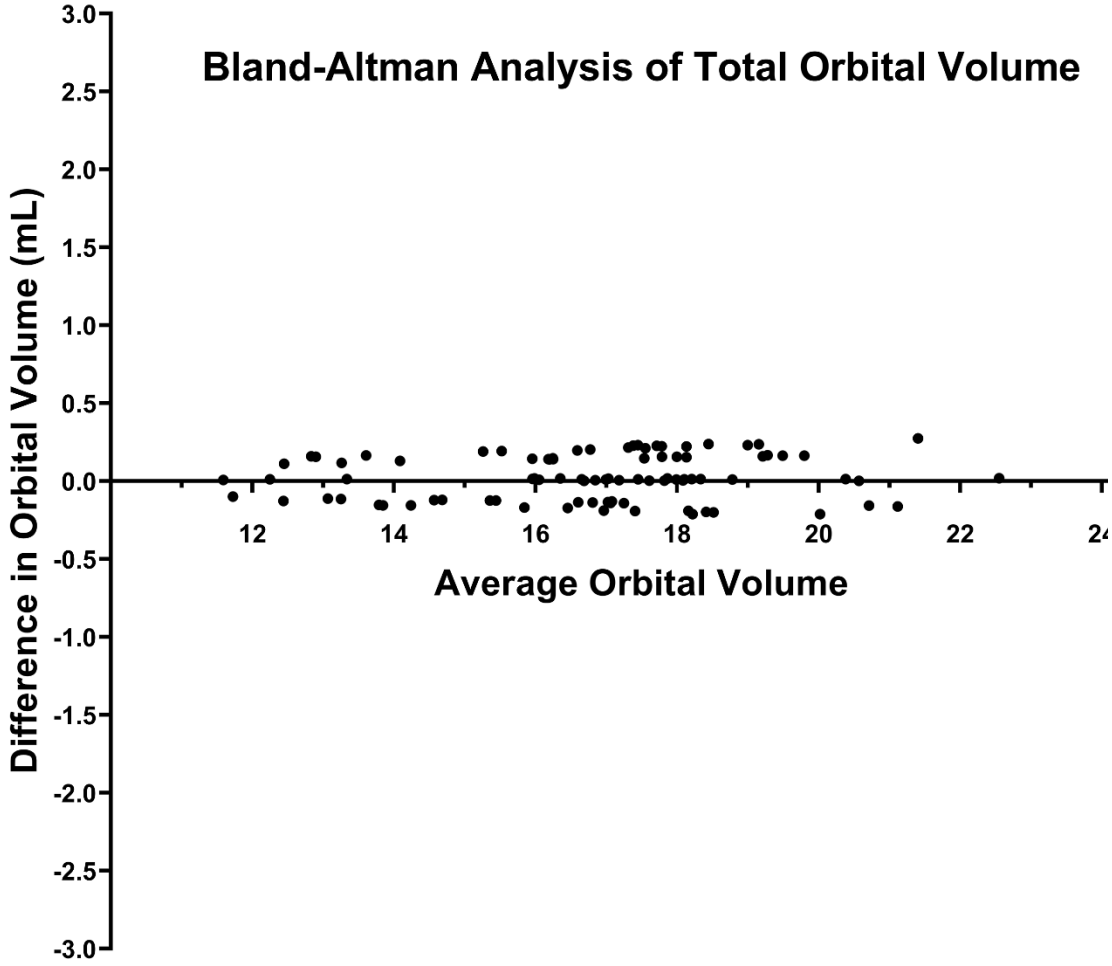

Figure 4. Bland-Altman plot of agreement between two independent observers measuring OV in all subjects. Abscissa plots the averages of each pair of measurements, and ordinate the differences within these pairs.

3.2.4 Results

Reproducibility

Agreement between measurements of OV by two independent observers was evaluated by Bland-Altman analysis, as illustrated in Fig. 4. This analysis yielded a minimal bias of 0.023 that is about 0.14% of the 16.8mL average.

Orbital Fat Volume

While total OFV from apex to trochlea in POAG was significantly less than in controls, the difference was driven by the posterior orbit, not by the anterior orbit. Volume of fat in the whole orbit measured from apex to trochlea (Fig. 5A) was significantly less in POAG without abnormally elevated IOP at 9.7±1.9mL (SD) than in controls at 10.9±1.3mL (P=0.019). Fat volume in only the deep orbit from the orbital apex to GONJ was also significantly less in POAG at 6.0±1.7mL for POAG than in controls at 7.5±1.6mL (P=0.001). However, in the anterior orbit between GONJ and the trochlea, the two groups had similar fat volumes: 3.7±0.9mL for POAG and 3.5±0.9mL for controls (P=0.465). The total volume of intraorbital tissues, comprising the globe, ON, muscle, nerves, and blood vessels, did not differ significantly between POAG (6.5±1.2mL) and controls (6.4±1.1mL, P=0.610).

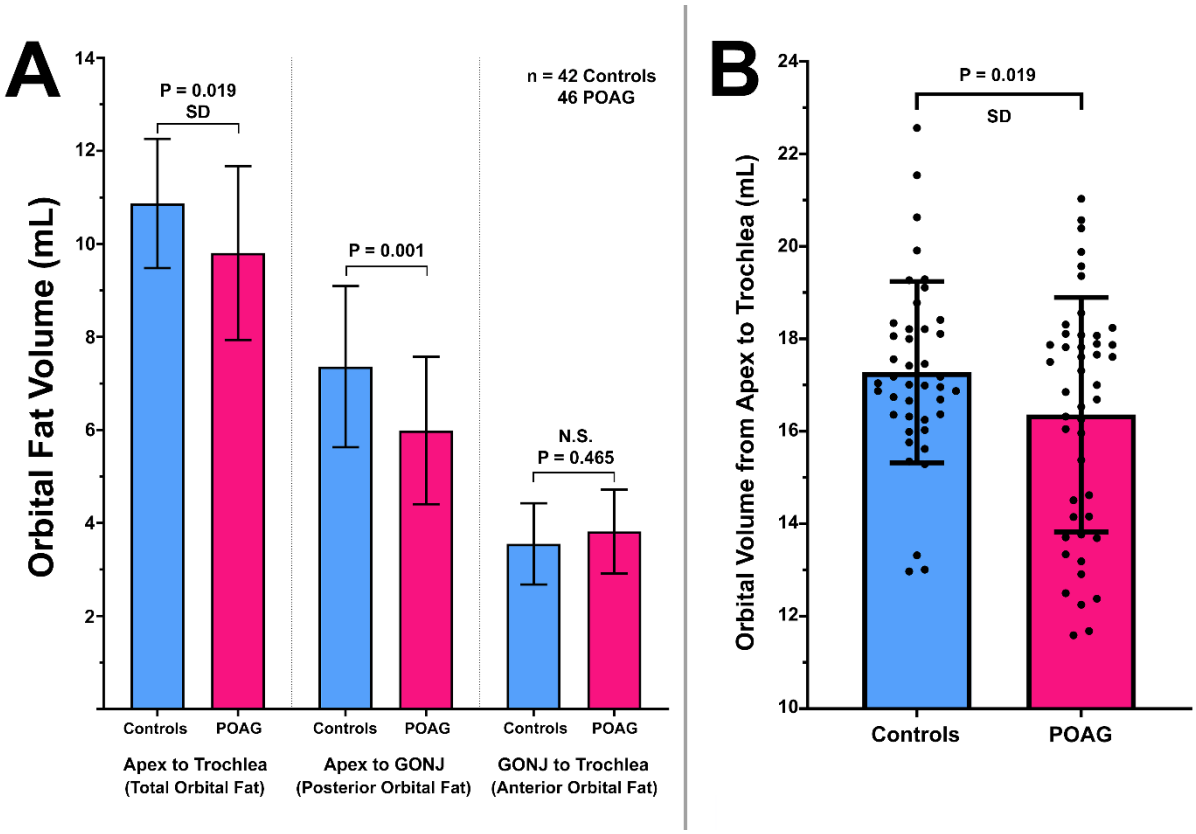

Figure 5. A. Orbital fat volume (OFV) in controls and patients with POAG without abnormally elevated IOP who were treated with topical PGAs. While total OFV from apex to trochlea in POAG was significantly less in patients than controls (left paired columns), the difference was driven by the posterior orbit from apex to the GONJ (middle paired columns). In the anterior orbit from the GONJ to the trochlea (right paired columns), OFV was similar in the two groups. B. Total orbital volume (OV) of patients with POAG was significantly less than in controls. SD – standard deviation. N.S. – not significant.

Total OV measured from the apex to the trochlea was significantly less in patients with POAG at 16.3±2.5mL than in controls at 17.4±2.0mL (P=0.019, Fig. 5B). The individual data points in Fig. 5B suggest a possible bimodal distribution in the POAG group. This pattern is not attributable to gender because males are females were similarly distributed throughout the range of measurements.

Orbital Depth

The distances between the apex, trochlea, and GONJ were similar at about 41 mm in POAG and controls (P>0.08, Fig. 6). Since the GONJ is a feature of the posterior globe, this indicates that anteroposterior globe position was similar in the two groups.

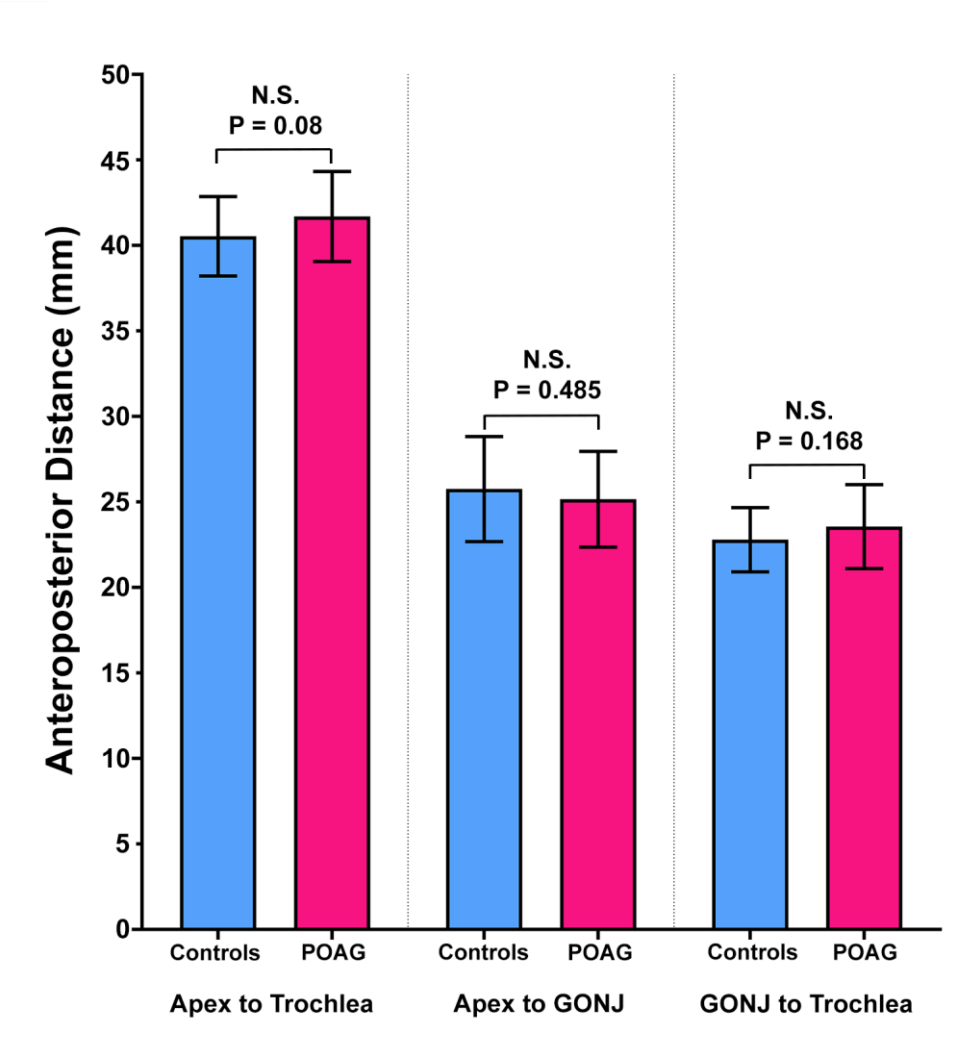

Figure 6. Anteroposterior dimensions of the orbit and position of the GONJ, did not differ between patients with POAG and the controls. N.S. – not significant.

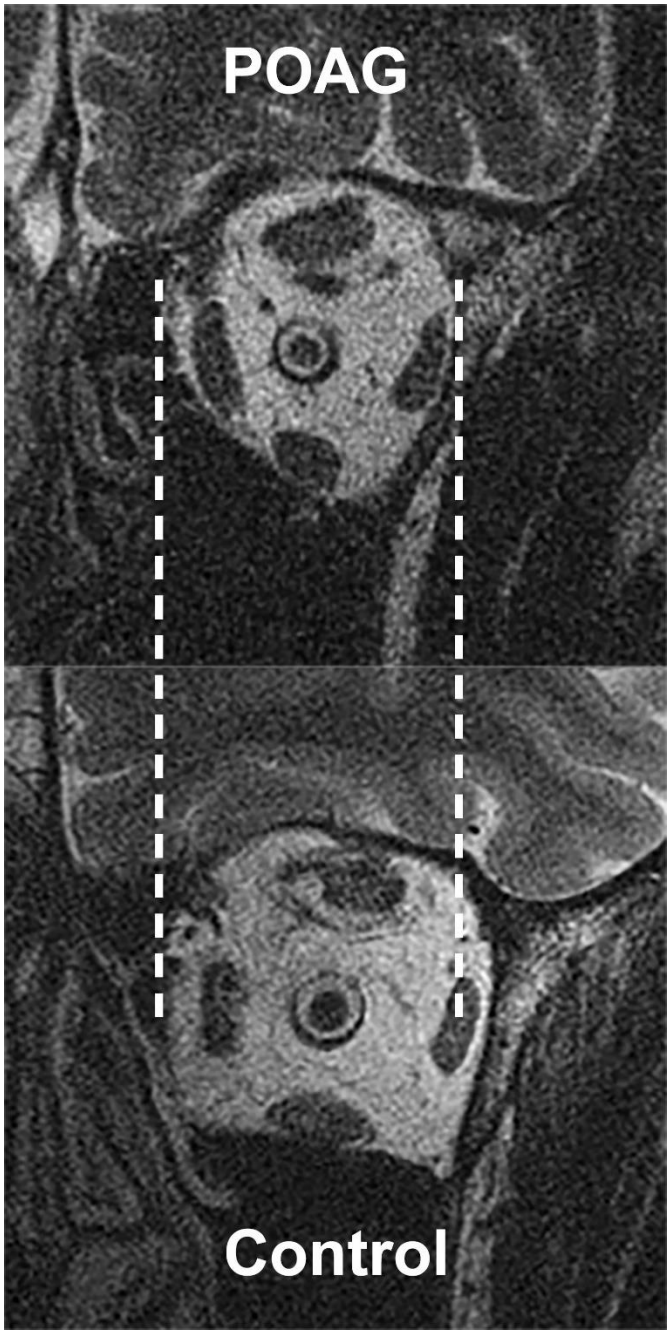

Figure 7. Quasi-coronal MRI just posterior to the GONJ illustrating that the orbit of a typical patient with POAG is horizontally narrower that than of a representative control.

Orbital Dimensions

This difference in OV between patients with POAG and controls is attributable to difference in orbital profile, exemplified by the two MRI images taken at the same image plane immediately posterior to the GONJ as illustrated in Fig. 7. Patients with POAG had

significantly smaller average orbital cross sectional areas than controls throughout the orbit, with the exception of only the two most anterior image planes that were similar (Fig. 8). In the range from 0 and 28mm posterior to the GONJ, the average difference in orbital cross-sectional areas between controls and patients with POAG was 68.2mm^2 (range 43.3 mm^2 to 79.7mm^2). Orbits were also significantly narrower horizontally in POAG than in controls (Fig. 9, P<0.001, ANOVA), again with the exception of only the two most anterior image planes. The average difference in width of the orbit from 0 and 28 mm posterior to the GONJ between controls and patients with POAG was 1.5mm (range 1.3 – 1.7mm). Similarly, the vertical dimension of the orbit was significantly greater in controls than in POAG (P<0.001, ANOVA). The average difference in orbital width between groups in the 28 mm region just posterior to the GONJ was 0.81mm (range 0.4-1.1mm).

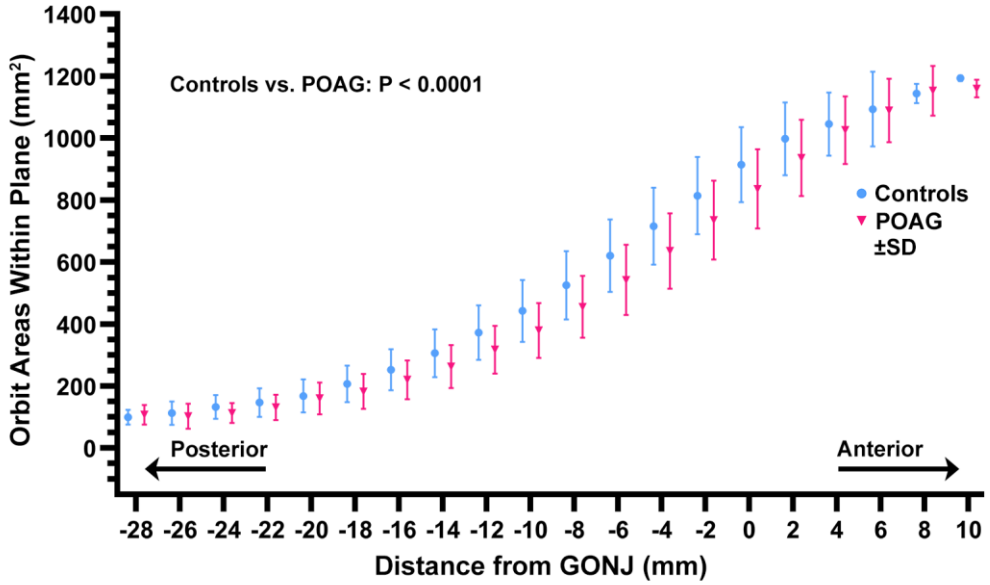

Figure 8. Mean cross sectional area of the orbit along its anteroposterior extent in patients with POAG and controls. Except at the extreme ends of the orbit, cross sectional area was significantly less in POAG than in controls. SD - standard deviation. Differences between groups were significant at P<0.0001 by ANOVA.

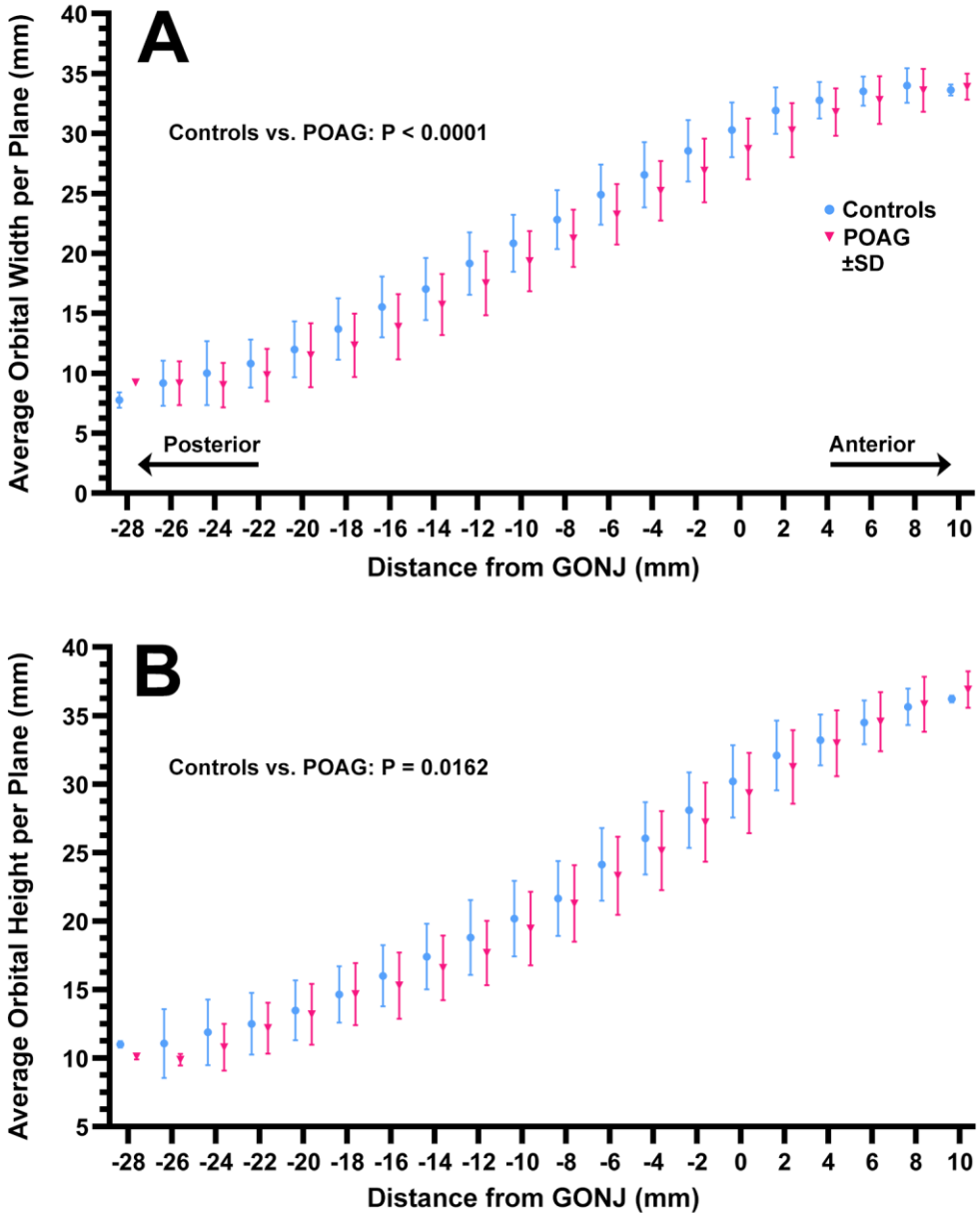

Figure 9. Mean orbital dimensions along the anteroposterior extent of the orbit in patients with POAG and controls. A. width. B. height. SD - standard deviation. Differences between groups were significant at P<0.0001 by ANOVA.

Effects of Age, Race, and Gender

Multivariate analysis showed that age and race had insignificant effects on overall OFV (P = 0.679 and P = 0.388, respectively), posterior fat volume between the apex and GONJ (P = 0.292, P = 0.154, respectively), and orbital volume anterior to the GONJ (P = 0.939, P = 0.840, respectively). Due to the observed imbalance in gender among controls with 15 females and 6 males, the possibility of confounding by differences based on gender was investigated. There was a significant difference in OV between females and males in both the control and POAG groups (P = 0.02, P = 0.003, respectively), with average OV 18.4±0.6mL in control males, 17.6±0.6mL in males with POAG. Both groups of females had lower OV than both groups of males: 16.89±0.3mL in control females, and 15.43±0.4mL in females with POAG. When controls and subjects with POAG were pooled, the OV of males was significantly greater at 17.9±0.4mL than females at 16.2±0.3mL (P = 0.001).

We employed a bootstrap approach to investigate whether these gender differences had confounded the apparent significant differences in OV and total OFV between controls and subjects with POAG. Multiple subgroup analyses with 5 random samples were performed after random exclusion of individual females from the control group to achieve the same gender balance as in the POAG group in whom the full sample already included gender balance. Statistical analyses were repeated after different random exclusions of female subjects. The 1.1-1.2mL less OV in patients with POAG than controls remained significant after gender-balancing (range: P = 0.0018 to P = 0.007), with 17.6±0.4mL OV in gender-balanced controls, and 16.4±0.4mL in subjects with POAG. The difference in total OFV also remained significant at about 1.2 mL after gender balancing the control subgroup (range: P = 0.002 to P = 0.005), with 11.0±0.3mL OFV in gender-balanced controls and 9.8±0.3mL in subjects with POAG. The

persistence of these statistically significant differences suggest that gender differences do not account for the findings of subnormal OV and OFV in subjects with POAG.

3.2.5 Discussion

This study demonstrates that patients with POAG at low IOP who have been treated with topical PGAs do indeed have less total orbital fat than age matched control subjects not treated with PGAs. However, the volume of fat in the orbit anterior to the GONJ, the region most directly exposed to topical PGA treatment, did not significantly differ between patients with POAG and controls. Only in the deeper orbit, beginning in planes 2 to 4mm anterior to the GONJ and deeper, did patients with POAG have less fat than controls. Since the combined volume of non-fat orbital structures such as extraocular muscles, nerves, and vessels, was similar in both groups, the lesser orbital fat in patients with POAG is due to their smaller bony orbits. Consequently, the lesser orbital fat volume in patients with POAG is unlikely to be the consequence of PGA exposure, but rather related to POAG itself. Direct measurement of orbital size confirmed that patients with POAG have both horizontally and vertically narrower bony orbits than controls throughout in the orbit except most anteriorly (Fig. 7), although orbital depth was similar in the two groups. Taken together, these findings fulfill the main aim of the study and support the inference that topical PGA exposure are not the cause of subnormal OFV in patients with POAG at normal IOP. Moreover, these results suggest instead that a horizontally narrower bony orbit may be a risk factor for POAG at normal IOP.

The Higashiyama et al. study used MRI to compare OFV in 9 patients treated monocularly with brimatoprost for secondary glaucomas for at least 11 months. In comparison to the untreated fellow eyes, they reported mean OFV to be significantly smaller in the treated than nontreated eye.[12] However, the modest 0.04 level of

statistical significance for this small study was driven by a single patient who had an abnormally high OFV in the untreated fellow orbit.[12]

The present study was motivated by recognition that adipogenesis is inhibited by PGAs through activation of the FP receptor, which may cause fat atrophy.[37, 38] Common PGAs used today to reduce IOP include latanoprost, timolol, bimatoprost, travoprost, and tafluprost, as well as fixed combinations like latanoprost-timolol, bimatoprost-timolol, travoprost-timolol, and tafluprost-timolol.[39] Several clinical features have been associated with prostaglandin periorbitopathy that may occur in about half of patients after more than one year bilateral treatment with topical latanoprost: deepening of the upper eyelid sulcus, upper blepharoptosis, effacement of the lower eyelid fat pads, and inferior scleral show.[11, 40, 41] One retrospective study has suggested that enophthalmos may occur in eyes unilaterally treated with latanoprost.[42] However, enophthalmos is not typically reported in patients with POAG, and would not have been significant in the Higashiyama et al.'s small unilateral treatment study, except with the inclusion of one marked outlier case.[12]

Orbital geometry appears to be a distinguishing feature of POAG. The bony orbit has been reported to be slightly larger in older than younger people,[43] and to enlarge in thyroid eye disease,[44] although we are unaware of any reports of changes in bony orbital size associated with exposure to PGA drugs. The present study showed that the orbit is smaller in females than males, but also suggest that orbital geometry may influence development of glaucoma through an IOP independent mechanism. There is evidence that when the globe adducts, the ON becomes tethered, pulls against the GONJ[25, 29, 45] and causes lateral translation and retraction of the globe. Since orbits of subjects with POAG are horizontally narrower and vertically shorter than normal even up to 4 mm anterior to the globe-optic nerve junction, this may restrict mediolateral globe translation,

increase globe retraction, and increase tension along the taut ON. If PGA had actually reduced posterior OVF, this might have ameliorated ON tethering in adduction by allowing the globe to shift posteriorly. However, the present study did not find evidence of reduction of retrobulbar OFV caused by topical PGA agents. Absence of topical PGA effects on posterior OFV is not surprising in view of the extensive anterior tissue barriers and high vascularity of the orbit that would inhibit penetration of topical agents into the deep orbit.

Not all patients with POAG at normal IOP exhibited a similar degree of orbital narrowing. The distribution of data raises the possibility that apparently lower OV in the POAG group might be attributable to a subgroup of at least 8 orbits of patients with POAG having OV both less than the other patients with POAG, and also less than the controls (Fig. 5B). This study took the unbiased approach of including every data observation. The current study was not designed with power to detect possible subgroup effects such as bimodal distribution of OV, so its significance, and the possible effects of outliers generally, cannot be known with certainty. However, even if OV is actually normal is some patients with POAG who do not have elevated IOP, the findings nevertheless argue against any effects of PGA therapy in reduction of posterior OFV in this disease.

3.2.6 References

1. Kapetanakis VV, Chan MP, Foster PJ, Cook DG, Owen CG, Rudnicka AR. Global variations and time trends in the prevalence of primary open angle glaucoma (POAG): A systematic review and meta-analysis. *Br J Ophthalmol* 2016;100:86-93.

2. Kingman S. Glaucoma is second leading cause of blindness globally. *Bulletin of the World Health Organization* 2004;82:887-888.

3. Li T, Lindsley K, Rouse B, et al. Comparative effectiveness of first-line medications for primary open-angle glaucoma: A systematic review and network meta-analysis. *Ophthalmology* 2016;123:129-140.

4. Wang K, Xu L, Yuan Z, et al. Intraocular pressure-lowering efficacy and safety of bimatoprost 0.03% therapy for primary open-angle glaucoma and ocular hypertension patients in China. *BMC Ophthalmol* 2014;14:21.

5. Winkler NS, Fautsch MP. Effects of prostaglandin analogues on aqueous humor outflow pathways. *J Ocul Pharmacol Ther* 2014;30:102-109.

6. Aptel F, Cucherat M, Denis P. Efficacy and tolerability of prostaglandin analogs: a meta-analysis of randomized controlled clinical trials. *J Glaucoma* 2008;17:667-673.

7. Shrirao N, Khurana M, Mukherjee B. Prostaglandin-associated periorbitopathy. *Indian J Ophthalmol* 2016;64:459.

8. Peplinski LS, Albiani Smith K. Deepening of lid sulcus from topical bimatoprost therapy. *Optom Vis Sci* 2004;81:574-577.

9. Jayaprakasam A, Ghazi-Nouri S. Periorbital fat atrophy - an unfamiliar side effect of prostaglandin analogues. *Orbit* 2010;29:357-359.

10. Tappeiner C, Perren B, Iliev ME, Frueh BE, Goldblum D. [Orbital fat atrophy in glaucoma patients treated with topical bimatoprost--can bimatoprost cause enophthalmos?]. *Klin Monbl Augenheilkd* 2008;225:443-445.

11. Rabinowitz MP, Katz LJ, Moster MR, et al. Unilateral prostaglandin-associated periorbitopathy: A syndrome involving upper eyelid retraction distinguishable from the aging sunken eyelid. *Ophthalmic Plast Reconstr Surg* 2015;31:373-378.

12. Higashiyama T, Minamikawa T, Kakinoki M, Sawada O, Ohji M. Decreased orbital fat and enophthalmos due to bimatoprost: Quantitative analysis using magnetic resonance imaging. *PLoS One* 2019;14:e0214065.

13. Chang I, Caprioli J, Ou Y. Surgical management of pediatric glaucoma. *Dev Ophthalmol* 2017;59:165-178.

14. Zhang X, Liu Y, Wang W, et al. Why does acute primary angle closure happen? Potential risk factors for acute primary angle closure. *Surv Ophthalmol* 2017;62:635-647.

15. Tan AN, Cornelissen MF, Webers CAB, Erckens RJ, Berendschot T, Beckers HJM. Outcomes of severe uveitic glaucoma treated with Baerveldt implant: can blindness be prevented? *Acta Ophthalmol* 2018;96:24-30.

16. Bai HQ, Yao L, Wang DB, Jin R, Wang YX. Causes and treatments of traumatic secondary glaucoma. *Eur J Ophthalmol* 2009;19:201-206.

17. Shi D, Funayama T, Mashima Y, et al. Association of HK2 and NCK2 with normal tension glaucoma in the Japanese population. *PLoS One* 2013;8:e54115.

18. Iwase A, Suzuki Y, Araie M, et al. The prevalence of primary open-angle glaucoma in Japanese: the Tajimi Study. *Ophthalmology* 2004;111:1641-1648.

19. Ha A, Kim YK, Jeoumg JW, Kim DM, Park KH. Association of angle width with progression of normal-tension glaucoma. A minimum 7-year follow-up study. *JAMA Ophthalmol* 2019;137:13-20.

20. Zhao J, Solano MM, Oldenburg CE, et al. Prevalence of normal-tension glaucoma in the Chinese population: A systematic review and meta-analysis. *Am J Ophthalmol* 2019;199:101-110.

21. Kim CS, Seong GJ, Lee NH, Song KC, Namil Study Group KGS. Prevalence of primary open-angle glaucoma in central South Korea the Namil study. *Ophthalmology* 2011;118:1024-1030.

22. Sakata R, Yoshitomi T, Iwase A, et al. Factors associated with progression of Japanese open-angle glaucoma with lower normal intraocular pressure. *Ophthalmology* 2019;126:1107-1116.

23. Kim JA, Kim TW, Lee EJ, Girard MJA, Mari JM. Lamina cribrosa morphology in glaucomatous eyes with hemifield defect in a Korean population. *Ophthalmology* 2019;126:692-701.

24. Killer HE, Pircher A. Normal tension glaucoma: review of current understanding and mechanisms of the pathogenesis. *Eye (Lond)* 2018;32:924-930.

25. Demer JL. Optic nerve sheath as a novel mechanical load on the globe in ocular duction. *Invest Ophthalmol Vis Sci* 2016;57:1826-1838.

26. Wang X, Fisher LK, Milea D, Jonas JB, Girard MJ. Predictions of optic nerve traction forces and peripapillary tissue stresses following horizontal eye movements. *Invest Ophthalmol Vis Sci* 2017;58:2044-2053.

27. Demer JL, Clark RA, Suh SY, et al. Magnetic resonance imaging of optic nerve traction during adduction in primary open-angle glaucoma with normal intraocular pressure. *Invest Ophthalmol Vis Sci* 2017;58:4114-4125.

28. Shin A, Yoo L, Park J, Demer JL. Finite element biomechanics of optic nerve sheath traction in adduction. *J Biomech Eng* 2017;139.

29. Suh SY, Le A, Shin A, Park J, Demer JL. Progressive deformation of the optic nerve head and peripapillary structures by graded horizontal duction. *Invest Ophthalmol Vis Sci* 2017;58:5015-5021.

30. Wang YX, Jiang R, Wang NL, Xu L, Jonas JB. Acute peripapillary retinal pigment epithelium changes associated with acute intraocular pressure elevation. *Ophthalmology* 2015;122:2022-2028.

31. Fortune B. Pulling and tugging on the retina: Mechanical impact of glaucoma beyond the optic nerve head. *Inv Ophtalmol Vis Sci* 2019;60:26-35.

32. Anastasopoulos D, Ziavra N, Hollands M, Bronstein A. Gaze displacement and inter-segmental coordination during large whole body voluntary rotations. *Exp Brain Res* 2009;193:323-336.

33. Tomlinson RD, Bahra PS. Combined eye-head gaze shifts in the primate. II. Interactions between saccades and the vestibuloocular reflex. *J Neurophysiol* 1986;56:1558-1570.

34. Demer JL, Dushyanth A. T2-weighted fast spin-echo magnetic resonance imaging of extraocular muscles. *J AAPOS* 2011;15:17-23.

35. Demer JL, Clark RA. Magnetic resonance imaging demonstrates compartmental muscle mechanisms of human vertical fusional vergence. *J Neurophysiol* 2015;113:2150-2163.

36. Huang J, Huang JY, Chen Y, Ying GS. Evaluation of Approaches to Analyzing Continuous Correlated Eye Data When Sample Size Is Small. *Ophthal Epidemiol* 2018;25:45-54.

37. Choi HY, Lee JE, Lee JW, Park HJ, Lee JE, Jung JH. In vitro study of antiadipogenic profile of latanoprost, travoprost, bimatoprost, and tafluprost in human orbital preadiopocytes. *J Ocul Pharmacol Ther* 2012;28:146-152.

38. Taketani Y, Yamagishi R, Fujishiro T, Igarashi M, Sakata R, Aihara M. Activation of the prostanoid FP receptor inhibits adipogenesis leading to deepening of the upper eyelid sulcus in prostaglandin-associated periorbitopathy. *Invest Ophthalmol Vis Sci* 2014;55:1269-1276.

39. Liu AW, Gan LY, Yao X, Zhou J. Long-term assessment of prostaglandin analogs and timolol fixed combinations vs prostaglandin analogs monotherapy. *Int J Ophthalmol* 2016;9:750-756.

40. Nakakura S, Yamamoto M, Terao E, et al. Prostaglandin-associated periorbitopathy in latanoprost users. *Clin Ophthalmol* 2015;9:51-56.

41. Yoshino T, Fukuchi T, Togano T, Seki M, Ikegaki H, Abe H. Eyelid and eyelash changes due to prostaglandin analog therapy in unilateral treatment cases. *Jpn J Ophthalmol* 2013;57:172-178.

42. Karslioglu MZ, Hosal MB, Tekeli O. Periocular changes in topical bimatoprost and latanoprost use. *Turk J Med Sci* 2015;45:925-930.

43. Ugradar S, Lambros V. Orbital volume increases with age: A computed tomography-based volumetric study. *Ann Plast Surg* 2019.

44. Ugradar S, Goldberg RA, Rootman DB. Bony orbital volume expansion in thyroid eye disease. *Ophthalmic Plast Reconstr Surg* 2018.

45. Chang MY, Shin A, Park J, et al. Deformation of optic nerve head and peripapillary tissues by horizontal duction. *Am J Ophthalmol* 2017;174:85-94.

Chapter 4: Conclusions

The current body of work gives evidence that repetitive traction on the optic nerve caused by numerous accumulated cycles of adduction eye movements throughout a lifetime may damage the optic nerve and peripapillary tissues. We shown anatomically that the optic nerve has a bi-layered sheath than serves as a protective coating to absorb mechanical force.

Around the globe's junction with the optic nerve, tissues are reinforced with a weave of dense collagen and elastin. The weave pattern becomes irregular with age, forming large dense clumps of elastin deposits. These deposits may be a byproduct of tissue damage, or an intentional protective mechanism for the eye to resist excessive strain. Further studies can elucidate the role of these dense elastin deposits.

Mechanical force that arise from traction in the optic nerve is transmitted to the sclera at the globe optic nerve junction and may damage tissue in the surrounding area. Our OCT studies show that indeed, tissues around the globe-optic nerve junction, including Bruch's membrane and the choroid, do undergo deformation during adduction. The degree of deformation is threshold by the adduction angle. These deformations can be seen from *en face* cSLO images of the retina surface. Surprisingly, younger individuals have greater deformations during large angle adduction than do older people. Diseased individuals have the least deformation, perhaps due to loss of tissue compliance.

Finally, our exploration of potential remedies yielded limited success. While collagen cross-linking can be used to stiffen the sclera, a diffusely stiffer sclera may not be advantageous when considering the findings from the cSLO studies. Prostaglandin agonists application is less invasive and less permanent, however topical drops do not

affect orbital fat in the retrobulbar region where a reduction in fat volume could allow the globe to rest backwards and create more optic nerve slack for rotation. Direct injection of prostaglandin agonists to the retrobulbar region maybe be required, yet intentionally causing the globe to shift posteriorly might cause other problems.

Appendix

The following is a subset of ImageJ scripts that was used for semi-automated image analysis with ImageJ.
Code for quantification of retina surface deformation using blood vessel fiducials.

```
////////////////////////////////
/////////   SET Scales   /////////
////////////////////////////////
run("Set Scale...", "distance=256 known=80 unit=mm");
run("Set Measurements...", "area centroid bounding stack limit display invert nan
redirect=None decimal=3");//////////////////////////////////////////
//////////   Custom Functions   //////////
//////////////////////////////////////////
function findInArray(array, value){  // return index of value, or -1 if not found
for (i = 0; i < array.length; i++) {
if( array[i]==value){return i;}}
return -1;
}function occurrencesInArray(array, value){  // returns number of times a value occurs in
given array
count=0;
for (i = 0; i < array.length; i++) {
if( array[i]==value){count++;}}
return count;
}function renameTo(ROIindex, newLabel){  // Rename given ROIindex to newLabel with
slice num, area, x-center, and y-center.
roiManager("deselect");
run("Clear Results");
roiManager("select", ROIindex);
run("Measure");
sliceNum = getResult("Slice", 0);
sliceArea = round(getResult("Area", 0));
sliceXcent = round(getResult("X", 0));       // Coordinates measured in mm from left
sliceYcent = round(getResult("Y", 0));       // Coordinates measured in mm from bottom
newName = "Slice: " + IJ.pad(sliceNum,2) + " _" + newLabel + "_  Area:" +
IJ.pad(sliceArea,4) + "  X:" + IJ.pad(sliceXcent,2) + "  Y:" + IJ.pad(sliceYcent,2);
roiManager("rename", newName);
run("Clear Results");
}function firstUnLabel(){  // Return first NON-Labeled ROI number or -1 if none found
currentROI = 0;
roiManager("select", currentROI);
currName = Roi.getName;
while (currentROI < roiManager("count")){
roiManager("select", currentROI);
currName = Roi.getName;
if (lengthOf(currName) == 14 ){  // Unlabeled Found
return currentROI;} //return currentROI;
else{currentROI++;}
}
```

```
return -1;
}function closeResults(){  // Clear and close Results window
run("Clear Results");
if (isOpen("Results")) {
selectWindow("Results");
run("Close");}
}function noNewPrompt(){  // Creates dialog popup - No new ROI found
title = "No New ROI";
width=512; height=512;
Dialog.create("No New ROI");
Dialog.addMessage(" ");
Dialog.addMessage("ERROR: No new ROI was found");
Dialog.addMessage(" ");
Dialog.show();
}function resetROIlist(sortList){  // Resets list so that all "000A" are removed.  take input
of "sortList" boolean to determine if list should be resorted after.
currentROI = 0;
while (currentROI < roiManager("count")){
roiManager("select", currentROI);
currName = Roi.getName;
if(startsWith(currName, "000A")){
currName = substring(currName, 5);
roiManager("rename", currName);
currentROI++;
}
else{currentROI++;}
}
if(sortList){sortROIList();}
}function findROInamed(name){ // return ROI index of first occurence of ROI containing
"name", return -1 if not found
currentROI = 0;
totalROI = roiManager("count");
while (currentROI < totalROI){
roiManager("select", currentROI);
currName = Roi.getName;
if(indexOf(currName, name) >-1 ) { // if input 'name' is found in name of ROI
return currentROI;
break;}
else{ currentROI++;}
}
return -1;   // name was not found
}function roiNameContains(ROIindex, name){
roiManager("select", ROIindex);
currentName = Roi.getName;
if (indexOf(Roi.getName, name) < 0) { // name not found in ROI name
return false;
}
else{
return true;
}
```

```
}*****************************************************************************
//**********************Functions used for ROI List
********************** ROI Update SUB-MENU
*********************************************************************
function ROIPrompt(){  // Creates Update ROI List dialog popup
title = "Update ROI List";
width=512; height=512;
Dialog.create("Update ROI List");
Dialog.addMessage(" ");
Dialog.addMessage("Select what action to take and the object of interest.");
Dialog.addMessage(" ");
Dialog.addChoice("Action:", newArray("Process New", "Rename All", "Bring Object to
Top", "Sort List", "Rename List by Slice Number", "Rename List by Globe Optic Nerve
Junction" , "Go Back to Main Menu", "Exit"));
Dialog.addChoice("Object:", newArray("Select an Object" , "Orbit", "Optic Nerve", "Nerve
Sheath", "Globe", "Medial Rectus", "Lateral Rectus" , "Superior Rectus", "Inferior
Rectus", "Superior Oblique", "Inferior Oblique", "LPS", "Globe-Optic Nerve Junction"));
//Dialog.addCheckbox("  Re-sort list?", false);
//Dialog.addCheckbox("  Rename with respect to Globe-optic nerve junction?", false);
Dialog.show();
ActionSetTo = Dialog.getChoice();
LabelSetTo = Dialog.getChoice();
//reorderList = Dialog.getCheckbox();
//GONJrename = Dialog.getCheckbox();
return newArray(LabelSetTo, ActionSetTo);
}function updateROIMenuLogic(){
promptAns = ROIPrompt();
LabelSetTo = promptAns[0];
ActionSetTo = promptAns[1];
//reorderList = promptAns[2];
//GONJrename = promptAns[3];// Reformat object label
if (LabelSetTo == "Select an Object") {LabelSetTo = "NONE";}
else if (LabelSetTo == "Orbit") {LabelSetTo = "ORBIT";}
else if (LabelSetTo == "Optic Nerve") {LabelSetTo = "ON";}
else if (LabelSetTo == "Nerve Sheath") {LabelSetTo = "ONS";}
else if (LabelSetTo == "Globe") {LabelSetTo = "GLOBE";}
else if (LabelSetTo == "Medial Rectus") {LabelSetTo = "MR";}
else if (LabelSetTo == "Lateral Rectus"){LabelSetTo = "LR";}
else if (LabelSetTo == "Superior Rectus"){LabelSetTo = "SR";}
else if (LabelSetTo == "Inferior Rectus"){LabelSetTo = "IR";}
else if (LabelSetTo == "Superior Oblique"){LabelSetTo = "SO";}
else if (LabelSetTo == "Inferior Oblique"){LabelSetTo = "IO";}
else if (LabelSetTo == "Globe-Optic Nerve Junction"){LabelSetTo = "GONJ";}
else {LabelSetTo = "LPS";}if (ActionSetTo == "Rename All"){ // Rename all ROI
if (LabelSetTo == "NONE"){
updateROIMenuLogic();
}
else{
showMessageWithCancel("Warning!","WARNING:\nThis will rename the whole list.\nAre
you sure?\nClick  OK  to continue otherwise, cancel.");
```

```
currentROI = 0;
while (currentROI < roiManager("count")){
renameTo(currentROI, LabelSetTo);
currentROI++;}
updateROIMenuLogic();
}
}// Special Case for GONJ
else if (ActionSetTo == "Process New" && LabelSetTo == "GONJ"){
if(findROInamed("GONJ") != -1){showMessageWithCancel("Warning!","WARNING:
Globe Optic Nerve Junction already set.");}
else{
currentROI = firstUnLabel();
if (currentROI != -1){
roiManager("select", currentROI);
run("Clear Results");
run("Measure");
slice = getResult("Slice", 0);
X = getResult("X", 0);
xCoord = X * 3.2;
Y = getResult("Y", 0);
yCoord = ((80-Y) * 3.2)-1;
X = d2s(X,2);
Y = d2s(Y,2);
setTool("point");
run("Point Tool...", "type=Dot color=Orange size=Small label");
makePoint(xCoord, yCoord, "small orange dot");
roiManager("update");
roiManager("rename", "Slice: " + IJ.pad(slice,2) + " _GONJ_  X:" + X + "  Y:" + Y);
setTool("freehand");
updateROIMenuLogic();
}
else{
showMessageWithCancel("Warning!","WARNING: No new entries found. Please mark
junction.");
placeGONJprompt();
updateROIMenuLogic();
}
}
}else if (ActionSetTo == "Process New"){   // Find all new objects and rename them
if (LabelSetTo == "NONE"){
updateROIMenuLogic();
}
else{
// Check to see if GONJ was already labeled AND slices are renamed with reference to
GONJ
GONJrenamedSetting = false;
for(i=0; i<roiManager("count"); i++){
roiManager("select",i);
if (indexOf(Roi.getName, " 0 _GONJ_") > -1){
GONJrenamedSetting = true;}
```

```
}
currentROI = firstUnLabel(); // Find first new unlabeled item
while (currentROI != -1 && currentROI < roiManager("count")){
roiManager("select", currentROI);
if (startsWith(Roi.getName, "00")){renameTo(currentROI, LabelSetTo);}  // Rename it to
what "LabelSetTo" is
currentROI++;
}
if(GONJrenamedSetting){ renameByGONJ();}
updateROIMenuLogic();}
}else if (ActionSetTo == "Bring Object to Top"){ // Moves objects of interest to top of list
if (LabelSetTo == "NONE"){
updateROIMenuLogic();
}
else{
LabelSetTo = LabelSetTo + "_  A";
for (i = 0; i < roiManager("count"); i++) {
roiManager("select", i);
currName = Roi.getName;
if( indexOf(currName, LabelSetTo) > -1 ){ // Label found in current ROI name
currName = "000A-" + currName;   // Add "000A" to the name so that when sorted, it will
go to the top of list
roiManager("rename", currName);
}
}
// Sort List with "000A-" on top
selectWindow("ROI Manager");
roiManager("deselect");
roiManager("sort");
// Remove "000A-"
currentROI = 0;
while (currentROI < roiManager("count")){
roiManager("select", currentROI);
currName = Roi.getName;
if(startsWith(currName, "000A")){
currName = substring(currName, 5);
roiManager("rename", currName);
currentROI++;}
else{currentROI++;}
}
//if(GONJrename){ renameByGONJ();}
updateROIMenuLogic();
}
}else if (ActionSetTo == "Sort List"){
sortROIList();
updateROIMenuLogic();
}else if (ActionSetTo == "Rename List by Slice Number"){
renameBySlice();
updateROIMenuLogic();
}else if (ActionSetTo == "Rename List by Globe Optic Nerve Junction"){
```

```
GONJindex = findROInamed("GONJ");  // Find GONJ slice
if(GONJindex != -1){  // GONJ was labeled and found
roiManager("select", GONJindex);
if(indexOf(Roi.getName, " 0 _GONJ_") > -1){  // List already named with respect to
GONJ
GONJrenamedSetting = true;
updateROIMenuLogic();
// Do nothing
}
else{  // Rename list by GONJ
renameByGONJ();
GONJrenamedSetting = true;
updateROIMenuLogic();
}
}
else{  // GONJ has NOT been labeled, prompt to label GONJ
showMessageWithCancel("Warning!","WARNING: No Globe Optic Nerve Junction
found.\nPlease label junction.");
placeGONJprompt();
renameByGONJ();
updateROIMenuLogic();
}
}else if (ActionSetTo == "Go Back to Main Menu"){
MainMenuPrompt();
}else{ // EXIT - Do Nothing}
}
}function renameByGONJ(){
// find GONJ
renameBySlice();
GONJroi = findROInamed("GONJ");
if (GONJroi == -1){
showMessageWithCancel("Warning!","WARNING: No Globe Optic Nerve Junction
found.\nPlease label junction.");
placeGONJprompt();
renameBySlice();
renameByGONJ();
}
else{
roiManager("select", GONJroi);
GONJsliceNum = getSliceNumber();
for (i = 0; i < roiManager("count"); i++){
roiManager("select", i);
currSliceNum = getSliceNumber();
newSliceNum = currSliceNum - GONJsliceNum;
currName = Roi.getName;
if(newSliceNum<0){newName = "Slice:  " + newSliceNum + substring(currName, 9);}
else{newName = "Slice:   " + newSliceNum + substring(currName, 9);}
roiManager("rename", newName);
}
GONJrenamedSetting = true;
```

```
}
}function placeGONJprompt(){
run("Point Tool...", "type=Dot size=Small label");
makePoint(3, 3, "small dot");
run("Point Tool...", "type=Dot color=Orange size=Small add label");
setTool("point");
waitForUser("Mark Globe Optic Nerve Junction Point", "Please mark where the Globe
Optic Nerve Junction is.\nClick  OK  when done.");
run("Point Tool...", "type=Dot color=Cyan size=Small label");
setTool("freehand");
roiManager("select", roiManager("count")-1);
run("Clear Results");
run("Measure");
slice = getResult("Slice", 0);
X = getResult("X", 0);
xCoord = X * 3.2;
Y = getResult("Y", 0);
yCoord = ((80-Y) * 3.2) - 1;
X = d2s(X,2);
Y = d2s(Y,2);
setTool("point");
run("Point Tool...", "type=Dot color=Orange size=Small label");
makePoint(xCoord, yCoord, "small orange dot");
roiManager("update");
roiManager("rename", "Slice: " + IJ.pad(slice,2) + " _GONJ_  X:" + X + "  Y:" + Y);
setTool("freehand");
}function renameBySlice(){
totalROI = roiManager("count");
for(i =0; i< totalROI; i++){
roiManager("select", i);
slice = getSliceNumber();
currName = Roi.getName;
start = indexOf(currName, "_");
newName = "Slice: " + IJ.pad(slice,2) + " " + substring(currName, start);
roiManager("rename", newName);
}
GONJrenamedSetting = false;
}function sortROIList(){
GONJreference = false;
// Check if slices are named by slice number or GONJ
GONJroi = findROInamed("GONJ");
if (GONJroi != -1){
roiManager("select", GONJroi);
if(indexOf(Roi.getName, " 0 _GONJ")>-1){
GONJreference = true;
}
}
renameBySlice();        // Rename by slice number, sort it, then rename back to GONJ
reference if needed
roiManager("deselect");
```

```
roiManager("sort");
if(GONJreference){ renameByGONJ();}
}//*************************************************************************************************
*****************************************************************************
//*********************Functions used for head rotation
correction:*************************************************************************************************
*****************************
//*************************************************************************************************
*****************************************************************************//
********************** HEAD ALIGNMENT SUB-MENU
*********************************************************************
function rotationPrompt(){  // Creates Correct Head Alignment dialog popup
title = "Correct Head Alignment";
width=512; height=512;
Dialog.create("Correct Head Alignment");
Dialog.addMessage(" ");
Dialog.addMessage("Select which rotational axis to correct.");
Dialog.addMessage(" ");
Dialog.addChoice("Action:", newArray("Set Markers", "Calculate Correction", "Apply Roll
Correction", "Go Back to Main Menu", "Exit"));
Dialog.addChoice("Rotation:", newArray("Yaw", "Pitch", "Roll", "ALL"));
Dialog.show();
ActionSetTo = Dialog.getChoice();
RotationSetTo = Dialog.getChoice();
return newArray(ActionSetTo,RotationSetTo);
}function headAlignMenuLogic(){
promptAns = rotationPrompt();
ActionSetTo = promptAns[0];
RotationSetTo = promptAns[1];if(ActionSetTo == "Set Markers"){   // Set markers for
corrections
setAlignmentMarkers(RotationSetTo);
// Ask again what you want to do
headAlignMenuLogic();}
else if (ActionSetTo == "Calculate Correction"){  // Calculate correction
calcCorrection(RotationSetTo);
headAlignMenuLogic();}
else if (ActionSetTo == "Apply Roll Correction"){ // Apply roll correction to image
applyRollCorrect();
headAlignMenuLogic();
}
else if(ActionSetTo == "Go Back to Main Menu"){
MainMenuPrompt();}
else{
run("Select None");
// Exit
}
}function getROIscontaining(roiNameContains){   // Returns an ARRAY of a pair of ROIs
that contain the input string "roiNameContains".
//  If ROI list does not contain 2 cases of the input string, returns (-1, -1)
// If ROI list only contains 1 cases, returns ROI number of the instance, and -1.
```

```
ans = newArray(-1,-1);
for(currentROI = 0; currentROI < roiManager("count"); currentROI++){
roiManager("select", currentROI);
currName = Roi.getName;
if (indexOf(currName, roiNameContains) >-1){
if(ans[0] ==-1){ans[0] = currentROI;}
else{ans[1] = currentROI;}
}
}
return ans;
}function yawPrompt(){  //  YAW Prompt. Wait for user to place 2 dots.
run("Point Tool...", "type=Dot size=Small label");
makePoint(3, 3, "small dot");
run("Point Tool...", "type=Dot color=Magenta size=Small add label");
setTool("point");
waitForUser("YAW Markers", "For YAW Correction: \nPlace a dot on the brain MIDLINE
in TWO SEPARATE slices.\nMake sure the slices are as far apart as possible.\nDots
should be multi-slices apart from each other.\n \nClick  'OK'  when done.");
run("Point Tool...", "type=Dot color=Magenta size=Small label");
setTool("freehand");
newMarkersROI = firstUnLabel();
if (newMarkersROI == -1){showMessageWithCancel("Warning!","WARNING: No
markers added.");}
else{
if(newMarkersROI != roiManager("count")-
2){showMessageWithCancel("Warning!","WARNING: Too many markers added.");}
else{
roiManager("select", newMarkersROI);
run("Clear Results");
run("Measure");
slice = getResult("Slice", 0);
X = d2s(getResult("X", 0),2);
Y = d2s(getResult("Y", 0),2);
newName = "Slice: " + IJ.pad(slice,2) + " _YAW-01_  X:" + X + "  Y:" + Y;
roiManager("rename", newName);
roiManager("select", newMarkersROI+1);
run("Measure");
slice = getResult("Slice", 0);
X = d2s(getResult("X", 0),2);
Y = d2s(getResult("Y", 0),2);
newName = "Slice: " + IJ.pad(slice,2) + " _YAW-02_  X:" + X + "  Y:" + Y;
roiManager("rename", newName);
run("Clear Results");}
}
}function pitchPrompt(){
run("Point Tool...", "type=Dot size=Small label");
makePoint(3, 3, "small dot");
run("Point Tool...", "type=Dot color=Green size=Small add label");
setTool("point");
```

```
waitForUser("PITCH Markers", "For PITCH Correction: \nPlace a dot on the anterior
ethmoid recess in TWO SEPARATE slices.\nMake sure the slices are as far apart as
possible.\nDots should be multi-slices apart from each other.\n \nClick  'OK'  when
done.");
run("Point Tool...", "type=Dot color=Green size=Small label");
setTool("freehand");
newMarkersROI = firstUnLabel();
if (newMarkersROI == -1){showMessageWithCancel("Warning!","WARNING: No
markers added.");}
else{
if(newMarkersROI != roiManager("count")-
2){showMessageWithCancel("Warning!","WARNING: Too many markers added.");}
else{
roiManager("select", newMarkersROI);
run("Clear Results");
run("Measure");
slice = getResult("Slice", 0);
X = d2s(getResult("X", 0),2);
Y = d2s(getResult("Y", 0),2);
newName = "Slice: " + IJ.pad(slice,2) + " _PITCH-01_  X:" + X + "  Y:" + Y;
roiManager("rename", newName);
roiManager("select", newMarkersROI+1);
run("Measure");
slice = getResult("Slice", 0);
X = d2s(getResult("X", 0),2);
Y = d2s(getResult("Y", 0),2);
newName = "Slice: " + IJ.pad(slice,2) + " _PITCH-02_  X:" + X + "  Y:" + Y;
roiManager("rename", newName);
run("Clear Results");}
}
}function rollPrompt(){
run("Point Tool...", "type=Dot size=Small label");
makePoint(3, 3, "small dot");
run("Point Tool...", "type=Dot color=Cyan size=Small add label");
setTool("point");
waitForUser("ROLL Markers", "For Roll Correction: \nPlace 2 dots on the brain midline in
the SAME slice.\n \nClick  'OK'  when done.");
run("Point Tool...", "type=Dot color=Cyan size=Small label");
setTool("freehand");
newMarkersROI = firstUnLabel();
if (newMarkersROI == -1){showMessageWithCancel("Warning!","WARNING: No
markers added.");}
else{
if(newMarkersROI != roiManager("count")-
2){showMessageWithCancel("Warning!","WARNING: Too many markers added.");}
else{
roiManager("select", newMarkersROI);
run("Clear Results");
run("Measure");
slice = getResult("Slice", 0);
```

```
X = d2s(getResult("X", 0),2);
Y = d2s(getResult("Y", 0),2);
newName = "Slice: " + IJ.pad(slice,2) + "_ROLL-01_  X:" + X + "  Y:" + Y;
roiManager("rename", newName);
roiManager("select", newMarkersROI+1);
run("Measure");
slice = getResult("Slice", 0);
X = d2s(getResult("X", 0),2);
Y = d2s(getResult("Y", 0),2);
newName = "Slice: " + IJ.pad(slice,2) + " _ROLL-02_  X:" + X + "  Y:" + Y;
roiManager("rename", newName);
run("Clear Results");}
}
}function calculateYaw(){
yawROIs = getROIscontaining("YAW");
// convert ROI index to slice number
roiManager("select", yawROIs[0])
run("Clear Results");
run("Set Measurements...", "area centroid bounding stack limit display invert nan
redirect=None decimal=3");
run("Measure");
yawSlice1 = getResult("Slice", 0);
yawX1 = getResult("X", 0);      roiManager("select", yawROIs[1])
run("Clear Results");
run("Set Measurements...", "area centroid bounding stack limit display invert nan
redirect=None decimal=3");
run("Measure");
yawSlice2 = getResult("Slice", 0);
yawX2 = getResult("X", 0);
run("Clear Results");
if (yawSlice1<yawSlice2){
backYawSlice = yawSlice1;
backYawX = yawX1;frontYawSlice = yawSlice2;
frontYawX = yawX2;
}
else{
backYawSlice = yawSlice2;
backYawX = yawX2;frontYawSlice = yawSlice1;
frontYawX = yawX1;
}
zdistance = (frontYawSlice - backYawSlice)*2;  // front slice minus back slice * 2 mm
xdistance = frontYawX - backYawX;
// calculate arctangent of xdistance / zdistance in radians, multiply by 180/PI to convert
to degree
angle = atan(xdistance/zdistance) * (180/PI);
return angle;
}function calculateRoll(){
rollROIs = getROIscontaining("ROLL");
roiManager("select", rollROIs[0])
run("Clear Results");
```

```
run("Set Measurements...", "area centroid bounding stack limit display invert nan
redirect=None decimal=3");
run("Measure");
rollX1 = getResult("X", 0);
rollY1 = getResult("Y", 0);        roiManager("select", rollROIs[1])
run("Clear Results");
run("Set Measurements...", "area centroid bounding stack limit display invert nan
redirect=None decimal=3");
run("Measure");
rollX2 = getResult("X", 0);
rollY2 = getResult("Y", 0);
run("Clear Results");
if (rollY1<rollY2){
bottomRollY = rollY1;
bottomRollX = rollX1;topRollY = rollY2;
topRollX = rollX2;
}
else{
bottomRollY = rollY2;
bottomRollX = rollX2;topRollY = rollY1;
topRollX = rollX1;
}
ydistance = topRollY - bottomRollY;  // top minus bottom
xdistance = topRollX - bottomRollX;
// calculate arctangent of xdistance / ydistance in radians, multiply by 180/PI to convert
to degree
angle = atan(xdistance/ydistance) * (180/PI);
return angle;
}function calculatePitch(){
pitchROIs = getROIscontaining("PITCH");
// convert ROI index to slice number
roiManager("select", pitchROIs[0])
run("Clear Results");
run("Set Measurements...", "area centroid bounding stack limit display invert nan
redirect=None decimal=3");
run("Measure");
pitchSlice1 = getResult("Slice", 0);
pitchY1 = getResult("Y", 0);      roiManager("select", pitchROIs[1])
run("Clear Results");
run("Set Measurements...", "area centroid bounding stack limit display invert nan
redirect=None decimal=3");
run("Measure");
pitchSlice2 = getResult("Slice", 0);
pitchY2 = getResult("Y", 0);
run("Clear Results");
if (pitchSlice1<pitchSlice2){
backPitchSlice = pitchSlice1;
backPitchY = pitchY1;frontPitchSlice = pitchSlice2;
frontPitchY = pitchY2;
}
```

```
else{
backPitchSlice = pitchSlice2;
backPitchY = pitchY2;frontPitchSlice = pitchSlice1;
frontPitchY = pitchY1;
}
zdistance = (frontPitchSlice - backPitchSlice)*2;  // front slice minus back slice * 2 mm
ydistance = frontPitchY - backPitchY;
// calculate arctangent of xdistance / zdistance in radians, multiply by 180/PI to convert
to degree
angle = atan(ydistance/zdistance) * (180/PI);
return angle;
}function setAlignmentMarkers(RotationSetTo){
if(RotationSetTo == "Yaw"){  // Magenta dots
yawPrompt();
run("Select None");
}
else if (RotationSetTo == "Pitch"){ // Green Dots
pitchPrompt();
run("Select None");
}
else if (RotationSetTo == "Roll"){ // Cyan Dots
rollPrompt();
run("Select None");
}
else if (RotationSetTo == "ALL"){  // Run all prompts
yawPrompt();
pitchPrompt();
rollPrompt();
run("Select None");
}
}function calcCorrection(RotationSetTo){
if(RotationSetTo == "Yaw"){  // YAW
yawArray = getROIscontaining("YAW");
if(yawArray[0] == -1 || yawArray[1] == -
1){showMessageWithCancel("Warning!","WARNING: Not enough points to calculate.");}
else{
yawDegree = calculateYaw();
print("The yaw correction is: " + yawDegree + " degrees");
run("Select None");}
}
else if (RotationSetTo == "Pitch"){ // PITCH
pitchArray = getROIscontaining("PITCH");
if(pitchArray[0] == -1 || pitchArray[1] == -
1){showMessageWithCancel("Warning!","WARNING: Not enough points to calculate.");}
else{
pitchDegree = calculatePitch();
print("The pitch correction is: " + pitchDegree + " degrees");
run("Select None");
}
}
```

```
else if (RotationSetTo == "Roll"){ // ROLL
rollArray = getROIscontaining("ROLL");
if(rollArray[0] == -1 || rollArray[1] == -
1){showMessageWithCancel("Warning!","WARNING: Not enough points to calculate.");}
else{
rollDegree = calculateRoll();
print("The roll correction is: " + rollDegree + " degrees");
run("Select None");
}
}
else if (RotationSetTo == "ALL"){  // ALL
yawArray = getROIscontaining("YAW");
pitchArray = getROIscontaining("PITCH");
rollArray = getROIscontaining("ROLL");
if(yawArray[0] == -1 || yawArray[1] == -1 || pitchArray[0] == -1 || pitchArray[1] == -1 ||
rollArray[0] == -1 || rollArray[1] == -1){showMessageWithCancel("Warning!","WARNING:
Not enough points to calculate.");}
else{
yawDegree = calculateYaw();
print("The yaw correction is: " + yawDegree + " degrees");
run("Select None");pitchDegree = calculatePitch();
print("The pitch correction is: " + pitchDegree + " degrees");
run("Select None");rollDegree = calculateRoll();
print("The roll correction is: " + rollDegree + " degrees");
run("Select None");
}
}
else{}
}function applyRollCorrect(){
rollArray = getROIscontaining("ROLL");
if(rollArray[0] == -1 || rollArray[1] == -1){
showMessageWithCancel("Warning!","WARNING: Not enough points to calculate.");
}
else{
// Get roll degree
rollDegree = calculateRoll();
rollDegree = -rollDegree;
print("The roll correction is: " + rollDegree + " degrees");
run("Select None");
run("Rotate... ", "angle=rollDegree grid=2 interpolation=Bicubic stack");
for(i=0; i<roiManager("count"); i++){
roiManager("select", i);
run("Rotate...", "rotate angle=rollDegree");
roiManager("Update");
run("Select None");}
print("Image stack was rotated " + rollDegree + " degrees");
}
}//*************************************************************************************************
*******************************************************************************
```

```
//**********Functions used for Geometry
Measurements:**********************************************************************************************
************************************
//*************************************************************************************************************
*****************************************************************************//
********** Geometry Analysis SUB-MENU
**********************************************************************
function analyzePrompt(){  // Creates Meaasure Geometry dialog popup
title = "Measure Geometry";
width=512; height=512;
Dialog.create("Measure Geometry");
Dialog.addMessage(" ");
Dialog.addMessage("Select what to analyze and what measurement to use.");
Dialog.addMessage(" ");
Dialog.addChoice("Action", newArray("Measure", "Extract Outlines" , "Go Back to Main
Menu", "Exit"));
Dialog.addChoice("Object:", newArray("Orbit", "Optic Nerve", "Nerve Sheath", "Globe"
,"Globe Optic Nerve Junction", "Medial Rectus", "Lateral Rectus" , "Superior Rectus",
"Inferior Rectus", "Superior Oblique", "Inferior Oblique", "LPS"));
Dialog.addChoice("Measurement:", newArray("Average Width", "Maximum Width" ,
"Average Height", "Area" , "Perimeter", "Centroid"));
Dialog.addCheckbox("  Re-sort list? Default leaves object of interest on top.", false);
Dialog.show();
ActionSetTo = Dialog.getChoice();
LabelSetTo = Dialog.getChoice();
MeasurementSetTo = Dialog.getChoice();
reorderList = Dialog.getCheckbox();
return newArray(LabelSetTo, MeasurementSetTo,reorderList, ActionSetTo);
}function measureGeoMenuLogic(){
promptAns = analyzePrompt();
LabelSetTo = promptAns[0];
MeasurementSetTo = promptAns[1];
reorderList = promptAns[2];
action = promptAns[3];if(LabelSetTo == "Globe Optic Nerve Junction"){
getGONJ();
measureGeoMenuLogic();}
else if (action == "Measure"){                                    // Measure
// Reformat object label
if (LabelSetTo == "Orbit"){LabelSetTo = "ORBIT";}
else if (LabelSetTo == "Optic Nerve"){LabelSetTo = "ON";}
else if (LabelSetTo == "Nerve Sheath"){LabelSetTo = "ONS";}
else if (LabelSetTo == "Globe"){LabelSetTo = "GLOBE";}
else if (LabelSetTo == "Globe Optic Nerve Junction"){LabelSetTo = "GONJ";}
else if (LabelSetTo == "Medial Rectus"){LabelSetTo = "MR";}
else if (LabelSetTo == "Lateral Rectus"){LabelSetTo = "LR";}
else if (LabelSetTo == "Superior Rectus"){LabelSetTo = "SR";}
else if (LabelSetTo == "Inferior Rectus"){LabelSetTo = "IR";}
else if (LabelSetTo == "Superior Oblique"){LabelSetTo = "SO";}
else if (LabelSetTo == "Inferior Oblique"){LabelSetTo = "IO";}
```

```
else if {LabelSetTo == "LPS";}// Reorder ROI list so that objects of interest are at the top
and begins with "000A-"
currentROI = 0;
while (currentROI < roiManager("count")){
roiManager("select", currentROI);
currName = Roi.getName;
if( indexOf(currName, LabelSetTo) < 0 ){
currentROI++;}
else{
currName = Roi.getName;
currName = "000A-" + currName;
roiManager("rename", currName);
currentROI++;
}
}
roiManager("sort");
// Find where objects of interest ends (ROI index)
currentROI = 0;
interestObjROIend = 0;
while (currentROI < roiManager("count")){
roiManager("select", currentROI);
currName = Roi.getName;
if(startsWith(currName, "000A")){
currentROI++;
interestObjROIend++;}
else{break;}
}// Clear Results window
run("Clear Results");// Compute MEASUREMENT that was set
selectWindow("ROI Manager");
roiManager("deselect");currentROI = 0;
while (currentROI < interestObjROIend){
if(MeasurementSetTo == "Average Width"){  // Get Average Width
roiManager("select", currentROI);
currentAverageWidth = getAvgWidth(currentROI);
currName = substring(Roi.getName, indexOf(Roi.getName, "_")+1);
currName = substring(currName, 0, indexOf(currName, "_"));
print(currName + " AverageWidth: " + currentAverageWidth);
currentROI++;}
else if (MeasurementSetTo == "Average Height"){ // Get Average Height
roiManager("select", currentROI);
currentAverageHeight = getAvgHeight(currentROI);
currName = substring(Roi.getName, indexOf(Roi.getName, "_")+1);
currName = substring(currName, 0, indexOf(currName, "_"));
print(currName + " AverageHeight: " + currentAverageHeight);
currentROI++;}
else if (MeasurementSetTo == "Area"){ // Get Area
currArea = getArea(currentROI);
currName = substring(Roi.getName, indexOf(Roi.getName, "_")+1);
currName = substring(currName, 0, indexOf(currName, "_"));
print(currName + " Area: " + currArea);
```

```
currentROI++;}
else if (MeasurementSetTo == "Perimeter"){ // Get Circumference/Perimeter
run("Set Measurements...", "area centroid perimeter bounding stack limit display invert
nan redirect=None decimal=3");
currPerim = getPerimeter(currentROI);
currName = substring(Roi.getName, indexOf(Roi.getName, "_")+1);
currName = substring(currName, 0, indexOf(currName, "_"));
print(currName + " Perimeter: " + currPerim);
currentROI++;}
else if (MeasurementSetTo == "Centroid"){ // Get Centroid
currXcent = getXcentroid(currentROI);
currYcent = getYcentroid(currentROI);
currName = substring(Roi.getName, indexOf(Roi.getName, "_")+1);
currName = substring(currName, 0, indexOf(currName, "_"));
print(currName + " Centroid X: " + currXcent + " Y: " + currYcent);
currentROI++;}
else {
  currentROI = 1000;}   //force currentROI to be large to exit while loop
}   //  End of While loop
currentROI=0;
if (MeasurementSetTo == "Maximum Width"){
maxWidthROI = findROIindexWithMaxWidth(LabelSetTo, currentROI,
interestObjROIend);   ////////////////////////////////////////BOOKNMARK
maxWidth = findMaxWidth(maxWidthROI, LabelSetTo, true) /  3.2;   // divide by 3.2
px/mm to convert to mmif (LabelSetTo == "ORBIT"){LabelSetTo = "Orbit";}
else if (LabelSetTo == "ON"){LabelSetTo = "Optic Nerve";}
else if (LabelSetTo == "ONS"){LabelSetTo = "Nerve Sheath";}
else if (LabelSetTo == "GLOBE"){LabelSetTo = "Globe";}
else if (LabelSetTo == "MR"){LabelSetTo = "Medial Rectus";}
else if (LabelSetTo == "LR"){LabelSetTo = "Lateral Rectus";}
else if (LabelSetTo == "SR"){LabelSetTo = "Superior Rectus";}
else if (LabelSetTo == "IR"){LabelSetTo = "Inferior Rectus";}
else if (LabelSetTo == "SO"){LabelSetTo = "Superior Oblique";}
else if (LabelSetTo == "IO"){LabelSetTo = "Inferior Oblique";}print("Maximum width of " +
LabelSetTo + " is " + maxWidth + " mm");
}
// Reset ROI list, Remove prefix "000A"
resetROIlist(reorderList);
} // End of Measure Actionelse if (action == "Extract Outlines"){
// Reformat object label
if (LabelSetTo == "Orbit"){LabelSetTo = "ORBIT_";}
else if (LabelSetTo == "Optic Nerve"){LabelSetTo = "ON_";}
else if (LabelSetTo == "Nerve Sheath"){LabelSetTo = "ONS_";}
else if (LabelSetTo == "Globe"){LabelSetTo = "GLOBE_";}
else if (LabelSetTo == "Medial Rectus"){LabelSetTo = "MR_";}
else if (LabelSetTo == "Lateral Rectus"){LabelSetTo = "LR_";}
else if (LabelSetTo == "Superior Rectus"){LabelSetTo = "SR_";}
else if (LabelSetTo == "Inferior Rectus"){LabelSetTo = "IR_";}
else if (LabelSetTo == "Superior Oblique"){LabelSetTo = "SO_";}
else if (LabelSetTo == "Inferior Oblique"){LabelSetTo = "IO_";}
```

```
else if {LabelSetTo == "LPS";}for(i=0; i<roiManager("count"); i++){
roiManager("select", i);
if(roiNameContains(i, LabelSetTo)){
object = substring(LabelSetTo, 0, indexOf(LabelSetTo, "_"));
Roi.getCoordinates(xpoints, ypoints);
slice = getSliceNumber();
for(k=0; k<xpoints.length; k++){
print(object + "  Slice-" + slice + "  X-" + xpoints[k] + "  Y-" + 256-ypoints[k]);
}
}
}}else if (action == "Go Back to Main Menu"){
MainMenuPrompt();
}
else{
// Exit
}
}function findROIindexWithMaxWidth(object, startROI, endROI){
maxWidthROI = -1;
maxWidthOfSet = 0;
for(i=startROI; i < endROI+1; i++){
roiManager("select", i);
if(indexOf(Roi.getName, object)>-1){
currentROImaxWid = findMaxWidth(i, object, false);
if( currentROImaxWid > maxWidthOfSet){
maxWidthROI = i;
maxWidthOfSet = currentROImaxWid;
}
}
}
return maxWidthROI;
}function findMaxWidth(ROIindex, object, drawMax){
roiManager("select", ROIindex);
Roi.getBounds(topX, topY, width, height);
incrementY = round(height / 20);
if (incrementY == 0){
incrementY = 1;}
upperLimitY = topY + incrementY;
lowerLimitY = topY + (incrementY*19);
if(lowerLimitY > topY + height){
lowerLimitY = topY + height;}
sampleArraySize = lowerLimitY - upperLimitY;
// Make array of all y coordinates to check width at
sampleY= newArray(sampleArraySize);
for (i=0; i<sampleArraySize; i++){
sampleY[i] = upperLimitY + i;}
Roi.getCoordinates(xpoints, ypoints);
X1atMax = -1;
X2atMax = -1;
YatMax = -1;
widthMax = 0;
```

```
for(i=0; i<sampleY.length; i++){
minX=10000;
maxX=-1;
for(k=0; k<ypoints.length; k++){
if(ypoints[k] == sampleY[i]){
if(minX>xpoints[k]){
minX=xpoints[k];}
if(maxX<xpoints[k]){
maxX=xpoints[k];}}
}
if( (maxX - minX) > widthMax ){
widthMax = maxX - minX;
YatMax = sampleY[i];
X1atMax = minX;
X2atMax = maxX;
}
}
if(drawMax){
makeLine(X1atMax, YatMax, X2atMax, YatMax, 0);
roiManager("add");
roiManager("select", roiManager("count")-1);
slice = getSliceNumber();
// Check if slice renamed with respect to GONJ
GONJrenamedSetting = false;
for(i=0; i<roiManager("count"); i++){
roiManager("select",i);
if (indexOf(Roi.getName, " 0 _GONJ_") > -1){
GONJrenamedSetting = true;}
}
newName = "NA";
if (GONJrenamedSetting){
GONJroi = findROInamed("GONJ");
sliceInfo = slice - GONJroi;
newName = "Slice:   " + sliceInfo + " _" + object + "_  MAX Width";
}
else{
newName = "Slice: " + IJ.pad(slice,2) + " _" + object + "_  MAX Width";
}
roiManager("rename", newName);
}
return widthMax;
}function getAvgWidth(ROIindex){   // function returns the Average width of the selection
as a double.  Input is ROI index.
// This function makes up to 15 measurements of the width in the middle 60% portion of
the object and averages them.
roiManager("select", ROIindex);
//////////////  Set number of sample widths per slice //////////////
samplingNum = 15;    // set Y sample points
Roi.getBounds(xbound,ybound,bwidth,bheight);
sampleYrange1 = ybound + (round(bheight/6));
```

```
sampleYrange2 = ybound + (5*round(bheight/6));maxSample = samplingNum;
increment = round((sampleYrange2-sampleYrange1)/samplingNum);
for(i=1; i<samplingNum+1; i++){
currentYsample = sampleYrange1+(increment*i);
if(sampleYrange2<currentYsample){
maxSample=i-1;
break;}
}
sampleY= newArray(maxSample);
for (i=0; i<maxSample; i++){
sampleY[i] = sampleYrange1 + (increment*(i));
}
Roi.getContainedPoints(xpoints, ypoints);
widthSum=0;
for(i=0; i<sampleY.length; i++){
minX=10000;
maxX=-1;
for(k=0; k<ypoints.length; k++){
if(ypoints[k] == sampleY[i]){
if(minX>xpoints[k]){
minX=xpoints[k];}
if(maxX<xpoints[k]){
maxX=xpoints[k];}}
}
// Now have 2 X points that have the same y value (sampleY[i])
widthSum += abs(maxX-minX);
}
return  (widthSum / sampleY.length)/3.2;   // Convert from pixel to mm
}function getAvgHeight(ROIindex){   // function returns the Average Height of the
selection as a double.  Input is ROI index
// This function makes up to 15 measurements of the height in the middle 60% portion of
the object and averages them.
roiManager("select", ROIindex);
//////////////  Set number of sample widths per slice //////////////
samplingNum = 15;    // set Y sample points
Roi.getBounds(xbound,ybound,bwidth,bheight);
sampleXrange1 = xbound + (round(bheight/6));
sampleXrange2 = xbound + (5*round(bheight/6));
maxSample = samplingNum;
increment = round((sampleXrange2-sampleXrange1)/samplingNum);
for(i=1; i<samplingNum+1; i++){
currentXsample = sampleXrange1+(increment*i);
if(sampleXrange2<currentXsample){
maxSample=i-1;
break;}
}
sampleX= newArray(maxSample);
for (i=0; i<maxSample; i++){
sampleX[i] = sampleXrange1 + (increment*(i));}
Roi.getContainedPoints(xpoints, ypoints);
```

```
heightSum=0;
for(i=0; i<sampleX.length; i++){
minY=10000;
maxY=-1;
for(k=0; k<xpoints.length; k++){
if(xpoints[k] == sampleX[i]){
if(minY>ypoints[k]){
minY=ypoints[k];}
if(maxY<ypoints[k]){
maxY=ypoints[k];}}
}
// Now have an array of X points that have the same y value (sampleY[i])
heightSum += abs(maxY-minY);
}
return (heightSum / sampleX.length)/3.2;  // Convert from pixel to mm
}function getArea(ROIindex){
roiManager("deselect");
run("Clear Results");
roiManager("select", ROIindex);
run("Measure");
area = getResult("Area", 0);
run("Clear Results");
selectWindow("Results");
run("Close");
return area;
}function getPerimeter(ROIindex){ // Get perimeter of object at ROIindex
roiManager("deselect");
run("Clear Results");
roiManager("select", ROIindex);
run("Measure");
perim = getResult("Perim.", 0);
run("Clear Results");
selectWindow("Results");
run("Close");
return perim;
}function getXcentroid(ROIindex){ // Get X coordinate centroid of object at ROIindex
roiManager("deselect");
run("Clear Results");
roiManager("select", ROIindex);
run("Measure");
Xc = getResult("X", 0);
run("Clear Results");
selectWindow("Results");
run("Close");
return Xc;
}function getYcentroid(ROIindex){ // Get Y coordinate centroid of object at ROIindex
roiManager("deselect");
run("Clear Results");
roiManager("select", ROIindex);
run("Measure");
```

```
Yc = getResult("Y", 0);
run("Clear Results");
selectWindow("Results");
run("Close");
return Yc;
}function getGONJ(){
GONJroi = findROInamed("GONJ");
if (GONJroi == -1){
showMessageWithCancel("Warning!","WARNING: No Globe Optic Nerve Junction
found.\nPlease label junction.");
placeGONJprompt();
renameBySlice();
getGONJ();
}
else{
roiManager("select", GONJroi);
run("Set Scale...", "distance=256 known=80 unit=mm");
run("Set Measurements...", "area centroid bounding stack limit display invert nan
redirect=None decimal=3");
run("Clear Results");
run("Measure");
slice = getSliceNumber();
x = getResult("X", 0);
y = getResult("Y", 0);
print("Globe Optic Nerve Junction is in slice " + slice + "  at X: " + x + "  Y: " + y);
run("Clear Results");
selectWindow("Results");
run("Close");
}
}
//*********************   MAIN MENU   ****************************
function MainMenuPrompt(){
Dialog.create("Main Menu");
Dialog.addMessage(" ");
Dialog.addMessage("Select what you want to do.");
Dialog.addMessage(" ");
Dialog.addChoice("      ", newArray("Update ROI List", "Head Alignment", "Measure
Geometry", "Exit"));
Dialog.show();
choice = Dialog.getChoice();
if (choice == "Update ROI List"){
updateROIMenuLogic();
}
else if (choice == "Head Alignment"){
headAlignMenuLogic();
}
else if (choice == "Measure Geometry"){
measureGeoMenuLogic();
}
else{
```

```
run("Select None");
// Exit
}
}////////////////////////////////////////
////////////   Main Program   ////////////
//////////////////////////////////////////// Check status of GONJ
GONJrenamedSetting = false;
GONJroi = findROInamed("GONJ");
if (GONJroi != -1){
roiManager("select", GONJroi);
if(indexOf(Roi.getName, " 0 _GONJ_") > -1){
GONJrenamedSetting = true;
}
}MainMenuPrompt();
```